Sar sensitivity to burn severity and forest recovery in mediterranean environments - backscatter and interferometric coherence analysis

Mihai Andrei Tanase

Tesis Doctoral
Universidad de Zaragoza

SAR sensitivity to burn severity and forest recovery in mediterranean environments

- backscatter and interferometric coherence analysis

Mihai Andrei Tanase

SAR Sensitivity to Burn Severity and Forest Recovery in Mediterranean Environments – backscatter and interferometric coherence analysis

Tesis doctoral realizada por
MIHAI ANDREI TANASE

Dirigida por:

Prof. Juan Ramón de la Riva Fernández
Departamento de Geografía y Ordenación del Territorio
Universidad de Zaragoza

Dr. Maurizio Santoro
Gamma Remote Sensing AG

Departamento de Geografía y Ordenación del Territorio
Universidad de Zaragoza
Septiembre, 2010

Agradecimientos

Durante los últimos años son muchas las personas que me han apoyado y ayudado a conseguir el título de doctor. Desde aquí, agradeceros a todos por vuestra colaboración.

En primer lugar quiero agradecer a mis directores de tesis, Juan de la Riva, por haberme dado la posibilidad de formar parte del grupo de investigación del Departamento de Geografía hace cuatro años y Maurizio Santoro sin cuya ayuda habría sido mucho más difícil conseguir entender el complejo 'mundo' radar. Les agradezco enormemente que me hayan dado independencia plena en todo el trabajo y que, a pesar de su grado de ocupación, nunca me hayan negado un ratito para hablar de ciencia, de logística o de cualquier otra cosa. Gracias por vuestro apoyo, vuestros sabios consejos y la paciencia infinita que me habéis mostrado. Además, quiero agradecer a Fernando Pérez-Cabello que ha sido una persona muy pendiente de mi trabajo, casi actuando como co-director de esta tesis, por sus consejos sobre los procesos post-incendio y su ayuda en los muestreos de campo.

Asimismo debo agradecer al Grupo de Investigación Geoforest del Departamento de Geografía y Ordenación del Territorio de la Universidad de Zaragoza y a las personas que lo integran ya que durante estos años me han proporcionado un buen ambiente de investigación y financiado algunas actividades como el trabajo de campo, las imágenes satélites o los costes incurridos por la publicación de algunos de mis trabajos.

También quiero agradecer a Thuy Le Toan, Urs Wegmüller y Eric Kasischke por las estancias realizadas bajo su supervisión en el Centre d`Etudes Spatiales de la Biosphère, Gamma Remote Sensing y la Universidad de Maryland. Aprovechando su experiencia y apoyo he

recortado de modo significativo mi periodo de aprendizaje lo que ha hecho posible acabar a tiempo esta tesis.

Queda también agradecer a mis colegas becarios que durante estos largos años han compartido conmigo sus alegrías y angustias, el trabajo de campo y las horas interminables de trabajo en la sala de becarios.

Por último, a Cristina, por sus consejos de estadística, porque ha sabido aguantar mis momentos de inquietud -'no tengo tesis'-, me ha animado y ha estado siempre a mi lado incondicionalmente.

Abstract

Worldwide, forests fires destroy annually millions of hectares from tropical to boreal region. In the European part of the Mediterranean basin alone about five hundred thousand hectares are affected each year making fires one of the most important ecological threats. Remotely sensed data can contribute to a better, cost effective, objective and time saving method to monitor and quantify location, extent and intensity of fire events. Despite the extensive archives of space borne SAR data few studies were carried out having as topic forest fires. This thesis explores the prospects of radar data for post-fire studies highlighting not only its strengths but also the potential sources of error.

Regional models for burn severity assessment were developed using the field assessed (composite burn index - CBI) and optical based spectral indices (differenced Normalized Burn Ratio - dNBR) to assess the relationship strength between these variables across five recently burned sites in northeastern Spain. Linear and non-linear models were tested and the estimation error of each model was assessed. Synthetic aperture radar (SAR) data at X-, C- and L-band were investigated to determine the relationship between radar metrics (backscatter and interferometric coherence) and forest burn severity over three burn scars. The dependency of the SAR backscatter upon local incidence angle and environmental conditions has been also analyzed. Finally, SAR data were used to analyze SAR backscatter and interferometric coherence in regrowing forests previously affected by fire. L-band data analysis was extended to burned boreal forests. Statistical analysis was used to assess the radar metrics as a function of burn severity level or forest regrowth phase after stratifying the data by local incidence angle. Determination coefficients were used to quantify the relationship between radar data and burn severity estimates.

Fire scar differentiation using optical based indices is attainable in Aragón pine forests. Burn severity estimation errors for highly burned sites were well below 10 % whereas for low and moderate severity errors increased up to 25%. A strong linear relation was found between burn severity at plot level and understory and overstory composites. The analysis demonstrated the consistency of model inversion for burn severity estimation at regional level and the need for new estimation methods in areas affected by low to moderate burn severities even for homogeneous forests.

SAR metrics (backscatter and coherence) were sensitive to burn severity. For co-polarized channels (HH and VV) the backscatter increased with burn severity for X- and C-band whereas for L-band it decreased. Cross-polarized (HV) backscatter decreased with burn severity for all frequencies. The sensitivity of the co-polarized backscatter to burn severity decreased for increasing local incidence angle for all frequencies except at L-band. For X- and C-band co-polarized data higher determination coefficients were observed for slopes oriented towards the sensors whereas for cross-polarized data the determination coefficients were higher for slopes oriented away from the sensor. At L-band the association strength of cross-polarized data to burn severity was high for all local incidence angles.

Co-polarized coherence increased with the increase of burn severity at X- and C-band whereas cross-polarized coherence was practically insensitive to burn severity. Higher sensitivity to burn severity was found at L-band for both co- and cross-polarized channels. The association strength between coherence and burn severity was strongest for images acquired under stable, dry environmental conditions. When the local

incidence angle is accounted for the determination coefficients increased from 0.6 to 0.9 for X- and C-band. At L-band the local incidence angle had less influence on the association strength to burn severity. L-band (both metrics) showed the highest potential for burn severity estimation in the Mediterranean environment. The small dynamic range observed for X-band data could hinder its use in forests affected by fires. At L-band, the results from boreal forest confirmed the data trends obtained in the Mediterranean basin at least for specific environmental conditions (images acquired during the growing season in relatively dry conditions).

Low sensitivity to forest regrowth was observed for X-band backscatter, the average backscatter increasing by 1-2 dB between the most recent fire scars and the unburned forest. Envisat Advanced Synthetic Aperture (ASAR) C-band backscatter showed increased sensitivity, the backscatter difference between burned and unburned forest being around 4 dB. L-band backscatter presented the highest sensitivity to forest regrowth, the backscatter difference being approximately 8 dB. For a given frequency the sensitivity of the SAR backscatter to forest regrowth varied with local incidence angle and polarization. The interferometric coherence showed low sensitivity to forest regrowth at all SAR frequencies. For mediterranean forests five phases of forest regrowth were discerned whereas for boreal forest, up to four different regrowth phases could be discerned with L-band SAR data which is sensitive to vegetation structure. In comparison, the Normalized Difference Vegetation Index (NDVI) provided reliable differentiation only for the most recent development stages, as it registers information related to the vegetation cover. The results obtained were consistent in both environments.

This study indicates that SAR systems have potential for burn severity estimation using either the back-scattering coefficient or the interferometric coherence. The joint use of the backscatter coefficient and the interferometric coherence did not significantly improved burn severity estimation in any of the studied frequencies. Promising results were achieved for forest regrowth monitoring when using the backscatter coefficient of low frequency bands (L-). The higher frequency bands (X- and C-) showed low sensitivity to changes in forest structure, having little potential for differentiating between forest regrowth stages.

ÍNDICE

Capítulo 1. JUSTIFICACIÓN, OBJETIVOS Y CONTENIDO

Los incendios forestales son procesos ecológicos importantes que tienen una profunda influencia en el ciclo natural de la sucesión de la vegetación y la dinámica de los ecosistemas. Las características particulares de los incendios, tales como la intensidad, tipo, periodicidad, etc. influyen en gran medida en la dinámica del bosque, siendo factores determinantes en la recuperación de la vegetación. El elevado número de incendios forestales que se producen cada año se traduce en miles de hectáreas de superficie quemada, siendo uno de los principales factores de degradación de los ecosistemas mediterráneos (Koutsias y Karteris 2000). La supresión de los incendios durante los últimos 60-70 años ha aumentado la cantidad de combustible disponible en muchas partes del Mediterráneo. Tal acumulación podría promover incendios forestales de grandes dimensiones que antes eran históricamente raros (Ferry et al. 1995).

Desde 1960, el número de incendios y áreas quemadas en la vertiente europea del Mediterráneo ha aumentado constantemente. Sólo en 1985 se quemaron más de 1 millón de hectáreas de bosque y matorral - la mayor superficie jamás registrada. Durante todo el periodo, más de medio millón de hectáreas han sido anualmente calcinadas en Europa. En la siguiente década, los años 90, aunque el número medio de incendios por año aumentó más del 70%, la superficie media quemada por incendio disminuyó en un 30%. Esta disminución se atribuye a una respuesta más rápida y eficaz de los servicios de extinción debido a la mejora en la detección, el seguimiento y la evaluación del riesgo de incendio. Después de 2000, el número medio de incendios y la superficie quemada ha permanecido más o menos al mismo nivel. La tendencia anterior hacia un aumento en el número de incendios parece haberse estabilizado debido a las campañas de información pública llevadas a cabo en todos los países y a las mejoras introducidas en la prevención y la lucha contra los incendios forestales. En 2009 se quemó en la cuenca mediterránea una superficie total por debajo de la media de los últimos 25 años (Tabla 1); por el contrario, el número de incendios que se produjeron fue superior a la media (Schmuck et al. 2010).

En España, el número de incendios forestales ha aumentado desde unos 5000 en 1980 hasta alrededor de 20000 en el año 2000, mientras que la superficie media quemada en cada incendio ha disminuido de 25 a 5 ha durante el mismo periodo. En 2009, último año del que se dispone de datos estadísticos, el número de incendios forestales y la superficie quemada se situaron entre los más bajos de los últimos 20 años. Sólo alrededor de 110.000 hectáreas de bosque denso se calcinaron ese año y el área media quemada en cada incendio fue de tan sólo 5 ha.

Los cambios en la ocurrencia de incendios durante las últimas décadas reflejan los recientes cambios socio-económicos en los países europeos del Mediterráneo. El

Tabla 1 Evolución del área quemada en el sur de Europa.

Área quemada (ha)	Portugal	España	Francia	Italia	Grecia	Total
2009	87.416	110.783	17.000	73.355	35.342	323.896
% of total in 2009	27	34	5	23	11	100
Media 1980-1989	73.484	244.788	39.157	147.150	52.417	556.995
Media 1990-1999	102.203	161.319	22.735	118.573	44.108	448.938
Media 2000-2009	150.101	125.239	22.342	83.878	49.238	430.798
Media 1980-2009	108.956	177.115	28.078	116.534	48.587	478.910
Total (1980-2009)	3.257.886	5.313.457	842.332	3.496.005	1.457.624	14.367.304

Fuente: Forest Fires in Europe 2008, European Commission, Directorate General-Joint Research Center

desarrollo industrial ha inducido la despoblación de las zonas rurales, el aumento de la mecanización agrícola, la disminución de la presión del pastoreo y la extracción de madera y el aumento de la urbanización de las zonas rurales (Houereau 1983). Estos cambios en el estilo de vida y la utilización tradicional de la tierra han supuesto el abandono de grandes extensiones de cultivo, que ha conllevado la recuperación de la vegetación y el aumento del combustible acumulado (Roxo et al. 1996). Además, la actividad humana ha aumentado la frecuencia de los incendios, como consecuencia de la presión turística (Pausas y Ramon 1999). Piñol y Terradas (1996) encontraron una relación significativa entre la densidad de población y la ocurrencia de incendios en la zona mediterránea de la Península Ibérica. Como consecuencia de estos procesos, los paisajes son cada vez más homogéneos.

Una gestión forestal eficiente (pre- o post-incendio) requiere información variada sobre el tipo y la densidad de la cubierta vegetal, la cantidad y el tipo de combustibles disponibles, el contenido de humedad de estos últimos, las características topográficas y climáticas, el nivel de severidad del incendio, el grado de recuperación de la vegetación, etc. Para la toma de decisiones esta información se necesita no sólo a diversas escalas espaciales sino también temporales. En este contexto, la teledetección es especialmente adecuada para la investigación relacionada con los incendios forestales ya que gran parte de los datos requeridos se pueden obtener fácilmente utilizando la información subministrada por satélites espaciales. Ello es especialmente válido para la gestión de grandes superficies; la capacidad de los sensores satélites para cubrir amplias áreas con una alta frecuencia temporal y proporcionar información en diferentes longitudes de onda los convierte en herramientas valiosas para la prevención, la detección y la cartografía de los incendios forestales y las propiedades de los ecosistemas relacionados con los incendios. Durante la última década, el uso de las imágenes de satélite ha aumentado considerablemente y la teledetección espacial se ha convertido en un eficaz aliado en muchos planes estratégicos. El uso de los satélites permite ahorrar tiempo y recursos para cuantificar la ubicación, la extensión y la intensidad de los incendios (Chuvieco 1999).Hasta el momento, la mayoría de los estudios de área quemada han utilizado sensores ópticos para determinar la extensión del incendio (Koutsias y Karteris 2000; López-García y Caselles 1991; Stroppiana et al. 2003) los niveles de severidad (Hall et al. 2008; Patterson y Yool 1998; Santis y Chuvieco 2007) o la recuperación de la vegetación en las áreas afectadas (Díaz-Delgado et al. 2002; Henry y Hope 1998; Viedma et al. 1997). Los sensores radar se han utilizado sólo de forma ocasional, principalmente para la cartografía de área quemada (Bourgeau-Chavez et al. 1997; Gimeno et al. 2004; Ruecker y Siegert 2000) y, en menor medida, para el reconocimiento de los patrones de severidad o de recuperación vegetal. Sin embargo, estos sistemas pueden proporcionar información complementaria para el estudio de los efectos del fuego en áreas boscosas dado que la señal reflejada contiene información relacionada más con la estructura que con la cubierta vegetal (el caso de los sensores ópticos), proporcionando una herramienta útil para el seguimiento de la recuperación de la vegetación tras el cierre del dosel. Además, la sensibilidad de las microondas a la cantidad de dispersores presentes en la copa proporciona una medida que puede ser relacionada directamente con el grado de combustión de la vegetación por el fuego.

En esta tesis doctoral se pretende examinar esta línea de investigación, explorando las posibilidades que ofrecen los sensores radar para la estimación de la severidad y de la recuperación de la vegetación. Para abordar este objetivo general se definieron cuatro objetivos específicos: *i) utilizar las técnicas convencionales para obtener una referencia cartográfica de la severidad del fuego; ii) evaluar la sensibilidad del coeficiente de*

retro-dispersión radar a la severidad del fuego; iii) evaluar la sensibilidad de la coherencia interferométrica radar a la severidad del fuego y *iv) valorar la sensibilidad de los sensores radar a la recuperación de la vegetación tras el fuego*. Cada objetivo específico ha sido desarrollado en forma de publicaciones, acogiéndose la presente tesis doctoral a la modalidad de "compendio de artículos". La relación de artículos publicados, aceptados o en proceso de evaluación se presenta a continuación:

Objetivo específico	**Publicación correspondiente**
i. la utilización de las técnicas empíricas convencionales para obtener una referencia cartográfica de la severidad del fuego	Tanase, M.A., de la Riva, J. and Pérez-Cabello, F. (2010) Estimating burn severity in Aragón pine forests using a single empirical model. *Canadian Journal of Forest Research*, undergoing review.
ii. evaluación de la sensibilidad del coeficiente de retro-dispersión a la severidad del fuego	Tanase, M.A., Pérez-Cabello, F., de la Riva, J. and Santoro, M. (2010) TerraSAR-X data for burn severity evaluation in mediterranean forests on sloped terrain. *IEEE Transactions on Geoscience and Remote Sensing, Vol. 48 No. 2, pp. 917-929, 2010.*
	Tanase, M.A., Santoro, M., de la Riva, J. and Pérez-Cabello, F. (2009) Backscatter properties of multi-temporal TerraSAR-X data and the effects of influencing factors on burn severity evaluation, in a Mediterranean pine forest. *Geoscience and Remote Sensing Symposium, 2009 IEEE International, vol. III pp. 593-596*.
	Tanase, M.A., de la Riva, J., Santoro M., Le Toan, T. and Pérez-Cabello, F., (2010) Sensitivity of X-, C- and L-band SAR backscatter to fire severity in a mediterranean pine forest. *IEEE Transactions on Geoscience and Remote Sensing*, doi: 10.1109/TGRS.2010.2049653,in press.
	Tanase, M.A., Santoro, M., de la Riva, J., Kasischke, E., and Korets, M. A. (2010) L-band SAR backscatter prospects for burn severity estimation in boreal forests. *ESA Living Planet Symposium, SP-668 (CD-ROM) ESA Publications Division, European Space Agency, Noordwijk, The Netherlands.*
iii. evaluación de la sensibilidad de la coherencia interferométrica a la severidad del fuego	Tanase, M.A., Santoro, M., Wegmüller, U., de la Riva, J. and Pérez-Cabello, F. (2010) Properties of X-, C- and L-band repeat-pass interferometric SAR coherence in Mediterranean pine forests affected by fires. *Remote Sensing of Environment, Vol. 114, Issue 10, pp. 2182-2194, 2010.*
iv. valoración de la sensibilidad de los sensores radar a la recuperación de la vegetación tras el fuego	Tanase, M.A., Santoro, M., de la Riva, J., Kasischke, E. and Pérez-Cabello, F. (2010) Sensitivity of SAR data to post-fire forest regrowth in mediterranean and boreal environments. *Remote Sensing of Environment*, undergoing review.
	Kasischke, E., Tanase, M.A., Bourgeau-Chavez, L. and Borr, M. "Soil moisture limitations on monitoring boreal forest regrowth using space borne L-band SAR data" *Remote Sensing of Environment*, accepted.

El presente trabajo se estructura en cinco capítulos. En el primero, en el que se incluye este epígrafe, se introducen los objetivos además de presentar la justificación general de la investigación realizada.

En el segundo capítulo se hace una revisión del estado de conocimiento y de los métodos actuales para la estimación de la severidad del incendio y la recuperación vegetal en áreas incendiadas utilizando sensores ópticos. Además se introducen conceptos generales sobre los sistemas radar de apertura sintética (*Synthetic Aperture*

Radar – SAR), la retro-dispersión y la coherencia interferométrica. Por último se resalta el estado actual del uso del SAR en el ámbito post-incendio.

El tercer capítulo describe los métodos utilizados para la evaluación de la severidad y la recuperación de la vegetación mediante trabajo de campo e imágenes de satélite ópticas y radar. La investigación se ha apoyado en trabajo de campo realizado, principalmente, en el sector central del Valle del Ebro que constituye la principal área de estudio; esta zona ha sido afectada por numerosos incendios durante el último siglo, siendo idónea para analizar la respuesta de las especies forestales a las perturbaciones causadas por el fuego.

En el cuarto capítulo se describen los resultados obtenidos y se aborda su discusión. En primer lugar se analizan los incendios forestales mediante los métodos convencionales o más habituales (sensores ópticos) con el fin de establecer un punto de referencia para el nivel de la severidad. Asimismo se cuantifica tanto la relación existente entre los modelos empíricos derivados para diferentes incendios como los errores de la estimación. Por último, se desarrolla un modelo único para la estimación de la severidad en los pinares aragoneses mediante información procedente de sensores ópticos. La segunda y la tercera parte del capítulo se dedican al estudio de la sensibilidad del coeficiente de retro-dispersión y la coherencia interferométrica a la severidad del fuego. Se estudia la influencia de la topografía y de las condiciones climáticas en la estimación de la severidad y se analiza el uso conjunto del coeficiente de retro-dispersión y la coherencia. Además, se extiende el análisis a bosques boreales de Alaska y Siberia, utilizando el sensor satelital más sensible a los patrones de severidad. La localización remota y de difícil acceso de estos bosques, la gran extensión de la superficie anualmente afectada por fuego y la casi permanente cubierta nubosa constituyen incentivos en el uso de la teledetección basada en sensores radar. Por lo tanto, en esta tesis se realiza un estudio preliminar para averiguar la medida en que el conocimiento obtenido en ámbitos mediterráneos se podría aplicar en el ámbito boreal donde los datos de campo son mucho más difíciles de obtener. La última parte del capítulo cuatro se dedica al estudio de la recuperación vegetal en áreas quemadas mediante la información procedente de sensores radar; se estudian y se comparan tanto bosques mediterráneos afectados por incendio como bosques boreales. Asimismo se realiza una comparación de los sensores ópticos y radar y se analiza la influencia de la humedad sobre la estimación de la biomasa en bosques boreales jóvenes.

En este trabajo de tesis doctoral se han analizado e identificado nuevas herramientas que permiten estimar la severidad y la recuperación vegetal en áreas incendiadas utilizando sensores satelitales activos sensibles a los cambios estructurales de la vegetación. Para estos sensores se han identificado la longitud de onda y la polarización más apropiada para el análisis post-incendio.

BIBLIOGRAFÍA

Bourgeau-Chavez, L.L., Harrell, P.A., Kasischke, E.S., y French, N.H.F. (1997). The detection and mapping of Alaskan wildfires using a spaceborne imaging radar system. *International Journal of Remote Sensing, 18*, 355-373.

Chuvieco, E. (1999). Remote sensing of large wildfires. In E. Chuvieco (Ed.) (p. 212): Springer.

Díaz-Delgado, R., Lloret, F., Pons, X., y Terradas, J. (2002). Satellite evidence of decreasing resilience in Mediterranean plant communities after recurrent wildfires. *Ecology, 83*, 2293-2303.

Ferry, G.W., Clark, R.G., Montgomery, R.E., Mutch, R.W., Leenhouts, W.P., y Zimmerman, G.T. (1995). Altered fire regimes within fire-adapted ecosystems. *Our Living Resources: a report to the nation on the distribution, abundance, and health of U.S. plants animals, and ecosystems* (pp. 222-224). Washington D.C.: USDI National Biological Survey.

Gimeno, M., San-Miguel-Ayanz, J., y Schmuck, G. (2004). Identification of burnt areas in Mediterranean forest environments from ERS-2 SAR time series. *International Journal of Remote Sensing, 25*, 4873-4888.

Hall, R.J., D, J.T.F., Groot, W.J.d., Pritchard, J.M., Lynham, T.J., y Landry, R. (2008). Remote sensing of burn severity: experience from western Canada boreal fires. *International Journal of Wildland Fire, 17*.

Henry, M.C., y Hope, A.S. (1998). Monitoring post-burn recovery of chaparral vegetation in southern California using multi-temporal satellite data. *International Journal of Remote Sensing, 19*, 3097-3107.

Houereau, L. (1983). Land degradation in Mediterranean Europe: can agro forestry be a part of the solution? A prospective review. *Agrofor Sys, 21*, 43-61.

Koutsias, N., y Karteris, M. (2000). Burned area mapping using logistic regression modeling of a single post-fire Landsat-5 Thematic Mapper image. *International Journal of Remote Sensing, 21*, 673-687.

López-García, M.J., y Caselles, V. (1991). Mapping burns and natural reforestation using Thematic Mapper data. *Geocarta International, 61*, 31-37.

Patterson, M.W., y Yool, S.R. (1998). Mapping Fire-Induced Vegetation Mortality Using Landsat Thematic Mapper Data: A Comparison of Linear Transformation Techniques. *Remote Sensing of Environment, 65*, 132-142.

Pausas, J., y Ramon, V. (1999). The role of fire in European Mediterranean ecosystems. In E. Chuvieco (Ed.), *Remote Sensing of Large Wildfires* (pp. 3-16): Springer.

Piñol, J., y Terradas, J. (1996). Els incendis forestals al litoral mediterrani catalano-valencià en el període 1968-1995. *Butlletí del Centre d'Estudis Selvatans, 4*, 69-96.

Roxo, M.J., Cortesao, P., y Soeiro, B. (1996). Inner Lower Alentajo field site: Cereal cropping, soil degradation and desertification In C.J. Brandt y J. Thornes (Eds.), *Mediterranean desertification and land use* (pp. 111-135): J. Wiley & Sons.

Ruecker, G., y Siegert, F. (2000). Burn scar mapping and fire damage assessment using ERS-2 Sar images in East Kalimantan, Indonesia. *International Archives of Photogrammetry and Remote Sensing, 33*, 1286-1293.

Santis, A.d., y Chuvieco, E. (2007). Burn severity estimation from remotely sensed data: Performance of simulation versus empirical models. *Remote Sensing of Environment, 108*, 422-435.

Schmuck, G., San-Miguel-Ayanz, J., Camia, A., Kucera, J., Libertá, G., Boca, R., Durrant, T., and Amatulli, G. (2010). Forest Fires in Europe 2009. In, *JRC Scientific and Technical Reports*. Ispra, Italy: Joint Research Center.

Stroppiana, D., Tansey, K., Grégoire, J.-M., y Pereira, J.M.C. (2003). An Algorithm for Mapping Burnt Areas in Australia Using SPOT-VEGETATION Data. *IEEE Transactions on Geoscience and Remote Sensing, 41*, 907-909.

Viedma, Melia, J., Segarra, D., y Garcia-Haro, J. (1997). Modeling Rates of Ecosystem Recovery after Fires by Using Landsat TM Data. *Remote Sensing of Environment, 61*, 383-398.

Capítulo 2. LOS INCENDIOS FORESTALES Y LA TELEDETECCIÓN: EL RADAR DE APERTURA SINTÉTICA

Los estudios sobre incendios se clasifican en tres tipos según su dimensión temporal: pre-incendio, durante y post-incendio. Los primeros tratan de determinar principalmente el riesgo de ignición y el potencial de propagación del fuego, la disponibilidad y las propiedades de los combustibles, etc. Los segundos se centran principalmente en la detección de los focos activos y su comportamiento mientras que los últimos se orientan a la estimación de la extensión del área quemada, los niveles de severidad y la dinámica de recuperación del medio afectado. Hoy en día el uso de la teledetección se ha generalizado principalmente en los estudios relacionados con la estimación del riesgo, la detección de los focos activos y la estimación de la área quemada, siendo utilizada de forma operacional, rutinaria y automática. Sin embargo la mayoría de las aplicaciones operacionales utilizan información obtenida mediante sensores pasivos, faltando por conocer el potencial ofrecido por los sensores activos de tipo radar. A continuación se revisa, principalmente, el estado de conocimiento en relación con el segundo segmento temporal post-incendio, que es en el que se desarrolla esta tesis doctoral.

2.1. El uso de técnicas convencionales basadas en el óptico

La cartografía de área quemada ha sido una de las primeras aplicaciones de la teledetección en el estudio de los incendios forestales dada la necesidad de las agencias nacionales e internacionales de evaluar de forma rápida y precisa la extensión de las áreas afectadas. La sensibilidad de los sensores ópticos a la disminución de la reflectividad en el infrarrojo cercano debida al deterioro de la vegetación y el aumento en el infrarrojo medio de onda corta relacionado con el menor contenido de humedad de la vegetación y los suelos, la mayor exposición del sustrato y la presencia de combustibles quemados ha facilitado la cartografía de las áreas quemadas mediante índices de vegetación como el *Normalized Differenced Vegetation Index* (NDVI) (Rouse et al. 1973) o índices especialmente diseñados como *Normalized Burn Ratio* (NBR) (Key y Benson 2006). Este último se utiliza de modo rutinario para la estimación de áreas quemadas en EEUU, siendo uno de los índices espectrales más utilizados. NBR combina información del infrarrojo cercano y del infrarrojo medio de onda corta; la diferencia entre NBRs calculados para imágenes pre-y post-incendio (dNBR) se utiliza comúnmente en la cartografía de los niveles de severidad. dNBR expresa una gradación escala de los cambios acaecidos con respecto del estado pre-fuego, mientras las zonas no quemadas mantienen valores próximos a cero (es decir, poco o ningún cambio). En los últimos años, NBR y dNBR se han aplicado intensamente para estimar la severidad en una amplia variedad de condiciones, desde los bosques boreales hasta los mediterráneos (Allen y Sorbel 2008; Cocke et al. 2005; Santis y Chuvieco 2007; Wagtendonk et al. 2004; Wimberly y Reilly 2007).

Por otra parte, se han utilizado también modelos empíricos para correlacionar la severidad estimada en campo con los resultados de los índices obtenidos mediante imágenes de satélite (Díaz-Delgado et al. 2003; Epting et al. 2005; Roy et al. 2006; Wagtendonk et al. 2004). La estimación de la severidad a través de dNBR utiliza como datos de referencia un indicador de campo denominado *Composite Burn Index* (CBI), ya

sea el inicialmente propuesto por Key y Benson (2004) o su versión adaptada a las condiciones locales (Epting et al. 2005 y Santis y Chuvieco 2009). CBI fue diseñado para evaluar la magnitud de los efectos del fuego en todos los estratos del bosque desde una perspectiva ecológica. Las condiciones de la vegetación se examinan visualmente en un radio de 15 metros, estimándose el grado de cambio con respecto al estado anterior al incendio, que se registra desde 0 (ningún cambio) a 3 (variación del 100%). En general, dNBR junto con el CBI proporcionan una detección precisa de la severidad en la mayoría de los ecosistemas, siendo generalmente altos los coeficientes de determinación obtenidos (R^2> 0,75) (Allen y Sorbel 2008; Cocke et al. 2005; Epting et al. 2005; Wagtendonk et al. 2004). Sin embargo, algunos autores (Allen y Sorbel 2008; Hoy et al. 2008; Murphy et al. 2008) consiguieron relaciones más débiles entre dNBR y CBI en bosques boreales, lo que se atribuyó, por una parte, a la incapacidad del índice para distinguir entre severidades moderadas y altas y, por otra, a variaciones en la topografía, el ángulo de elevación solar (Verbyla et al. 2008) o las condiciones específicas de los combustibles. Para entornos mediterráneos los coeficientes de determinación entre dNBR y CBI son generalmente altos (Miller et al. 2009; Santis y Chuvieco 2009).

Los cambios en los valores de reflectividad causados por la desaparición de la ceniza, el aumento de la cobertura vegetal y la consiguiente disminución del suelo visible producen aumentos de la reflectividad en el infrarrojo próximo y disminuciones en las longitudes de onda del rojo y del azul (causadas por el aumento de la clorofila) que son fácilmente registrados por los sensores ópticos. Numerosos estudios han utilizado estas propiedades para estimar la recuperación de la cobertura vegetal después del incendio (Díaz-Delgado y Pons 2001; Henry y Hope 1998; Pérez-Cabello 2002; Wagtendonk et al. 2004). El índice NDVI ha sido la herramienta más utilizada para el seguimiento, el análisis y la cartografía espacial y temporal posterior al fuego (Díaz-Delgado et al. 2003; Díaz-Delgado et al. 2002; Viedma et al. 1997). Sin embargo, el NDVI es más sensible a los cambios en el área foliar que a los cambios en la biomasa (Henry y Hope 1998) y su relación con el *Leaf Area Index* (LAI) varía, llegando a la saturación para valores altos de LAI (Wang et al. 2005). Como consecuencia de ello, el seguimiento de la recuperación de la vegetación mediante el uso de índices basados en información proveniente de sensores ópticos se limita a los primeros años después del fuego, antes de que el dosel se cierre. El análisis de la recuperación vegetal en un bosque de robles en España mostró que los valores de NDVI se saturan después de sólo siete años (Díaz-Delgado y Pons 2001). Tendencias similares fueron detectadas en otros estudios en el entorno mediterráneo (Clemente et al. 2009; Vila y Barbosa 2010), mientras que en los bosques boreales la saturación del NDVI de produjo después de trece años (Cuevas-Gonzalez et al. 2009). Finalmente, hay que destacar que muchos de estos estudios consideran concluida la recuperación de la vegetación cuando los índices ópticos llegan a saturarse, aunque la estructura forestal y los niveles de biomasa anteriores al incendio no se alcancen hasta mucho después de la saturación de la señal óptica.

Los índices espectrales a menudo producen resultados imprecisos (Allen y Sorbel 2008; Hoy et al. 2008; Murphy et al. 2008) ya que se sirven de propiedades indirectas de las áreas quemadas, tales como el menor contenido de humedad de la vegetación y el suelo, el aumento de la exposición del sustrato y la presencia de cenizas. Estas propiedades son relativamente estables para niveles altos de severidad, pero se vuelven inconsistentes para niveles intermedios o bajos donde se combinan múltiples efectos. La mayoría de los estudios encontraron problemas para discriminar niveles intermedios de severidad (Chuvieco et al. 2006). Además los índices basados en información óptica son

también sensibles a la fenología de las plantas y la elevación solar, de modo que la evaluación de la severidad y el seguimiento temporal de la recuperación de la vegetación quedan sujetos a errores (Verbyla et al. 2008). Finalmente, los sensores ópticos son limitados en zonas de alta nubosidad, como las zonas tropicales o boreales, donde es muy difícil conseguir imágenes útiles con una alta resolución temporal.

2.2. El radar de apertura sintética

Tal y como se ha señalado en el primer capítulo, para cumplir el objetivo de esta tesis se utilizan imágenes procedente de sensores radar de apertura sintética *(Synthetic Aperture Radar* – SAR). La información proporcionada por los sensores radar difiere considerablemente de la obtenida mediante sensores ópticos por lo que, en las siguientes páginas, se presentan las características y propiedades generales de dichos sensores utilizados para obtener imágenes. Estos conceptos harán posible la comprensión de las publicaciones que constituyen la tesis doctoral.

2.2.1. Conceptos generales

El radar es un sistema coherente que se caracteriza por el uso de una fuente propia de energía. Por coherencia de la señal se entiende que la energía emitida proviene de una fuente puntual y es monocromática (es decir, que tiene la misma longitud de onda y fase), lo que implica que las ondas reflejadas por la superficie se combinan de manera vectorial. La mayoría de los sensores radar tienen la capacidad de registrar tanto la magnitud de la señal reflejada en su dirección como la fase. La magnitud depende del potencial de dispersión de las superficies y cambia con la forma, la posición y las propiedades dieléctricas de los objetos. La fase de cada objeto varía entre 0 y 2π y está principalmente relacionada con la distancia (ida y vuelta) hasta el sensor, describiendo la orientación del vector electromagnético. Los ecos recibidos son una forma modificada del pulso emitido, dependiendo de las características físicas y estructurales de la superficie detectada y de su distancia al sensor. La teledetección mediante técnica radar emplea longitudes de onda entre 1 mm y 1 m, siendo las más utilizadas las bandas (longitud de onda / frecuencia): X (2,4-3,75 cm / 12,5-8 GHz), C (3,75-7,5 cm / 8-4 GHz), S (7,5-15 cm / 4-2 GHz), L (15-30 cm / 2-1 GHz) y la P (30-100 cm / 1-0,3 GHz).

Una de las principales ventajas de los sensores radar es su independencia de la iluminación solar, dado que incorporan su propia fuente de energía. Además, las longitudes de onda utilizadas los hacen insensibles a la influencia de las nubes o la niebla, siendo sistemas idóneos para el análisis de regiones habitualmente cubiertas. En contraste con los sensores ópticos los radares pueden identificar con mayor precisión otras características de la superficie terrestre como la rugosidad, la humedad del suelo, las estructuras geológicas, la estructura de la vegetación, etc. En función de la escala del fenómeno a estudiar o de las características del terreno que se desean identificar se pueden seleccionar longitudes de onda más pequeñas o más grandes; en general, en el estudio de la vegetación se emplean longitudes de onda más grandes, que tienen mayor capacidad de penetración a través del follaje.

La antena del sistema radar se puede configurar para transmitir y recibir radiación electromagnética polarizada, horizontal o vertical (Fig. 1). Cuando la energía transmitida es polarizada en la misma dirección que la recibida, al sistema se le conoce como de

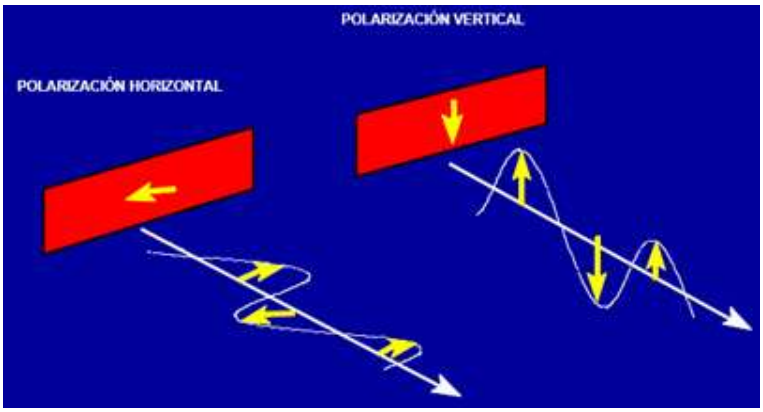

Fig. 1 Tipo de polarización de las ondas radar.
Fuente: Canada Centre for Remote Sensing (http://ccrs.nrcan.gc.ca/resource/index_e.php).

polarización similar: HH indica que la energía se transmite y se recibe en horizontal mientras que VV significa que la energía se transmite y se recibe de forma vertical. Si la energía transmitida se polariza en una dirección ortogonal a la recibida el sistema es de polarización cruzada (HV o VH, en función de la transmisión/recepción). La superficie puede modificar la polarización de las ondas reflejadas haciendo posible la identificación del tipo de superficie a partir de imágenes polarimétricas.

La resolución de las imágenes radar tiene dos dimensiones: alcance y azimut. El alcance es la distancia entre el sensor y la superficie detectada en dirección perpendicular a la trayectoria de la plataforma, mientras que el azimut es la distancia a lo largo de la trayectoria. Para incrementar la resolución espacial en la dirección del alcance los radares se sirven de una configuración lateral. Esto hace que los ecos reflejados por superficies situadas a distancia diferente con respecto al sensor lleguen con cierta separación temporal. La resolución espacial en alcance depende principalmente de la longitud del pulso; cuanto más corto es el pulso, mayor resolución se obtiene. Sin embargo, en la práctica no es posible emitir pulsos muy cortos debido a las pérdidas de energía en el trayecto de ida y vuelta de la señal. Por tanto, la resolución en alcance está limitada por características técnicas como la altura de la plataforma, la longitud de onda, la fuente de energía, etc. La mejora de la resolución en alcance es posible modulando la frecuencia de los pulsos emitidos; dicha modulación implica un aumento de la anchura de banda de la señal radar, lo que conlleva un aumento de la resolución espacial en alcance.

En la dirección del azimut la resolución espacial de un radar de apertura real (RAR) depende de la huella del haz que se relaciona con la longitud de onda, la dimensión de la antena y la altura de vuelo. Para un sensor situado en el espacio, la resolución en azimut de un RAR podría pasar de los 5 km, lo que resulta muy poco útil para numerosas aplicaciones. El radar de apertura sintética (SAR) reduce este tamaño hasta un orden de metros, sintetizando una antena (virtual) mucho más grande. Al moverse a lo largo de su trayectoria, el radar ilumina hacia un lado de la dirección de vuelo franjas continuas y paralelas entre sí de la superficie y acumula la información que se refleja. Una superficie se detecta desde múltiples posiciones acumulando el radar estos ecos; mediante procesamiento digital de la señal estos ecos son combinados, mejorándose la resolución en azimut.

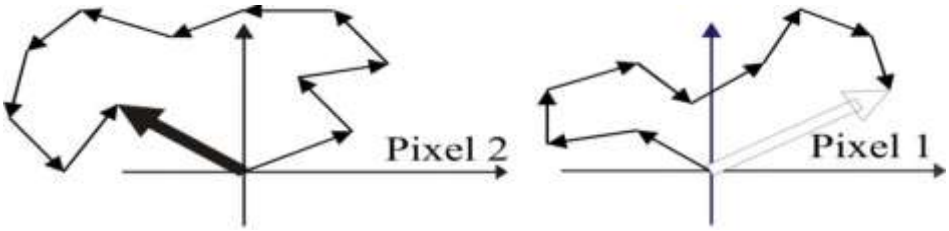

Fig. 2 Interferencia constructiva y destructiva de las contribuciones de cada objeto en el caso de blancos distribuidos.

La dirección de observación lateral ocasiona una distorsión del terreno en la dirección de alcance, siendo desplazados los objetos más altos hacia el sensor. En zonas con desnivel topográfico importante la iluminación lateral induce la aparición del escorzo (compresión de las características de la escena inclinadas hacia el sensor) o la inversión por relieve (los ecos reflejados por la porción superior de un objeto se reciben antes que los que provienen de la porción inferior). Además, hay porciones del terreno que no reciben energía, lo que ocasiona zonas de sombra que se presentan detrás de las cumbres en la dirección del alcance.

Cuando dentro de un píxel existen varios objetos, la señal reflejada es resultado de la combinación, por suma vectorial, de la contribución de cada uno (Fig. 2). El resultado es la interferencia constructiva y destructiva de las señales individuales, que modula la intensidad de la señal en cada píxel, produciendo el efecto de sal y pimienta de las imágenes radar. Este moteado (*speckle*) se puede reducir promediando conjuntos diferentes de datos para la misma superficie del terreno: *i)* dividiendo la apertura sintética en sub-aperturas, generándose observaciones independientes (sub-imágenes) de la región, que se promedian *a posteriori*; *ii)* promediando los píxeles adyacentes de una imagen de apertura completa. Ambos métodos implican una pérdida de resolución espacial proporcional a la atenuación del moteado. Sin embargo, la reducción del moteado no se relaciona de modo lineal con el número de sub-imágenes utilizada debido a la correlación existente entre píxeles adyacentes.

2.2.2. La retro-dispersión (*backscatter*)

Los pulsos emitidos por los sistemas radar llegan a la superficie terrestre siendo dispersados, transmitidos o absorbidos en diferentes proporciones en función del tipo de superficie; la parte dispersada que llega al receptor se llama retro-dispersión (*backscatter*). La retro-dispersión tiene como componentes tanto la magnitud como la fase. La fuerza de la señal radar que se conoce como coeficiente de retro-dispersión está relacionada con el cuadrado de la magnitud registrada por el sensor, se expresa como un número adimensional en decibelios (dB) y proporciona el promedio por metro cuadrado del potencial de retro-dispersión de las superficies.

La forma y la amplitud (magnitud y fase) del eco dependen de las propiedades de la superficie. Cuando dentro del píxel se encuentra sólo un objeto, la magnitud de la señal depende únicamente de su potencia de dispersión, mientras que la fase está relacionada principalmente con la distancia entre el objetivo y el sensor, aunque, en función del tipo de superficie, pueden introducirse pequeñas variaciones. Cuando el píxel está formado por objetos múltiples, la amplitud depende tanto de la potencia de dispersión de cada objeto como de las posiciones relativas dentro del píxel. La señal

individual de los objetos tiende a sumarse o a contrarrestarse en virtud de la combinación vectorial de la contribución de cada uno.

La capacidad de la señal radar para penetrar la atmosfera, la vegetación o la superficie terrestre aumenta con la longitud de onda. Los radares con longitudes de onda superiores a 2 cm son poco sensibles a los efectos de las nubes, mientras que las longitudes de onda superiores a 4 cm dejan de ser sensibles a la lluvia. La longitud de onda también determina la sensibilidad del SAR a la rugosidad de la superficie y a los componentes de la vegetación que contribuyen a la retro-dispersión total. En general, la longitud de onda utilizada debe ser función de las dimensiones de los objetos que se desean observar. Por ello, las bandas X y C son adecuadas para observar elementos de pequeñas dimensiones (nieve, superficie cubiertas por vegetación herbácea, cultivos, etc.), mientras que las bandas L y P son más apropiadas para detectar objetos de grandes dimensiones (vegetación arbórea, formaciones geológicas, áreas urbanas, estructuras arqueológicas, etc.). Otra característica importante a la hora de elegir un sistema radar es la polarización; en general, las ondas polarizadas horizontal (HH) son dispersadas en mayor medida por elementos cilíndricos con orientación horizontal, mientras que las ondas con polarización vertical (VV) lo son por elementos de orientación vertical. Las polarizaciones cruzadas (HV y VH) son más sensibles al volumen del reflector y menos sensibles al cambio en el ángulo de incidencia local. A continuación se exponen los principales factores que influyen la retro-dispersión.

2.2.2.1. La topografía

El relieve ejerce una influencia destacada sobre la retro-dispersión radar. La dependencia de la señal de la topografía se analiza mediante el ángulo de incidencia (θ_i) entre la dirección de la iluminación del radar y la superficie terrestre que cambia en la dirección del alcance en función de la altura de la plataforma (Fig. 3). Por lo tanto, la geometría de visualización en una misma imagen es diferente de punto a punto en la dirección del alcance. Diferencias sustanciales (> 20°) en el ángulo de incidencia son registradas en el caso de los sensores aeroportados o de las imágenes adquiridas en modo *scansar* por los sensores espaciales. Sin embargo, en el caso de las imágenes adquiridas en modo *stripmap* por sensores espaciales, como las analizadas en esta tesis, la diferencia en el ángulo de incidencia en alcance es pequeña (alrededor 5°-10°), debido a la altura del satélite y a la relativamente pequeña franja perpendicular de la superficie terrestre observada (*swath*). En zonas montañosas, la geometría de visualización también depende de la pendiente de la superficie iluminada, que determina el ángulo de incidencia local (θ_{loc}).

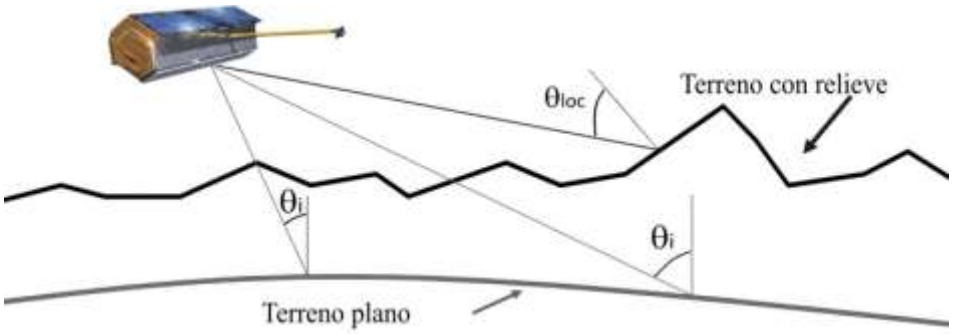

Fig. 3 El ángulo de incidencia en zonas con relieve y en zonas planas.

El ángulo de incidencia local influye de forma determinante en el brillo de la imagen; influencia que es más acusada para las ondas co-polarizadas, pues una pequeña inclinación del terreno modifica el mecanismo de la dispersión (van Zyl 1993). El cambio en el ángulo de incidencia local supone cambios sustanciales en la respuesta de la señal, especialmente en el caso de satélites con geometrías de visualización empinada. El brillo es sensible a la topografía (Raney 1999) y, por lo tanto, el ángulo de incidencia local resulta muy relevante en zonas con pronunciada energía de relieve, como la cuenca Mediterránea. El coeficiente de retro-dispersión disminuye con el incremento del ángulo de incidencia; sin embargo, el camino recorrido a través de las capas vegetales aumenta con el ángulo de incidencia, generando respuestas más altas para ángulos de incidencia elevados, especialmente para la polarización cruzada. Por el contrario, la dispersión directa del suelo se reduce con el ángulo de incidencia, lo que puede incrementar el contraste entre bosques y matorrales. La dependencia de la retro-dispersión respecto del ángulo de incidencia ha sido estudiada en bosques y pastizales (Luckman 1998), registrándose diferentes tendencias entre la polarización cruzada y las ondas co-polarizadas. En la banda C, la retro-dispersión de la copa parece dominar, pero este dominio se reduce en los ángulos de incidencia bajos dado el incremento de la dispersión de la superficie. Por lo tanto, el coeficiente de retro-dispersión debe ser compensado por el efecto angular (Holecz et al. 1995).

2.2.2.2. La constante dieléctrica

La propagación de las ondas electromagnéticas depende de la permeabilidad magnética y eléctrica del medio. La permeabilidad magnética es la misma para cualquier tipo de objeto de interés para las aplicaciones radar; sin embargo, la permeabilidad eléctrica varia de un medio a otro, y además, lo hace en función de la humedad dentro del mismo medio. La respuesta del objeto a la existencia del campo eléctrico está definida por la constante dieléctrica (ε_c), que depende principalmente de la constante dieléctrica relativa del material (ε`). Para la mayoría de los materiales, la constante dieléctrica varía entre 3 y 8; sin embargo, la constante dieléctrica del agua es de en torno a 80 (Lewis y Henderson 1999). Por tanto, cambios en el contenido de humedad alteran fuertemente el coeficiente de retro-dispersión (Grover et al. 1999), siendo menos adecuados los datos obtenidos después de periodos de lluvias para la clasificación (Ranson y Sun 2000; Saatchi et al. 1997) o la estimación de parámetros biofísicos en zonas boscosas (Harrell et al. 1995).

2.2.2.3. La rugosidad

La rugosidad de la superficie se expresa, según el criterio de Rayleigh, como la desviación estándar de las alturas de las irregularidades de la superficie y depende de la longitud de onda y del ángulo de incidencia (Lewis y Henderson 1999). Si la diferencia entre las fases de los objetos dentro de un píxel es pequeña (alturas similares de los objetos) las ondas reflejadas tienden a sumarse en la dirección especular, resultando mínima la señal recibida por el sensor. Cuando entre los objetos hay mayores diferencias de altura se produce un desfase entre las ondas reflejadas, tendiendo a cero la energía reflejada en la dirección especular. En conformidad con el principio de conservación de energía, las ondas se reflejarán hacia otras direcciones, siendo una de ellas la de la antena receptora del radar; por lo tanto, con el aumento de la rugosidad la retro-dispersión en la dirección del sensor radar aumentará (Fig. 4).

Fig. 4 Formas de retro-dispersión en función de la rugosidad del terreno.
Fuente: Canada Centre for Remote Sensing (http://ccrs.nrcan.gc.ca/resource/index_e.php).

2.2.3. La coherencia interferométrica

La interferometría se basa en el uso de un par de imágenes SAR adquiridas sobre la misma región desde ángulos de observación ligeramente distintos para generar el producto interferométrico complejo formado por: *i)* el interferograma, que representa la diferencia de fase entre las dos imágenes y, *ii)* la coherencia interferométrica, que representa la correlación entre la señal de las dos imágenes. El par de imágenes SAR pueden ser adquirido mediante una única pasada (*single-pass*), utilizando dos antenas a bordo de la misma plataforma espacial, pero separadas ligeramente, o constelaciones de dos o más satélites que sobrevuelan una misma zona simultáneamente (Fig. 5). Sin embargo, el método más utilizado por las plataformas espaciales es la adquisición de las imágenes por el mismo satélite durante orbitas sucesivas (*repeat-pass*). Para que las imágenes adquiridas en modo *repeat-pass* sean útiles para el procesamiento interferométrico las dos orbitas deben ser ligeramente diferentes y la escena debe mantener una coherencia razonable entre las dos pasadas sucesivas del satélite.

La información de la fase contenida en una única imagen SAR no se puede utilizar, dada la presencia del moteado; sin embargo, dos imágenes registradas desde una posición parecida tienen un patrón del moteado casi idéntico. La interferencia de la señal mediante el procesamiento interferométrico cancela la distribución aleatoria de la fase en el producto obtenido (el interferograma). La precisión de la estimación de la diferencia de las fases se relaciona con el grado de coherencia que se mide en una escala normalizada entre 0 (decorrelación total) y 1 (máxima coherencia).

La diferencia de la fase entre las dos imágenes se utiliza para obtener información sobre la altura o el movimiento de la superficie terrestre, mientras que la coherencia se

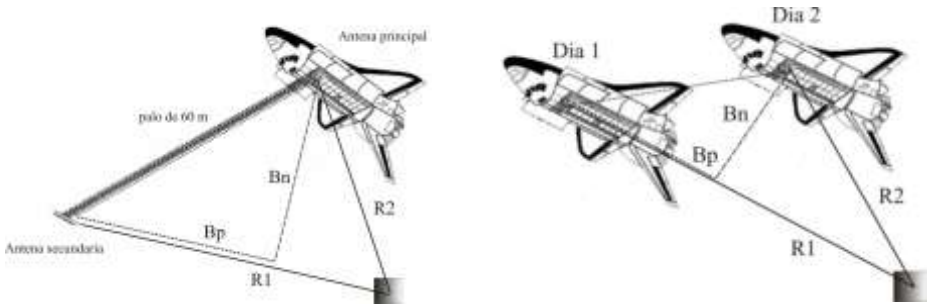

Fig. 5 Configuración de vuelo para la adquisición de imágenes interferométricas. La naveta espacial en su misión *single-pass* SRTM (izquierda) y *repeat-pass* SIR-C (derecha).

puede utilizar para analizar las propiedades bio-geofísicas de los objetos. El grado de coherencia interferométrica mide la correlación entre la señal de la retro-dispersión de un objeto determinado desde dos puntos de observación distintos, por lo que se relaciona con los efectos de decorrelación temporal y espacial (Zebker y Villasenor 1992). Como se ha expuesto anteriormente, la retro-dispersión de una misma superficie puede variar en el tiempo, principalmente en función de los cambios en la posición relativa de los objetos dentro del píxel o en la constante dieléctrica; por tanto, el mayor grado de correlación se obtiene para las adquisiciones *single-pass*. En las adquisiciones *repeat-pass* la coherencia depende del tipo de objeto, disminuyendo en aquellos que tienen una retro-dispersión de tipo volumen (vegetación) o que cambian en sus propiedades entre adquisiciones sucesivas (suelo seco a suelo mojado). En consecuencia las áreas boscosas tiene una coherencia mucho menor que, por ejemplo, las zonas urbanas, que se caracterizan por una retro-dispersión de tipo superficie y cambian poco entre adquisiciones sucesivas.

La coherencia y la fase interferométrica se ven afectadas por una serie de factores relacionados con la frecuencia del sistema SAR, la separación espacial entre las antenas y el intervalo temporal entre adquisiciones (Bamler y Hartl 1998). En un escenario de tomas secuenciales (*repeat-pass*), la coherencia está influenciada principalmente por la separación espacial de las antenas (decorrelación espacial) y la separación temporal de las adquisiciones (decorrelación temporal).

2.2.3.1. La decorrelación espacial

La ligera separación en el espacio entre las antenas, conocida como línea base (Bn) interferométrica (ver Fig. 5), implica que las distribuciones de las frecuencias que componen la señal radar (i.e. los espectros de las dos imágenes utilizadas) son ligeramente distintos. Si este desfase no se tiene en cuenta, el desplazamiento espectral origina la decorrelación espacial (Gatelli et al. 1994). Aunque este desplazamiento se puede compensar para la retro-dispersión de tipo superficie si se conoce la orientación del píxel, persiste aún una parte residual en el caso de los medios con retro-dispersión de tipo volumen, como los bosques (Hagberg et al. 1995); esta decorrelación residual se conoce como decorrelación del volumen. La decorrelación espacial residual, en el caso de la topografía no compensada, y la decorrelación del volumen, en el caso de medios estratificados, aumentan con el incremento de la componente perpendicular (Bn) de la línea base interferométrica (Hagberg et al. 1995). Para la misión tándem de los satélites ERS-1 y 2 y para el satélite TerraSAR-X la línea base perpendicular es despreciable, especialmente para introducir decorrelaciones geométricas importantes. En cambio, el tubo orbital más grande de la misión Envisat ha dado lugar a líneas base mayores, lo que limita su uso para la interferometría. La decorrelación del volumen está también directamente relacionada con el espesor de la copa.

2.2.3.2. La decorrelación temporal

La decorrelación temporal viene determinada por los cambios en la disposición de los dispersores dentro del píxel, por lo que la sensibilidad a la decorrelación temporal depende de la frecuencia del sistema. En las zonas boscosas el viento se considera la principal fuente de decorrelación temporal (Askne et al. 2003; Castel et al. 2000). Una rápida decorrelación aparece incluso para bajas velocidades de viento (Askne et al. 2003), en particular para los sistemas SAR de alta frecuencia (bandas X y C) donde una gran parte de la dispersión se origina en los primeros metros de la copa, donde se

encuentran los dispersores más inestables (ramas, ramitas, acículas, etc.). Otra fuente de decorrelación temporal es la variación de las condiciones ambientales, como el contenido de humedad y la congelación /descongelación del suelo (Koskinen et al. 2001). La oscilación diurna del contenido de humedad de la vegetación varía con la topografía (orientación) o con la evapotranspiración del bosque, lo que puede incrementar la decorrelación (Drezet y Quegan 2006). Finalmente, la variabilidad espacial de la distribución de la humedad del suelo dentro de un píxel se considera como fuente adicional de decorrelación (Luo et al. 2001). En general, la decorrelación temporal aumenta con el intervalo de tiempo entre adquisiciones cuando las condiciones ambientales se mantienen constantes.

2.3. Propiedades de las microondas en áreas boscosas

2.3.1. El coeficiente de retro-dispersión

La retro-dispersión de zonas boscosas incluye los componentes directos de la copa, de los troncos y del suelo, así como la retro-dispersión de rebote entre la copa y el suelo y entre los troncos y el suelo. En las ondas de baja frecuencia (L), la retro-dispersión de las ramas grandes y los troncos es significativa, mientras que en las altas frecuencias (X y C) domina la dispersión proveniente de hojas, ramillas y ramas dentro de la copa (Dobson et al. 1992; Harrell et al. 1997; Rignot et al. 1994b). La sensibilidad del coeficiente de retro-dispersión SAR a la biomasa depende de la longitud de onda y la polarización siendo mayor para los sensores de baja frecuencia y polarización cruzada. Por lo general, el coeficiente de retro-dispersión aumenta con el aumento de la biomasa, hasta llegar a un punto de estancamiento (saturación) en el que alcanza su máximo valor. El nivel de saturación de la señal depende, además de las características del sensor (longitud de onda y polarización), del tipo de bosque, de su estructura y de las condiciones ambientales. La diferencia entre el valor mínimo del coeficiente de retro-dispersión (suelo desnudo o zonas de crecimiento) y el nivel máximo (bosque denso) se conoce como rango dinámico y para las superficies forestales aumenta con el aumento de la longitud de onda.

En la banda X ($\lambda \approx 3$ cm; $f \approx 9$ GHz) las ondas interactúan sobre todo con hojas, ramitas y ramas pequeñas, siendo el componente predominante la dispersión de las copas. La contribución del sotobosque y del suelo está condicionada principalmente por la arquitectura de la copa (la forma, el grado de cerramiento, etc.) y el ángulo de incidencia, pudiéndose producir atenuaciones de hasta 20 dB (ida y vuelta) para bosques de coníferas (Hoekman 1987). Se ha demostrado que la eliminación de las hojas reduce el coeficiente de retro-dispersión (Leckie 1999), constituyendo una fuente importante para la dispersión de las microondas los elementos de tamaño similar a la longitud de onda (peciolos, por ejemplo). La sensibilidad a los parámetros forestales (biomasa de los troncos, altura, etc.) es relativamente baja en la banda X co-polarizada, alcanzando entre 2 y 3 dB para volúmenes de hasta 400 m^3/ha (Martínez et al. 2000; Pulliainen et al. 1994). Una mayor correlación lineal ($r = 0,60$) entre el coeficiente de retro-dispersión y el volumen del tronco se ha constatado en el caso de las ondas de polarización cruzada (HV), siendo inferior para ondas co-polarizadas (HH o VV, $r = 0,31$ y $0,38$, respectivamente) (Pulliainen et al. 1994). Una penetración de hasta 7,5 m ha sido documentada en bosques de pino en la banda X, registrándose valores más altos en

bosques maduros de baja densidad en los que la exposición del suelo y la penetración a través de aperturas en la copa era mayor (Martínez et al. 2000).

En las bandas C ($\lambda \approx 6$ cm; $f \approx 5$ GHz) y L ($\lambda \approx 23$ cm; $f \approx 1.2$ GHz) la retro-dispersión de la polarización cruzada que se origina principalmente por la dispersión múltiple dentro de la copa está menos influida por las condiciones de la superficie (Ranson y Sun 1994) y se relaciona sobre todo con la biomasa de las ramas, mientras que la retro-dispersión de las ondas co-polarizadas se relaciona más con la biomasa de los troncos (Rignot et al. 1995). La respuesta del radar para la biomasa forestal permanece baja en las banda C, con un rango dinámico de alrededor de 3 dB para las ondas co-polarizadas (Pulliainen et al. 1994), y 5 dB para la polarización cruzada (Dobson et al. 1992), mientras que para la banda L el rango dinámico aumenta hasta alrededor de 10 dB para la polarización cruzada (Dobson et al. 1992). En la banda C (HV), la saturación de la señal se alcanza entre 20 y 50 t/ha (Imhoff 1995; Rignot et al. 1994a), mientras que para la banda L (HV) el límite de saturación oscila entre 40 y 100 t/ha (Dobson et al. 1992; Imhoff 1995; Rignot et al. 1994a). Las ondas co-polarizadas son menos sensibles a los niveles de biomasa, pero presentan una mayor sensibilidad a las diferencias en la estructura de la cubierta.

2.3.2. La coherencia interferométrica

El coeficiente de retro-dispersión expresa la intensidad total recibida por el radar después de la dispersión; por lo tanto, no aporta información acerca de la disposición estructural de los dispersores individuales en el volumen de los bosques. La interferometría SAR ofrece, en su lugar, una medida directa de la distribución de los dispersores a través de la información de fase. En general, las imágenes de coherencia muestran un contraste importante, apareciendo brillantes las zonas ocupadas por suelo desnudo o por zonas urbanas (estables), mientras que los ríos o los bosques (inestables) aparecen en tonos oscuros. La coherencia disminuye con el incremento del espesor de la vegetación (Santoro et al. 2007), siendo significativamente menor en los bosques cerrados que en los bosques abiertos (Wegmüller y Werner 1995). La coherencia está vinculada a parámetros convencionales como la biomasa de los troncos o las etapas de crecimiento, debido a la menor contribución del terreno y al aumento de la retro-dispersión de tipo volumen de la copa, debido al incremento de los elementos dispersores (agujas, hojas, ramas) con la edad del bosque.

La utilidad de la coherencia interferométrica ha sido demostrada para una serie de aplicaciones temáticas, incluidas la clasificación del uso del suelo, la detección de cambios y la estimación de las propiedades de la cubierta vegetal. Durante la última década, la coherencia interferométrica (bandas C y L) ha sido utilizada para determinar la cantidad de biomasa forestal, proporcionando resultados precisos para imágenes adquiridas en condiciones atmosféricas idóneas (Askne et al. 2003). La precisión de la clasificación de la biomasa forestal en zonas boreales mediante el uso combinado de la coherencia y el coeficiente de retro-dispersión ha sido superior al 70% (Tansey et al. 2004), mientras que las zonas taladas han sido detectadas con una probabilidad de 95% (Smith y Askne 2001). Además, el uso de la coherencia ha hecho posible la identificación de diferentes tipos de bosques o cultivos utilizando datos multi-temporales (Strozzi et al. 2000; Wegmüller y Werner 1995). Una ventaja del uso de la coherencia interferométrica es su menor dependencia del relieve en comparación con el coeficiente de retro-dispersión (Castel et al. 2000; Santoro et al. 2007; Wegmüller y Werner 1995).

2.4. Aplicaciones del radar de apertura sintética a la estimación de áreas quemadas, la severidad de los incendios y la recuperación de la vegetación

A pesar de los extensos archivos de imágenes SAR existentes, se han llevado a cabo pocos estudios orientados al análisis de los incendios forestales. La mayoría de ellos se han centrado en la cartografía de área quemada en bosques boreales y tropicales (Bourgeau-Chavez et al. 1997; Bourgeau-Chavez et al. 2002; French et al. 1999; Huang y Siegert 2004; Liew et al. 1999; Menges et al. 2004; Siegert y Hoffmann 2000; Siegert y Nakayama 2000; Siegert y Ruecker 2000). El periodo de tiempo relativamente corto transcurrido desde que tales sensores están disponibles, la diferente geometría de visualización, la falta de herramientas para el procesamiento de las imágenes y la dificultad que entraña el moteado para su comprensión han sido algunos de los principales factores que han retardado el uso habitual de las imágenes SAR. Sin embargo, el aumento en la última década del número de satélites radar en orbita, la puesta a punto de nuevos métodos de tratamiento de las imágenes, la necesidad de obtener información sistemática en zonas habitualmente cubiertas y la disponibilidad de sensores con longitudes de ondas y polarizaciones adecuadas a la observación de la superficie terrestre explican su uso creciente y significativo en muy diversos ámbitos de aplicación de la teledetección.

2.4.1. El coeficiente de retro-dispersión

2.4.1.1. Estimación de área quemada y de la severidad del incendio

La combustión de la copa a menudo tiene como resultado la eliminación completa de las acículas, las ramas y las ramitas convirtiéndose en la fuente más importante de retro-dispersión. Para especies mediterráneas, los primeros 30 cm de la copa contienen la mayor parte del follaje, siendo el contenido relativo de humedad de las hojas más elevado que para las partes leñosas (Sternberg y Shoshany 2001). La alta densidad de hojas y su alto contenido de humedad impide la penetración de las ondas de alta frecuencia (bandas X y C) a las capas más bajas, con mayor contenido de ramas, y al suelo (Svoray y Shoshany 2003), que pueden tener un potencial superior de retro-dispersión (Svoray et al. 2001). Las ondas de baja frecuencia (banda L) penetran en mayor medida en el dosel, interactuando más con las grandes ramas, los troncos de los árboles y el suelo (Le Toan et al. 1992). La combustión de las hojas y las ramas tiene un efecto directo sobre la dispersión de la copa. Para niveles altos de severidad se espera la reducción del coeficiente de retro-dispersión en el caso de la polarización cruzada. El fuego también aumenta la exposición del suelo, que se puede utilizar para la estimación de la severidad con las ondas co-polarizadas. Sin embargo, la destrucción de la vegetación hace las mediciones del radar sensibles al estado del terreno subyacente (Saich et al. 2001), dependiendo la retro-dispersión no sólo de las características del bosque, sino también de la humedad del suelo y de su rugosidad.

Efectos ambiguos han sido encontrados al estudiar el impacto del fuego sobre el coeficiente de retro-dispersión. Una fuerte disminución fue observada para la banda C polarización VV en los bosques tropicales durante periodos caracterizados por poca humedad, debido a la disminución de la retro-dispersión de la copa y al incremento de la energía solar, que disminuyó la humedad del suelo (Ruecker y Siegert 2000; Siegert et

al. 1999). Después de las lluvias, la mayor retro-dispersión del área quemada, debida al incremento de la humedad del suelo, dificultó su discriminación de las zonas no quemadas (Siegert y Ruecker 2000). Para los bosques templados el coeficiente de retro-dispersión (bandas C y L en cualquier polarización) fue más bajo en las zonas afectadas por el fuego que en el bosque no quemado próximo (Rignot et al. 1999), mientras que para los bosques abiertos y los matorrales quemados de Australia el coeficiente de retro-dispersión en la banda L aumentó para las ondas co-polarizado y disminuyó para la polarización cruzada (Menges et al. 2004). En los bosques boreales afectados por incendios, el coeficiente de retro-dispersión en la banda C (polarización VV) fue más alto en comparación con las zonas adyacentes no quemadas en condiciones de humedad del suelo alta (Bourgeau-Chavez et al. 1997; Bourgeau-Chavez et al. 2002; Huang y Siegert 2006; Kasischke et al. 1994), mientras que se registraron niveles más bajos en las zonas con mejor drenaje (Kasischke et al. 1994). Por último, para los bosques mediterráneos, Gimeno et al. (2004) encontraron que el coeficiente de retro-dispersión en la banda C incrementa para las ondas co-polarizadas independientemente de la precipitación acumulada. No obstante, en algunos estudios se ha observado una mejora en la diferenciación de las zonas quemadas tras la lluvia (Gimeno y San-Miguel-Ayanz 2004), mientras que estudios anteriores mostraron la fuerte dependencia de la señal radar a cambios en las propiedades dieléctricas de las superficies quemadas (Bourgeau-Chavez et al. 1994; Bourgeau-Chavez et al. 2007).

La topografía ejerce una gran influencia en el coeficiente de retro-dispersión de las zonas quemadas, apareciendo más brillantes las laderas orientadas hacia el sensor. Pequeños ángulos de incidencia local han resultado más útiles para discriminar áreas quemadas en una región montañosa del Mediterráneo mediante imágenes co-polarizadas de banda C (Gimeno y San-Miguel-Ayanz 2004).

2.4.1.2. Estimación de la recuperación vegetal tras el incendio

El uso de las imágenes SAR para la evaluación de la recuperación vegetal post-incendio proporciona información relacionada con la estructura forestal, influyendo directamente la cantidad de biomasa en la magnitud de la energía dispersada. Así, el coeficiente de retro-dispersión aumenta con la densidad del bosque, alcanzando la saturación en función del tipo de bosque y su estructura. Una mayor sensibilidad a la estimación de la recuperación de los bosques se ha obtenido utilizando la banda L (polarización HH), frente a la banda C (polarización VV), en una área quemada de diez años de edad en China (Sun et al. 2002); la mayor longitud de onda (banda L) permitió la diferenciación entre el bosque joven y los rodales maduros. En un ambiente mediterráneo, los cambios temporales en la biomasa forestal después de incendios han sido estimados mediante el análisis temporal de la respuesta en la banda C (polarización VV) para caracterizar el proceso de la recuperación de la vegetación (Minchella et al. 2009). Estos estudios utilizaron el coeficiente de retro-dispersión de ondas co-polarizadas; sin embargo, la polarización cruzada, más sensible a los cambios en biomasa y estructura vegetal, podría proporcionar una mejor diferenciación entre las etapas de recuperación de los bosques afectados por incendios.

2.4.2. La coherencia interferométrica

La mayoría de las investigaciones se han llevado a cabo utilizando los satélites ERS-1 y ERS-2 durante la misión tándem, dados el corto intervalo de adquisición (1 día)

y la disponibilidad casi global de los datos. En la banda X, imágenes espaciales de uso interferométrico han sido previamente adquiridas durante la misión SIR-C en un solo paso, mientras que las imágenes en banda L han estado disponibles mediante el satélite Japanease Earth Remote Sensing (JERS-1) de la Agencia Espacial Japonesa (JAXA). El potencial de la coherencia interferométrica (*repeat-pass*) para las aplicaciones relacionadas con los bosques ha sido demostrado en una serie de aplicaciones temáticas, como la cartografía del uso del suelo y de la cubierta vegetal (Castel et al. 2000; Wegmüller y Werner 1997), la detección de cambios temporales y la estimación de propiedades bio-geofísicas (Askne et al. 2003; Santoro et al. 2002). En zonas forestales afectadas por incendios, la coherencia aumenta de modo significativo con respecto a los bosques no quemados (Liew et al. 1999; Takeuchi y Yamada 2002); esperándose una menor coherencia en las zonas afectadas por baja severidad, debido a la cubierta vegetal restante. Con el incremento de la severidad se eliminan de modo progresivo los elementos dispersores pequeños (acículas, hojas, ramas), lo que conduce a una mayor coherencia, aproximándose los valores al nivel de suelo desnudo en las áreas donde la combustión de la vegetación es completa. A corto plazo, después de aumentar, la coherencia gradualmente se desvanece como consecuencia de la recuperación del bosque, ya que la dispersión de la copa combinada con la decorrelación temporal son factores importantes en las zonas boscosas.

BIBLIOGRAFÍA

Allen, J.L., y Sorbel, B. (2008). Assessing the differenced Normalized Burn Ratio's ability to map burn severity in the boreal forest and tundra ecosystems of Alaska's national parks. *International Journal of Wildland Fire, 17*, 463-475.

Askne, J.I.H., Santoro, M., Smith, G., y Fransson, J.E.S. (2003). Multitemporal Repeat-Pass SAR Interferometry of Boreal Forests. *IEEE Transactions on Geoscience and Remote Sensing, 41*, 1540-1550.

Bamler, R., y Hartl, P. (1998). Synthetic aperture radar interferometry. *Inverse Problems, 14*, 1-54.

Bourgeau-Chavez, L.L., Harrell, P.A., Kasischke, E.S., y French, N.H.F. (1997). The detection and mapping of Alaskan wildfires using a spaceborne imaging radar system. *International Journal of Remote Sensing, 18*, 355-373.

Bourgeau-Chavez, L.L., Kasischke, E.S., Brunzell, S., y Mudd, J.P. (2002). Mapping fire scars in global boreal forests using imaging radar data. *International Journal of Remote Sensing, 23*, 4211-4234.

Bourgeau-Chavez, L.L., Kasischke, E.S., French, N.H.F., Szeto, L.H., y Kherkher, C.M. (1994). Using ERS-1 SAR Imagery to Monitor Variations in Burn Severity in an Alaskan Fire-Disturbed Boreal Forest Ecosystem. In, *Geoscience and Remote Sensing Symposium, 1994. IGARSS '94. Proceedings. 1994 IEEE International* (pp. 243-245). Pasadena, California.

Bourgeau-Chavez, L.L., Kasischke, E.S., Riordan, K., Brunzell, S., Nolan, M., Hyer, E., Slawski, J., Medvecz, M., Walters, T., y Ames, S. (2007). Remote monitoring of spatial and temporal surface soil moisture in fire disturbed boreal forest ecosystems with ERS SAR imagery. *International Journal of Remote Sensing, 28*, 2133-2162.

Castel, T., Martinez, J.-M., Beaudoin, A., Wegmüller, U., y Strozzi, T. (2000). ERS INSAR Data for Remote Sensing Hilly Forested Areas. *Remote Sensing of Environment, 73*, 73-86.

Clemente, R.H., Cerrillo, R.M.N., y Gitas, I.Z. (2009). Monitoring post-fire regeneration in Mediterranean ecosystems by employing multitemporal satellite imagery. *International Journal of Wildland Fire, 18*, 648-658.

Cocke, A.E., Fule, P.Z., y Crouse, J.E. (2005). Influence of fire severity on plant regeneration by means of remote sensing imagery. *International Journal of Wildland Fire, 14*, 189-198.

Cuevas-Gonzalez, M., Gerard, F., Balzter, H., y Riano, D. (2009). Analysing forest recovery after wildfire disturbance in boreal Siberia using remotely sensed vegetation indices. *Global Change Biology, 15*, 561-577.

Chuvieco, E., Riaño, D., Danson, F.M., y Martín, P. (2006). Use of a radiative transfer model to simulate the postfire spectral response to burn severity. *Journal of Geophysical Research, 111*, 1-15.

Díaz-Delgado, R., Lloret, F., y Pons, X. (2003). Influence of fire severity on plant regeneration by means of remote sensing imagery. *International Journal of Remote Sensing, 24*, 1751-1763.

Díaz-Delgado, R., Lloret, F., Pons, X., y Terradas, J. (2002). Satellite evidence of decreasing resilience in Mediterranean plant communities after recurrent wildfires. *Ecology, 83*, 2293-2303.

Díaz-Delgado, R., y Pons, X. (2001). Spatial patterns of forest fires in Catalonia (NE Spain) along the period 1975-1995 Analysis of vegetation recovery after fire. *Forest Ecology and Management, 147*, 67-74.

Dobson, M.C., Ulaby, T., Le Toan, T., Beaudoin, A., y Kasischke, E.S. (1992). Dependence of radar backscatter on coniferous forest biomass. *IEEE Transactions on Geoscience and Remote Sensing, 30* 412-415.

Drezet, P.M.L., y Quegan, S. (2006). Environmental Effects on the Interferometric Repeat-Pass Coherence of Forests. *IEEE Transactions on Geoscience and Remote Sensing, 44*, 825-837

Epting, J., Verbyla, D., y Sorbel, B. (2005). Evaluation of remotely sensed indices for assessing burn severity in interior Alaska using Landsat TM and ETM+. *Remote Sensing of Environment, 96*, 328-339.

French, N.H.F., Bourgeau-Chavez, L.L., Wang, Y., y Kasischke, E.S. (1999). Initial Observations of Radarsat Imagery at Fire-Disturbed Sites in Interior Alaska. *Remote Sensing of Environment, 68*, 89-94.

Gatelli, F., Guarnieri, A.M., Parizzi, F., Pasquali, P., C.Prati, y Rocca, F. (1994). The wavenumber shift in SAR interferometry. *IEEE Transactions on Geoscience and Remote Sensing, 32*, 855-865.

Gimeno, M., y San-Miguel-Ayanz, J. (2004). Evaluation of RADARSAT-1 data for identification of burnt areas in Southern Europe. *Remote Sensing of Environment, 92*, 370-375.

Gimeno, M., San-Miguel-Ayanz, J., y Schmuck, G. (2004). Identification of burnt areas in Mediterranean forest environments from ERS-2 SAR time series. *International Journal of Remote Sensing, 25*, 4873-4888.

Grover, K., Quegan, S., y Freitas, C.d.C. (1999). Quantitative Estimation of Tropical Forest Cover by SAR. *IEEE Transactions on Geoscience and Remote Sensing, 37*, 479-489.

Hagberg, J.O., Ulander, L.M.H., y Askne, J. (1995). Repeat-Pass SAR Interferometry Over Forested Terrain. *IEEE Transactions on Geoscience and Remote Sensing, 33*, 331-340.

Harrell, P.A., Bourgeau-Chavez, L.L., Kasischke, E.S., French, N.H.F., y Christensen, N.L. (1995). Sensitivity of ERS-1 and JERS-1 Radar Data to Biomass and Stand Structure in Alaskan Boreal Forest. *Remote Sensing of Environment, 54*, 247-260.

Harrell, P.A., Kasischke, E.S., Bourgeau-Chavez, L.L., Haney, E.M., y Jr., N.L.C. (1997). Evaluation of Approaches Aboveground Biomass in Using SIR-C Data to Estimating Southern Pine Forests *Remote Sensing of Environment, 59*, 223-233.

Henry, M.C., y Hope, A.S. (1998). Monitoring post-burn recovery of chaparral vegetation in southern California using multi-temporal satellite data. *International Journal of Remote Sensing, 19*, 3097-3107.

Hoekman, D.H. (1987). Measurements of the Backscatter and Attenuation Properties of Forest Stands at X-, C- and L-band. *Remote Sensing of Environment, 23*, 397-416.

Holecz, F., Wegmüller, U., Rignot, E., y Wang, Y. (1995). Observed radar backscatter from forested areas with terrain variations. In, *Geoscience and Remote Sensing Symposium, 1995. IGARSS '95. Proceedings. 1995 IEEE International* (pp. 613-615). Firenze, Italy.

Hoy, E.E., French, N.H.F., Turetsky, M.R., Trigg, S.N., y Kasischke, E.S. (2008). Evaluating the potential of Landsat TM/ETM+ imagery for assessing fire severity in Alaskan black spruce forests. *International Journal of Wildland Fire, 17*, 500-514.

Huang, S., y Siegert, F. (2004). ENVISAT multisensor data for fire monitoring and impact assessment. *International Journal of Remote Sensing, 25*, 4411-4416.

Huang, S., y Siegert, F. (2006). Backscatter Change on Fire Scars in Siberian Boreal Forests in ENVISAT ASAR Wide-Swath Images. *IEEE Transactions on Geoscience and Remote Sensing Letters, 3*, 154-158.

Imhoff, M.L. (1995). Radar Backscatter and Biomass Saturation: Ramifications for Global Biomass Inventory. *IEEE Transactions on Geoscience and Remote Sensing, 33*, 511-518.

Kasischke, E.S., Bourgeau-Chavez, L.L., y French, N.H.F. (1994). Observations of Variations in ERS-1 SAR Image Intensity Associated with Forest Fires in Alaska. *IEEE Transactions on Geoscience and Remote Sensing, 32*, 206-210.

Key, C.H., y Benson, N.C. (2004). *Ground Measure of Severity, The Composite Burn Index*. Ogden, UT: U.S. Department of Agriculture, Forest Service, Rocky Mountain Research Station.

Key, C.H., y Benson, N.C. (2006). Landscape assessment (LA). In D.C. Lutes, R.E. Keane, J.F. Caratti, C.H. Key, N.C. Benson, S. Sutherland y L.J. Gangi (Eds.), *FIREMON: Fire effects monitoring and inventory system* (pp. 1-55). Fort Collins, CO: U.S. Department of Agriculture, Forest Service, Rocky Mountain Research Station, Gen. Tech. Rep. RMRS-GTR-164-CD.

Koskinen, J.T., Pulliainen, J.T., Hyyppä, J.M., Marcus E. Engdahl, y Hallikainen, M.T. (2001). The Seasonal Behavior of Interferometric Coherence in Boreal Forest. *IEEE Transactions on Geoscience and Remote Sensing, 39*, 820-829.

Leckie, D.G. (1999). Forestry Applications Using Imaging Radar. In F.M. Henderson y A.J. Lewis (Eds.), *Principles and Applications of Imaging Radar* (p. 866): John Wiley & Sons.

Lewis, A.J., y Henderson, F.M. (1999). Radar Fundamentals: The Geoscience perspective. In F.M. Henderson y A.J. Lewis (Eds.), *Principles and Applications of Imaging Radar* (p. 866): John Wiley & Sons.

Liew, S.C., Kwoh, L.K., Padmanabhan, K., Lim, O.K., y Lim, H. (1999). Delineating Land/Forest Fire Burnt Scars with ERS Interferometric Synthetic Aperture Radar. *Geophysical Research Letters, 26*, 2409-2412.

Luckman, A.J. (1998). The Effects of Topography on Mechanism of Radar Backscatter from Coniferous Forest and Upland Pasture. *IEEE Transactions on Geoscience and Remote Sensing, 36*, 1830-1834.

Luo, X., Askne, J., Smith, G., y Dammert, P. (2001). Coherence characteristics of radar signals from rough soil. *Progress in Electromagnetic Research, 31*, 69-88.

Martínez, J.M., Floury, N., Le Toan, T., Beaudoin, A., Hallikainen, M.T., y Makynen, M. (2000). Measurements and Modeling of Vertical Backscatter Distribution in Forest Canopy. *IEEE Transactions on Geoscience and Remote Sensing, 38*, 710-719.

Menges, C.H., Bartolo, R.E., Bell, D., y Hill, G.J.E. (2004). The effect of savanna fires on SAR backscatter in northern Australia. *International Journal of Remote Sensing, 25*, 4857-4871.

Miller, J.D., Knapp, E.E., Key, C.H., Skinner, C.N., Isbell, C.J., Creasy, R.M., y Sherlocke, J.W. (2009). Calibration and validation of the relative differenced Normalized Burn Ratio (RdNBR) to three measures of fire severity in the Sierra Nevada and Klamath Mountains, California, USA. *Remote Sensing of Environment, 113*, 645-656.

Minchella, A., Del Frate, F., Capogna, F., Anselmi, S., y Manes, F. (2009). Use of multitemporal SAR data for monitoring vegetation recovery of Mediterranean burned areas. *Remote Sensing of Environment, 113*, 588-597.

Murphy, K.A., Reynolds, J.H., y Koltun, J.M. (2008). Evaluating the ability of the differenced Normalized Burn Ratio (dNBR) to predict ecologically significant burn severity in Alaskan boreal forests. *International Journal of Wildland Fire, 17*, 490-499.

Pérez-Cabello, F. (2002). *Paisajes forestales y fuego en el Prepirineo occidental oscense. Un modelo regional de reconstrucción ambiental*. Zaragoza.

Pulliainen, J.T., Heiska, K., Hyyappa, J., y Hallikainen, M.T. (1994). Backscattering properties of boreal forests at the C- and X-Bands. *IEEE Transactions on Geoscience and Remote Sensing, 32*, 1041-1050.

Raney, K. (1999). Radar Fundamentals: Technical Perspective. In F.M. Henderson y A.J. Lewis (Eds.), *Principles and Applications of Imaging Radar* (p. 866): John Wiley & Sons.

Ranson, K.J., y Sun, G. (1994). Mapping Biomass of a Northem Forest Using Multifrequency SAR Data. *IEEE Transactions on Geoscience and Remote Sensing, 32*, 388-396.

Ranson, K.J., y Sun, G. (2000). Effects of Environmental Conditions on Boreal Forest Classification and Biomass Estimates with SAR. *IEEE Transactions on Geoscience and Remote Sensing, 38*, 1242-1252.

Rignot, E., Despain, D.G., y Holecz, F. (1999). The 1988 Yellowstone fires observed by imaging radars. In, *Proceedings of the Joint Fire Sciences Conference and Workshop*.

Rignot, E., Way, J., Williams, C., y Viereck, L. (1994a). Radar Estimates of Aboveground Biomass in Boreal Forests of Interior Alaska. *IEEE Transactions on Geoscience and Remote Sensing, 32*, 1117-1124.

Rignot, E.J., Zimmermann, R., y van Zyl, J.J. (1995). Spacebome Applications of P Band Imaging Radars for Measuring Forest Biomass. *IEEE Transactions on Geoscience and Remote Sensing, 33*, 1162-1169.

Rignot, J., CL, W., J, W., y LA, V. (1994b). Mapping of forest types in Alaskan boreal forests using SAR imagery. *IEEE Transactions on Geoscience and Remote Sensing, 32*, 1051-1059

Rouse, J.W., Haas, R.H., Schell, J.A., y D.W., D. (1973). Monitoring vegetation systems in the Great Plains with ERTS In, *Third ERTS Symposium* (pp. 309-317).

Roy, D.P., Boschetti, L., y Trigg, S.N. (2006). Remote Sensing of Fire Severity: Assessing the Performance of the Normalized Burn Ratio. *IEEE Transactions on Geoscience and Remote Sensing Letters*, 1-5.

Ruecker, G., y Siegert, F. (2000). Burn scar mapping and fire damage assessment using ERS-2 Sar images in East Kalimantan, Indonesia. *International Archives of Photogrammetry and Remote Sensing, 33*, 1286-1293.

Saatchi, S.S., Soares, J.V., y Alves, D.S. (1997). Mapping Amazon Deforestation and Land Use in Amazon Rainforest by Using SIR-C Imagery. *Remote Sensing of Environment, 59*, 191-202.

Saich, P., Rees, W.G., y Borgeaud, M. (2001). Detecting Pollution Damage to Forests in the Kola Peninsula Using the ERS SAR. *Remote Sensing of Environment, 75*.

Santis, A.d., y Chuvieco, E. (2007). Burn severity estimation from remotely sensed data: Performance of simulation versus empirical models. *Remote Sensing of Environment, 108*, 422-435.

Santis, A.d., y Chuvieco, E. (2009). GeoCBI: A modified version of the Composite Burn Index to estimate burn severity for remote sensing applications. In, *Remote Sensing of Environment* (pp. 554-562).

Santoro, M., Askne, J., Smith, G., y Fransson, J.E.S. (2002). Stem volume retrieval in boreal forests from ERS-1/2 interferometry. *Remote Sensing of Environment, 81*, 19-35.

Santoro, M., Askne, J.I.H., Wegmüller, U., y Werner, C.L. (2007). Observations, Modeling, and Applications of ERS-ENVISAT Coherence Over Land Surfaces. *IEEE Transactions on Geoscience and Remote Sensing, 45*, 2600-2611.

Siegert, F., y Hoffmann, A.A. (2000). The 1998 Forest Fires in East Kalimantan (Indonesia): A Quantitative Evaluation Using High Resolution, Multitemporal ERS-2 SAR Images and NOAA-AVHRR Hotspot Data. *Remote Sensing of Environment, 72*, 64-77.

Siegert, F., y Nakayama, M. (2000). Comparison of ERS-2 and JERS for fire impact assessment in tropical rainforests. In, *Geoscience and Remote Sensing Symposium, 2000. IGARSS '00. Proceedings. 2000 IEEE International* (pp. 2709-2711). Honolulu, HI, USA.

Siegert, F., Rucker, G., y Hoffman, A. (1999). Evaluation of the 1998 Forest Fires in East-Kalimantan (Indonesia) Using NOAA-AVHRR hotspot Data and Multitemporal ERS-2 SAR images. In, *Geoscience and Remote Sensing Symposium, 1999. IGARSS '99. Proceedings. 1999 IEEE International* (pp. 185-187). Hamburg, Germany.

Siegert, F., y Ruecker, G. (2000). Use of multitemporal ERS-2 SAR images for identification of burned scars in south-east Asian tropical rainforest. *International Journal of Remote Sensing, 21*, 831-837.

Smith, G., y Askne, J. (2001). Clear-cut detection using ERS interferometry. *International Journal of Remote Sensing, 22*, 3651-3664.

Sternberg, M., y Shoshany, M. (2001). Aboveground biomass allocation and water content relationships in Mediterranean trees and shrubs in two climatological regions in Israel. *Plant Ecology, 157*, 171-179.

Strozzi, T., Dammert, P.B.G., Wegmüller, U., Martinez, J.-M., Askne, J.I.H., Beaudoin, A., y Hallikainen, M.T. (2000). Landuse Mapping with ERS SAR Interferometry. *IEEE Transactions on Geoscience and Remote Sensing, 38*, 766-775.

Sun, G.Q., Rocchio, L., Masek, J., Williams, D., y Ranson, K.J. (2002). Characterization of forest recovery from fire using Landsat and SAR data. In, *Geoscience and Remote Sensing Symposium, 2002. IGARSS '02. Proceedings. 2002 IEEE International* (pp. 1076-1078). Toronto, Canada.

Svoray, T., y Shoshany, M. (2003). Herbaceous Biomass Retrieval in Habitats of Complex Composition: A Model Merging SAR Images With Unmixed Landsat TM Data. *IEEE Transactions on Geoscience and Remote Sensing, 41*, 1592-1601.

Svoray, T., Shoshany, M., Curran, P.J., Foody, G.M., y Perevolotsky, A. (2001). Relationship between green leaf biomass volumetric density and ERS-2 SAR backscatter of four vegetation formations in the semi-arid zone of Israel. *International Journal of Remote Sensing, 22*, 1601-1607.

Takeuchi, S., y Yamada, S. (2002). Monitoring of Forest Fire Damage by Using JERS-1 InSAR. In, *Geoscience and Remote Sensing Symposium, 2002. IGARSS '02. Proceedings. 2002 IEEE International* (pp. 3290-3292). Toronto, Canada.

Tansey, K.J., Luckman, A.J., Skinner, L., Balzter, H., Strozzi, T., y Wagner, W. (2004). Classification of forest volume resources using ERS tandem coherence and JERS backscatter data. *International Journal of Remote Sensing, 25*, 751-768.

Le Toan, T., Beaudoin, A., y D.Guyon (1992). Relating forest biomass to SAR data. *IEEE Transactions on Geoscience and Remote Sensing, 30*, 403-411.

Verbyla, D.L., Kasischke, E.S., y Hoy, E.E. (2008). Seasonal and topographic effects on estimating fire severity from Landsat TM/ETM+ data *International Journal of Wildland Fire, 17*, 527-534.

Viedma, Melia, J., Segarra, D., y Garcia-Haro, J. (1997). Modeling Rates of Ecosystem Recovery after Fires by Using Landsat TM Data. *Remote Sensing of Environment, 61*, 383-398.

Vila, J.P.S., y Barbosa, P. (2010). Post-fire vegetation regrowth detection in the Deiva Marina region (Liguria-Italy) using Landsat TM and ETM+ data. *Ecological Modelling, 221*, 75-84.

Wagtendonk, J.W.v., Root, R.R., y Key, C.H. (2004). Comparison of AVIRIS and Landsat ETM+ detection capabilities for burn severity. *Remote Sensing of Environment, 92*, 397-408.

Wang, Q., Adiku, S., Tenhunen, J., y Granier, A. (2005). On the relationship of NDVI with leaf area index in a deciduous forest site. *Remote Sensing of Environment, 94*, 244-255.

Wegmüller, U., y Werner, C. (1997). Retrieval of Vegetation Parameters with SAR Interferometry. *IEEE Transactions on Geoscience and Remote Sensing, 35*, 18-24.

Wegmüller, U., y Werner, C.L. (1995). SAR Interferometric Signatures of Forest. *IEEE Transactions on Geoscience and Remote Sensing, 33*, 1153-1161.

Wimberly, M.C., y Reilly, M.J. (2007). Assessment of fire severity and species diversity in the southern Appalachians using Landsat TM and ETM+ imagery. *Remote Sensing of Environment, 108*, 189-197.

Zebker, H.A., y Villasenor, J. (1992). Decorrelation in interferometric radar echoes. *IEEE Transactions on Geoscience and Remote Sensing, 30*, 950-959.

van Zyl, J.J. (1993). The Effect of Topography on Radar Scattering from Vegetated Areas. *IEEE Transactions on Geoscience and Remote Sensing, 31*, 153-160.

Capítulo 3. ÁREA DE ESTUDIO, MATERIAL Y MÉTODOS

Una vez abordado el estado de la cuestión y las propiedades de los sistemas radar de apertura sintética y antes del Capítulo 4, en el que se da cumplimiento a los objetivos fijados en esta tesis doctoral, en este Capítulo 3 se presentan tanto el área de estudio como la metodología del trabajo de campo y gabinete. Asimismo, se refieren las características principales de las imágenes ópticas y radar utilizadas y su procesamiento.

3.1. Área de estudio

La Comunidad Autónoma de Aragón, situada en el noreste de España, tiene una superficie de 47.719 km^2 y se extiende desde la Cordillera Pirenaica, al norte, hasta el Sistema Ibérico, al sur. La diversidad geológica y morfo-estructural se manifiesta en una importante variabilidad topográfica, que oscila desde 100 a más de 3000 m sobre el nivel del mar. Su clima mediterráneo de matiz continental se caracteriza por inviernos muy fríos y veranos cálidos y secos. Los bosques se extienden sobre más de 1,5 millones ha, de las que aproximadamente un 50% están poblados por coníferas, un 15% por frondosas y el resto por bosques mixtos de coníferas y frondosas; además de los anteriores los bosques abiertos (< 20% de cobertura de árboles) y los matorrales ocupan 1 millón de ha. Durante las últimas décadas la superficie cubierta por bosques ha aumentado debido a los proyectos de reforestación y al abandono rural. Las principales especies arbóreas son *Pinus halepensis, P. sylvestris, P. pinaster, Quercus ilex* y *Q. pyrenaica* mientras que *Quercus coccifera, Juniperus oxycedrus* y *Thymnus vulgaris* se encuentran habitualmente en los matorrales. En los últimos veinte años alrededor de 5.000 ha se han visto afectadas cada año por incendios en Aragón, de las cuales casi 3.000 son bosques densos. La extensión del área quemada anualmente es, por lo general, reducida, pero en años excepcionales -como 1994 y 2009- el área afectada puede llegar hasta 30.000 ha.

En este contexto, la principal área de estudio se encuentra en la Depresión del Ebro, la región semiárida más septentrional de Europa (Fig. 6). Rodeado por cadenas montañosas, el Valle del Ebro tiene un clima mediterráneo con matices continentales y marcadas variaciones estacionales de las precipitaciones; la precipitación media anual es de alrededor de 350 mm. El área cubre un relieve accidentado, con altitudes entre 400 y

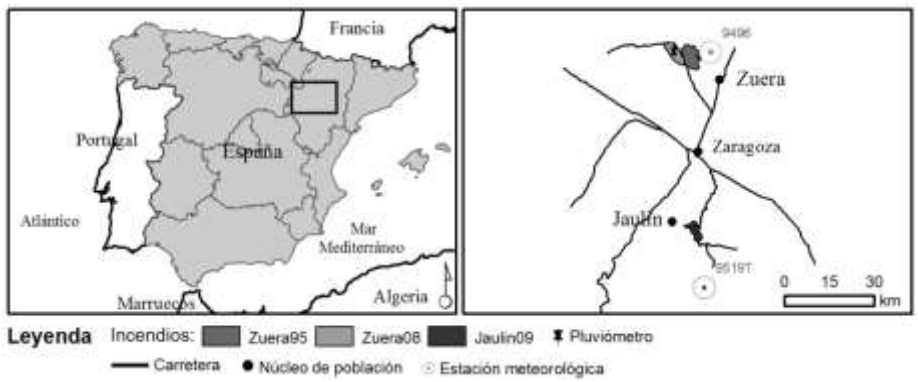

Fig. 6 Localización del área de estudio y de los principales incendios estudiados.

750 m sobre el nivel del mar (Fig. 7). La cubierta predominante del suelo incluye bosques y cultivos de cereales. La litología de la zona se caracteriza por calizas y sedimentos de yesos dispuestos en capas horizontales que contribuyen a su aridez, ya que los suelos son incapaces de retener el agua como consecuencia de la alta conductividad hidráulica.

La mayor parte del área principal de estudio (Fig. 6) está cubierta por bosques, como resultado de las actividades de reforestación y del abandono de áreas de cultivo. Los bosques cubren aproximadamente 22.000 ha y están en su mayoría conformados por *Pinus halepensis* siendo *Quercus coccifera* la principal especie del sotobosque. Los bosques tienden a presentar una estructura homogénea, perteneciendo más del 85% de los árboles al estrato co-dominante. Alrededor del 50% de los árboles tienen entre 35 y 55 años de edad, mientras que el 75% tienen menos de 65 años. El número medio de árboles por hectárea es de 440, con un máximo de 2.900 y un mínimo de 20 árboles en las zonas abiertas. La altura media es de alrededor de 6,5 m y la biomasa media alrededor de 45 t/ha. Los rodales más viejos alcanzan alturas de 12-13 metros y 90 t/ha.

Para cumplir el primer objetivo específico de la tesis se estudiaron también incendios ocurridos en la provincia de Teruel, que se encuentra situada en la parte sur de Aragón (Fig. 7). El área forestal de esta provincia constituye un tercio del área forestal de la Comunidad Autónoma (alrededor de 405.000 ha). Su clima mediterráneo está caracterizado por el efecto de barrera del relieve que aísla la mayor parte del territorio de la influencia de los vientos húmedos procedentes del Atlántico o del mar Mediterráneo. El promedio anual de las temperaturas mínimas y máximas se sitúa 6-8° C por debajo de

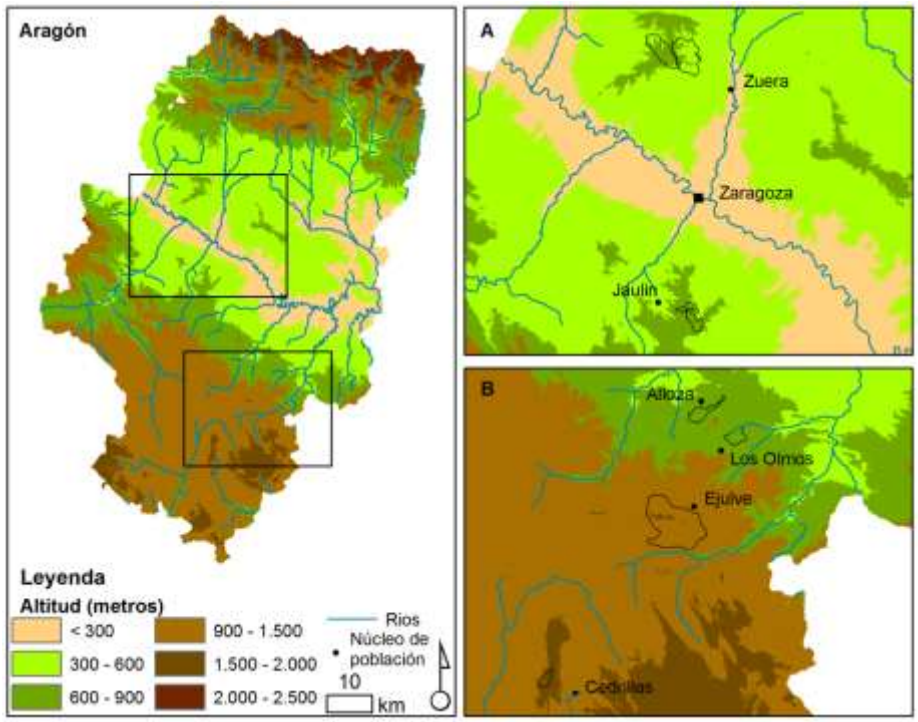

Fig. 7 Mapa fisiográfico de Aragón y detalle de las áreas de estudio. Localización de los incendios analizados en el Valle del Ebro (A) y en Teruel (B).

la Depresión del Ebro, mientras que el promedio de las precipitaciones es ligeramente superior (400 mm). El relieve es accidentado, localizándose el 60% del territorio por encima de los 1.000 m de altitud sobre el nivel del mar (Fig. 7). La vegetación forestal está constituida por *Pinus uncinata, P. sylvestris, P. nigra, P. spinaster, P. halepensis Quercus ilex rotundifolia, Q.pirenaica y Q. faginea*; una cuarta parte de la provincia está ocupada por matorrales de *Juniperus sp., Thymus vulgaris* y *Genista sp*.

El análisis de esta tesis se ha centrado principalmente en tres incendios situados en el sector central del Valle del Ebro, cerca de la ciudad de Zaragoza (Fig. 8). En el primero -Zuera95- ardieron aproximadamente 3.100 ha de bosque entre el 23 y 25 de junio de 1995, después de que una chispa de un tractor incendiara el matorral junto al pinar. En el segundo -Zuera08- el fuego se inició tras un accidente de tráfico; alrededor de 2.200 ha de bosque fueron calcinadas entre el 6 y el 16 de agosto de 2008. En el tercer incendio -Jaulin09, a unos 60 km en dirección sur- la causa del incendio fue un rayo, producido en una tormenta de verano, el 21 de julio de 2009, quemándose

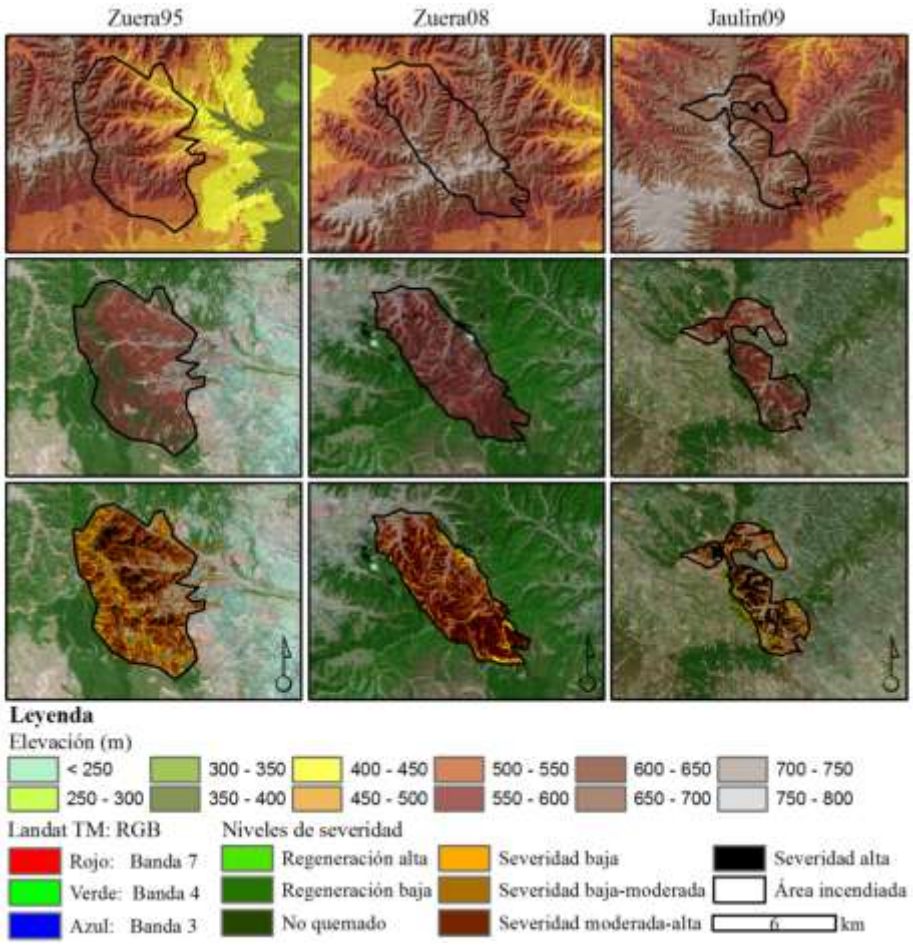

Fig. 8 Cartografía de detalle de los principales incendios estudiados: mapa de elevaciones (arriba), imagen Landsat post-incendio (centro) y niveles dNBR de severidad (abajo).

Fig. 9 Fotografías panorámicas del área afectada por el fuego. Zuera08 (izquierda) y Jaulin09 (derecha).

alrededor de 1.800 hectáreas. La mayoría del bosque fue afectado por alta severidad mientras que áreas de baja y moderada severidad se encuentran en los límites del bosque donde los servicios de extinción pudieron controlar la propagación del fuego.

La Fig. 8 representa la topografía específica de estos tres incendios junto con los niveles de severidad estimadas mediante imágenes ópticas; además, se muestra la imagen Landsat TM registrada poco tiempo después de cada incendio, menos de dos meses. Fotografías panorámicas del área afectada por el fuego para los dos incendios más recientes se presentan en la Fig. 9.

Información detallada sobre el área analizada para el estudio preliminar de la severidad y la recuperación vegetal en bosques boreales se puede encontrar en la Sección 4.2.4 y 4.4.

3.2. Material

3.2.1. Estimación de la severidad en el terreno

Los datos obtenidos mediante teledetección pueden relacionarse estadísticamente con las características particulares de interés del terreno para lo que es necesario determinar tales características y utilizar métodos estables de medición, que sean complementarios al tipo de sensor utilizado y su resolución espacial y espectral.

El *Composite Burn Index* – CBI es un índice para la estimación de la severidad en el campo que valora los efectos del fuego combinando información proveniente de múltiples estratos de la vegetación dentro de un valor único característico para un sitio de muestreo. El índice incorpora estimaciones sobre factores tales como la condición y color del suelo, la cantidad de la vegetación o del combustible consumido, el rebrote de las plantas quemadas, la aparición de nuevas especies, la altura de la quema, etc. En cuanto expresado por un valor numérico continuo, el CBI se puede correlacionar con variables ambientales, como la productividad de las plantas o la carga de combustible, y ha sido diseñado para estimar el nivel de variación de las condiciones biofísicas de un sitio tras el incendio. Su diseño permite la comparación de comunidades que ocupan diferentes situaciones topográficas, climáticas y edáficas en diferentes tipos de ecosistemas, composición de especies o estructuras de la vegetación (Key y Benson 2004). El CBI se puede utilizar para estimar los efectos del incendio a largo plazo mediante series cronológicas, estimándose los cambios temporales y validándose las predicciones sobre la evolución de la vegetación post-incendio.

El objetivo principal del CBI es el análisis de la asociación estadística entre la severidad observada en el terreno y la severidad estimada mediante imágenes de satélite. Por lo tanto, el índice no está diseñado para la estimación de la estructura espacial de la severidad, siendo los productos obtenidos tras el procesamiento de datos de teledetección los que proporcionan esta información para todos los píxeles analizados. En la mayoría de los casos, en función del tamaño y la complejidad de la vegetación, se necesitan entre 50 y 100 parcelas de muestreo, que se distribuyen de modo uniforme entre los rangos generales de severidad: no quemado, severidad baja, severidad baja-moderada, severidad moderada-alta y severidad alta. En cada uno de estos rangos se recomienda el muestreo de 10 a 20 sitios (Key y Benson 2004). Cada sitio de muestreo representa zonas de condiciones homogéneas tanto respecto del tipo de vegetación como del nivel de severidad. El estado de la vegetación se examina visualmente por estratos y el grado de cambio con respecto al estado previo se registra desde 0 (ninguna) hasta 3 (variación del 100%). En cada estrato los factores son evaluados de modo independiente, utilizando una escala decimal, siendo promediados para obtener el valor de la severidad media. Los factores o los estratos que no se encuentran en el sitio de muestreo son descartados.

En los primeros meses tras el incendio se establecieron parcelas de muestreo en zonas no quemadas y en zonas de alta, moderada y baja severidad. En total, se han evaluado 258 parcelas entre los cinco incendios ocurridos en 2008 y 2009 (Tabla 2). En los dos incendios situados en el sector central del valle de Ebro (Zuera08 y Jaulin), área principal de estudio de esta tesis doctoral, se ubicaron más de la mitad de las parcelas (168). La localización de los puntos de muestreo en cada incendio se incluye en el capítulo 4, sección 4.1.

Las parcelas de muestreo se establecieron en sitios con vegetación homogénea y pendiente constante. La vegetación presente en el área de estudio consiste principalmente en hierbas y arbustos de menos de 1 m, arbustos y árboles hasta 5 m y árboles hasta 20 m de altura. En cada parcela se tomaron fotografías digitales (dirección N, S, E y O y primeros planos de la copa, el suelo y el sotobosque) y el centro se georreferenció mediante GPS; el error de localización, después de la corrección diferencial, se situó por debajo de 1 m para la mayoría de las parcelas. La severidad se evaluó en cada parcela dentro de un radio de 15 m. Las principales variables estimadas fueron el consumo de combustible, la alteración del follaje, los cambios en la cubierta vegetal, la mortalidad de los árboles y la altura de la llama. La alta intensidad del fuego y el área quemada relativamente pequeña determinó una distribución desigual de la severidad por rangos de gravedad en todos los incendios. La mayoría de los bosques están afectados por severidad alta o moderada mientras que menos de una cuarta parte del área estudiada está afectada por niveles bajos de severidad. Por lo tanto, los puntos de muestro no se distribuyen proporcionalmente por rangos de severidad (Tabla 3).

Tabla 2 Grandes incendios en Aragón (2008-2009) y número de parcelas evaluadas en cada uno.

Incendio	Fecha	Causa	Área quemada (ha)	Nº parcelas CBI
Zuera08	08.2008	accidente de trafico	2200	123
Jaulín	07.2009	rayo	1800	45
Aliaga	07.2009	rayo	9000	45
Los Olmos	07.2009	rayo	500	34
Cedrillas	07.2009	rayo	600	11
Zuera09	08.2009	desconocida	7500	-
Alloza	07.2009	rayo	1450	-
Valdetormo	07.2009	rayo	300	-

Tabla 3 Distribución de las parcelas CBI por rangos de severidad (dosel arbóreo).

Incendio	No quemado	Severidad baja	Severidad moderada	Severidad moderad-alta	Severidad alta	Total parcelas CBI
Zuera08	16	11	18	4	74	123
Jaulín	13	0	12	2	18	45
Aliaga	9	4	10	3	19	45
Los Olmos	4	3	4	4	19	34
Cedrillas	2	3	1	0	5	11

Fig. 10 Ilustración de la severidad en pinares de Aragón. Jaulin (ariba) y Los Olmos (abajo).

En zonas de baja severidad la base de los árboles se quemó, la hojarasca fue parcialmente consumida y el sotobosque fue afectado según un patrón irregular; el follaje del sotobosque fue chamuscado y parcialmente consumido mientras que las copas de los árboles generalmente no se vieron afectadas. En las zonas de gravedad moderada el sotobosque se conservó parcialmente; las hojas y las ramas de los arbustos pequeños (menos de 1 m) fueron consumidas mientras que los arbustos altos (más de 1 m) presentaron un follaje chamuscado. Las copas de los árboles fueron parcialmente quemadas, lo que causó una pérdida parcial de la cobertura de las copas. El consumo del sotobosque aumentó en las zonas de severidad moderada-alta y las copas de los árboles se quemaron en gran parte. La pérdida de ramas y ramitas pequeñas no fue significativa en el estrato arbóreo; sin embargo, el estrato arbustivo perdió la mayoría de las ramas pequeñas, especialmente para arbustos de menos de 1 m.

En las zonas de alta severidad la combustión de la hojarasca, el sotobosque y la copa de los arboles fue completa. En los más altos niveles de gravedad, las ramas pequeñas y medianas también fueron consumidas. Por último, las zonas no afectadas por el incendio presentaron acumulación de hojarasca un estrato arbustivo denso y ramas vivas a baja altura en el estrato arbóreo. En la Fig. 10 se presentan fotografías de las parcelas de muestreo correspondientes a los principales tipos de severidad encontrados en el área de estudio (ejemplos adicionales se pueden encontrar en la Sección 4.1 y 4.2.1).

3.2.2. Características de las imágenes ópticas utilizadas

Entre los sensores ópticos de media-alta resolución espacial el programa Landsat es la única fuente de información temporal y espacial coherente y continua a nivel global. Esto permite comparar información previa y posterior al fuego para la evaluación de la magnitud del cambio causado en la vegetación. Este tipo de evaluación requiere tanto información obtenida mediante trabajo de campo, para calibrar los modelos y validar los resultados, como información obtenida mediante sensores espaciales. Además, los indicadores actualmente más utilizados para la estimación de la severidad (CBI y dNBR) han sido diseñados específicamente para el uso de imágenes con las características espectrales y la resolución espacial del programa Landsat. Por lo tanto, las imágenes ópticas utilizadas en esta investigación provienen del satélite Landsat 5. El conjunto de imágenes ópticas analizado está formado por ocho escenas (*Path* 199, *Row* 031 y 032). Las escenas utilizadas fueron registradas en fechas cercanas al incendio para todas las áreas estudiadas. En la Tabla 4 se proporciona la fecha de adquisición de cada imagen junto con la del incendio forestal correspondiente. La elección de estas imágenes cumple con la necesidad de obtener datos con un mínimo espaciamiento temporal, ya que la variabilidad de la respuesta espectral de la vegetación no quemada se reduce al mínimo. Dichas imágenes han sido obtenidas mediante el Plan Nacional de Teledetección (PNT) con un nivel de procesamiento mínimo que consiste en la eliminación de los errores sistemáticos de calibración y de localización de los píxeles en una matriz regular. Las imágenes están proyectadas en un sistema de proyección Universal Transverse Mercator (UTM), utilizándose la información sobre la posición de la plataforma en el momento de la adquisición. El error sistemático residual de localización se sitúa en torno a 250 m y las imágenes resultantes son proporcionadas sin ningún tipo de corrección atmosférica.

Pre-tratamiento: es un término común para operaciones con imágenes de satélite. El objetivo del pre-tratamiento es mejorar la imagen inicial, eliminando las distorsiones no deseadas o mejorando algunos aspectos importantes para el procesamiento posterior. Según la naturaleza de los cambios, los pre-tratamientos se pueden agrupar en: i) operaciones "cosméticas" (p. ej.: restauración de píxeles o líneas perdidos); ii) correcciones geométricas (p. ej.: registro, georreferenciación, orto-rectificación) y iii) correcciones radiométricas (p. ej.: pérdida de sensibilidad del sensor, variación en la geometría de la iluminación, variaciones ocasionadas por la topografía e interferencias atmosféricas ocasionadas por la absorción, la dispersión y la emisión de las ondas electromagnéticas). La eliminación de los errores sistemáticos por el proveedor hizo redundante la aplicación del primer tipo de pre-tratamientos; en consecuencia, la primera operación de tratamiento previo aplicada ha sido la corrección geométrica, seguida de la corrección radiométrica.

Tabla 4 Imágenes Landsat TM analizadas.

Incendio	Fecha del inicio	Imágenes Landsat utilizadas		*Path/Row*
Zuera95	23.06.1995	28.03.1995	03.08.1995	199/31
Zuera08	06.08.2008	21.07.2008	22.08.2008	199/31
Jaulin09	29.07.2009	22.06.2009	26.09.2009	199/31
Aliaga, Los Olmos y Cedrillas	22.07.2009	22.06.2009	26.09.2009	199/32

Corrección geométrica: Los errores geométricos se clasifican en: i) sistemáticos - inducidos por el tipo de sensor, el movimiento y la curvatura de la Tierra y ii) no sistemáticos – inducidos por la topografía y el movimiento aleatorio de la plataforma. Los errores sistemáticos son eliminados por el procesamiento del proveedor antes del subministro de las imágenes. Para eliminar los errores no sistemáticos se utilizó el método de los puntos de control (GCPs), que consiste en la identificación de puntos comunes entre la imagen original y la imagen de referencia, la modelización de la transformación entre los dos sistemas de coordenadas y la transferencia de los valores digitales originales a la nueva posición. En zonas con diferencias de topografía es necesario el uso de un modelo digital de elevaciones (MDE) para la determinación precisa de la posición de los píxeles en el nuevo sistema de coordenadas. Para el cálculo de la transformación se empleó un modelo polinómico que utiliza la información del MDE como una nueva variable independiente.

Para todas las imágenes ópticas procesadas se utilizó la misma proyección cartográfica que en el caso de las imágenes SAR (UTM, zona 30 N, datum Europeo 1950), por cuanto iban a ser objeto de análisis posterior conjunto. Como referencia se utilizaron orto-fotografías aéreas de 0,5 m de resolución espacial del vuelo del Plan Nacional de Ortofotografía Aérea (PNOA), de 2001, disponibles en el Sistema de Información Territorial de Aragón (SITAR). El número de puntos necesario para la orto-rectificación varía en función del tamaño de la imagen y de la complejidad topográfica, siendo recomendable, para una escena Landsat completa, el uso de alrededor de 100 puntos de control (Chuvieco et al. 2002). Sin embargo, el área relativamente pequeña afectada por los incendio permitió reducir este número a unos 50 puntos, por cuanto se utilizó sólo un tercio de las escenas Landsat originales. Los puntos fueron distribuidos de modo uniforme en las imágenes recortadas y ubicados en zonas claramente identificables, utilizando especialmente elementos muy estables como cruces de caminos o edificaciones. Para la modelización de la transformación se utilizó un polinomio de segundo orden dada la complejidad topográfica del área de estudio. La bondad del ajuste se estimó mediante el error cuadrático medio (RMSE), siendo el nivel de tolerancia generalmente aceptado de menos de un píxel; el ajuste finalmente obtenido se situó entre 0,5 y 0,65 píxeles. Para la transformación de las imágenes al nuevo sistema de coordenadas se pueden utilizar diferentes métodos, siendo los más comunes la interpolación bilineal, la convolución cubica y el vecino más próximo. Por cuanto las imágenes ópticas iban a ser utilizadas para obtener una estimación cuantitativa de la severidad, el objetivo del pre-tratamiento era conservar los valores originales sin incorporar ningún tipo de procesamiento estadístico; por lo tanto, en la transformación se utilizó el método del vecino más próximo. Al mismo tiempo se reasignó el tamaño del píxel, utilizando una nueva matriz de 25 m en lugar de los 30 m originales de las bandas Landsat TM. El cambio en la resolución espacial fue necesario para adecuar la geometría de las imágenes ópticas a la geometría de las imágenes SAR que, en general, son procesadas a una cadencia de valores adecuada al sistema métrico decimal.

Corrección radiométrica: La superficie terrestre recibe no sólo radiación solar directa, sino también la radiación dispersada por la atmósfera. La energía electromagnética reflejada por un objeto no coincide con la energía que llega a un sensor a bordo de una plataforma espacial debido a la geometría de iluminación del sol, las condiciones atmosféricas o la influencia del relieve. Un sensor recibe no sólo la radiación directamente reflejada por un objeto, sino también la radiación difusa y dispersada por la atmósfera; por lo tanto, para obtener la reflectividad real es necesario compensar estas distorsiones. Las variaciones radiométricas se pueden agrupar en: *i)*

variaciones en la sensibilidad del sensor, *ii)* variaciones debidas a la posición relativa del sensor con respecto a la iluminación solar, *iii)* variaciones debidas a la topografía y iv) dispersión atmosférica. En la bibliografía la corrección radiométrica se refiere al conjunto de procesos necesarios para eliminar o reducir todas estas distorsiones, algo que se puede lograr utilizando diferentes enfoques en función de los datos disponibles para la calibración.

Para la corrección radiométrica de las imágenes Landsat se han utilizado los modelos de transferencia radiativa. El algoritmo implementado en la mayoría de los paquetes de programas comerciales trabaja con un elenco de condiciones atmosféricas (en función de la latitud, la altitud y los tipos de aerosoles) y de valores de visibilidad atmosférica. El usuario determina la función apropiada para la corrección atmosférica en pasos iterativos y convierte el número digital (DN) a valores de reflectividad. El MDE se ha utilizado para compensar los valores en función de la topografía local. La normalización entre escenas no fue necesaria debido al alto coeficiente de determinación obtenido para las superficies estables consideradas ($R^2 > 0,98$), dado el corto lapso de tiempo entre las adquisiciones sucesivas.

3.2.3. Características de las imágenes radar utilizadas

Las imágenes SAR utilizadas proceden de *European Remote Sensing* (ERS) SAR, *Environmental Satellite* (Envisat) *Advanced SAR* (ASAR), *Advanced Land Observing Satellite* (ALOS) *Phased Array type L-band SAR* (PALSAR) y *TerraSAR-X* (TSX) SAR. En la Tabla 5 se proporcionan las características principales de los sensores radar utilizados. Los datos han sido suministrados sea como imágenes complejas (SLC) sea como imágenes de precisión (PRI). Las imágenes en formato complejo (amplitud y fase) han sido utilizadas para el análisis de la coherencia interferométrica mientras que las imágenes PRI (solo amplitud) se han utilizado para el análisis del coeficiente de retro-dispersión.

3.2.3.1. Procesamiento de las imágenes SAR – el coeficiente de retro-dispersión

El proceso seguido para el procesamiento de las imágenes radar, que se presenta de forma esquemática en la Fig. 11, consiste en la calibración radiométrica, el re-muestreo, la referenciación y la normalización topográfica.

Calibración radiométrica relativa: Para compensar la variación de la retro-dispersión a lo largo del alcance y permitir comparaciones entre imágenes tomadas con diferentes sensores y ángulos de incidencia, la señal radar debe ser calibrada. Las imágenes distribuidas por las agencias espaciales tienen ya aplicado un procesamiento básico que consta de una calibración radiométrica relativa y, en función del nivel de procesamiento, de un pre-tratamiento para la reducción del moteado. La calibración radiométrica relativa consta de la corrección del coeficiente de retro-dispersión en función del patrón de la antena y de las pérdidas de energía en alcance que dependen de las características técnicas de cada sensor.

Calibración radiométrica absoluta: Las imágenes con calibración relativa expresan la respuesta radiométrica del sistema como el promedio de la potencia en cada píxel (brillo – β). La normalización del brillo se hace sobre la dirección del alcance y no depende del ángulo de incidencia. Sin embargo, por lo general se necesitan estimaciones de reflectividad de áreas proyectadas sobre el geoide, por lo que hay que normalizar el

Tabla 5 Las principales características de las imágenes SAR utilizadas.

Satélite/Parámetro	TSX	ASAR	ERS 1 / 2	ASAR	PALSAR	PALSAR
Banda [longitud de onda - cm]	X- [3,1]	C- [5,7]	C- [5,7]	C- [5,7]	L- [23,6]	L- [23,6]
Modo de adquisición	SM	IM	-	AP	PLR	FBD
Ángulo de incidencia	25º o 40°	23º	23°	23º	26°	34°
Polarización	HH,HV	HH o VV	VV	HH,HV	HH,VV,HV,VH	HH,HV
Resolución en alcance (m)	0,9	7,8 o 12,5	12,5	12,5	9,4	9,4
Resolución en azimut (m)	2,2	4,0 o 12,5	12,5	12,5	3,8	3,2
Nivel de procesamiento	SLC	SLC o PRI	PRI	PRI	SLC	SLC

SM - strip map / IM – imaging / AP – alternating polarization / PLR – polarimetric / FBD – fine beam dual

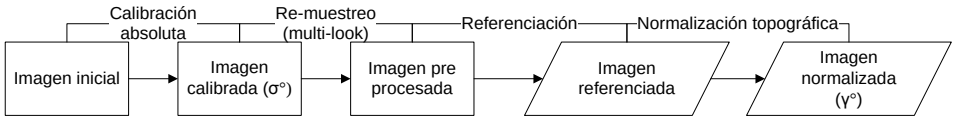

Fig. 11 Diagrama de flujos del procesamiento SAR – el coeficiente de retro-dispersión.

coeficiente retro-dispersión por la unidad de superficie horizontal (sigma nought - σ°) o la superficie frente a la onda incidente (gamma nought - γ°). Para ello es necesario tener en cuenta la constante de calibración radiométrica absoluta (proporcionada por las agencias espaciales correspondientes) y el ángulo de incidencia local que depende de la pendiente y la geometría de vista del satélite. Los coeficientes de retro-dispersión obtenidos después de la calibración radiométrica absoluta (σ° o γ°) se expresan en decibelios (dB) y están normalizados en función de la unidad de superficie sobre el terreno.

$$\beta^\circ = ND^2 * CC \quad \{1\}$$

$$\sigma^\circ = \beta^\circ * \sin\theta i \quad \{2\}$$

$$\gamma^\circ = \beta^\circ * \tan\theta i = {}^{\sigma^\circ}/_{\cos\theta i} \quad \{3\}$$

donde: ND – número digital
CC – coeficiente de calibración absoluta
θ_i – ángulo de incidencia

Multi-looking: La reducción del moteado se puede conseguir promediando diferentes sub-imágenes (*looks*) generadas mediante el procesador SAR a partir de los impulsos individuales recibidos. Las sub-imágenes se obtienen dividiendo la señal en lugar de utilizar toda la amplitud de observación del SAR en azimut (*multi-look* en frecuencia). Por otra parte, la reducción del moteado también se puede conseguir mediante un promedio espacial del coeficiente de retro-dispersión de los píxeles con la correspondiente pérdida de resolución (*multi-look* espacial). La reducción del moteado es proporcional al número de sub-imágenes utilizadas en el caso del *multi-look* en frecuencia o al número de píxeles promediados en el caso del *multi-look* espacial. Es muy habitual que los dos métodos se utilicen conjuntamente para obtener una mejor estimación del coeficiente de retro-dispersión de los objetos detectados ya que el usuario no dispone normalmente de un procesador SAR para poder dividir la señal compleja en sub-imágenes. Además, este proceso requiere una rigurosa aplicación y ordenadores de gran potencia. En consecuencia, las imágenes procesadas por las agencias espaciales, que contienen una reducción del moteado mediante el proceso *multi-look* en frecuencia, se pueden re-muestrear para una reducción complementaria del moteado, mediante el proceso de *multi-look* espacial.

Georreferenciación: La georreferenciación consiste en la transformación de una imagen en coordenadas radar (alcance y azimut) a una proyección cartográfica. Dada la influencia de la topografía en la ubicación final de los píxeles en el mapa, se recomienda utilizar un modelo digital de elevaciones. Esta transformación se puede hacer mediante el método de los puntos de control o, de modo más preciso y automatizado, utilizando tablas de transferencia (tablas *look-up*) entre la matriz de la imagen SAR y la matriz del MDE tomado como referencia (Wegmüller et al. 1999; Wegmüller et al. 2002). Este segundo método se divide en tres etapas: (i) determinación de la transformación geométrica inicial; (ii) mejora de la transformación geométrica inicial; (iii) re-muestreo de la imagen SAR a la proyección cartográfica. La transformación geométrica inicial se obtiene a partir de la información sobre la órbita del satélite y el MDE. El segundo paso es necesario como consecuencia de las inexactitudes en la información orbital, especialmente cuando se trabaja en áreas con relieve contrastado. El refinamiento se lleva a cabo en forma de compensaciones de la tabla *look-up* basadas en la comparación de la imagen SAR con una imagen de referencia (por ejemplo, una imagen SAR simulada a partir del MDE). La imagen simulada se transforma a la geometría de la imagen SAR y las compensaciones se calculan utilizando un algoritmo de correlación cruzada. Las compensaciones se distribuyen homogéneamente en la imagen, dependiendo el número estrictamente de las características del terreno identificadas conjuntamente en la imagen SAR y la imagen simulada que se toma como referencia. La calidad del perfeccionamiento se mide mediante el error cuadrado medio (RMSE) de las compensaciones. Se considera aceptable un error medio por debajo del tamaño de un píxel en la geometría radar. Sin embargo, los errores medios logrados en azimut y alcance se sitúan normalmente por debajo de la mitad del tamaño del píxel, lo que indica una alta precisión de este proceso automático. Sobre la base de los desplazamientos se estima un modelo lineal simple que se usa para refinar la tabla *look-up*. Por último, la imagen SAR se re-muestrea a la geometría del mapa usando la tabla refinada.

Normalización topográfica: La topografía también introduce errores en la estimación del coeficiente de retro-dispersión y, por lo tanto, en la interpretación de los resultados (Castel et al. 2001). Por esta razón es necesaria la normalización topográfica para compensar la variación del ángulo de incidencia local y el área real de los píxeles (Ulander 1996) (eq. 4). Esta información se deriva del MDE (Wegmüller et al. 1999). El resultado es una imagen en formato gamma nought ($\gamma°$) que sólo incluye las variaciones de las propiedades de dispersión de un objetivo debido a la topografía local diferente.

$$\gamma° = \sigma° * {}^{Ar}/_{cos\theta_{loc}} \quad \{4\}$$

donde: Ar - área real del píxel
θ_{loc} - ángulo de incidencia local

La Tabla 6 contiene información sobre las fechas de adquisición de las imágenes SAR, la temperatura máxima (Tmax) y mínima (Tmin) diaria y las precipitaciones acumuladas (PA) durante los cuatro días anteriores a la adquisición. Las temperaturas se ajustaron con el gradiente ambiental (-2° C / 300 m) debido a la localización de las estaciones meteorológicas. Para el incendio de Zuera08 se han adquirido imágenes de todos los satélites, mientras que para el de Zuera95 tan sólo han estado disponibles imágenes procedentes de los satélites ERS (1 y 2). Para el tercer incendio (Jaulin09) se

Tabla 6 La fecha de adquisición y los principales parámetros climáticos para las imágenes analizadas – el coeficiente de retro-dispersión. Temperatura máxima (Tmax) y mínima (Tmin) diaria y precipitaciones acumuladas (PA) de los 4 días previos.

Sensor y polarización	Modo	Fecha	PA	Tmax	Tmin
ERS-1 VV[a]	IM	1992.08.31[1]	0,0	24	13
ERS-1 VV[a]	IM	1995.07.05	0,0	26	11
ERS-2 VV[a]	IM	1995.08.10	6,5[*]	29	16
ERS-2 VV[a]	IM	1995.09.14	0,0	23	9
ERS-2 VV[a]	IM	2008.06.12[1]	-	-	-
ERS-2 VV[a]	IM	2008.08.21	0,0	30	15
ERS-1 VV[a]	IM	1995.12.14	0,0	4	-4
ERS-2 VV[a]	IM	1995.12.15	2,7[*]	0	-5
ERS-2 VV[a]	IM	1996.01.19	1,0[*]	10	-2
ERS-1 VV[a]	IM	1996.03.28	0,0	15	5
ERS-2 VV[a]	IM	1996.03.29	0,0	17	6
ERS-1 VV[a]	IM	1995.11.28	0,0	12	-4
ERS-1 VV[a]	IM	1996.01.02	4,5	11	4
ERS-2 VV[a]	IM	1996.01.03	1,5	11	0
ASAR VV[b]	IM	2008.07.04[1]	0,0	31	8
ASAR VV[b]	IM	2008.09.12	1,6	18	11
ASAR HH[b]	IM	2009.01.08	0,5	0	-6
ASAR HH[b]	IM	2009.02.12	0,5[*]	10	4
ASAR HH, HV[b]	AP	2009.03.19	0,0	20	-1
ASAR HH, HV[c]	AP	2009.09.29	5,0[*]	22	11
TSX HH,HV[b]	SM	2008.11.16	0,0	14	-2
TSX HH,HV[b]	SM	2008.12.19	0,0	11	4
TSX HH,HV[b]	SM	2008.12.24[2]	0,0	-3	-6
TSX HH,HV[b]	SM	2009.01.21	2,3	7	-3
TSX HH,HV[b]	SM	2009.02.12	0,5[*]	10	4
TSX HH,HV[b]	SM	2009.02.23	0,0	12	5
TSX HH,HV[b]	SM	2009.03.06	11,8[*]	9	1
TSX HH, HV[c]	SM	2009.09.20	5,0	20	8
PALSAR[b]	PLR	2009.04.28	3,5[*]	18	10
PALSAR[c]	FBD	2009.10.05[3]	0,0	28	10

1. pre-fuego // 2. imágenes adquiridas con un ángulo de incidencia de 25° // 3. imágenes adquiridas con un ángulo de incidencia de 34° // * precipitaciones registradas parcialmente en el día de adquisición de la imagen SAR // a. Zuera95 // b. Zuera08 // c. Jaulin09

ha analizado una imagen para cada banda SAR disponible a bordo de sensores espaciales. Las imágenes de doble polarización TerraSAR-X fueron registradas en modo *StripMap* (SM), mientras que para el sensor ENVISAT ASAR se obtuvieron imágenes de simple o doble polarización, en modo *Imaging* (IM) y *Alernating polarization* (AP), respectivamente. Las imágenes ALOS PALSAR fueron adquiridas en el modo *Polarimetric* (PLR) o *Fine Beam Dual* (FBD) con dos polarizaciones (HH y HV). Los datos procedentes del satélite TerraSAR-X se registraron con dos ángulos de incidencia (25° y 40°), mientras que el resto de las imágenes SAR lo fueron con ángulos de incidencia similares (23°-26°). La única excepción fue la imagen ALOS PALSAR FBD que ha sido registrada con ángulo de incidencia mayor (Tabla 6).

3.2.3.2. Procesamiento de las imágenes SAR – coherencia interferométrica

En este apartado se expone, de forma breve, el procesamiento necesario para obtener estimaciones de coherencia interferométrica. El proceso seguido se presenta esquemáticamente en la Fig. 12. La georreferenciación de la imagen de coherencia se

realiza posteriormente, utilizando los mismos procedimientos que en el caso del coeficiente de retro-dispersión.

La estimación de la coherencia interferométrica entre dos escenas implica una serie de fases de procesamiento que podrían agruparse en: i) tratamiento previo ii) generación del interferograma y estimación de la coherencia; iii) post-procesamiento. El primer paso consiste principalmente en la mejora de la información sobre el movimiento de la plataforma en el espacio (vectores de estado), especialmente en los satélites más antiguos (ERS-1 / 2 y Envisat ASAR). También en este paso se realiza el co-registro de las escenas. El error máximo de localización entre las escenas analizadas no puede superar un cuarto de píxel sin que se introduzca, de modo artificial, la decorrelación espacial de la señal. La última tarea de la primera fase consiste en un filtrado para considerar sólo la parte común del espectro (Gatelli et al. 1994) entre las dos imágenes. Este pequeño desfase se debe a la separación espacial en la posición del satélite durante la adquisición de las imágenes. El desfase se estima a partir de una línea base inicial calculada a partir de los vectores de estado de la plataforma.

En la siguiente fase se procede a la generación del interferograma inicial y a la estimación de la línea base mejorada en función del interferograma inicial. La línea base mejorada se utiliza para eliminar la tendencia casi lineal de la fase, debida a las diferencias de trayecto (ida y vuelta) de las microondas en el alcance y la inclinación de la línea base – el aplanamiento del interferograma. Como resultado de este proceso, la fase del interferograma aplanado contiene sólo información relacionada con diferencias topográficas o desplazamientos. Para limitar el ruido, durante el procesamiento interferométrico se utiliza el *multi-look* espacial, tanto para la estimación de la fase interferométrica como para la de la coherencia.

Posteriormente, se genera el interferograma diferencial restando la fase topográfica simulada a partir de un MDE. El segundo paso concluye con la estimación de la coherencia, utilizando el interferograma diferencial para la corrección de la fase. El método de estimación utiliza ventanas adaptadas a la variabilidad local (Wegmüller et al. 1998). Estos pasos constituyen una secuencia estándar del procesamiento interferométrico; sin embargo, no deben considerarse como algo fijo y, en función de los productos necesarios y la precisión de las estimaciones, algunos pasos se pueden repetir en varias etapas a lo largo del procesamiento. El post-procesamiento incluye la georreferenciación de los productos interferométricos.

Las Tablas 7 y 8 contienen información sobre las fechas de adquisición y el componente perpendicular de la línea base para las combinaciones de imágenes SAR analizadas. Las líneas base se estimaron a partir de los vectores de estado. Para facilitar la interpretación, se adquirieron datos meteorológicos registrados en estaciones cercanas de la Agencia Estatal de Meteorología (AEMET). La temperatura máxima (Tmax) y

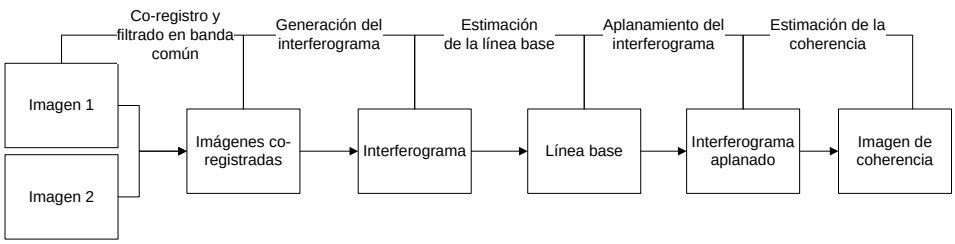

Fig. 12 Diagrama de flujos del procesamiento SAR – coherencia interferométrica.

mínima (Tmin) diaria y las precipitaciones acumuladas (PA) durante los cuatro días anteriores a la adquisición se presentan en las mismas tablas. Dado que los incendios se sitúan a diferentes altitudes con respecto a las estaciones meteorológicas, las temperaturas se ajustaron con el gradiente ambiental (-2° C / 300 m). Para el incendio de Zuera08, las precipitaciones fueron también obtenidas a partir de un pluviómetro automático (ARG) instalado aproximadamente en el centro del perímetro. La estación más cercana para la que se dispone de datos de velocidad del viento es la del Aeropuerto de Zaragoza, localizada a unos 35 km al sur del incendio de Zuera08 y a 25 km al norte del incendio de Jaulin09. La velocidad media del viento se calculó utilizando intervalos de 3 horas centrados en el momento de la adquisición de las imágenes.

Tabla 7 Línea base perpendicular y condiciones meteorológicas para las imágenes ERS- 1/2 analizadas en el incendio de Zuera95: temperatura máxima (Tmax), temperatura mínima (Tmin) y precipitación acumulada de los 4 días previos (PA).

Pista	Fecha 1	Fecha 2	Línea base perpendicular (m)	Línea base temporal (días)	Velocidad del viento (m/s)	Tmax (°C) fecha1	Tmin (°C) fecha1	AcPp (mm) fecha1	Tmax (°C) fecha2	Tmin (°C) fecha2	PA (mm) fecha2
	1995.12.14	1995.12.15	262,9	1	2,9 / 0,0	4,0	-6,0	1,0	0,0	-5,5	27,5
	1995.12.14	1996.01.19	599,2	35	2,9 / 2,5	4,0	-6,0	1,0	10,0	-2,0	1,3
	1995.12.14	1996.03.28	688,7	105	2,9 / 5,3	4,0	-6,0	1,0	15,0	5,0	0,0
58	1995.12.14	1996.03.29	746,5	106	2,9 / 2,1	4,0	-6,0	1,0	17,5	6,0	0,0
	1995.12.15	1996.01.19	336,4	34	0,0 / 2,5	0,0	-5,5	27,5	10,0	-2,0	1,3
	1995.12.15	1996.03.28	425,9	104	0,0 / 5,3	0,0	-5,5	27,5	15,0	5,0	0,0
	1995.12.15	1996.03.29	483,7	105	0,0 / 2,1	0,0	-5,5	27,5	17,5	6,0	0,0
	1996.01.19	1996.03.28	89,5	70	2,5 / 5,3	10,0	-2,0	1,3	15,0	5,0	0,0
	1996.01.19	1996.03.29	147,4	71	2,5 / 2,1	10,0	-2,0	1,3	17,5	6,0	0,0
	1996.03.28	1996.03.29	57,8	1	5,3 / 2,1	15,0	5,0	0,0	17,5	6,0	0,0
	1995.11.28	1996.01.02	137,8	35	1,8 / 2,4	12,0	-4,0	0,0	12,0	4,0	17,5
330	1995.11.28	1996.01.03	-112,6	36	1,8 / 1,7	12,0	-4,0	0,0	11,0	0,0	4,5
	1996.01.02	1996.01.03	250,5	1	2,4 / 1,7	12,0	4,0	17,5	11,0	0,0	4,5

Tabla 8 Línea base perpendicular y condiciones meteorológicas para las imágenes analizadas en los incendios de Zuera08 (Envisat ASAR y TerrsaSAR-X) y Jaulin09 (ALOS PALSAR): temperatura máxima (Tmax), temperatura mínima (Tmin) y precipitación acumulada de los 4 días previos (PA).

Sensor	Fecha 1	Fecha 2	Línea base perpendicular (m)	Línea base temporal (días)	Velocidad del viento (m/s)	Tmax (°C) fecha1	Tmin (°C) fecha1	PA (mm) fecha1	Tmax (°C) fecha2	Tmin (°C) fecha2	PA (mm) fecha2
ASAR	2009.01.08	2009.02.12	33,7	35	2,3 / 6,7	0,0	-6,0	0,5	10,0	4,0	0,5
	2008.11.16	2008.12.19	-230,8	33	4,4 / 7,4	14,0	-2,0	0,0	11,0	4,0	0,0
	2008.11.16	2009.01.21	-108,9	66	4,4 / 3,8	14,0	-2,0	0,0	7,0	-3,0	2,3
	2008.11.16	2009.02.12	-242,5	88	4,4 / 7,8	14,0	-2,0	0,0	10,0	4,0	0,5
	2008.11.16	2009.02.23	3,5	99	4,4 / 9,0	14,0	-2,0	0,0	12,0	5,0	0,0
	2008.11.16	2009.03.06	165,8	110	4,4 / 8,4	14,0	-2,0	0,0	9,0	1,0	21,3
	2008.12.19	2009.01.21	121,9	33	7,4 / 3,8	11,0	4,0	0,0	7,0	-3,0	2,3
TSX	2008.12.19	2009.02.12	-11,7	55	7,4 / 7,8	11,0	4,0	0,0	10,0	4,0	0,5
	2008.12.19	2009.02.23	234,3	66	7,4 / 9,0	11,0	4,0	0,0	12,0	5,0	0,0
	2008.12.19	2009.03.06	65,0	77	7,4 / 8,4	11,0	4,0	0,0	9,0	1,0	21,3
	2009.01.21	2009.02.12	-133,6	22	3,8 / 7,8	7,0	-3,0	2,3	10,0	4,0	0,5
	2009.01.21	2009.02.23	112,4	33	3,8 / 9,0	7,0	-3,0	2,3	12,0	5,0	0,0
	2009.01.21	2009.03.06	-56,9	44	3,8/ 8,4	7,0	-3,0	2,3	9,0	1,0	21,3
	2009.02.12	2009.02.23	246,0	11	7,8 / 9,0	10,0	4,0	0,5	12,0	5,0	0,0
	2009.02.12	2009.03.06	76,7	22	7,8 / 8,4	10,0	4,0	0,5	9,0	1,0	21,3
	2009.02.23	2009.03.06	169,3	11	9,0 / 8,4	12,0	5,0	0,0	9,0	1,0	21,3
ALOS	2009.08.20	2009.10.05	503,6	46	-	34,0	15,0	0,0	26,0	11,0	0,0

3.3. Métodos

3.3.1. Estimación de la severidad mediante imágenes de satélite ópticas

Las bandas espectrales registradas por los sensores ópticos responden de manera diferente a las características de la superficie terrestre como el contenido de agua, la estructura de la vegetación, la productividad, la composición mineral del suelo, etc. Cuando la reflectividad de múltiples bandas se combina en algoritmos matemáticos la información sobre las propiedades de las superficies puede mejorar.

El índice desarrollado para la estimación de la severidad mediante sensores ópticos se conoce como *Normalized Burn Ratio* (NBR) y es similar en su construcción al Índice de Vegetación de Diferencia Normalizada (NDVI), siendo la diferencia principal la integración las dos bandas que mejor responden a los efectos del incendio: banda 4 (infrarrojo próximo - 0,76-0,9 µm) y banda 7 (infrarrojo medio de onda corta - 2,08-2,35 µm) (Key y Benson 2004):

$$NBR = \frac{(R4-R7)}{(R4+R7)} \quad \{5\}$$

donde: R - reflectividad de las bandas Landsat TM

Por lo general, la reflectividad posterior al incendio disminuye en el infrarrojo próximo mientras que aumenta en el infrarrojo medio de onda corta. Estas bandas registran el mayor cambio en magnitud en comparación con las otras longitudes de ondas disponibles a bordo del satélite y su combinación mejora considerablemente la distinción entre las áreas quemadas y no quemadas. Las mismas bandas también proporcionan información útil para diferenciar entre distintos niveles de severidad dentro del perímetro del incendio. La diferencia R4-R7 se divide por su suma para normalizar el resultado minimizando las variaciones ocasionadas por la topografía y la iluminación solar dentro de la escena, aislando así las diferencias reales entre la reflectividad de las diferentes bandas, y permitiendo la comparación espacial y temporal de los valores NBR derivados. Para aislar las zonas quemadas de aquellas sin quemar y proporcionar una medida cuantitativa del cambio, el NBR post incendio se resta al NBR obtenido a partir de imágenes anteriores al incendio:

$$dNBR = NBR_{anterior} - NBR_{posterior} \quad \{6\}$$

Se presume que los cambios en NBR y dNBR se correlacionan con la magnitud de los cambios ambientales provocados por el fuego, mientras que el CBI se refiere al cambio de las comunidades vegetales. Cuando las zonas no quemadas mantienen la fenología entre los pasos del satélite, el dNBR adopta valores próximos a cero. La relación del NBR y el dNBR con las características de las superficies quemadas depende de la respuesta espectral en cada banda. El infrarrojo próximo está positivamente correlacionado con la superficie foliar y la productividad vegetal, mientras que el infrarrojo medio de onda corta responde positivamente a la desecación: a mayor vigor vegetal mayor respuesta en la banda 4 y menor en la banda 7. Por tanto, el NBR es positivo en las zonas con actividad fotosintética intensa y negativo en zonas de baja

Tabla 9 Clases de severidad (Key y Benson 2006).

Severidad	Rango (dNBR *10^3)
Aumento de productividad (alto)	de -500 hasta – 251
Aumento de productividad (bajo)	de -250 hasta – 101
No quemado	de -101 hasta + 99
Severidad baja	de +100 hasta +269
Severidad baja-moderada	de +269 hasta +439
Severidad moderada-alta	de +440 hasta +659
Severidad alta	de +660 hasta +1300

productividad (vegetación herbácea durante un periodo seco) o sin vegetación. Las áreas quemadas se caracterizan por la disminución de la actividad fotosintética de la vegetación que influye de modo negativo en la respuesta en la banda 4, junto con la mayor exposición del sustrato y los combustibles quemados, que incrementan la reflectividad registrada en la banda 7. Por lo tanto, el NBR muestra valores negativos en las zonas quemadas (Key y Benson 2006).

El dNBR provee un rango continuo de valores que pueden ser utilizados directamente para la cartografía y el análisis de las áreas quemadas. En teoría, el dNBR (multiplicado por 10^3) puede oscilar entre -2.000 y 2.000, pero, en realidad, los datos válidos oscilan entre -550 y 1.350, en función de factores perturbadores que puedan afectar a los paisajes naturales. Los valores negativos son frecuentemente el resultado de la presencia de nubes en la imagen anterior al incendio o del incremento de productividad vegetativa en la imagen post-fuego (-500 < dNBR < -100). Los valores positivos se originan cuando la imagen posterior al incendio contiene zonas nubosas o, directamente, por el efecto del fuego, que suele asociarse a un rango entre 100 y 1.300. Valores por encima de 1.350 se corresponden normalmente a zonas nubosas. En general, la escala continua del dNBR se divide en clases de severidad para simplificar la descripción y la comparación de diferentes incendios. Una clasificación en siete niveles se ha revelado útil en una gran variedad ecosistemas (Tabla 9). Las dos primeras clases reflejan áreas en la que la productividad aumenta después del incendio, que normalmente se encuentra en zonas donde se ha producido un intenso rebrote de la vegetación herbácea. Las zonas no quemadas se corresponden a valores cercanos a cero, mientras que las últimas clases incluyen toda el área quemada. Sin embargo los umbrales pueden variar en función de la fenología de la vegetación, el ángulo solar de iluminación y el tiempo transcurrido entre el momento del incendio y el de estimación de la severidad (Key y Benson 2006).

3.3.2. La relación entre el CBI y el dNBR en el valle del Ebro

La correspondencia entre los niveles de severidad estimados en el terreno (CBI) y la estimación de la severidad mediante imágenes ópticas de satélite (dNBR) se ha abordado mediante el análisis de regresión. Para alcanzar un número similar de parcelas en cada uno de los rangos generales de severidad se ha utilizado un sub-muestreo de las parcelas CBI, tal y como sugieren Key y Benson (2006). Para el incendio de Zuera08 se han seleccionado todas las parcelas no quemadas, de severidad baja y moderada así como otras 22 de severidad alta, al azar, hasta conseguir un total de 65 parcelas. En el incendio de Jaulín09 se han utilizado todas las parcelas de muestreo dada su mejor distribución por rangos de severidad. El diagrama de dispersión de dNBR v. CBI (Fig. 13) muestra los altos coeficientes de determinación ($p<0,05$) obtenidos para ambos

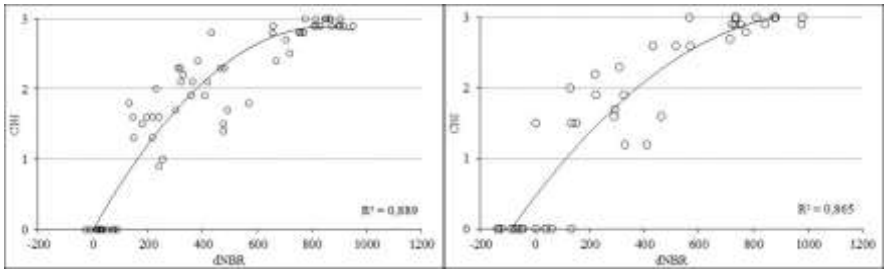

Fig. 13 Relación entre el CBI y el dNBR para los incendios de Zuera08 (izquierda) y Jaulín (derecha).

incendios analizados. Este resultado avala la hipótesis de que el dNBR se puede utilizar como índice radiométrico fuertemente relacionado con los niveles de severidad registrados en el campo. Por lo general, se han encontrado correlaciones más altas entre el dNBR y la severidad del dosel que con el sotobosque o con la severidad total de las parcelas, lo que no es en absoluto sorprendente habida cuenta de que los datos ópticos registran principalmente la reflectividad de la parte superior del dosel.

La estimación de la severidad en el terreno sólo está disponible para los incendios recientes; sin embargo, la contigüidad espacial, la estructura similar del bosque y la alta correlación entre el CBI y el dNBR permiten el uso de imágenes de satélite (dNBR) para la estimación de la severidad en incendios anteriores, como el ocurrido en los Montes de Zuera en 1995.

3.3.3. Establecimiento de los modelos de relación entre los niveles de severidad de las imágenes de satélite SAR y su verificación

Esta tesis doctoral se centra principalmente en el estudio de la relación entre la severidad de los incendios forestales y los parámetros derivados de las imágenes de satélite radar, como el coeficiente de retro-dispersión y la coherencia. También se intenta estimar la bondad de estos parámetros para la estimación de la severidad mediante el desarrollo de modelos empíricos en los que la severidad del incendio se convierte en la variable dependiente, que se estima mediante el uso de imágenes radar de apertura sintética. Se investigan todas las frecuencias radar (X, C y L) disponibles hoy en día a bordo de las plataformas espaciales, utilizándose no sólo las polarizaciones más sensibles para el estudio de la vegetación (HV o VH) sino también las demás (HH y VV). Para tales fines se utiliza tanto un conjunto de parcelas de muestreo (CBI) como un conjunto sustitutivo de parcelas generadas de modo aleatorio, denominadas en adelante 'pseudo-parcelas'.

3.3.3.1. Parcelas de muestreo en el terreno (CBI)

La presencia del moteado en las imágenes SAR hace que el estudio a nivel de píxel sea menos fiable, especialmente cuando no se dispone de imágenes de muy alta resolución espacial. Por tanto, para reducir este efecto, se trabaja con el promedio de los píxeles situados dentro de un radio de 55 m (aproximadamente 1 ha) desde el centro de cada parcela muestreada. Como consecuencia de la superficie original muestreada en el campo (700 m^2), la elevada fragmentación del paisaje y la necesidad de mantener cierta homogeneidad de la estructura forestal, la pendiente y el nivel de severidad, no se ha

Fig. 14 Puntos de muestreo CBI sobre ortofotografía de alta resolución.

considerado utilizar una superficie mayor a 1 ha. Este límite establecido conduce a considerar alrededor de 15 píxeles por punto de muestreo. Cada buffer correspondiente a las parcelas de muestro se ha analizado mediante ortofotografías de alta resolución con objeto de eliminar del perímetro las áreas no arboladas (Fig. 14). Únicamente las parcelas con una área mínima de 0,3 ha (correspondiente a cinco píxeles de 25x25 m) se han tenido en cuenta para el análisis posterior.

3.3.3.2. Pseudo-parcelas

El uso de las pseudo-parcelas se ha adoptado debido al gran número de muestras necesarias para el análisis estadístico, que no se pueden conseguir fácilmente mediante trabajo de campo. Las pseudo-parcelas se han generado promediando píxeles con valores similares de dNBR para el mismo ángulo de incidencia local, que se calcula en función de la geometría de adquisición de cada imagen SAR, la pendiente local y la orientación. Valores similares de severidad (dNBR) se han obtenido mediante la reclasificación del rango de severidad inicial en clases, cada una de ellas de 50 unidades (ej. 101-150, 151-200, 201-250 etc.). Únicamente se han seleccionado píxeles con altos valores del NDVI en la imagen óptica anterior al incendio (es decir, con mayor cobertura vegetal) para la generación de las pseudo-parcelas (Fig. 15).

Para evitar sesgos relacionados con el tamaño se utilizan sólo pseudo-parcelas que contienen un número fijo de píxeles. La elección de este número implica una compensación entre la variabilidad de las pseudo-parcelas (varianza menor para mayor número de píxeles por parcela) y el número de pseudo-parcelas disponibles para cada nivel de severidad (menos parcelas disponibles cuando se promedia un mayor número de píxeles por parcela). Así se utilizan 9 píxeles (0,5 ha) para la resolución espacial de trabajo de 25 m, mientras que se usan 25 píxeles (0,25 ha) en el caso de imágenes SAR de muy alta resolución (TerraSAR-X) para la estimación de la coherencia interferométrica. Para el análisis estadístico se han seleccionado al azar entre 700 y 900 pseudo-parcelas en función del incendio estudiado.

3.3.3.3. Análisis estadístico

La sensibilidad de la información procedente de sensores tipo SAR y su utilidad para el análisis de las áreas quemadas ha sido analizada mediante técnicas de estadística descriptiva e inferencial. Utilizando métodos descriptivos se han estudiado las

Fig. 15 Generación de pseudo-parcelas.

tendencias del coeficiente de retro-dispersión y la coherencia interferométrica en función del nivel de severidad, la topografía y las condiciones ambientales o la recuperación de la vegetación tras los incendios.

Por otra parte, se han utilizado modelos empíricos (lineales o cuadráticos) para el estudio del poder predictivo y los errores de estimación de las medidas SAR para el análisis post-incendio de las áreas quemadas. El uso conjunto del coeficiente de retro-dispersión y de la coherencia interferométrica se ha apoyado en modelos lineales generalizados (GLZ), que permiten el uso de múltiples variables independientes relacionadas de modo no lineal con la variable respuesta (Agresti 2007). El ajuste estadístico de los modelos (el coeficiente de determinación - R^2 o la desviación - D^2) se ha utilizado para evaluar la proporción de la variabilidad explicada y el potencial del coeficiente de retro-dispersión y la coherencia interferométrica procedente de diferentes sensores y polarizaciones para la estimación de la severidad. El error de estimación entre los valores predichos y los observados se ha evaluado mediante el error cuadrático medio (RMSE), utilizándose una parte de los datos (75%) para calibrar el modelo y otra (25%) para su validación. El ajuste de los modelos GLZ se ha evaluado mediante el criterio de información de Akaike (AIC), que constituye una referencia a la hora de elegir entre modelos basados en diferentes variables independientes (Akaike 1974). El estudio del potencial de las medidas SAR para la recuperación vegetal en áreas quemada se ha llevado a cabo mediante el análisis de varianza y la comparación por pares, utilizando el test Games-Howell, que no requiere varianzas ni número de muestras iguales (Games y Howel 1976).

Para minimizar el efecto de la topografía los análisis se han realizado por grupos de 5° de ángulo de incidencia local. Este intervalo de frecuencia de muestreo se ha revelado óptimo para el estudio de los efectos del ángulo de incidencia local (apartado 4.2.1). Un mayor intervalo de muestreo incrementa el ruido en los datos, mientras que utilizando un intervalo menor los efectos de la topografía son menos evidentes. La homogeneidad de los bosques y la gran extensión del área afectada por alta severidad permitieron la evaluación de la influencia del ángulo de incidencia local y de las condiciones climáticas en el coeficiente de retro-dispersión.

BIBLIOGRAFÍA

Agresti, A. (2007). *An Introduction to Categorical Data Analysis*. New Jersey: John Wiley.

Akaike, H. (1974). A new look at the statistical model identification. *IEEE Transactions on Automatic Control, 19*, 716-723.

Castel, T., Beaudoin, A., Stach, N., Stussi, N., Le Toan, T., y Durand, P. (2001). Sensitivity of space-borne SAR data to forest parameters over sloping terrain. Theory and experiment. *International Journal of Remote Sensing, 22*, 2351-2376.

Chuvieco, E., Riano, D., Aguadi, I., y Cocero, D. (2002). Estimation of fuel moisture content from multitemporal analysis of Landsat Thematic Mapper reflectance data: applicatios in fire danger assessement. *International Journal of Remote Sensing, 23*, 2145-2162.

Games, P.A., y Howel, J.F. (1976). Pairwise Multiple Comparison Procedures with Unequal N's and/or Variances: A Monte Carlo Study. *Journal of Education and Behavioral Statistics, 1*, 113-125.

Gatelli, F., Guarnieri, A.M., Parizzi, F., Pasquali, P., C.Prati, y Rocca, F. (1994). The wavenumber shift in SAR interferometry. *IEEE Transactions on Geoscience and Remote Sensing, 32*, 855-865.

Key, C.H., y Benson, N.C. (2004). *Ground Measure of Severity, The Composite Burn Index*. Ogden, UT: U.S. Department of Agriculture, Forest Service, Rocky Mountain Research Station.

Key, C.H., y Benson, N.C. (2006). Landscape assessment (LA). In D.C. Lutes, R.E. Keane, J.F. Caratti, C.H. Key, N.C. Benson, S. Sutherland y L.J. Gangi (Eds.), *FIREMON: Fire effects monitoring and inventory system* (pp. 1-55). Fort Collins, CO: U.S. Department of Agriculture, Forest Service, Rocky Mountain Research Station, Gen. Tech. Rep. RMRS-GTR-164-CD.

Ulander, L.M.H. (1996). Radiometric slope correction of synthetic-aperture radar images. *IEEE Transactions on Geoscience and Remote Sensing, 34*, 1115-1122.

Wegmüller, U., Strozzi, T., y Bitelli, G. (1999). Validation of ERS differential SAR interferometry for land subsidence mapping: the Bologna case study. In, *IGARSS'99* (pp. 1131-1133). Hamburg, 28 June - 2 July 1999.

Wegmüller, U., Werner, C., y Strozzi, T. (1998). SAR interferometric and differential interferometric processing. In, *Geoscience and Remote Sensing Symposium, 1998. IGARSS '98. Proceedings. 1998 IEEE International* (pp. 1106-1108). Seattle, USA.

Wegmüller, U., Werner, C., Strozzi, T., y Wiesmann, A. (2002). Automated and precise image registration procedures. In L. Bruzzone y P. Smits (Eds.), *Analysis of multi-temporal remote sensing images* (pp. 37-49). Singapore: World Scientific 2002.

Capítulo 4. ESTIMACIÓN DE LA SEVERIDAD Y LA RECUPERACIÓN DE LA VEGETACIÓN MEDIANTE LA TELEDETECCIÓN

En este capítulo se describen los resultados obtenidos y se aborda su discusión según los objetivos fijados. En primer lugar se estima la severidad de los incendios mediante sensores ópticos y se cuantifica la relación existente entre los modelos empíricos derivados para diferentes incendios, desarrollándose un modelo único para todos los pinares aragoneses.

Los siguientes apartados se dedican al estudio de la sensibilidad del radar de apertura sintética a la severidad del fuego en el entorno mediterráneo. El análisis se extiende brevemente a los bosques boreales utilizándose la longitud de banda más sensible a los patrones de severidad.

La última parte de este capítulo se dedica al estudio de la recuperación vegetal en áreas quemadas en entornos mediterráneos y boreales afectados por incendios. Además, se analiza la influencia de la humedad sobre la estimación de la biomasa en bosques boreales jóvenes.

4.1. Estimación de la severidad mediante sensores ópticos y trabajo de campo

4.1.1. Estimating burn severity in Aragón pine forests using optical based indices

Tanase, M.A., de la Riva, J. and, Pérez-Cabello, F. Estimating burn severity in Aragón pine forests using a single empirical model. *Canadian Journal of Forest Research,* undergoing review.

Resumen

Se desarrollan modelos regionales para la estimación de la severidad utilizando el Composite Burn Index (CBI) y el Normalized Burn Ratio (NBR). En este trabajo se evalúa la relación entre estas variables en cinco áreas quemadas en Aragón, nordeste de España. Se evalúan también índices espectrales adicionales con el objeto de estudiar su valor operativo para la estimación de la severidad del incendio. Se aplican modelos lineales y no lineales, evaluándose el error de estimación en cada caso.

Los modelos no lineales proporcionan el mejor ajuste estadístico de los datos tanto para cada incendio por separado como para el conjunto de los analizados. Los resultados sugieren la idoneidad de establecer un único modelo para la discriminación del área quemada en los pinares aragoneses. El error de estimación de la severidad para parcelas muy quemadas se sitúa por debajo del 10%, mientras que para parcelas menos afectadas el error de estimación aumenta hasta un 25%. Se obtiene una relación lineal ajustada para la severidad a escala de parcela, sotobosque y dosel arbóreo.

El presente trabajo permite concluir: (i) la coherencia de la inversión de un único modelo para la estimación de la severidad a nivel regional y (ii) la necesidad de desarrollar nuevos métodos de estimación para las zonas afectadas por incendio con baja y moderada severidad, incluso en el caso de bosques homogéneos.

Estimating burn severity in Aragón pine forests using optical based indices

M. A. Tanase[(1)], J. de la Riva[(1)], and F. Pérez-Cabello[(1)]

[(1)]Department of Geography,
University of Zaragoza,
Pedro Cerbuna 12, 50009 Zaragoza, Spain
Email: mihai@tma.ro, delariva@unizar.es, fcabello@unizar.es

Abstract

Regional models for burn severity assessment were developed using the composite burn index (CBI) and the differenced Normalized Burn Ratio (dNBR). The study assessed the relationship between these variables across five recently burned sites in northeastern Spain. Additional remotely sensed indices were studied to test their practical value for burn severity estimation. Linear and non-linear models were tested and the estimation error of each model was assessed. A non-linear model provided the best statistical fit of the data at each individual site and for the pooled dataset. Our results suggest a single model is practical for burned area differentiation in Aragón pine forests. Burn severity estimation errors for highly burned sites were well below 10 % whereas for low and moderate severity errors increased up to 25%. A strong linear relation was found between burn severity at plot level and understory and overstory composites. This study demonstrates: (i) the consistency of model inversion for burn severity estimation at regional level and (ii) the need for new estimation methods in areas affected by low to moderate burn severities even for homogeneous forests.

Keywords*: burn severity, dNBR, CBI, mediterranean forest*

INTRODUCTION

Worldwide forests fires destroy annually millions of hectares from tropical to boreal region. In the European part of the Mediterranean basin alone about five hundred thousand hectares are affected each year (Schmuck et al. 2008) making fires one of the most important ecological threats. Discriminating the impact of fire on ecosystems is important since burn severity can be related to socio-economic or ecological factors such as fuel treatments effectiveness (Wimberly et al. 2009), post-fire evolution of plant communities and species richness across landscape (Wimberly and Reilly 2007), seedling recruitment (Turner et al. 1997), soil erosion (Ice et al. 2004), water quality (Minshall et al. 2001), risk evaluation and post-fire management options. Burn severity maps could also provide a means for fuel map updates without the need for collecting supplementary field data (Allen and Sorbel 2008). In addition, emissions from forest fires substantially contribute to the release of green-house gasses (Simmonds et al. 2005). Fire properties have significant effects on gas emission from burned areas (Andreae and Merlet 2001), fire duration and intensity being the primary factors controlling the amount of released gases.

Description of the fire effects depends widely on the assessment objectives such as socio-economic or ecological impact evaluation. Although a common standard for fire ecological impact is yet to emerge, during the last decade burn severity has been increasingly used to assess both short- and long-term post fire effects on vegetation. For a comprehensive review of fire terminology and its use across different research communities we refer the reader to Lentile et al. (2006). Burn severity was commonly defined and assessed based on the vegetation type and fire characteristics (French et al. 2008). Ecological burn severity as defined by (Key and Benson 2006) is the magnitude of change between pre- and post-fire forest components. To sample these changes and summarize the general fire effects at a given plot the composition burned index (CBI) was developed (Key and Benson 2006). The index averages the conditions of many factors (e.g. duff and litter consumption, percentage of foliage altered, char height, canopy mortality etc.) across multiple vegetation layers (i.e. substrate, low shrubs, high shrubs, small trees and tall trees) to derive the severity at each site. CBI was initially developed to assess variations in fire and burn severity in western USA pine forests but it was adopted and adapted (Epting et al. 2005; Kasischke et al. 2008; Santis and Chuvieco 2007, 2009) to a wide range of environments from mediterranean to boreal (Allen and Sorbel 2008; Hall et al. 2008; Santis and Chuvieco 2007; Wagtendonk et al. 2004).

Remotely sensed data constitutes the method of choice when estimates of burn severity are needed over large areas due to the reduced spatial representation, the prohibitive costs and the time needed by field work. The detection of burn severity from space is accomplished using per band reflectance or vegetation indices derived from optical sensors of different spatial resolutions from 1km (e.g. Advanced Very High resolution Radiometer-AVHRR) down to 1 m (e.g. QuickBird). The launch of Landsat 5 Thematic Mapper (TM) in the early `80s greatly influenced the way burn severity is derived today at local and regional levels. Research carried out in Spanish burns (Lopez-Garcia and Caselles 1991) demonstrated the value of Landsat bands 4 and 7 to estimate vegetation variability within the fire perimeters which led to the development of the Normalized Burn Ratio (NBR) commonly used nowadays in a bi-temporal approach with pre- and post-fire data (dNBR). The index takes advantage of the opposite response to burning of band 4 (post-fire decrease) sensitive to vegetation productivity and band 7 (post-fire increase) sensitive to substrate exposure (Key and Benson 2006; Wagtendonk et al. 2004). A relative version of dNBR (RdNBR) was proposed by (Miller and Thode 2007) in order convert the absolute change measured by dNBR to a relative measure which varies linearly with severity. The main advantage of using a relative index is the opportunity of comparing fire severity across space and time since RdNBR removes biasing of the pre-fire vegetation conditions (Miller et al. 2009). Differenced indices like dNBR and RdNBR are more sensitive to absolute and relative changes in forest structure whereas NBR is most sensitive to post-fire forest structure such as vegetation fill, crown closure and changes in average canopy height (Wulder et al. 2009).

Field and remotely sensed estimates of burn severity are commonly related using linear, quadratic or exponential models. Recently, a non-linear saturated growth (SG) model form was proposed in order to better fit the relation between field and remotely sensed data. The saturated growth model addresses the unrealistic projections of the second order polynomial models which, beyond the asymptote point, predict smaller CBI values for increasing dNBR (Hall et al. 2008). Empirical modeling of burn severity (CBI) as a function of dNBR provided accurate detection of burn severity the reported determination coefficients being usually high (R^2>0.7) (Allen and Sorbel 2008; Cocke et

al. 2005; Epting et al. 2005; Hall et al. 2008; Wagtendonk et al. 2004; Wimberly and Reilly 2007). However, for non-forested areas (e.g. herb, scrub and open forests) the use of this index might be less be appropriate (Epting et al. 2005). Some authors (Hoy et al. 2008; Landmann 2003; Murphy et al. 2008) reported weaker relationships between dNBR and CBI in savannas, tropical or boreal forests. This was attributed to dNBR`s inability to discern between high severity sites, to variations in topography and solar elevation angle (Verbyla et al. 2008), to the specific fuel conditions and the design of dNBR index (Roy et al. 2006). For the mediterranean region the reported determination coefficients were high (Miller et al. 2009; Santis and Chuvieco 2009).

The aim of this study was to produce a single model useful for burn severity estimation at regional level without the need of gathering costly and time consuming field data at each site. This resulted in the four questions addressed by this study:

1. Which model better describes the relation between field and remotely sensed severity estimations in Aragón pine forests?
2. Is one model appropriate for the estimation of severity at regional level?
3. Are other spectroscopic indices valid substitutes?
4. It is possible to reliably estimate burn severity beyond the forest canopy?

STUDY AREA

Aragón autonomous region (47,719 km^2) is located in northeastern Spain (Fig. 1) stretching from the Pyreneans mountain range in the north to the Iberian range in the south. The central part is occupied by the Ebro valley which is the northernmost semi-

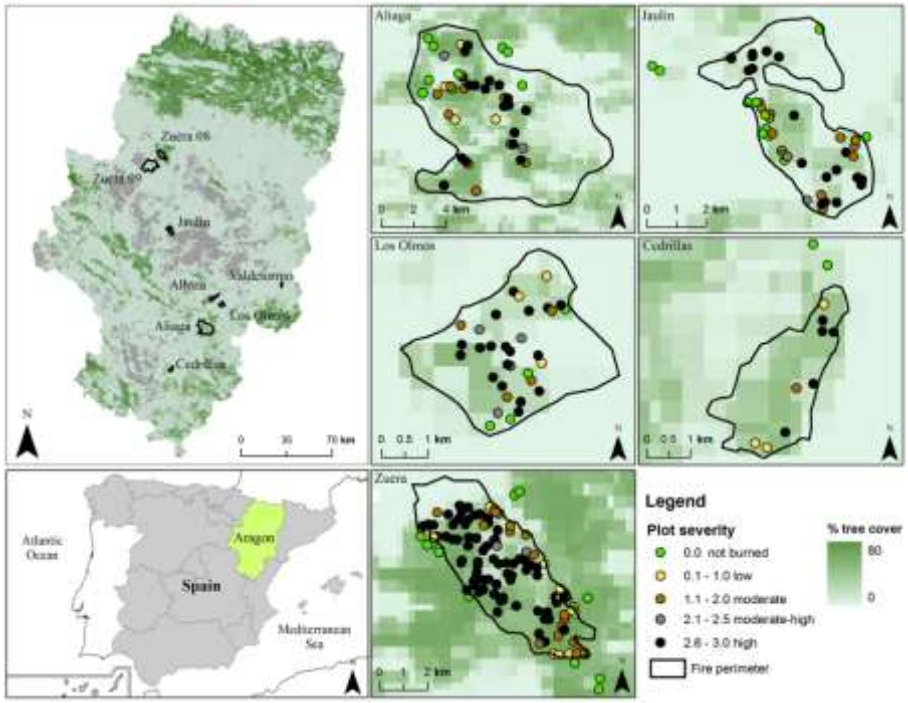

Fig. 1 Aragón study area, the location of the 2008-2009 large fires and the field assessed CBI plots.

arid region in Europe. The geological diversity results in high topographic variation which ranges from 100 to more than 3000 m above sea level. The continental climate is characterized by very cold winters and hot and dry summer seasons. In the Ebro valley the mean annual precipitations is below 350 mm. Forests extend on more than 1.5 million hectares out of which approximately 50% are coniferous, 35% are mixed whereas the rest are deciduous. The open forests (less than 20% tree cover) and shrublands occupy another 1 million hectares. During the last decades the area covered by forest increased due to past afforestation projects and rural abandonment. The main tree species are *Pinus halepensis* Mill., *Pinus sylvestris* L., *Pinus pinaster* Aiton, *Quercus ilex* L. and *Quercus Pyrenaica* Willd. whereas *Quercus coccifera* L., *Juniperus oxycedrus* Sibth. & Sm, *Thymnus vulgaris* L. are commonly encountered in shrublands.

In the past twenty years about 5000 hectares were annually affected by fire in Aragón out of which almost 3000 were dense forests. The annual burned area is usually well below the average, but in exceptional years such as 1994 and 2009 the affected area could spike up to 30,000 hectares. During 2008 and 2009 eight large fires (> 100 ha) were declared in Aragón. The affected area was around 23,000 hectares most of which burned in 2009 (Table 1). All fires affected pine forests, most of them being ignited by natural causes (e.g. extremely dry hot weather coupled with storms).

METHODS

Field data collection

Initial assessment (Key and Benson 2006) was conducted within two months after fire at five of the eight affected sites (Fig. 1 and Table 1). Zuera09 fire was not accessible due to its location in one of the largest military maneuver areas in Europe. Two other sites were not field assessed due to the small proportion of dense forest (Alloza) or the small area affected (Valdetormo). At each sample site fire severity was evaluated on a 15 m radius using the magnitude of the environmental change with respect to the presumed pre-fire state as described in (Key and Benson 2006). The plots were located in areas of homogeneous forest structure and fire effects. The vegetation layers characteristic of the studied pine forests consisted of substrate, herbs and low shrubs less than 1 m tall, shrubs and trees up to 5 m tall and intermediate trees up to 20 m tall. In each plot digital photos (N, S, W and E directions and close-ups of crown, soil and shrub layer burns) were taken and the center was measured with Global Positioning System (GPS). The positioning error after differential correction was less than 1 meter.

The similar forest structure and fire regime resulted in comparable burn conditions for all areas (Fig. 2): i) in low severity areas the trees were scorched at the base, the litter was partially consumed and the understory layer was affected in a patchy pattern. The

Table 1 Large fire events in Aragón (2008-2009 seasons) and the field assessed plots.

Fire	Date	Cause	Burned area (ha)	CBI plots
Zuera08	08. 2008	car accident	2200	123
Jaulin	07.2009	storm	1800	45
Aliaga	07.2009	storm	9000	45
Los Olmos	07.2009	storm	500	34
Cedrillas	07.2009	storm	600	11
Zuera09	08.2009	unknown	7500	-
Alloza	07.2009	storm	1450	-
Valdetormo	07.2009	storm	300	-

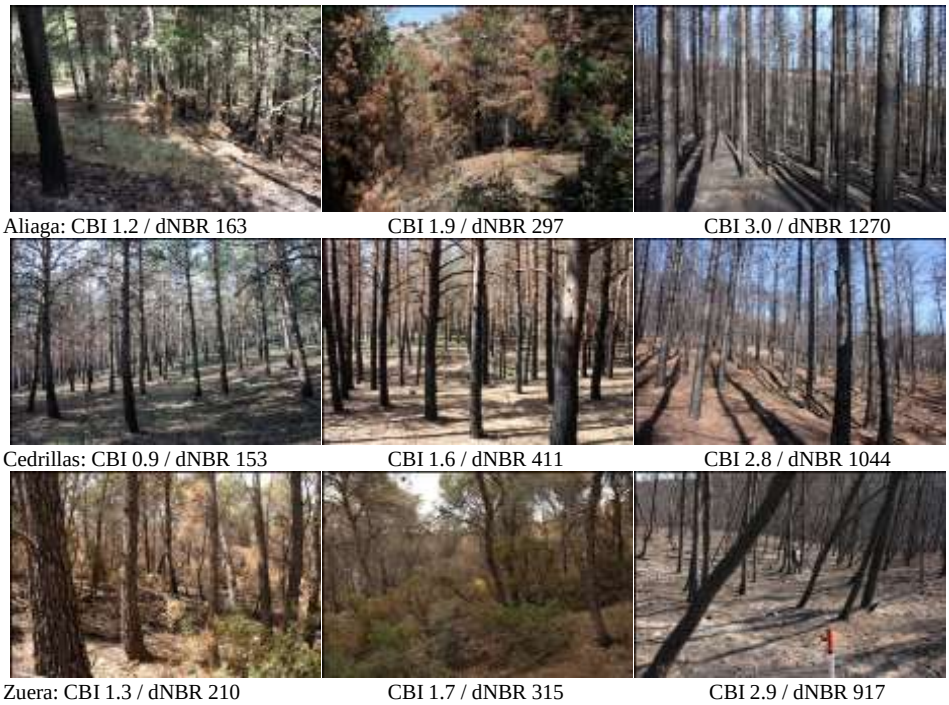

Fig. 2 Examples of low severity (left), moderate severity (center) and high severity (right) for three of the analyzed fires.

foliage of the understory was scorched and partially consumed whereas the tree crowns remained largely unaffected; ii) in moderate severity areas some of the understory layer was preserved. The needles/leaves and the small branches of the short shrubs (<1 m height) were consumed whereas the tall shrubs (> 1 m height) presented scorched foliage. The tree crowns were partially scorched which resulted in incomplete foliage loss; iii) the consumption of the understory layer increased for moderate-high severity areas whereas tree crowns were usually scorched and only some of the foliage was retained. The loss of branches and small twigs was small for the tree layer. The understory layer lost the twigs and small branches especially for small shrubs (i.e. less than one meter tall) and iv) in high severity areas the combustion of the litter, understory layer and tree crowns elements (i.e. needles, and twigs) was complete. At the highest severities small and medium sized branches were also consumed.

The high fire intensity resulted in an unequal distribution by range of severity. Most of the affected forests were in high or moderate-high burn severity classes whereas low burn severity areas were mainly encountered along the fire borders. As a result, CBI sampled plots were not proportionally distributed over the entire severity range: 42 unburned, 18 low severity (CBI < 1), 42 moderate severity (1< CBI < 2), 18 moderate-high severity (2 < CBI < 2.5) and 138 high severity (CBI >2.5).

Satellite image data and spectroscopic indices

The Landsat TM dataset was formed by six scenes from path 199 row 031 (Zuera08 and Jaulin fires) and row 032 (Aliaga, Los Olmos and Cedrillas fires). Zuera08

fire was images on 21, July 2008 (pre-fire) and 22, August 2008 (post fire) whereas the other fires were imaged on 22, June 2009 (pre-fire) and 26, September 2009 (post-fire). The images were geometrically rectified to the Universal Transverse Mercator (UTM) projection zone 30 North (Ellipsoid International 1909, Datum European 1950) using a linear polynomial model and incorporating information of the local topography using a digital elevation model (DEM). Around 100 ground control points were used to register each scene to high resolution orthophotos. For all images, a root mean square error of less than one píxel (approximately 0.65) was achieved. The nearest neighbor resampling method was utilized in order to preserve the original radiometric values. All images underwent radiometric corrections to compensate for variation in sensor radiometric response, sun angle, sun azimuth and topography. There was no need for between scene normalization (pre- / post-fire) because the coefficient of determination among stable targets was greater than 0.98 (Key and Benson 2006).

To estimate burn severity by means of remote sensed data two indices were used: i) Normalized Differenced Vegetation Index (NDVI) and ii) Normalized Burn Ratio. These indices were selected based on their sensitivity to changes in forest status and burn severity estimation demonstrated by previous work (Allen and Sorbel 2008; Epting et al. 2005; Hudak et al. 2007; Santis and Chuvieco 2007; Wagtendonk et al. 2004). A second reason for NDVI selection was the opportunity it gives to model severity using optical sensors that lack information on the shortwave infrared part of the spectrum. Thus, burn severity estimates could be generated for very old fires and subsequently used to relate fire effects with spatio-temporal patterns of forest recovery. The two indices were used in a single-date approach ($NDVI_{post\text{-}fire}$ and $NBR_{post\text{-}fire}$) and a two-date approach (dNBR, RdNBR and differenced NDVI – dNVDI) were values of the post fire image are subtracted from the pre-fire image. Table 2 presents the method of calculation for each spectroscopic metric based on Landsat TM band number. For the two-date approach we scaled the indices by 1000.

Data analysis

The relationship between CBI and dNBR was analyzed using both linear and quadratic models and the new saturated growth model proposed by Hall et al. (2008). The models were fit with data from each individual fire and their prediction power was compared using the level of significance, the association strength between variables expressed by the determination coefficient (R^2) and the amount of error expressed by the root mean squared error (RMSE). At each site the CBI plots were randomly divided in training and validation sets using a 70/30 ratio. Ten iterations were used in order to obtain the average fit of each model and avoid exceptional high determination coefficients and low errors due to random effects. Regional models were developed using a sub-sample of the pooled dataset (PSS 150).

In order to assess the practical value of the regional models, the quadratic and the saturated forms developed for each fire were fit to the remaining burns and the magnitude of RMSE was studied. Likewise, an iterative cross-validation method was

Table 2 Spectroscopic indices used for burn severity assessment.

Spectroscopic metric	Method of calculation	Spectroscopic metric	Method of calculation
NDVI	$(B4 - B3)/(B4 + B3)$	dNDVI	$NDVI_{pre-fire} - NDVI_{post-fire}$
NBR	$(B4 - B7)/(B4 + B7)$	dNBR	$NBR_{pre-fire} - NBR_{post-fire}$
RdNBR	$(NBR_{pre-fire} - NBR_{post-fire})/(\sqrt{\lvert NBR_{pre-fire}\rvert})$		

used to estimate the fit parameters. For the PSS 150 models the errors were further studied by burn severity classes. This comparison was useful since model errors are not constant along the entire burn severity range. Using the PSS 150 dataset we evaluated the utility of other spectroscopic indices for burn severity estimation using the quadratic model form. This form was chosen since for one-date approach the saturated growth model poorly fitted the data. Finally, the relationship between overall burn severity and its two composites (understory and overstory) was analyzed for the pooled dataset using scatterplot graphs.

RESULTS AND DISCUSSION

Average fit parameters (R^2 and RMSE) together with model coefficients are presented in Table 3. The values of the coefficients were obtained using the entire sample from each site whereas the fit parameters were obtained as described above. At each site the best fit and lowest error appears in bold. Across all burns CBI and dNBR were significantly correlated ($p<0.001$), determination coefficients obtained varying from 0.576 to 0.954 according to the model form and site (Table 1). The average estimation error remained always below 20% of the CBI range. Significantly better model fit was obtained for the smallest sites (Los Olmos and Cedrillas) most likely due to the higher forest homogeneity which resulted in less burn variability. The highest association strength and lowest errors were obtained for the quadratic model form. However, these statistics could be misleading due to the unrealistic projections of the quadratic model at high burn severities as shown in (Hall et al. 2008). The use of the saturated growth model which resulted in similar fit statistics could be more appropriate when taking into account the fire regime across Aragón pine forests where large areas are affected by high burn severity. A graphic representation of the PSS 150 models (Fig. 3) showed the asymptote of the quadratic function at about 900 dNBR. The determination coefficients of the quadratic model for individual sites are similar with those obtained by Santis and Chuvieco (2007) for a Spanish pine forest or for burned coniferous or mixed forests in Alaska (Allen and Sorbel 2008; Epting et al. 2005) and California (Wagtendonk et al. 2004).

Table 3 Linear, quadratic and saturate growth model results for each site and for the pooled dataset. In bold the highest determination coefficient (R^2) and the lowest error at each site.

Model	Parameter a	b	c	R^2	RMSE	Parameter a	b	c	R^2	RMSE
	Aliaga					Jaulin				
CBI=a+b(dNBR)	0.857	2.12-E03		0.659	0.55	0.945	2.71-E03		0.623	0.52
CBI=a+b(dNBR)+c(dNBR)^2	0.402	5.51-E03	-2.9-E06	**0.786**	0.36	0.736	6.59-E03	-4.6-E06	**0.768**	**0.29**
CBI=dNBR(a|dNBR|+b)$^{-1}$	0.267	75.23		0.778	**0.30**	0.243	71.21		0.576	0.32
Calibration / Validation (*n*)	30 / 15					30 / 15				
	Los Olmos					Cedrillas				
CBI=a+b(dNBR)	1.015	2.97-E03		0.776	0.45	0.383	2.73-E03		0.896	0.34
CBI=a+b(dNBR)+c(dNBR)^2	0.706	7.10-E03	-5.5-E06	**0.936**	**0.23**	-0.031	6.08-E03	-3.2-E06	**0.954**	**0.16**
CBI=dNBR(a|dNBR|+b)$^{-1}$	0.241	63.66		0.836	0.38	0.206	134.46		**0.954**	0.19
Calibration / Validation (*n*)	24 / 10					8 / 3				
	Zuera08					PSS 150				
CBI=a+b(dNBR)	0.581	2.74-E03		0.801	0.42	0.861	2.44-E03		0.669	0.52
CBI=a+b(dNBR)+c(dNBR)^2	0.296	5.62-E03	-3.0-E06	**0.876**	**0.24**	0.566	5.14-E03	-2.8-E06	**0.782**	**0.38**
CBI=dNBR(a|dNBR|+b)$^{-1}$	0.235	100.77		0.868	0.26	0.252	83.13		0.730	0.42
Calibration / Validation (*n*)	55 / 25					100 / 50				

all models were extremely significant $p<0.001$

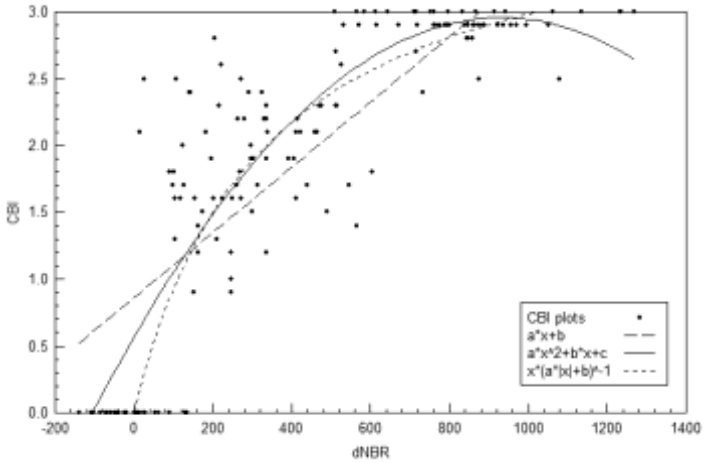

Fig. 3 PSS 150 scatter plot and modeled relation between CBI and dNBR.

The relatively small differences in magnitude between the fit parameters of the site specific models indicated a unified model would result in similar predictions. The regional models were developed using a sub-sample of the 258 pooled CBI plots. Under-sampling the data was necessary in order to preserve a balance between the number of plots for each general range of severity as suggested by (Key and Benson 2006). The better prediction power of dNBR for low and high burn severity would have resulted in overestimating the model fit due to the much higher number of CBI plots sampled within these severity ranges. Basically, for the pooled models, all the plots with CBI values between 0.1 and 2.5 were kept whereas a random sample was selected from the unburned and highly burned plots. In total, 150 plots (around 30 plots per severity class) were included in the PSS 150 dataset. For the same reasons, a sub-sample of 80 plots was used for modeling the fire effects at Zuera08 site. The five site specific models were similar to the model generated from the sub-sampled pooled data and the fit parameters were comparable (Table 3). This suggested that a single model could be appropriate for burn severity estimation for Aragón all pine forests.

To evaluate the interchangeability of the models we analyzed the RMSEs obtained when fitting a site specific model to all the remaining sites. As expected, errors increased with respect to those obtained when fitting the site specific models (Table 4). However, the most significant trend was the lower error obtained for the saturated growth form compared to the quadratic one which also held true when using the PSS 150 dataset. On average the error increase was 10-20% lower for the saturated growth model form suggesting better adaptability across different burns. The much lower average errors obtained for Zuera08 fire are caused by the use of all 123 CBI samples collected at this site. The large number of high severity plots (77) decreased the average error since both models seemed to better estimate unburned and highly burned areas. To confirm this assumption we carried out an analysis using all 258 CBI plots and the PSS 150 models. The results showed that for low and moderate severity areas the estimation errors could be two times bigger than for unburned or highly burned areas (Table 4). Moderate-high severity plots were more likely to be wrongly labeled, the estimation errors reaching 25% of the CBI range. The use of radiative transfer models could further decrease the

estimation error of such sites as recently shown in (Santis et al. 2009). For the other severity classes the errors were below 20% when using the saturated growth model. In fires with large areas affected by high burn severity the estimation errors should be well below 10 %. Accurate classification of such areas is important due to the slower vegetation recovery, higher erosion potential, landscape esthetic and changes in wildlife habitat (Miller and Thode 2007).

Additional spectroscopic indices were evaluated for burn severity estimation using the sub-sampled dataset. The model coefficients were derived using the entire PSS 150 dataset whereas the information on the parametric fit was derived using the cross-validation method replicated across ten trials on a 30 percent random sample (Table 5). The use of spectroscopic indices which lack information in the shortwave infrared part of the electromagnetic spectrum (NDVI and dNDVI) resulted in decreased association strength to burn severity. Our results are somewhat lower than those achieved by previous work (Epting et al. 2005; Hudak et al. 2007; Santis and Chuvieco 2007). The pooling process might have enhanced the indices sensitivity to spatial variation of forest properties. A site specific analysis revealed consistently higher association strength of NDVI and dNDVI with burn severity for most of the burns. The estimation errors reached around 20%. Despite higher errors these models could provide useful information on severity level for the retrospective analysis of sites burned before the launch of Landsat TM (Hudak et al. 2007). The remaining two indices produced very similar results compared with dNBR so they could be used when only post-fire images are available (NBR) or when analyzing multiple fires (RdNBR) without additional data for calibration (Miller et al. 2009).

An analysis of the CBI composites with respect to the plot burn severity was carried out using all burned field assessed plots (216). The scatterplots (Fig. 4) showed a

Table 4 Average error (RMSE) obtained by fitting site specific models to the remaining sites.

Reference model	Model	RMSE Aliaga	Jaulin	Los Olmos	Cedrillas	Zuera08
Aliaga	$a+b(x)+c(x)^2$	-	0.42	0.33	0.30	0.08
	$x(a\|x\|+b)^{-1}$	-	0.53	0.45	0.25	0.10
Jaulin	$a+b(x)+c(x)^2$	0.56	-	0.19	0.53	0.11
	$x(a\|x\|+b)^{-1}$	0.39	-	0.33	0.37	0.15
Los Olmos	$a+b(x)+c(x)^2$	0.67	0.38	-	0.57	0.22
	$x(a\|x\|+b)^{-1}$	0.45	0.50	-	0.47	0.25
Cedrillas	$a+b(x)+c(x)^2$	0.38	0.59	0.55	-	0.10
	$x(a\|x\|+b)^{-1}$	0.37	0.62	0.62	-	0.16
Zuera	$a+b(x)+c(x)^2$	0.33	0.46	0.39	0.23	-
	$x(a\|x\|+b)^{-1}$	0.32	0.53	0.48	0.23	-
PSS 150	$a+b(x)+c(x)^2$	0.35	0.41	0.33	0.31	0.05
	$x(a\|x\|+b)^{-1}$	0.30	0.52	0.45	0.25	0.07

Average error (RMSE) by burn severity classes after fitting the PSS 150 model to all CBI plots.

Severity	Model PSS 150 RMSE (258 plots) $a+b(x)+c(x)^2$	$x(a\|x\|+b)^{-1}$
unburned	0.33	0.35
low	0.66	0.60
moderate	0.63	0.60
mod.-high	0.74	0.76
high	0.20	0.26
all data	0.36	0.39

Table 5 Model forms and fit parameters for the studied spectroscopic indices.

Model	Parameter a	b	c	R^2	RMSE
CBI=a+b(NDVI)+c(NDVI)2	2.721	1.473	-5.113	0.591	0.55
CBI=a+b(dNDVI)+c(dNDVI)2	0.646	5.07-E03	-2.3-E06	0.529	0.61
CBI=a+b(NBR)+c(NBR)2	2.067	-2.620	-1.525	0.774	0.43
CBI=a+b(RdNBR)+c(RdNBR)2	0.668	2.82-E03	-8.6-E07	0.794	0.38
CBI=a+b(dNBR)+c(dNBR)2	0.566	5.14-E03	-2.8-E06	0.801	0.40

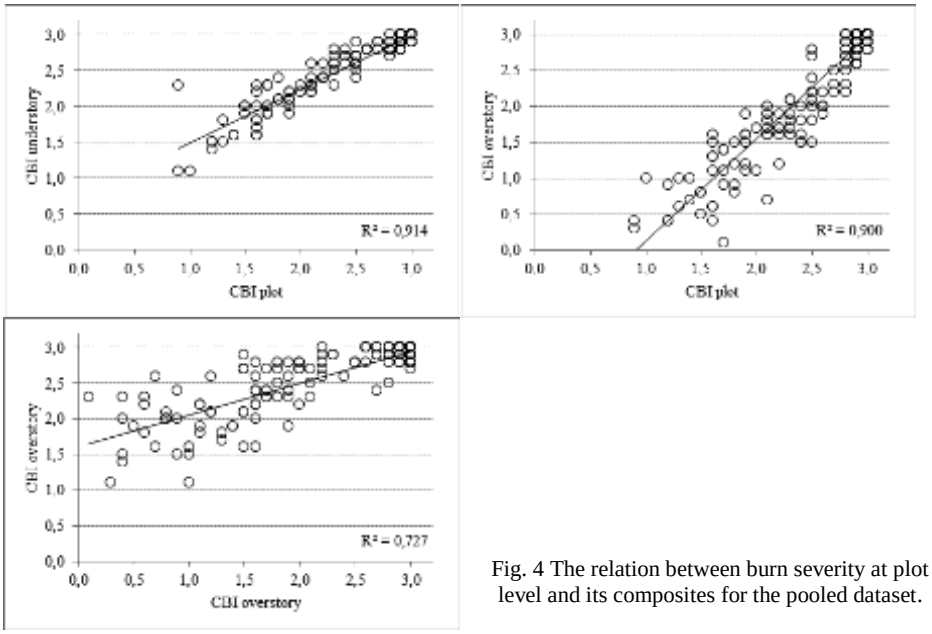

Fig. 4 The relation between burn severity at plot level and its composites for the pooled dataset.

very strong linear relationship between burn severity at plot level and the burn severity for understory and respectively overstory vegetation layers. Such strong relations could explain the high correlations found for the pooled data in the pine forests of Aragón. Discrepancy between overstory and understory burn severity could considerably reduce overall model fit since remotely sensed data mainly register information at canopy level in sites of low to moderate severity. Sites where only the substrate or the shrub layers are affected (surface fires) would appear as unburned in satellite images when canopy cover is dense. The relationship between burn severity at understory and overstory layers was weaker due to disagreements at low and moderately affected plots. These sites are usually characterized by moderate to high consumption of the substrate and the shrub layers and low effects at canopy level which results in very different ratings for the two CBI composites.

The results presented here suggest the usefulness of a single model for burn severity estimation in Aragón pine forests without the need for collecting exhaustive field data at each site. Although the models presented here seemed to cope with burned pine forests variability, users could use additional field data for further calibration/validation of the chosen model. Such data collection is fast and could be accomplished within one or two days by an experienced team. Research conducted across a range of ecoregions demonstrated the stability of the quadratic and saturated growth models over wide areas for coniferous boreal and mediterranean communities (Hall et al. 2008; Miller et al. 2009). This suggests a single model could be used for all coniferous forest in the Iberian Peninsula since their structure and fire regime do not differ significantly. However, since data from additional burns are not available the use of the presented models over other areas should be done with caution. Landsat TM scenes acquired during different forest phenological stages could diminish the accuracy

of burn severity predictions. Therefore we suggest the use of scenes from the same vegetation season as the one from this study.

One of the possible limitations of the regional models presented here is their calibration using only data from pine forests. However, at this date is not certain if a single model is sufficient for all types of burned forests. Other communities could present different trends (Allen and Sorbel 2008; White et al. 1996) thus needing particular models (Hall et al. 2008). A second constraint could be the use of initial assessment for evaluating burn severity. Species can have different adaptations to resist fire effects which could result in different degrees of initial burn severity depending on the community structure and composition (Key and Benson 2006). In addition, the amount of vegetation recovery is taken into account by CBI and could provide further insight on burn severity levels. Previous research showed that extended assessment could be more appropriate to evaluate burn severity in certain environments such as tundra. However, no significant difference was found when comparing initial and extended assessment within boreal black spruce forests (Allen and Sorbel 2008). The characteristic of the Mediterranean basin is the intense human intervention which makes extended assessment less appropriate since fire affected areas are usually subject to some type of intervention within the first year after burn. With increasing time larger parts of the affected forest is felled and removed by forest management agencies which considerably reduce the sampling opportunities. Monitoring activities at Zuera08 site did not reveal significant post-fire mortality rates; the only change being the increasing presence of recovering vegetation with time. The main limitation of the models was the significantly higher estimation errors found at low to moderate burn severities which reduces model effectiveness in fires scars presenting low burn severity on extensive areas.

CONCLUSIONS

This study presented an operational approach to map burn severity at local to regional levels. We demonstrated that results are not site specific and could be easily extrapolated over large areas at least for the same plant community. An inexpensive model for estimating burn severity was developed for the pine forests of Aragón. With proper calibration the model presented here could be extended to the national level. The error analysis showed that reliable estimates could be obtained for burn severity from remotely sensed data. However, for areas affected by lower fire intensities the estimation error increases and the model inversion is less accurate. Nevertheless, forest fire in Spanish pine forest usually results in large areas being affected by high burn severity. Therefore, the increased mapping errors associated with low and moderate severity levels would not significantly influence the overall accuracy.

ACKNOWLEDGMENTS

This work has been financed by the Spanish Ministry of Science and Education and the European Social Fund: FPI grant BES-2006-11684 and projects CGL2005-04863 and CGL2008-01083.

REFERENCES

Allen, J.L., and Sorbel, B. (2008). Assessing the differenced Normalized Burn Ratio's ability to map burn severity in the boreal forest and tundra ecosystems of Alaska's national parks. *International Journal of Wildland Fire, 17*, 463-475.

Andreae, M.O., and Merlet, P. (2001). Emission of trace gases and aerosols from biomass burning. *Global Biogeochemical Cycles, 15*, 955-966.

Cocke, A.E., Fule, P.Z., and Crouse, J.E. (2005). Influence of fire severity on plant regeneration by means of remote sensing imagery. *International Journal of Wildland Fire, 14*, 189-198.

Epting, J., Verbyla, D., and Sorbel, B. (2005). Evaluation of remotely sensed indices for assessing burn severity in interior Alaska using Landsat TM and ETM+. *Remote Sensing of Environment, 96*, 328-339.

French, N.H.F., Kasischke, E.S., Hall, R.J., Murphy, K.A., Verbyla, D.L., Hoy, E.E., and Allen, J.L. (2008). Using Landsat data to assess fire and burn severity in the North American boreal forest region: an overview and summary of results *International Journal of Wildland Fire, 17*, 443-462.

Hall, R.J., D, J.T.F., Groot, W.J.d., Pritchard, J.M., Lynham, T.J., and Landry, R. (2008). Remote sensing of burn severity: experience from western Canada boreal fires. *International Journal of Wildland Fire, 17*.

Hoy, E.E., French, N.H.F., Turetsky, M.R., Trigg, S.N., and Kasischke, E.S. (2008). Evaluating the potential of Landsat TM/ETM+ imagery for assessing fire severity in Alaskan black spruce forests. *International Journal of Wildland Fire, 17*, 500-514.

Hudak, A.T., Morgan, P., Bobbitt, M.J., Smith, A.M.S., Lewis, S.A., Lentile, L.B., Robichaud, P.R., Clark, J.T., and McKinley, R.A. (2007). The relationship of multispectral satellite imagery to immediate fire effects. *Fire Ecology Special Issue, 3*, 64-89.

Ice, G.G., Neary, D.G., and Adams, P.W. (2004). Effects of wildfire on soils and watershed processes. *Journal of Forestry, 102*, 16-20.

Kasischke, E.S., Turetsky, M.R., Ottmar, R.D., French, N.H.F., Hoy, E.E., and Kane, E.S. (2008). Evaluation of the composite burn index for assessing fire severity in Alaskan black spruce forests. *International Journal of Wildland Fire, 17*, 515-526.

Key, C.H., and Benson, N.C. (2006). Landscape assessment (LA). In D.C. Lutes, R.E. Keane, J.F. Caratti, C.H. Key, N.C. Benson, S. Sutherland and L.J. Gangi (Eds.), *FIREMON: Fire effects monitoring and inventory system* (pp. 1-55). Fort Collins, CO: U.S. Department of Agriculture, Forest Service, Rocky Mountain Research Station, Gen. Tech. Rep. RMRS-GTR-164-CD.

Landmann, T. (2003). Characterizing sub-pixel Landsat ETM+ fire severity on experimental fires in the Kruger National Park, South Africa. *South African Journal of Science, 99*, 357-359.

Lentile, L.B., Holden, Z.A., SmithA, A.M.S., Falkowski, M.J., Hudak, A.T., Morgan, P., Lewis, S.A., Gessler, P.E., and Bwnson, N.C. (2006). Remote sensing techniques to assess active fire characteristics and post-fire effects. *International Journal of Wildland Fire, 15*, 319-345.

Lopez-Garcia, M., and Caselles, V. (1991). Mapping burns and natural reforestation using Thematic Mapper data. *Geocarta International, 6*, 31-37.

Miller, J.D., Knapp, E.E., Key, C.H., Skinner, C.N., Isbell, C.J., Creasy, R.M., and Sherlocke, J.W. (2009). Calibration and validation of the relative differenced Normalized Burn Ratio (RdNBR) to three measures of fire severity in the Sierra Nevada and Klamath Mountains, California, USA. *Remote Sensing of Environment, 113*, 645-656.

Miller, J.D., and Thode, A.E. (2007). Quantifying burn severity in a heterogeneous landscape with a relative version of the delta Normalized Burn Ratio (dNBR). *Remote Sensing of Environment, 109*, 66-80.

Minshall, G., Brock, J., Andrews, D., and Robinson, C. (2001). Water quality, substratum and biotic responses of five central Idaho (USA) streams during the first year following the Mortar Creek fire. *International Journal of Wildland Fire, 10*, 185-199.

Murphy, K.A., Reynolds, J.H., and Koltun, J.M. (2008). Evaluating the ability of the differenced Normalized Burn Ratio (dNBR) to predict ecologically significant burn severity in Alaskan boreal forests. *International Journal of Wildland Fire, 17*, 490-499.

Roy, D.P., Boschetti, L., and Trigg, S.N. (2006). Remote Sensing of Fire Severity: Assessing the Performance of the Normalized Burn Ratio. *IEEE Transactions on Geoscience and Remote Sensing Letters*, 1-5.

Santis, A.de., and Chuvieco, E. (2007). Burn severity estimation from remotely sensed data: Performance of simulation versus empirical models. *Remote Sensing of Environment, 108*, 422-435.

Santis, A.de., and Chuvieco, E. (2009). GeoCBI: A modified version of the Composite Burn Index to estimate burn severity for remote sensing applications. In, *Remote Sensing of Environment* (pp. 554-562).

Santis, A.de., Chuvieco, E., and Vaughan, P.J. (2009). Short-term assessment of burn severity using the inversion of PROSPECT and GeoSail models. *Remote Sensing of Environment, 113*, 126-136.

Schmuck, G., San-Miguel-Ayanz, J., Camia, A., Kucera, J., Libertá, G., Boca, R., Durrant, T., and Amatulli, G. (2008). Forest Fires in Europe 2007. In, *JRC Scientific and Technical Reports*. Ispra, Italy: Joint Research Center.

Simmonds, P.G., Manning, A.J., Derwent, R.G., Ciais, P., Ramonet, M., Kazan, V., and Ryall, D. (2005). A burning question. Can recent growth rate anomalies in the greenhouse gases be attributed to large-scale biomass burning events? *Atmospheric Environment, 39*, 2513-2517.

Turner, M.G., Romme, W.H., Gardner, R.H., and Hargroved, W.W. (1997). Effects of Fire Size and Pattern on Early Succession in Yellowstone National Park. *Ecological Monographs, 67*, 411-433.

Verbyla, D.L., Kasischke, E.S., and Hoy, E.E. (2008). Seasonal and topographic effects on estimating fire severity from Landsat TM/ETM+ data*International Journal of Wildland Fire, 17*, 527-534.

Wagtendonk, J.W.van., Root, R.R., and Key, C.H. (2004). Comparison of AVIRIS and Landsat ETM+ detection capabilities for burn severity. *Remote Sensing of Environment, 92*, 397-408.

White, J.D., Ryan, K.C., Key, C.C., and Running, S.W. (1996). Remote Sensing of Forest Fire Severity and Vegetation Recovery. *International Journal of Wildland Fire, 6*, 125-136.

Wimberly, M.C., Cochrane, M.A., Baer, A.D., and Pabst, K. (2009). Assessing fuel treatment effectiveness using satellite imagery and spatial statistics. *Ecological Applications, 19*, 1377-1384.

Wimberly, M.C., and Reilly, M.J. (2007). Assessment of fire severity and species diversity in the southern Appalachians using Landsat TM and ETM+ imagery. *Remote Sensing of Environment, 108*, 189-197.

Wulder, M.A., White, J.C., Alvarez, F., Han, T., Rogan, J., and Hawkes, B. (2009). Characterizing boreal forest wildfire with multi-temporal Landsat and LIDAR data. *Remote Sensing of Environment, 113*, 1540-1555.

4.2. Sensibilidad del coeficiente de retro-dispersión a la severidad del incendio. Factores que influyen en la estimación

4.2.1. TerraSAR-X data for burn severity evaluation in Mediterranean forests on sloped terrain

Tanase, M.A., Pérez-Cabello, F., de la Riva, J. and, Santoro, M. (2010) TerraSAR-X data for burn severity evaluation in mediterranean forests on sloped terrain. ***IEEE Transactions on Geoscience and Remote Sensing, Vol. 48 No. 2, pp. 917-929, 2010.***

Resumen

Se utilizan imágenes de doble polarización, procedentes del radar de apertura sintética TerraSAR-X, para estimar la relación existente entre la severidad del incendio y el coeficiente de retro-dispersión. Se analiza la influencia del ángulo de incidencia local en el coeficiente de retro-dispersión. Para el diagnóstico de la severidad del incendio se emplea el Composite Burn Index (CBI) y el Normalized Burn Ratio (NBR). Con objeto de inferir el potencial del sensor TerraSAR-X para la estimación de la severidad se utilizan los coeficientes de determinación obtenidos mediante análisis de regresión lineal.

Para la polarización HH, el coeficiente de retro-dispersión aumenta al incrementarse la severidad en las pendientes orientadas hacia el sensor, mientras que para la polarización HV el coeficiente de retro-dispersión es mayor en laderas con orientación opuesta al sensor y áreas afectadas por baja severidad. La dependencia del coeficiente de retro-dispersión de la topografía se confirma en las áreas afectadas por incendios forestales. La retro-dispersión HH presenta una clara tendencia decreciente al aumentar el ángulo de incidencia local, mientras que para la polarización HV la tendencia es ascendente. Los coeficientes de determinación muestran que mediante la polarización HH se estima mejor la severidad en ángulos de incidencia bajos, mientras que para la polarización HV las mejores estimaciones se obtienen a altos ángulos de incidencia local.

Se pone de manifiesto el potencial de los datos polarizados de banda X para la estimación de la severidad del incendio en un entorno mediterráneo siempre que se tenga en cuenta la influencia del ángulo de incidencia local.

TerraSAR-X data for burn severity evaluation in Mediterranean forests on sloped terrain

M. A. Tanase[(1)], F. Pérez-Cabello[(1)], J. de la Riva[(1)], and M. Santoro[(2)]

[(1)]Department of Geography,
University of Zaragoza,
Pedro Cerbuna 12, 50009 Zaragoza, Spain
Email: mihai@tma.ro, delariva@unizar.es, fcabello@unizar.es

[(2)]Gamma Remote Sensing AG,
Worbstr. 225, CH-3073 Gümligen, Switzerland
Email: santoro@gamma-rs.ch

Abstract

TerraSAR-X dual-polarized SAR data from a test site in Spain has been investigated to determine the relationship between forest burn severity and SAR backscatter. The role of the local incidence angle on the backscatter coefficient has been also studied. Burn severity was estimated by means of Composition Burn Index (CBI) plots and the remotely sensed differenced Normalized Burn Ratio (dNBR) index. To infer the potential of TerraSAR-X data for burn severity assessment the determination coefficients obtained from linear regression analysis have been used. At HH polarization backscatter increased for slopes oriented towards sensor and areas affected by high burn severity while at HV polarization higher backscatter occurred for slopes oriented away from sensor in areas of low burn severity. The dependence of the backscatter coefficient on topography for areas affected by forest fire has been confirmed. HH backscatter presented a clear descending trend with the increase of local incidence angle while the HV backscatter presented an ascending trend. Determination coefficients showed that at HH polarization better estimates of burn severity are obtained at low local incidence angles while for HV polarization the best estimates are obtained at high local incidence angles. The dual polarized X-band SAR data showed potential for burn severity estimation in the Mediterranean environment if local incidence angle is accounted for.

Keywords*: burn severity, TerraSAR-X, Mediterranean forest, topography*

INTRODUCTION

Forest fire is a major ecological accident that has a profound influence on the natural cycle of vegetation succession and on ecosystem dynamics. The high number of forest fires occurring every year constitutes one of the major degradation factors of Mediterranean ecosystems (Koutsias and Karteris 2000). Effective fire suppression during the last 60–70 years has increased surface and crown fuel loadings in many forests and woodlands settings, such high accumulations fostering large, intense, and severe wildland fires (Ferry et al. 1995). Rural abandonment in the European Mediterranean Basin has implied an unusual accumulation of forest fuels, which coupled

with the increasing use of forests as a recreational resource has incurred a higher incidence of man-induced fires (Chuvieco 1999). Since 1960, the number of fires and surface burns in the European Mediterranean areas has increased constantly. During the 1990s the average number of fires per year increased by more than 70% while the average burnt area per annum decreased by approximately 30%. A total of 575,531 ha were burned in southern EU member states during 2007, which is above the average of the last 28 years (Schmuck et al. 2008) making fires an important environmental problem.

Remotely sensed data can contribute to a better, cost effective, objective and timesaving method to monitor (Laneve et al. 2006) and quantify location (Stroppiana et al. 2003), extent and intensity of fire events (Chuvieco 1999). Burn severity is an important indicator of fire impacts on ecosystem being defined as the magnitude of change between pre-fire and post-fire status of the site. Usually detecting burn severity from space is accomplished using vegetation indices derived from optical sensors. Empirical modeling was used to correlate ground measured burn severity to remotely sensed indices derived from a single post-burn image or from using a bi-temporal approach (pre- and post-burn images) (Díaz-Delgado et al. 2003; Epting et al. 2005; Roy et al. 2006; Wagtendonk et al. 2004). Nowadays, the Normalized Burn Ratio (NBR) (Key and Benson 2006) is one of the most widely used remotely sensed spectral indexes for burn severity assessment. It combines information from near-infrared and mid-infrared wavelengths to compute values in a similar way as the normalized differenced vegetation index (NDVI). The difference between NBRs computed for pre-fire and post-fire images (dNBR) is commonly used for burn severity mapping. dNBR provides a scale of changes with respect to the pre-fire status, unburned area retaining values close to zero (i.e. little or no change). In the recent years NBR and dNBR were intensively used to estimate burn severity across a wide variety of sites from boreal to mediterranean forests (Allen and Sorbel 2008; Cocke et al. 2005; Santis and Chuvieco 2007; Wagtendonk et al. 2004; Wimberly and Reilly 2007).

Burn severity estimation by means of dNBR uses as reference data a field indicator called Composition Burn Index (CBI) proposed by (Key and Benson 2004) or its version adapted to local conditions (Epting et al. 2005) and (Santis and Chuvieco 2009). CBI was designed to evaluate the magnitude of fire effects across all strata from an ecological perspective by evaluating ground fire effects. Average conditions of the vegetation are visually examined within a radius of 15 m and the degree of change with respect to the pre-fire status is recorded in values from 0 (no change) to 3 (100% change). Generally, dNBR coupled with CBI provided accurate detection of burn severity in most of the environments, determination coefficients reported being usually high (R^2>0.75) (Allen and Sorbel 2008; Cocke et al. 2005; Epting et al. 2005; Wagtendonk et al. 2004). However, some authors (Allen and Sorbel 2008; Hoy et al. 2008; Murphy et al. 2008) reported weaker relationships between dNBR and CBI in boreal forests. This was attributed partly to dNBR`s inability to discern between moderate and high severity burn sites and partly to the variation in topography, solar elevation angle (Verbyla et al. 2008) or specific fuel conditions. For mediterranean climate high determination coefficients between dNBR and CBI have been reported (Miller et al. 2009; Santis and Chuvieco 2009).

Despite the extensive archives of space borne SAR data few studies were carried out having as topic forest fires. Most of them were focused on burnt area mapping in boreal or tropical forests (Bourgeau-Chavez et al. 1997; Bourgeau-Chavez et al. 2002; French et al. 1999; Huang and Siegert 2004; Liew et al. 1999; Menges et al. 2004;

Siegert and Hoffmann 2000; Siegert and Nakayama 2000; Siegert and Ruecker 2000). Increased backscatter from burned areas was attributed to decreased attenuation, strong trunk-ground interactions and changes in soil moisture (Bourgeau-Chavez et al. 1994; Kasischke et al. 1994). For the Mediterranean basin (Gimeno and San-Miguel-Ayanz 2004; Gimeno et al. 2004) showed that multi-temporal SAR data could be used for burnt area mapping and suggested that accurate results could be achieved if slope is taken into account. Previous studies (Bourgeau-Chavez et al. 1994; Bourgeau-Chavez et al. 2007) showed a strong dependence of fire scar discrimination power on the changes in dielectric properties of the scattering surfaces due to changes in moisture conditions of the burned area. Precipitations during fire season are rare in Mediterranean basin and therefore dry conditions could limit the applicability of SAR data for burn scar identification. However, the lack of rain eliminates one of the most important sources of radar backscatter variability: moisture. The lack of moisture could be important when trying to differentiate among fire severity levels since backscatter variability due to moisture variation could mask the variability due to burn severity.

Backscatter from forests includes components from crown, direct backscatter form trunk, direct backscatter from ground, crown-ground backscatter and trunk-ground backscatter (double bounce). At X-band ($\lambda \approx 3$ cm; $f \approx 9$GHz) microwaves mostly interact with leaves, twigs, and small branches scattering from tree crowns being the predominant backscattering component. The contribution of the understory and forest floor is primarily conditioned by canopy architecture (e.g. crown closure, shape etc.) and look angle, attenuation of 20 dB (two-ways) being found for coniferous trees (Hoekman 1987). It was shown (Leckie 1999) that removal of leaves reduces the backscatter and the elements of a size similar with the wavelength (e.g. petioles) can constitute important sources for microwave scattering. In general horizontally polarized beams are scattered more by cylindrical elements with near horizontal orientation while vertically polarized beams are scattered more by vertically oriented elements. Sensitivity to forest parameters (e.g. stem biomass, tree height etc.) is relatively low at X-band, reaching 2 to 3 dB for volumes up to 400 m^3/ha (Martinez et al. 2000; Pulliainen et al. 1994). Higher linear correlation (r) between radar backscatter and stem volume was found at HV polarization (r=0.60) than at HH or VV polarizations (r=0.31 and 0.38 respectively) (Pulliainen et al. 1994). Penetration depths of up to 7.5 meters were documented for pine forests at X-band, the highest values being registered for mature forests (i.e. decrease stand density) (Martinez et al. 2000), ground exposure or penetration through crown gaps being of major influence for backscattering mechanism.

Crown fire in coniferous forests often results in complete needle removal small branches and twigs becoming the most important backscatter source. Due to the lack of needles at high burn severities an increase in backscatter ground component is expected while the backscatter from the crown should decrease (Kasischke et al. 1992). Therefore, at HH polarization higher backscatter coefficients are expected for increased severity levels while at HV polarization backscatter levels should diminish in highly burned areas. Nevertheless, the amount of each component should be strongly affected by the local incidence angle (i.e. the angle of incident illumination with respect to the local slope). Substantial changes in signal response are expected for local incidence angle variations especially for steep satellite viewing geometries. The image brightness per pixel is sensitive to topography (Raney 1999) and therefore local incidence angle could be extremely relevant in rough environments such as the Mediterranean basin. The path traveled through forest layers increases with local incidence angle higher return being expected at high incidence angles especially for cross-polarized beams. Conversely the

direct scatter from the ground decreases leading to an increase of the forest/non-forest contrast. Backscatter dependence on incidence angle has been studied by (Luckman 1998) for forest and pastures, different trends being registered between cross-polarized and co-polarized beams. At C-band volume scattering appears to dominate but this dominance is reduced at low incidence angles as surface scattering begins to take over. Wavelength dependent crossover points where volume scattering becomes more important than surface scattering were found for both forest and pastures.

Few studies have dealt with burn severity assessment (Bourgeau-Chavez et al. 1994; Czuchlewski and Weissel 2005; Siegert and Hoffmann 2000; Siegert and Nakayama 2000) using SAR data, most of them having as main objective other fire related ecosystem properties. None of the authors used as reference data CBI which nowadays is widely accepted for field burn damage estimation and more important no research was undertaken in the Mediterranean basin which present specific challenges to remote sensing systems: steep topography, high landscape fragmentation and intensive human intervention. In this study we assumed that fire impacts on forests could be assessed using X-band SAR data and we further investigated on the hypothesis of local incidence angle influence on the relation between burn severity and backscatter. Although X-band backscatter presents in general weak forest/non-forest contrast the metric scale of data acquired by TerraSAR-X sensor in stripmap mode can be of advantage in highly fragmented landscape such as the Mediterranean environment where large, uninterrupted tracts of forest are rare. The overall goal was to evaluate to what extent the X-band backscatter could be used for burn severity assessment taking into consideration the relative rough topography of a typical Mediterranean landscape. The high homogeneity of the forest structure, the lack of different tree species and the large area extent presenting high burn severity made the study area ideal for isolating/studying external factors such as local incidence angle and evaluate its influence on backscatter response. The objectives of the study were to:

1. determine the relations between burn severity and X-band SAR backscatter (HH and HV polarizations);
2. infer the prediction power of HH, HV, HH/HV ratio and HH and HV channels for burn severity estimation; and
3. asses the role of local incidence angle on the SAR backscatter for a variety of burn severity conditions.

STUDY AREA AND IN SITU DATA

Zuera study area is located in central Ebro Valley, Spain (Fig.1), the northernmost semi-arid region in Europe. Surrounded by mountain chains, the Ebro Valley has a Mediterranean climate with continental characteristics and marked seasonal variations in precipitation, the dry season occurring during summer. The annual average precipitation in the study area is higher than the average of the Ebro valley reaching 450-550 mm. The study area covers a hilly relief, elevations ranging from 500 m to 750 m above sea level. The dominant land cover includes forests and winter cereal crops. Most of the area is covered by homogeneous, even aged pine forests of *Pinus halepensis L.* as a result of past reforestation activities. The lithology of the area is characterized by limestone and marl sediments arranged on horizontal layers that contribute to its aridity, since soils are unable to retain water as a consequence of the high hydraulic conductivity. On August 6th, 2008 a fire was ignited by a traffic accident and spread rapidly through the dense

Fig. 1 General location of Zuera study area.

pine forests. By the second day 2200 ha of vegetation had already been affected. In total around 2500 ha burned by August 16th, when the fire was declared extinguished.

During August and September 2008 123 CBI plots were established in high severity, moderate severity, low severity and unburned areas at locations with homogeneous forest structure and constant slope. The vegetation layers present in Zuera area consisted of substrate, herbs and low shrubs less than 1 m tall, shrubs and trees up to 5 m tall and intermediate trees up to 20 m tall. In each plot digital photos (N, S, W and E directions and close-ups of crown, soil and shrub layer burns) were taken and the center was measured with Global Positioning System (GPS). The positioning error after differential correction was for most of the plots less than 2 meters.

At each plot burn severity was evaluated on a 15 m radius. The main variables assessed were litter and fuel consumption, foliage alteration, change in cover, canopy and tree mortality, and char height. High severity areas presented complete combustion of the litter, the understory layer and the crowns of intermediate sized trees. Moderate severity areas retained some of the understory layer while the tall shrubs and crowns of intermediate sized trees were usually scorched. Low severity areas were lightly burned, intermediate sized trees being scorched at the base, the litter being partially consumed and the understory layer being affected in a patchy pattern (Fig. 2). Finally, unburned areas presented litter accumulation, a dense understory layer and low live branches for the tree layer. Burn severity was evaluated as described by (Key and Benson 2004) using the magnitude of environmental change at each site with respect to the presumed pre-fire state. CBI provided continuous numeric values for the understory, overstory and the entire plot.

The high fire intensity and its relatively small area resulted in an unequal distribution by range of severity. Most of the affected forests were in high or moderate-high burn severity classes (68%) while only 12% belonged to the low burn severity class. As a result, CBI sampled plots were not proportionally distributed over the entire severity range. Of the 123 plots sixteen were unburned, twelve presented low burn severities, and nineteen presented moderate severities. The remaining seventy six plots presented high severities.

Fig. 2 Examples of unburned (top left – Plot 8, CBI 0, dNBR 35.5), low severity (top right – Plot 28, CBI 1, dNBR 256.5), moderate severity (bottom left – Plot 11, CBI 1.7, dNBR 302.7) and high severity (bottom right – Plot 17, CBI 2.9, dNBR 870.1) plots.

SATELLITE DATA

The satellite dataset consisted of a TerraSAR-X (TSX) image and a pair of Landsat 5 Thematic Mapper (TM) images. Dual polarization TSX data were acquired after the fire on November 16, 2008 in Stripmap (SM) mode. This acquisition mode is characterized by a swath width of ~15 km, an azimuth resolution of 6.6 m and a ground range resolution of around 2 m at 40° incidence angle. The incidence angle ranges from 20° to 45° (Fritz and Einder 2008). The Landsat dataset was formed by two scenes (pre-fire-July 21st, 2008 and post-fire-August 22nd, 2008) from path 199 row 031 (orbit numbers 129722 and 130188). Atmospheric conditions were stable during the acquisition of all datasets, no precipitations being registered neither during acquisition nor throughout the previous week (SAR data). In Fig. 3 the fire scar as imaged by Landsat TM and TerraSAR-X sensors can be easily distinguished from the surrounding unburned forest displayed as different shades of green.

SAR data

The TerraSAR-X dataset was acquired at 40° incidence angle and provided in Single Look Slant format (SSC). SSC data have a pixel spacing of 0.91 m in slant range and 2.43 m in azimuth (Table 1). However, considering the decametric scale (30 m diameter) reference plots and the Landsat dataset with similar pixel spacing, the high resolution of the TerraSAR-X data was not considered to be fundamental for the scope of this work. Of major importance was to have SAR backscatter measurements as least affected by speckle as possible. For this reason the images were multi-looked in order to

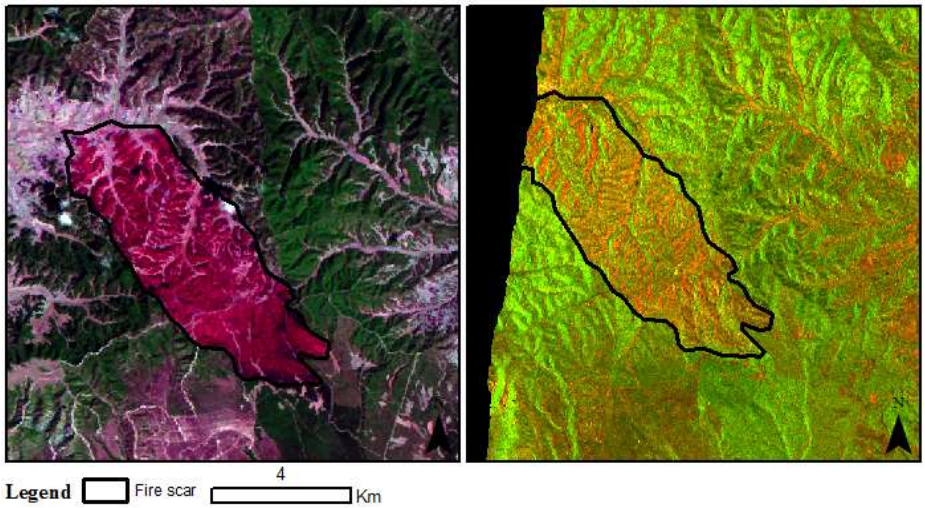

Fig. 3 The fire scar as revealed by Landsat TM (RGB: 7 4 3) and TerraSAR-X images (RGB: HH, HV, HH/HV).

Table 1 SAR Data characteristics and processing parameters – summary.

Parameter	Value
SSC pixel spacing	Slant range 0.91 m / Azimuth 2.43 m
Multi-look factors	Range 17 / Azimuth 10
MLI pixel spacing	Slant range 15.5 m / Azimuth 24.3 m
Calibration gain	49.9 dB HH / 56.9 dB HV
Pixel spacing	25 m (geocoded image)
Projection / Ellipsoid	UTM / International 1924
Datum	European 1950
Geolocation error	~ 0.75 m

obtain a ground pixel spacing around 25 m in both directions, i.e. close to the size of the reference plots. The Equivalent number of Looks (ENL) obtained after multi looking was around 55 for both polarizations. Prior to geocoding, images were absolutely calibrated using the calibration factor provided with the SSC data. The SAR intensity images were then geocoded to UTM projection using a Digital Elevation Model (DEM) with 20 m pixel spacing which was resampled to 25 m for the analysis. Geocoding of the SAR data was based on a lookup table describing the transformation between the radar and the map geometry (Wegmüller et al. 1999; Wegmüller et al. 2002). The lookup table is generated on the basis of orbital information and elevation in the DEM. To correct for possible inaccuracies in the input data a refinement of the lookup table can be applied. This is implemented in the form of offsets estimation between the SAR image and a reference image (e.g. a simulated SAR image from the DEM) transformed to the radar geometry. Offsets are estimated using a cross-correlation algorithm. Offsets are distributed homogeneously on the image data, the number being strictly dependent on the correlating features between the SAR image and the reference image. Quality of the refinement is given by the root mean square error (RMSE) of the offsets. In this case the offset was about 30 m in range and azimuth and the RMSE was approximately 0.75 m. Based on the estimated offsets a simple linear model for refining the lookup table is then

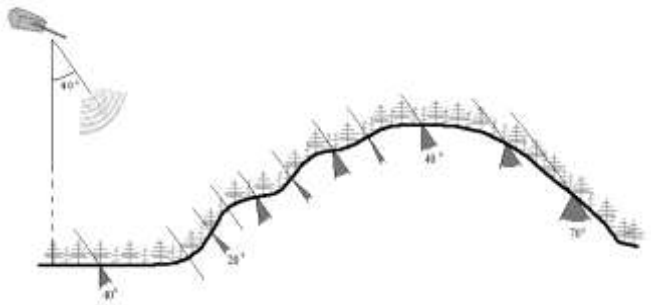

Fig.4 Local incidence angles – profile from Zuera study area.

derived and applied. Finally the SAR image is transformed to the map geometry using the refined lookup table.

The geocoded backscatter images still present radiometric distortions due to topographic effects and varying incidence angles from near to far range. Uncompensated topographic effects could induce backscatter dispersion and thus results misinterpretation as shown in (Castel et al. 2001). For this reason topographic normalization for the varying incidence angle and the effective pixel area was applied (Ulander 1996). This information was derived from the DEM. The result is an image in gamma nought ($\gamma°$) format that only includes variations of the scattering properties of a target due to different local topography. Fig. 4 presents a typical topographic transect and the local incidence angles (i.e. 20° to 70°) resulting from TSX viewing geometry in Zuera.

Optical data

Subsets of the two Landsat scenes were geometrically rectified to the UTM projection zone 30 North (International 1909 Ellipsoid, European 1950 Datum) using a linear polynomial model and incorporating information of the local topography from the same DEM used to geocode the TSX data. Around 50 ground control points (GCPs) were used to register each subset to high resolution orthophotos. For both images, a root mean square error of less than one pixel (0.65 and 0.6 respectively) was achieved. The nearest neighbor resampling method was utilized in order to preserve original radiometry and the pixels were re-projected from the original 30 m to 25 m. dNBR was computed from pre- and post-fire Landsat images after atmospheric corrections had been applied using a radiative transfer equation model. Raw digital number (DN) values were converted to satellite reflectance using gain and bias, the daily sun angle, sun azimuth and exo-atmospheric irradiance. There was no need for between scene normalization because the coefficient of determination among stable targets was greater than 0.98 (Key and Benson 2006).

METHODS

The goal of the study was to infer relations between burn severity and X-band SAR backscatter at HH and HV polarization in a topographically varied landscape. For this scope linear regression analysis was used. The investigation was carried out using a set of field estimated plots as well as a set of "surrogate" plots, further on referred as "pseudo-plots". The generation of pseudo-plots was considered since multiple regression

analysis requires large number of samples which cannot be easily achieved by field work. Other factors that supported the choice of using pseudo-plots were the small area presenting low and moderate burn severity and the small number of plots for a given severity level and incidence angle. In the following detailed information about the plots and the pseudo-plots datasets is provided. Determination coefficients (R^2) were used to relate SAR data to field estimates (i.e. plots) or optical sensor based estimates (i.e. pseudo-plots) of burn severity. Multiple linear regression analysis was carried out after grouping the pseudo-plots in 3°, 5° and 10° intervals of local incidence angle to evaluate the strength of association between burn severity and radar backscattering coefficient.

CBI plots

For further speckle reduction backscatter values were averaged for all forest pixels located within 55 m from the center of each plot. The limit was not set higher due to the low radius (15 m) used for field burn severity assessment, high fragmentation of the landscape and the need of preserving certain homogeneity for forest structure, local slope conditions and burn severity. The limit was set in order to accumulate around 15 pixels for each plot. Only plots containing at least five forest pixels were kept for further analysis. This condition was satisfied for 115 plots. Forward stepwise linear regression was used for modeling the correlation between burn severity and HH, HV HH/HV ratio and HH&HV backscatter. General linear regression assumptions were evaluated to check for model validity.

Pseudo-plots

Pseudo-plots were generated by averaging pixels of similar dNBR for the same local incidence angle rounded to unity. The local incidence angle was computed as a function of SAR image acquisition geometry, local slope and orientation (Wegmüller et al. 1999). Similar dNBR values were obtained by reclassifying the continuous dNBR interval (-150 to 1050) into twenty-four dNBR classes each being 50 units wide. Only forest pixels presenting high NDVI values (i.e. higher biomass) were selected for the generation of the pseudo-plots. Around 25,000 pixels were selected from burned and unburned areas out of which 840 pseudo-plots were generated and used for the regression analysis. Pseudo-plots which contained less than five pixels were discarded.

The consistency between CBI and dNBR estimates of fire severity was evaluated using regression analysis. Sub-sampling of the CBI plots was necessary to achieve a similar number of plots for each of the general ranges of severity (unburned, low, moderate and high) as suggested by (Key and Benson 2006). All unburned, low and moderate severity CBI plots were included in the analysis. Twenty-two high severity CBI plots were randomly selected to reach a total of 65 plots. Table 2 shows the determination coefficients between CBI of the total plot, understory and overstory and

Table 2 Determination coefficient (R^2) between CBI and spectral indices derived from TM image/s.

Variables	R^2 coefficient		
	CBI plot	CBI overstory	CBI understory
TM4 (0.76-0.90 µm)	0.73	0.72	0.66
TM7 (2.08-2.35 µm)	0.66	0.74	0.54
NBR	0.82	0.88	0.70
dNBR	0.81	0.87	0.70

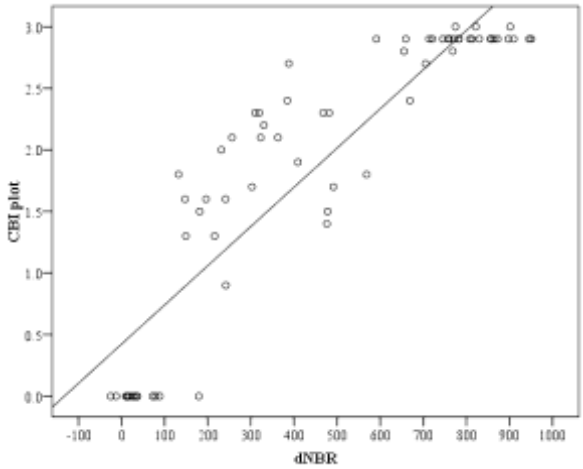

Fig. 5 dNBR vs. CBI measurements at plot level.

some reflective bands of the post-fire TM image and the derived spectral indices. Scatterplot of dNBR v. CBI (Fig.5) illustrates the high determination coefficient (R^2 = 0.81, $p<0.05$) obtained. This result supports the assumption that dNBR can be considered for further use as a radiometric index strongly related to the severity levels recorded in the field. Generally higher correlations were found for the overstory layer than for the total plot or understory estimations. This is not unexpected considering that optical data mainly register the reflectivity from the upper part of canopy.

RESULTS

Backscatter properties: plots

The trend of HH and HV backscatter coefficients in terms of burn severity, estimated through CBI plots, and local incidence angle is shown in Fig. 6. Both scatter plots show a certain dependence upon CBI. Nonetheless there are clear differences depending on the local incidence angle. This is exemplified in Fig. 7 where mean values and standard deviations of SAR backscatter are reported as a function of local incidence angle for the plots affected by high burn severity (i.e. CBI $\geq$ 2.5) (CI 95%). At both polarizations the backscatter showed clear dependence upon local incidence angle. Since few samples (74) were used to compute the statistics (limited number of CBI plots, Table 3), for some incidence angle groups large vertical bars (i.e. deviation from mean) were observed. A similar illustration for low CBI plots is not significant because of the very small number of plots (see also Fig. 6).

To infer the utility of SAR data for burn severity estimation, liner regression determination coefficients (R^2) expressing the proportion of burn severity variance predicted by radar backscatter are presented in Table 3 for HH, HV polarizations, HH & HV and the ratio HH/HV. The table also includes the beta standardized regression coefficients (Beta°) which can be used to compare the relative strength of the various predictors included in the model as well as the sign of the relation between burn severity and the backscatter coefficient. The beta coefficients for each of the variables indicates

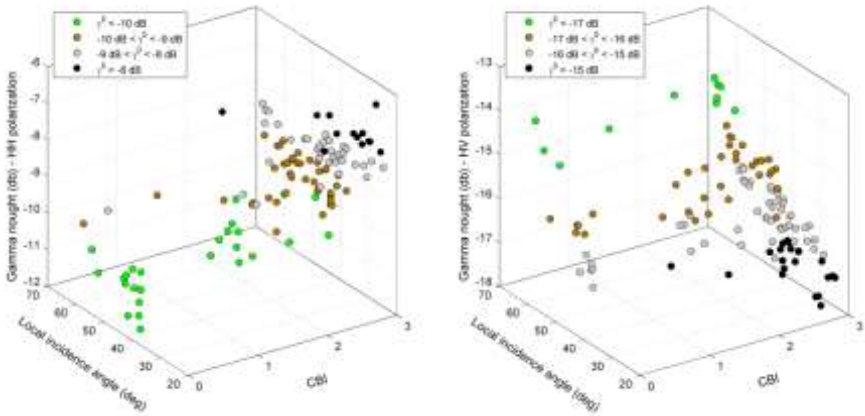

Fig. 6 Gamma nought (γ°) vs. overstory burn severity (CBI field etimates) and local incidence angle (left HH and right HV polarization).

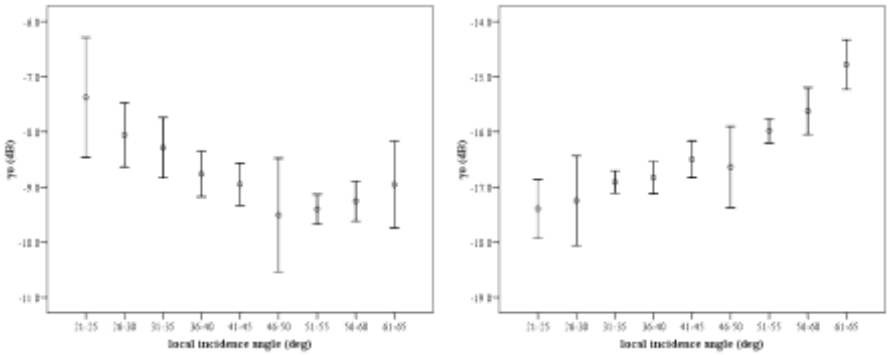

Fig. 7 Gamma nought (γ°) vs. local incidence angle for high burn severity (i.e. CBI > 2.5) plots (left HH and right HV polarization).

Table 3 Determination coefficients explaining the agreement between CBI and TerraSAR-X backscatter.

	HH		HV		HH/HV		HH&HV				
Level	R^2	Std. err. estim.	R^2	Std. err. estim.	R^2	Std. err. estim.	R^2	Std. err. estim.	HH Beta°	HV Beta°	Plots
CBI overstory	0.314	0.925	0.120	1.048	0.480	0.805	0.399	0.870	0.531	-0.292	115
CBI understory	0.277	0.834	0.108	0.927	0.433	0.739	0.353	0.793	0.498	-0.278	115
CBI plot	0.299	0.848	0.125	0.948	0.470	0.737	0.389	0.796	0.516	-0.301	115
Determination coefficients at plot level – groups of local incidence angle											
21-25	0.002	0.061	0.980	0.009	0.148	0.057	0.999	0.003	0.139	1.002	4
26-30	0.390	0.265	0.310	0.282	0.796	0.154	0.849	0.148	0.745	-0.688	7
31-35	0.186	0.606	0.528	0.462	0.731	0.349	0.829	0.295	0.555	-0.811	11
36-40	0.663	0.823	0.420	1.080	0.755	0.702	0.786	0.677	0.660	-0.382	19
41-45	0.373	0.782	0.134	0.919	0.571	0.647	0.628	0.611	0.719	-0.517	35
46-50	0.017	0.969	0.631	0.594	0.676	0.556	0.794	0.474	0.495	-1.080	10
51-55	0.357	0.909	0.511	0.793	0.742	0.576	0.777	0.557	0.520	-0.653	15
56-60	0.008	1.109	0.745	0.562	0.753	0.553	0.886	0.411	0.395	-0.985	8
61-65*	-	-	-	-	-	-	-	-	-	-	5
66-70**	-	-	-	-	-	-	-	-	-	-	1

* all plots of same burn severity / ** insufficient samples for regression analysis

the amount of change one could expect in dNBR given a one-standard deviation change in the value of the backscatter (HH or HV polarization), when all other variables in the model are held constant. Finally, the standard deviation of the error term was also included in the table.

Backscatter properties: pseudo-plots

Similarly to the analysis carried out for the CBI plots Fig. 8 illustrates backscatter dependence on burn severity and local incidence angle for the pseudo-plots. Compared to the CBI analysis the trend between backscatter and burn severity and its dependency upon local incidence angle becomes more evident. For a better understanding of burn severity and local incidence angle influences on the backscatter, the effect of each factor at a time was studied. Fig. 9 presents the backscatter in terms of dNBR for different intervals of local incidence angle. To provide a measure of reference in an 'ideal' case of completely burnt forest, the average backscatter of bare soils outside the fire perimeter was computed. This is represented by the horizontal line. Bare soils were located mostly on rather flat terrain so that the average backscatter could be determined only for intervals of local incidence angles close to 40 degrees. In Fig. 10 mean values and standard deviations of SAR backscatter are reported with respect to local incidence angle for the pseudo-plots with high burn severity levels (i.e. dNBR $\geq$ 600). Keeping burn severity constant (i.e. less variability due to severity levels) helped understanding the influence of the local incidence angle on the backscatter coefficient.

Table 4 presents the determination coefficients and the standard error of estimate after grouping the pseudo-plots for different incidence angle intervals (3°, 5° and 10°). Evaluation of the best grouping intervals for modeling burn severity is possible by comparing not only the R^2 but also the standard deviation of the error term. Only intervals containing at least thirty pseudo-plots are shown.

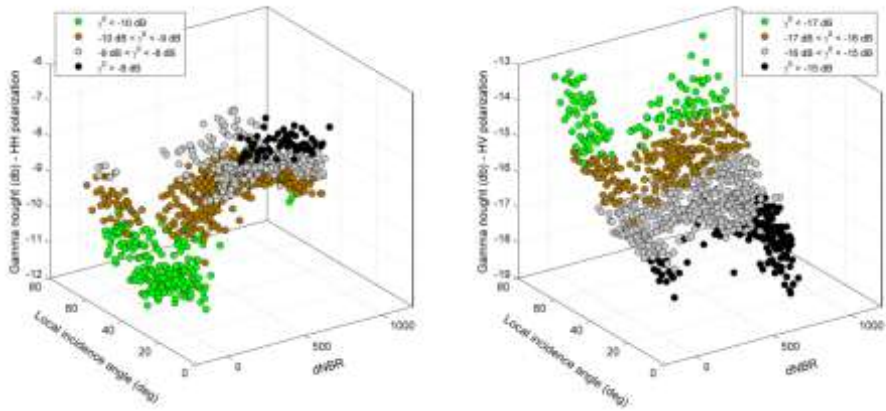

Fig. 8 Gamma nought (γ^o) vs. burn severity (dNBR) and local incidence angle (left HH and right HV polarization).

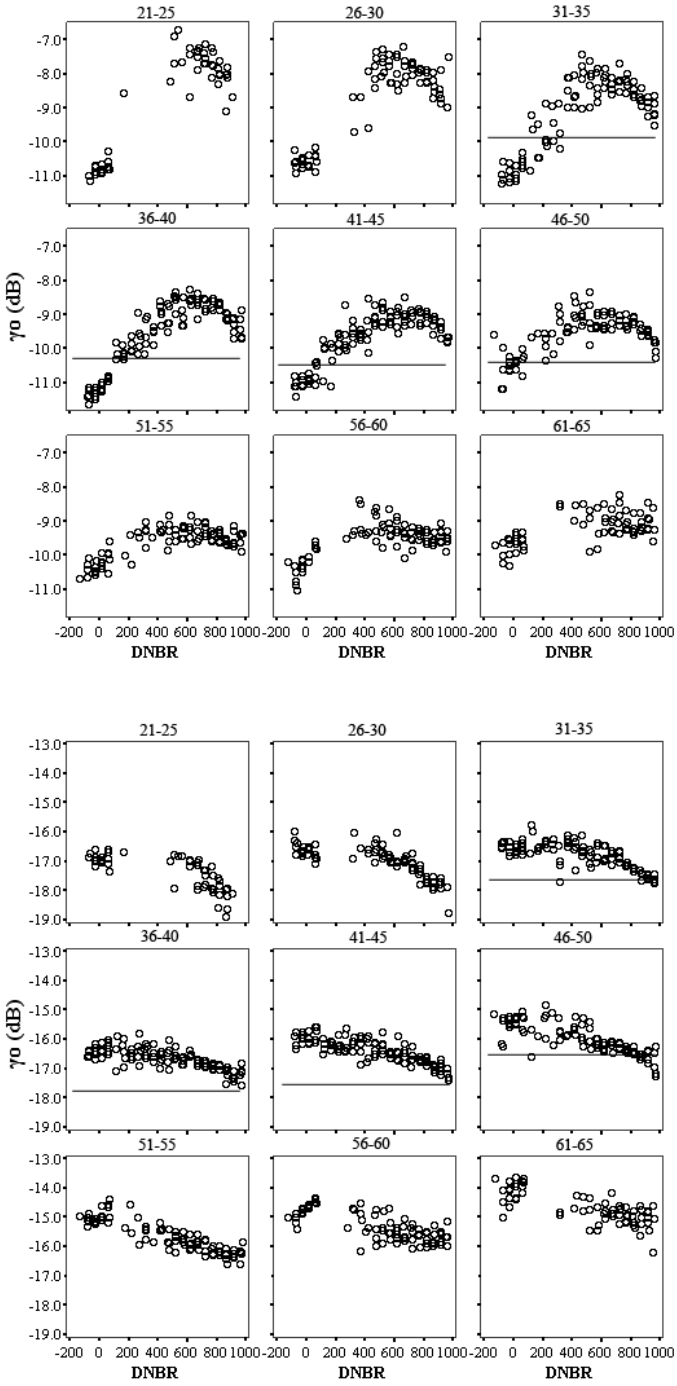

Fig. 9 Gamma nought (γ^{o}) vs. burn severity (dNBR) for a given interval of local incidence angle. For each case the range of angles is 5° (top HH and bottom HV polarization).

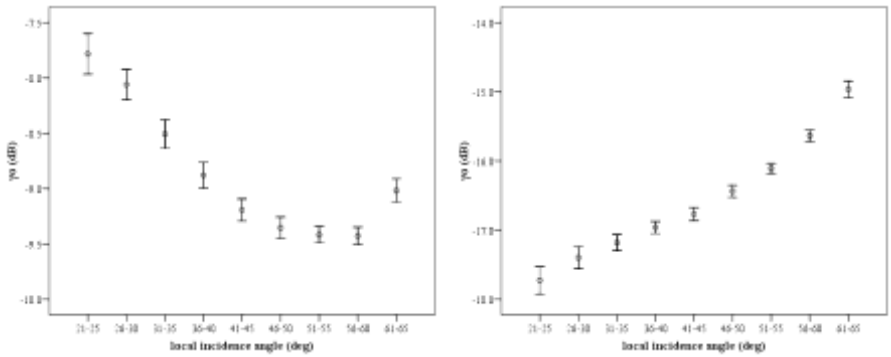

Fig. 10 Gamma nought (γ°) vs. local incidence angle for high burn severity (i.e. dNBR > 600) pseudo-plots (left HH and right HV polarization).

Table 4 Determination coefficients: burn severity (dNBR) as a function of HH and HV polarization.

Interval (deg)	HH		HV		HH/HV		HH&HV				
	R^2	Std. err. estim.	R^2	Std. err. estim.	R^2	Std. err. estim.	R^2	Std. err. estim.	HH Beta°	HV Beta°	Pseudo -plots
23-25	0.695	194.1	0.543	237.7	0.882	120.7	0.918	102.0	0.655	-0.505	36
26-28	0.690	195.2	0.621	216.0	0.874	124.3	0.919	100.9	0.604	-0.529	43
29-31	0.499	232.2	0.494	233.3	0.815	141.3	0.859	124.3	0.611	-0.607	55
32-34	0.541	219.8	0.489	231.8	0.811	141.2	0.839	131.2	0.607	-0.561	62
35-37	0.653	192.2	0.587	209.6	0.856	124.0	0.890	109.2	0.599	-0.530	62
38-40	0.596	204.8	0.516	224.0	0.801	143.8	0.812	141.0	0.585	-0.501	63
41-43	0.603	205.8	0.666	188.7	0.848	127.5	0.865	120.8	0.505	-0.580	67
44-46	0.473	233.5	0.630	195.7	0.829	133.0	0.822	136.7	0.468	-0.631	63
47-49	0.257	287.2	0.664	193.2	0.760	163.3	0.805	148.6	0.381	-0.751	56
50-52	0.446	255.1	0.860	128.1	0.821	144.9	0.877	121.2	0.163	-0.828	59
53-55	0.279	286.9	0.756	167.0	0.787	155.9	0.812	148.1	0.253	-0.780	52
56-58	0.282	293.6	0.629	210.9	0.689	193.1	0.725	183.4	0.324	-0.697	52
59-61	0.232	300.2	0.537	233.2	0.758	168.5	0.813	149.6	0.527	-0.764	49
62-64	0.322	298.6	0.721	191.4	0.708	196.0	0.759	180.5	0.218	-0.747	41
21-25	0.713	191.3	0.538	242.6	0.906	109.3	0.924	99.6	0.666	-0.493	52
26-30	0.623	207.5	0.540	229.3	0.847	132.3	0.882	117.1	0.617	-0.537	77
31-35	0.517	224.7	0.514	225.4	0.796	145.9	0.847	127.3	0.591	-0.588	102
36-40	0.616	199.0	0.499	227.5	0.799	144.0	0.808	141.5	0.603	-0.474	106
41-45	0.540	218.8	0.645	192.3	0.830	133.0	0.848	126.4	0.492	-0.606	109
46-50	0.297	277.1	0.630	201.0	0.751	164.8	0.773	158.2	0.388	-0.708	98
51-55	0.411	259.6	0.764	164.4	0.803	150.2	0.823	143.3	0.279	-0.737	90
56-60	0.276	292.2	0.539	233.1	0.687	192.1	0.722	182.2	0.432	-0.674	84
61-65	0.301	299.1	0.560	237.3	0.732	185.2	0.745	182.0	0.436	-0.676	68
21-30	0.657	201.0	0.471	249.5	0.834	139.8	0.856	130.9	0.656	-0.472	129
31-40	0.531	219.7	0.492	228.5	0.743	162.7	0.780	150.7	0.565	-0.525	208
41-50	0.422	247.0	0.509	227.6	0.748	162.9	0.745	164.6	0.501	-0.587	207
51-60	0.335	276.3	0.568	222.7	0.702	184.8	0.722	179.2	0.407	-0.645	174
61-70	0.252	325.2	0.391	293.3	0.711	202.1	0.722	199.5	0.578	-0.689	98

DISCUSSION

Backscatter properties: plots

Backscatter dependence on burn severity levels is primarily the result of the scattering mechanism occurring in the trees remained after the fire event, the proportion of the exposed ground and the tree moisture. In areas heavily affected by fire, where the

canopy covers only minor fractions of the forest floor due to removal of needles and/or leaves, the ground contribution to the backscatter is important especially for HH polarized beams. In areas less affected by fire the canopy covers much larger parts of the ground, the volume scattering within the vegetation layer decreasing the importance of the ground contribution. Fig. 6 shows that at HH polarization the backscatter coefficient increases both with incidence angle and burn severity spanning 5 dB from -11 dB (unburned forest) to a maximum of -6 dB (high burn severity). For HV polarization the backscatter coefficient varied by 4 dB, lower variability being observed within plots of similar CBI value (i.e. similar burn severity). The relatively high backscatter variability (both polarizations) for similar severity levels was thought to be largely the results of the different local incidence angle of CBI plots. At HH polarization the backscatter coefficient showed (Table 3) positive relation (i.e. positive beta coefficients) with burn severity due to increasing proportion of the exposed ground. On the other hand for HV polarization, which is more sensitive to volume scattering (i.e. vegetation structure), a decrease in backscatter was observed for increasing burn severities. The opposite trends of the backscatter as a function of burn severity suggest the complementary nature of the HH and HV polarizations for burn severity assessment at X-band.

Fig. 7 shows the strong effects of the local incidence angle on the backscatter. For increasing local incidence angles a clear decreasing trend was registered at HH polarization whereas at the HV polarization the backscatter increased. The average backscatter of the plots affected by high burn severity decreased around 2 dB at HH polarization. The highest values were registered for plots with smallest local incidence angles where the proportion of scattering from the forest floor is greatest. The lowest values were registered for plots with a local incidence angle of 46-50°. For larger incidence angles the average backscatter increased probably as a consequence of increased scattering from the vegetation layer. At HV polarization the backscatter increased by around 2.5 dB, from -15.5 dB at the steepest angles to -13.0 dB at the shallowest angles. The increase of the backscatter for increasing incidence angle can be explained in terms of increasing interaction of the radar waves with the scattering elements due to longer path traveled by the radar wave through the vegetation layer. The larger standard deviations registered for some intervals (e.g. 20-25 degrees) were consequence of the few available samples.

Empirical fitting showed modest relations between CBI values for the total plot, understory and overstory layers and the backscatter intensity of HH and HV polarizations when local incidence angle was not accounted for (Table 3). For all models the independent variables were significant, reliably predicting burn severity ($p<0.05$). Since all models were similar only the statistics of CBI overstory analysis which presented the highest R^2 are discussed. Stronger relation with burn severity was found for HH polarization ($R^2= 0.56$) than for HV ($R^2= 0.35$) the proportion of ground exposure being probably more important for burn severity evaluation when using both polarizations without separating for the local incidence angle. Beta coefficients confirm this assumption being larger for HH (0.531) than for HV (-0.292) polarization. Analysis of CBI as a function of backscatter coefficient after grouping by 5^0 local incidence angle intervals showed increased values of the determination coefficients. For instance, for the 41-45° interval which contains the highest number of plots, R^2 increased with 0.1 to 0.3 depending on the predictor variables used in the model. However, sample limitation makes the results less reliable and therefore the pseudo-plots analysis was used to confirm the observations made at plot level.

CBI was designed to match field sampling data with characteristics of optical based indices obtained from medium resolution sensors such as Landsat TM/ETM+. Considering mostly aspects related to vegetation chromatic properties makes CBI, in its actual form, less suited for radar data analysis. A revised version taking into account canopy structure properties (e.g. percentage of foliage or branches removed, size of remaining branches, height of first branches, etc.) should improve the association strength between field samples and backscatter coefficient.

Backscatter properties: pseudo-plots

The behavior of the backscatter for the pseudo-plots confirmed the results obtained for the CBI (Fig. 8). At HH polarization the backscatter increased for slopes oriented towards the sensor (i.e. local incidence angles smaller than 40^0) and areas affected by high burn severity (i.e. high dNBR). The higher backscatter variability for high burn severity levels and small local incidence angles (HH polarized beams) should be related to spatial heterogeneity of the soil moisture or roughness. At HV polarization the backscatter was higher for slopes oriented away from sensor (i.e. local incidence angles higher than 40^0) than for slopes oriented toward the sensor.

The analysis of the backscatter in terms of burn severity (dNBR) for a given range of local incidence angles (Fig.9) showed that at HH polarization the backscatter coefficient increased for low and medium burn severity (i.e. dNBR < 600). For higher dNBR the backscatter either decreased (for steep incidence angles) or reached saturation level (for shallow angles). This behavior could be explained by gaps in the canopy (complete combustion of tree crowns) and the presence of scattering elements that with increasing burn severity become transparent to the radar wave. In other words, the number of small branches and the moisture content of the vegetation at highest burn severity levels decreased. Therefore, vegetation component of backscatter diminished and the total backscattered energy decreased. The dynamic range of backscatter at HH polarization decreased with the increase of local incidence angle from around 4 dB to slightly more than 2 dB. While the level of backscatter in unburned forests remained rather constant (-11 dB) in burned forests the backscatter decreased with increasing incidence angle from -7 to -9 dB. At HV polarization the backscatter presented steady decrease for increasing dNBR and the dynamic range stayed around 2 dB at all incidence angles being slightly larger for high local incidence angles. The HV backscatter increased for increasing incidence angle, the increase being slightly larger for unburned forests where waves interact with a larger number of scatterers.

For highly burned areas Fig. 10 demonstrates the backscatter dependence on local incidence angle when keeping burn severity factor constant. At HH polarization the backscatter presented a clear descending trend which indicates strong sensitivity to the scattering from the forest floor especially at steep viewing geometries. Higher backscatter associated to sensor oriented slopes decreased with the increase of local incidence angle reaching similar levels for the flat and near flat terrain. The increased backscatter observed at the highest incidence angles (61-65°) could be a consequence of an increased vegetation contribution: the decrease of ground backscatter is lower than the increase of backscattered energy from the vegetation component, the total backscatter increasing with respect to the flat or near flat areas. The HV backscatter presented an ascending trend, the mean value increasing with the increase of local incidence angle. Since HV backscatter is less sensitive to the ground component, backscatter variations between high burn severity pseudo-plots were smaller than for HH polarization, i.e. 0.3 dB at all local incidence angles except 21-25° interval where it

reached around 0.5 dB. This small increment for the lowest local incidence angles could be explained by the proportion of ground backscatter component which plays a more important role at steep angles. The higher variability (i.e. standard deviation from the mean value) of HH polarization is explained by variation in ground properties (roughness and moisture) and roughness dependence on the incidence angle.

The strength of association (i.e. R^2) at HH polarization decreased with increasing incidence angle while the error increased (Table 4) validating the supposition on the role of ground component for backscatter return at HH polarization. For HV polarization the relation is inverse, the strength of association increasing up to around 55^0 where it reached the peak level. Combining the two polarizations within a simple ratio index (HH/HV) increased the strength of association between burn severity and backscatter coefficient while reducing the error of the estimates by at least 30% percent. Finally, the simultaneous use of HH and HV polarizations provided the highest R^2 coefficients and the smallest errors although the improvement was not significant over the ratio index. However, analysis of the residual scatter plots showed that only when using HH and HV polarization within a multiple regression analysis the assumptions of linear regression are met (Fig. 11). All other three approaches presented abnormal distribution of the residuals and heteroscedasticity implying that predictions made using linear regression are not reliable when one polarization or polarizations` ratio is used. Analysis of data (HH & HV) grouped in 3^0 intervals resulted in slight increase of the determination coefficients and smaller estimation error due to narrower angle intervals. For the 10^0 groups the results are slightly worse breaking of homoscedasticity appearing for some groups. Overall, 5^0 groups provided the best balance between the number of models needed, the strength of association and fulfillment of linear regression assumptions.

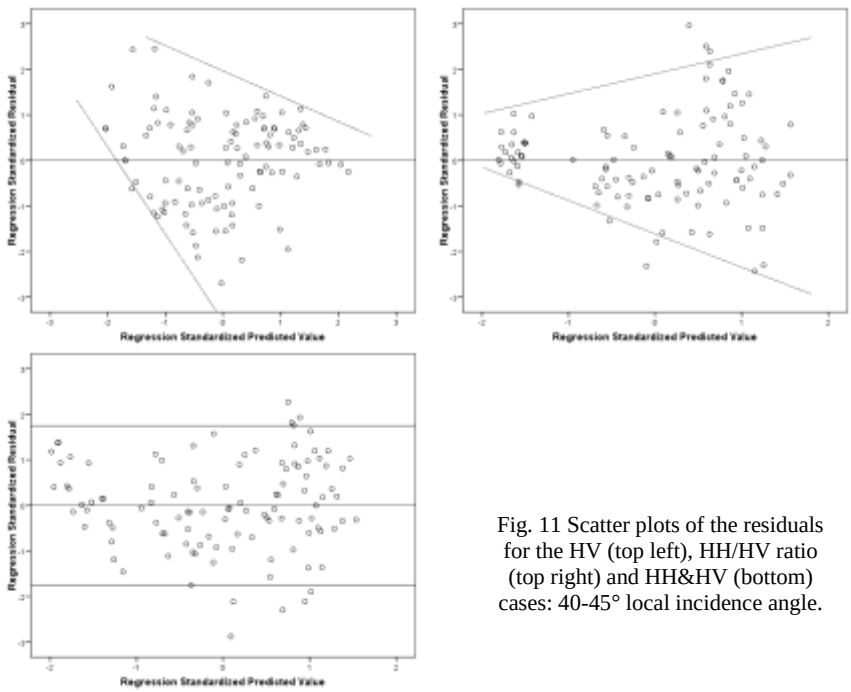

Fig. 11 Scatter plots of the residuals for the HV (top left), HH/HV ratio (top right) and HH&HV (bottom) cases: 40-45° local incidence angle.

CONCLUSIONS

This paper covered several aspects concerning burn severity assessment using TerraSAR-X backscatter data. More than one hundred field plots have been analyzed, allowing a detailed evaluation of the relations between burn severity assessed by means of CBI and X-band SAR backscatter at HH and HV polarizations. The influence of local incidence angle on backscatter coefficient was studied using pseudo-plots generated from pixels affected by similar burn severity.

At HH polarization backscatter was consistently higher for high severity burns while for HV polarized beams the backscatter coefficient increased with the decrease of burn severity and the increase of local incidence angle. The main variables affecting the backscatter at HH polarization were the proportion of exposed forest floor and the decreased attenuation after removal of needles. At HV polarization the amount of remaining vegetation determined the backscatter. The local incidence angle was found to play an important role at both polarizations, burn severity estimation without its consideration being subject to large errors. At HH polarization the backscatter coefficient was higher for sensor oriented slopes. At HV polarization the backscatter was less sensitive to slope effects, average backscatter increasing with the increase of local incidence angle. Both polarizations presented consistent trends across all local incidence angle ranges, HH polarization being positively while HV polarization negatively correlated with burn severity. Future investigations shall clarify how much weather conditions might affect such trends. The highest determination coefficients of burn severity as a function of SAR backscatter were observed for slopes oriented towards sensor at HH polarization and for slopes oriented away from the sensor at HV polarization. Finally, the degree of burn severity variance predicted from SAR data is modest when local incidence angle is not accounted for. Higher proportion of explained burn severity variance and smaller errors were obtained when using simultaneously HH and HV polarizations or their ratio in linear regression models after grouping for similar incidence angles. However, only when using both polarizations the assumptions of linear regression were met completely. The optimum interval for incidence angle grouping appeared to be 5^0 for the hilly terrain present in Zuera study area.

High resolution SAR data could provide more consistent estimates over the entire range of burn severities than reflectance based indices. Reflectance based indices provide good estimates for low and high burn severities but often fail when estimating intermediate levels because they express fire severity using indirect properties of the burned areas: NIR reflectance decrease due to loss of healthy green vegetation; SWIR reflectance increases due to less moisture content of vegetation and soils, increased substrate exposure and the presence of charred fuels. These properties are more stable for unburned or highly burned areas but become inconsistent for intermediate severity levels were multiple effects combine; most studies have found it problematic to discriminate intermediate severity values (Chuvieco et al. 2006). In addition, reflectance based indices are sensitive to plant phenology and solar elevation monitoring severity trends over time or across regions being subject to errors (Verbyla et al. 2008). In contrast, SAR data provide distinct information related more to forest structure. Scattering from tree crown is the predominant component of the backscatter from forested areas at X-band, the contribution of the understory and forest floor being conditioned primarily by canopy architecture. Removal of leaves and branches by fire has a direct effect on volume scattering at HV polarization, reduced backscatter levels being registered for increased burn severities. Moreover, indirect fire effects (e.g.

increased soil exposure) at HH polarization provide additional information which improves the estimation of severity levels. Finally, the determination coefficients presented were obtained based on reflectance based estimates of severity which are subject to the specific challenges of optical sensors derived indices already mentioned. Therefore, the actual association strength between backscatter levels and burn severity could be higher. Nevertheless, SAR data has its own challenges (e.g. backscattered energy is dependent on environmental conditions, wavelength, polarization, etc.), appropriate selection of acquisition time being often crucial for successful retrieval of bio-geophysical parameters.

The results presented are valid for typical pine forests found in the Mediterranean basin. However, fire produces similar effects (e.g. loss of crown foliage and branches, removal of understory layers etc.) in many forests at mid-latitudes so we believe that general data trends would be similar for other forest types and tree species at least in temperate climates. In significantly different environments such as boreal or tropical forests trends could be however, different. Dissimilarity could arise due to fire effects on distinct forest structures, moisture effects on backscatter response etc. This study indicates that dual polarization (HH, HV) X-band SAR data have potential for burn severity estimation in the mediterranean environments as long as the local incidence angle is accounted for. Determination coefficients reported for groups of local incidence angle are similar or higher than those reported when using indices obtained from optical sensors.

ACKNOWLEDGMENT

This work has been financed by the Spanish Ministry of Science and Education and the European Social Fund: FPI grant BES-2006-11684 and project CGL2005-04863. TerraSAR-X data were provided by Deutsches Zentum für Luft- und Raumfahrt (DLR) in the framework of LAN0464 project (PI Mihai Tanase).

REFERENCES

Allen, J.L., and Sorbel, B. (2008). Assessing the differenced Normalized Burn Ratio's ability to map burn severity in the boreal forest and tundra ecosystems of Alaska's national parks. *International Journal of Wildland Fire, 17*, 463-475.

Bourgeau-Chavez, L.L., Harrell, P.A., Kasischke, E.S., and French, N.H.F. (1997). The detection and mapping of Alaskan wildfires using a spaceborne imaging radar system. *International Journal of Remote Sensing, 18*, 355-373.

Bourgeau-Chavez, L.L., Kasischke, E.S., Brunzell, S., and Mudd, J.P. (2002). Mapping fire scars in global boreal forests using imaging radar data. *International Journal of Remote Sensing, 23*, 4211-4234.

Bourgeau-Chavez, L.L., Kasischke, E.S., French, N.H.F., Szeto, L.H., and Kherkher, C.M. (1994). Using ERS-1 SAR Imagery to Monitor Variations in Burn Severity in an Alaskan Fire-Disturbed Boreal Forest Ecosystem. In, *Geoscience and Remote Sensing Symposium, 1994. IGARSS '94. Proceedings. 1994 IEEE International* (pp. 243-245). Pasadena, California.

Bourgeau-Chavez, L.L., Kasischke, E.S., Riordan, K., Brunzell, S., Nolan, M., Hyer, E., Slawski, J., Medvecz, M., Walters, T., and Ames, S. (2007). Remote monitoring of spatial and temporal surface soil moisture in fire disturbed boreal forest ecosystems with ERS SAR imagery. *International Journal of Remote Sensing, 28*, 2133-2162.

Castel, T., Beaudoin, A., Stach, N., Stussi, N., Le Toan, T., and Durand, P. (2001). Sensitivity of space-borne SAR data to forest parameters over sloping terrain. Theory and experiment. *International Journal of Remote Sensing, 22*, 2351-2376.

Cocke, A.E., Fule, P.Z., and Crouse, J.E. (2005). Influence of fire severity on plant regeneration by means of remote sensing imagery. *International Journal of Wildland Fire, 14*, 189-198.

Czuchlewski, K.R., and Weissel, J.K. (2005). Synthetic Aperture Radar (SAR)-based mapping of wildfire burn severity and recovery. In, *Geoscience and Remote Sensing Symposium, 2005. IGARSS '05. Proceedings. 2005 IEEE International* Seoul, Korea.

Chuvieco, E. (1999). Measuring changes in landscape pattern from satellite images: short-term effects of fire on spatial diversity. *International Journal of Remote Sensing, 20*, 2331-2346.

Chuvieco, E., Riaño, D., Danson, F.M., and Martín, P. (2006). Use of a radiative transfer model to simulate the postfire spectral response to burn severity. *Journal of Geophysical Research, 111*, 1-15.

Díaz-Delgado, R., Lloret, F., and Pons, X. (2003). Influence of fire severity on plant regeneration by means of remote sensing imagery. *International Journal of Remote Sensing, 24*, 1751-1763.

Epting, J., Verbyla, D., and Sorbel, B. (2005). Evaluation of remotely sensed indices for assessing burn severity in interior Alaska using Landsat TM and ETM+. *Remote Sensing of Environment, 96*, 328-339.

Ferry, G.W., Clark, R.G., Montgomery, R.E., Mutch, R.W., Leenhouts, W.P., and Zimmerman, G.T. (1995). Altered fire regimes within fire-adapted ecosystems. *Our Living Resources: a report to the nation on the distribution, abundance, and health of U.S. plants animals, and ecosystems* (pp. 222-224). Washington D.C.: USDI National Biological Survey.

French, N.H.F., Bourgeau-Chavez, L.L., Wang, Y., and Kasischke, E.S. (1999). Initial Observations of Radarsat Imagery at Fire-Disturbed Sites in Interior Alaska. *Remote Sensing of Environment, 68*, 89-94.

Fritz, T., and Einder, M. (2008). TerraSAR-X Ground segment, Basic Product Specification Document. In C.A.R. Sensing (Ed.) (p. 103).

Gimeno, M., and San-Miguel-Ayanz, J. (2004). Evaluation of RADARSAT-1 data for identification of burnt areas in Southern Europe. *Remote Sensing of Environment, 92*, 370-375.

Gimeno, M., San-Miguel-Ayanz, J., and Schmuck, G. (2004). Identification of burnt areas in Mediterranean forest environments from ERS-2 SAR time series. *International Journal of Remote Sensing, 25*, 4873-4888.

Hoekman, D.H. (1987). Measurements of the Backscatter and Attenuation Properties of Forest Stands at X-, C- and L-band. *Remote Sensing of Environment, 23*, 397-416.

Hoy, E.E., French, N.H.F., Turetsky, M.R., Trigg, S.N., and Kasischke, E.S. (2008). Evaluating the potential of Landsat TM/ETM+ imagery for assessing fire severity in Alaskan black spruce forests. *International Journal of Wildland Fire, 17*, 500-514.

Huang, S., and Siegert, F. (2004). ENVISAT multisensor data for fire monitoring and impact assessment. *International Journal of Remote Sensing, 25*, 4411-4416.

Kasischke, E.S., Bourgeau-Chavez, L.L., and French, N.H.F. (1994). Observations of Variations in ERS-1 SAR Image Intensity Associated with Forest Fires in Alaska. *IEEE Transactions on Geoscience and Remote Sensing, 32*, 206-210.

Kasischke, E.S., Bourgeau-Chavez, L.L., French, N.H.F., Harrell, P., and Christensen, N.L. (1992). Initial observations on using SAR to monitor wildfire scars in boreal forests. *International Journal of Remote Sensing, 13*, 3495-3501.

Key, C.H., and Benson, N.C. (2004). *Ground Measure of Severity, The Composite Burn Index*. Ogden, UT: U.S. Department of Agriculture, Forest Service, Rocky Mountain Research Station.

Key, C.H., and Benson, N.C. (2006). Landscape assessment (LA). In D.C. Lutes, R.E. Keane, J.F. Caratti, C.H. Key, N.C. Benson, S. Sutherland and L.J. Gangi (Eds.), *FIREMON: Fire effects monitoring and inventory system* (pp. 1-55). Fort Collins, CO: U.S. Department of Agriculture, Forest Service, Rocky Mountain Research Station, Gen. Tech. Rep. RMRS-GTR-164-CD.

Koutsias, N., and Karteris, M. (2000). Burned area mapping using logistic regression modeling of a single post-fire Landsat-5 Thematic Mapper image. *International Journal of Remote Sensing, 21*, 673-687.

Laneve, G., Castronuovo, M.M., and Cadau, E.G. (2006). Continuous Monitoring of Forest Fires in the Mediterranean Area Using MSG. *IEEE Transactions on Geoscience and Remote Sensing, 44*, 2761-2768.

Leckie, D.G. (1999). Forestry Applications Using Imaging Radar. In F.M. Henderson and A.J. Lewis (Eds.), *Principles and Applications of Imaging Radar* (p. 866): John Wiley & Sons.

Liew, S.C., Kwoh, L.K., Padmanabhan, K., Lim, O.K., and Lim, H. (1999). Delineating Land/Forest Fire Burnt Scars with ERS Interferometric Synthetic Aperture Radar. *Geophysical Research Letters, 26*, 2409-2412.

Luckman, A.J. (1998). The Effects of Topography on Mechanism of Radar Backscatter from Coniferous Forest and Upland Pasture. *IEEE Transactions on Geoscience and Remote Sensing, 36*, 1830-1834.

Martinez, J.M., Floury, N., Le Toan, T., Beaudoin, A., Hallikainen, M.T., and Makynen, M. (2000). Measurements and Modeling of Vertical Backscatter Distribution in Forest Canopy. *IEEE Transactions on Geoscience and Remote Sensing, 38*, 710-719.

Menges, C.H., Bartolo, R.E., Bell, D., and Hill, G.J.E. (2004). The effect of savanna fires on SAR backscatter in northern Australia. *International Journal of Remote Sensing, 25*, 4857-4871.

Miller, J.D., Knapp, E.E., Key, C.H., Skinner, C.N., Isbell, C.J., Creasy, R.M., and Sherlocke, J.W. (2009). Calibration and validation of the relative differenced Normalized Burn Ratio (RdNBR) to three measures of fire severity in the Sierra Nevada and Klamath Mountains, California, USA. *Remote Sensing of Environment, 113*, 645-656.

Murphy, K.A., Reynolds, J.H., and Koltun, J.M. (2008). Evaluating the ability of the differenced Normalized Burn Ratio (dNBR) to predict ecologically significant burn severity in Alaskan boreal forests. *International Journal of Wildland Fire, 17*, 490-499.

Pulliainen, J.T., Heiska, K., Hyyappa, J., and Hallikainen, M.T. (1994). Backscattering properties of boreal forests at the C- and X-Bands. *IEEE Transactions on Geoscience and Remote Sensing, 32*, 1041-1050.

Raney, K. (1999). Radar Fundamentals: Technical Perspective. In F.M. Henderson and A.J. Lewis (Eds.), *Principles and Applications of Imaging Radar* (p. 866): John Wiley & Sons.

Roy, D.P., Boschetti, L., and Trigg, S.N. (2006). Remote Sensing of Fire Severity: Assessing the Performance of the Normalized Burn Ratio. *IEEE Transactions on Geoscience and Remote Sensing Letters*, 1-5.

Santis, A.de., and Chuvieco, E. (2007). Burn severity estimation from remotely sensed data: Performance of simulation versus empirical models. *Remote Sensing of Environment, 108*, 422-435.

Santis, A.de., and Chuvieco, E. (2009). GeoCBI: A modified version of the Composite Burn Index to estimate burn severity for remote sensing applications. In, *Remote Sensing of Environment* (pp. 554-562).

Schmuck, G., San-Miguel-Ayanz, J., Camia, A., Kucera, J., Libertá, G., Boca, R., Durrant, T., and Amatulli, G. (2008). Forest Fires in Europe 2007. In, *JRC Scientific and Technical Reports*. Ispra, Italy: Joint Research Center.

Siegert, F., and Hoffmann, A.A. (2000). The 1998 Forest Fires in East Kalimantan (Indonesia): A Quantitative Evaluation Using High Resolution, Multitemporal ERS-2 SAR Images and NOAA-AVHRR Hotspot Data. *Remote Sensing of Environment, 72*, 64-77.

Siegert, F., and Nakayama, M. (2000). Comparison of ERS-2 and JERS for fire impact assessment in tropical rainforests. In, *Geoscience and Remote Sensing Symposium, 2000. IGARSS '00. Proceedings. 2000 IEEE International* (pp. 2709-2711). Honolulu, HI, USA.

Siegert, F., and Ruecker, G. (2000). Use of multitemporal ERS-2 SAR images for identification of burned scars in south-east Asian tropical rainforest. *International Journal of Remote Sensing, 21*, 831-837.

Stroppiana, D., Tansey, K., Grégoire, J.-M., and Pereira, J.M.C. (2003). An Algorithm for Mapping Burnt Areas in Australia Using SPOT-VEGETATION Data. *IEEE Transactions on Geoscience and Remote Sensing, 41*, 907-909.

Ulander, L.M.H. (1996). Radiometric slope correction of synthetic-aperture radar images. *IEEE Transactions on Geoscience and Remote Sensing, 34*, 1115-1122.

Verbyla, D.L., Kasischke, E.S., and Hoy, E.E. (2008). Seasonal and topographic effects on estimating fire severity from Landsat TM/ETM+ data. *International Journal of Wildland Fire, 17*, 527-534.

Wagtendonk, J.W.van., Root, R.R., and Key, C.H. (2004). Comparison of AVIRIS and Landsat ETM+ detection capabilities for burn severity. *Remote Sensing of Environment, 92*, 397-408.

Wegmüller, U., Strozzi, T., and Bitelli, G. (1999). Validation of ERS differential SAR interferometry for land subsidence mapping: the Bologna case study. In, *Geoscience and Remote Sensing Symposium, 1999. IGARSS '99. Proceedings. 1999 IEEE International* (pp. 1131 -1133). Hamburg, Germany.

Wegmüller, U., Werner, C., Strozzi, T., and Wiesmann, A. (2002). Automated and precise image registration procedures. In L. Bruzzone and P. Smits (Eds.), *Analysis of multi-temporal remote sensing images* (pp. 37-49). Singapore: World Scientific 2002.

Wimberly, M.C., and Reilly, M.J. (2007). Assessment of fire severity and species diversity in the southern Appalachians using Landsat TM and ETM+ imagery. *Remote Sensing of Environment, 108*, 189-197.

4.2.2. Backscatter properties of multi-temporal TerraSAR-X data and the effects of the influencing factors on burn severity evaluation, in a Mediterranean pine forest

Tanase, M.A., Santoro, M., de la Riva, J. and, Pérez-Cabello, F. (2009) Backscatter properties of multi-temporal TerraSAR-X data and the effects of influencing factors on burn severity evaluation, in a Mediterranean pine forest. ***Geoscience and Remote Sensing Symposium, 2009 IEEE International, vol. III pp. 593-596.***

Resumen

Se evalúa la estabilidad temporal del coeficiente de retro-dispersión en un incendio del nordeste de España utilizando imágenes TerraSAR-X de doble polarización (HH y HV). Se aborda también el análisis de los principales factores que influyen en la evaluación de la severidad mediante imágenes SAR.

Se pone de manifiesto la alta estabilidad temporal de la retro-dispersión, arrojando diferencias, para las zonas sin quemar, de menos de 0,6 dB. Con el incremento de la severidad, la variación del coeficiente de retro-dispersión asciende hasta 2 dB en zonas muy afectadas por el incendio y situadas en laderas orientadas hacia el sensor. La ocurrencia de fuertes lluvias o la presencia de vegetación mojada suponen un incremento de la retro-dispersión de hasta 1 dB. Los ángulos de incidencia elevados se traducen en un incremento significativo del coeficiente de retro-dispersión en el caso de la polarización HH, mientras que para la polarización HV tan sólo se ha observado un aumento leve. El coeficiente de determinación entre la retro-dispersión y la severidad del incendio se ve mejorado con el tamaño de la ventana multi-look a expensas de la resolución espacial. Se podrían obtener mejores resultados, a mayor resolución espacial, mediante la aplicación de filtros multi-temporales.

Backscatter properties of multi-temporal TerraSAR-X data and the effects of the influencing factors on burn severity evaluation, in a Mediterranean pine forest*

M. A. Tanase[(1)], M. Santoro[(2)], J. de la Riva[(1)], and F. Pérez-Cabello[(1)]

[(1)]Department of Geography,
University of Zaragoza,
Pedro Cerbuna 12, 50009 Zaragoza, Spain
Email: mihai@tma.ro, delariva@unizar.es, fcabello@unizar.es

[(2)]Gamma Remote Sensing AG,
Worbstr. 225, CH-3073 Gümligen, Switzerland
Email: santoro@gamma-rs.ch

Abstract

TerraSAR-X dual-polarized (HH and HV polarization) backscatter data have been investigated to assess the temporal backscatter stability of a burn scar in Spain. Analysis of the main factors influencing burn severity evaluation has been also carried out. The temporal stability of the backscatter was strong, unburned areas showing differences of less than 0.6 dB. For increasing burn severity the backscatter varied by up to 2 dB in highly burned areas located on slopes tilted towards the sensor. Heavy rainfall or moist vegetation increased the backscatter up to 1 dB. Steeper look angles resulted in significantly higher backscatter coefficients for HH polarization, while for HV polarization only marginal increase was observed. Association strength between backscatter and burn severity estimates improved with the size of the multi-look window, at the expenses however of spatial resolution. Even better results could be achieved at higher spatial resolution by applying a multi-temporal speckle filtering algorithm.

***Keywords**: burn severity, TerraSAR-X, backscatter*

* *Interactive Session Prize Paper Award*, Geoscience and Remote Sensing Society, 2010.

INTRODUCTION

Forest fires are an important source of atmospheric aerosols and green-house gasses, causal relationship between biomass burning and inter-annual variability of related emissions being observed (Simmonds et al. 2005). The duration and intensity of a fire determines not only the quantity of the green-house gasses and aerosols emissions (Andreae and Merlet 2001) but also the recovery processes years after the event. Burn severity is nowadays used to express fire effects on ecosystems and is defined as the degree of the environmental changes caused by fire. One of the most widely employed optical-based spectral indexes for burn severity assessment is the Normalized Burn Ratio (NBR) (Key and Benson 2006) used in a bi-temporal approach with pre- and post-fire datasets (dNBR). dNBR provides a scale of changes with respect to the pre-fire status, unburned area retaining values close to zero (i.e. little or no change). Nevertheless,

reflectance based indexes often fail to produce accurate results especially for intermediate burn severity levels where multiple effects combine. Most studies found it problematic to discriminate intermediate burn severities (Chuvieco et al. 2006).

An alternative method for burn severity estimation is the use of synthetic aperture radar (SAR) images since they contain information related to forest structure, removal of leaves and branches by fire directly influencing the radar backscatter. Previous work confirmed the utility of SAR data for remote estimation of burned areas (Gimeno et al. 2002). Statistically significant relations have been found between TerraSAR-X (X-band) HH and HV polarizations and burn severity when both channels were used in linear regression models (Tanase et al. 2010). To further assess the capability of TerraSAR-X backscatter to map burn severity, the temporal stability and the backscatter response over a burned area for data acquired at different look angles and under variable weather condition were investigated. The radar signal is influenced by viewing geometry (i.e. look angle), soil and vegetation moisture and ephemeral effects of forests (e.g. changes in leaf orientation due to wind). Consequently, backscatter coefficient could increase or decrease as a function of other factors such as vegetation type, structure, orientation etc. Because of the high resolution of the data, we could also investigate the effect of speckle reduction techniques (spatial multi-looking and multi-temporal filtering) on the association strength between the backscatter and burn severity.

STUDY AREA AND DATA SETS

The Zuera study area is located in central Ebro Valley and has a semi-arid mediterranean climate with continental characteristics and marked seasonal precipitation variations. Most of the area is covered by homogeneous, even aged pine forests of *Pinus halepensis* L. interspersed with agricultural fields. The forest fire under investigation occurred between 6-16th August, 2008 after a traffic accident and burned approximately 2200 ha of vegetation.

The dataset consisted of seven TerraSAR-X (TSX) and one pair of Landsat 5 TM images. Dual polarization TSX data were acquired between November 2008 and March 2009 in Stripmap (SM) mode at look angles of 25° and 40°. The six SAR images acquired at 40° look angle were calibrated and then multi-looked with two sets of factors in order to obtain images at different spatial resolutions (10 and 25 m pixel spacing). Subsequently, the images were co-registered, achieving sub-pixel accuracy, using a cross-correlation algorithm based on intensity tracking (Wegmüller et al. 1998). Adaptive multi-temporal filtering (AdMTF) (Oliver and Quegan 1998) was carried out at both spatial resolutions using stacks of three and six co-registered images. The ENL after multi looking and temporal filtering together with the main SAR data characteristics and processing parameters are presented in Table 1. The image acquired at 25° was processed to 25 m spatial resolution. All images were geocoded to UTM projection using a digital elevation model (DEM) with 20 m pixel spacing. Detailed information on SAR geocoding process is given in (Tanase et al. 2010). Topographic normalization for the varying incidence angle and effective pixel area was applied (Ulander 1996) using information derived from the DEM. All resulting images, obtained in gamma nought (γ°) format, were scaled to the look angle at mid swath.

The Landsat scenes (path 199, row 031) were acquired on July 21st (pre-fire) and August 22nd, 2008 (post-fire). Subsets of the scenes were geometrically rectified to the same coordinate system as SAR data using a linear polynomial model and incorporating

Table 1 SAR Data characteristics and processing parameters – summary.

Parameter	Value
Acquisition dates for 40° look angle data	2008.11.16 / 2008.12.19 / 2009.01.21 / 2009.02.12 / 2009.02.23 / 2009.03.06
Acquisition date for 25° look angle data	2008.12.24
SSC pixel spacing (slant range, azimuth)	0.91 m × 2.43 m
Multi-look factors (range x azimuth pixels)	a) 17 × 10, b) 8 × 5
ML images pixel spacing (slant range, azimuth)	a) 15.5 m × 24.3 m, b) 7.3. m × 12.1 m
Pixel spacing of geocoded images	a) 25 m × 25 m, b) 10 m × 10 m
ENL (25 m spatial resolution)	no AdTMF: 55 / AdMTFimages: 90 / AdMTF 6 images: 125
ENL (10 m spatial resolution)	no AdMTF: 9 / AdMTF 3 images: 25 / AdMTF 6 images: 32

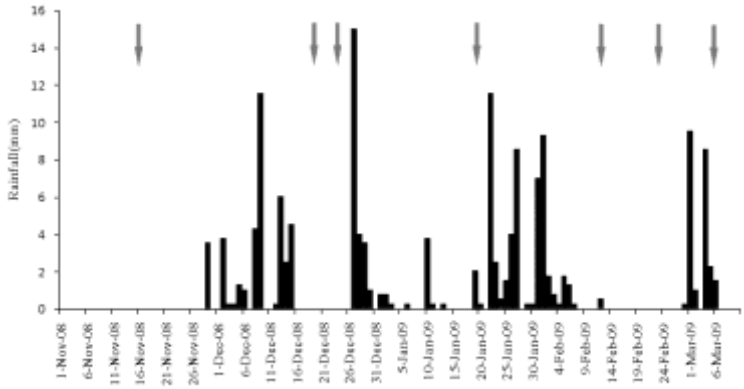

Fig. 1 Daily precipitation and image acquisition dates (arrows).

information of the local topography (Tanase et al. 2010). Landsat TM data were used to derive optical based estimates (dNBR) of burn severity.

For the interpretation of backscatter signatures precipitation recorded during the period of image acquisitions (Fig. 1) was obtained from an automatic rain gauge installed roughly at the center of the fire perimeter.

METHODS

Backscatter temporal trends, weather and viewing geometry effects on backscatter coefficient were analyzed using descriptive statistics (i.e. mean backscatter values by groups of local incidence angle). To evaluate the performance of speckle suppression methods linear regression analysis was employed. Since multiple regression requires large number of samples which cannot be easily achieved by field work the investigation was carried out using a set of automatically generated pseudo-plots. Pseudo-plots were generated by averaging pixels of similar burn severity (i.e. dNBR) for the same local incidence angle rounded to unity. To avoid possible bias only pseudo-plots containing a specific number of pixels (i.e. 4, 9, 10, 16, 25 and 50) were selected. High determination coefficient were found between field estimates of burn severity by means of Composite Burn Index (CBI) and dNBR ($R^2 = 0.81$, $p<0.05$). This result supported the assumption that dNBR can be considered for further use as a radiometric index strongly related to the severity levels recorded in the field. Detailed information on pseudo-plots generation and CBI assessment is given in (Tanase et al. 2010).

Determination coefficients (R^2) were used to relate SAR data to optical sensor based estimates (dNBR) of burn severity. Multiple linear regression analysis was employed after grouping pseudo-plots in 5° intervals of local incidence angle to evaluate the association strength between burn severity and radar backscatter. Regression analysis was carried out using 900 randomly selected pseudo-plots. The effect of speckle reduction techniques on burn severity estimates were assessed using pseudo-plots formed by 10, 25 and 50 pixels for data geocoded to 10 m pixel spacing and by 4, 9 and 16 pixels for data geocoded to 25 m pixel spacing.

RESULTS AND DISCUSSION

Backscatter signatures in relation to weather conditions and image viewing geometry

The backscatter signatures at HH and HV polarizations are presented in Fig. 2 for the images acquired at 40° look angle. To minimize the effect of topography the averages were calculated for groups of local incidence angles from data geocoded at 10 m pixel spacing using 0.1 ha (i.e. 10 pixels) pseudo-plots. For unburned areas the backscatter was rather constant in time, the variation being within the absolute radiometric accuracy (0.6 dB). For a given severity, the backscatter coefficient varied by 1-2 dB, larger variations being observed for high burn severity levels at both polarizations. This can be explained by taking into account that at higher burn severity levels soil exposure increases; hence, soil roughness and soil moisture induce larger backscatter variations. For smaller local incidence angles (i.e. slopes oriented towards the sensor) the spread increased slightly while for larger local incidence angles (i.e. slopes oriented away from sensor) the maximum spread showed a certain decrease when compared to flat or near flat areas (i.e. 35-45° local incidence angle). This behavior is explained by the higher soil backscatter component at lower incidence angles, which translates in higher variability due to roughness and moisture. Light precipitation did not have large impact on the backscatter. The average backscatter level of the 2009.01.21 dataset was similar to the level observed for the datasets acquired under dry conditions. An explanation for the apparent lack of precipitation effects is the low rainfall quantity registered (2 mm on 2009.01.21 and 0.25 mm on 2009.02.12) and the soils of the area which are unable to retain water as a consequence of the high hydraulic conductivity. However, heavy rainfall (11 mm on 2009.03.04 and 2009.03.05 before the image acquired on 2009.03.06) and vegetation surface moisture (0.25 mm registered three hours before acquisition on 2009.02.12) caused higher average backscatter coefficients (0.5-1 dB) at both polarizations and for all burn severities especially on slopes tilted towards the sensor.

The effect of look geometry on the backscatter of burned areas is illustrated by two datasets (2008.12.19 and 2008.12.24) acquired four days apart at 40° and 25° look angles respectively. Fig. 3 presents the average backscatter by burn severity levels of flat or near flat areas. The short acquisition interval and the stable weather conditions suggest that observed differences are due to the steeper viewing geometry of the image acquired on the second date. The 2 dB higher values registered for HH polarization at all severity levels in the image acquired at 25° could be explained in terms of higher portion of direct scattering from the ground at steeper incidence angles and the lower attenuation of the forest canopy. At HV polarization forest floor plays a less important role, which explains the much smaller backscatter difference.

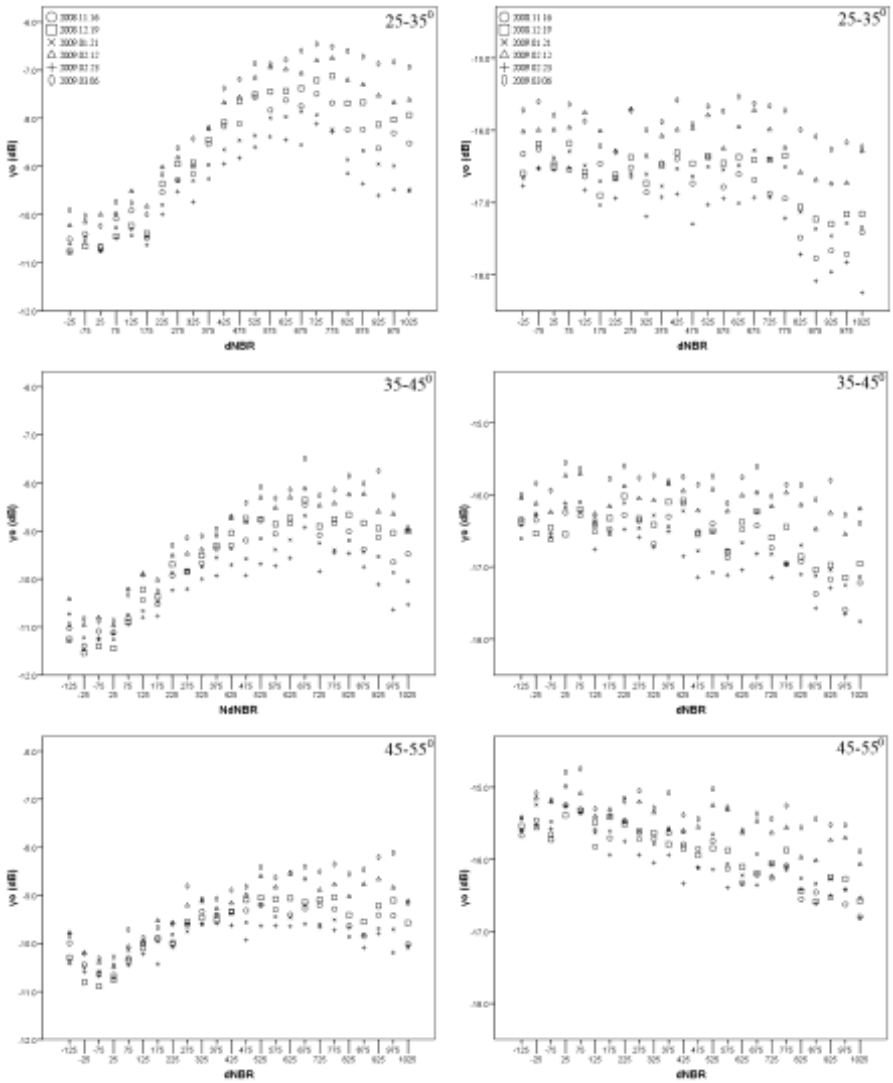

Fig. 2 Backscatter signatures for HH (left) and HV (right) polarizations for the six images acquired at 40° look angle. Measurements have been grouped for 10° local incidence angle intervals.

Analysis of the association strength

Fig. 4 illustrates the determination coefficient for all images processed at 25 m pixel spacing with multi-looking, without applying multi-temporal filtering (ENL equal to 55). The almost negligible effect of the weather conditions on the backscatter resulted in similar determination coefficients. No significant differences were noticed for data acquired at steeper look angle (2008.12.24) or for data acquired after light rainfall (2009.01.21 and 2009.02.12). However, for the image acquired after heavy rainfall (2009.03.06) a decrease of the determination coefficients was evident at higher local incidence angles. At these angles HV polarization accounts for a larger part of the

variability explained by the regression model (Tanase et al. 2010). For the image acquired when vegetation was wet (2009.02.12) the dynamic range was smaller compared to the other images, which influenced the association strength to burn severity levels.

The use of larger plots eliminates variability due to speckle, increasing the association strength to burn severity. Fig. 5 illustrates the influence of plot size on the association strength for the image acquired on 2008.12.19 processed to 10 m (ENL equal to 9) and to 25m (ENL equal to 55). A marked increase of the determination coefficients with the number of pixels per plot is evident. For lower ENL, more samples within a plot are needed to obtain similar determination coefficients as for the data processed with stronger multi-look factors.

The effect of additional multi-temporal filtering is presented in Fig. 6. To obtain different levels of speckle suppression before filtering the 2008.11.16 image was multi-looked with different factors (17×10 and 8×5). The images with 25 and 32 ENL were obtained after applying AdMTF to the 10 m spatial resolution data using 3 or 6 images respectively, while the images with 90 and 125 ENL were obtained after applying

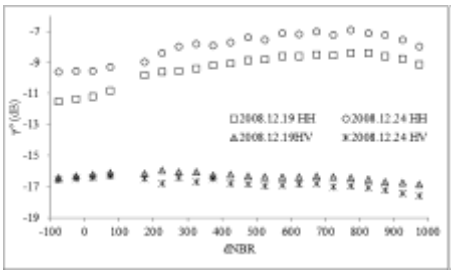

Fig. 3 Backscatter with respect to dNBR for an image acquired with 40° look angle (2008.12.29) and 25° look angle (2008.12.24). Only pseudo-plots on flat or near flat areas are considered.

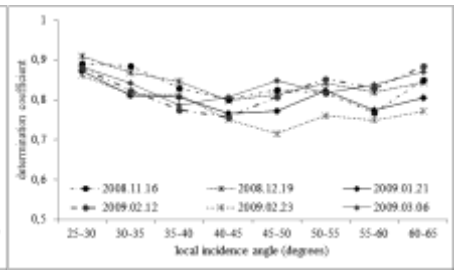

Fig. 4 Determination coefficients between burn severity and backscatter coefficient with respect to local incidence angle for images with ENL equal to 55 and 9 pixels per pseudo-plot.

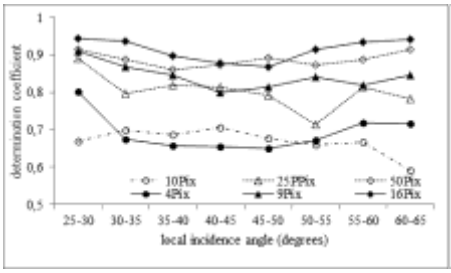

Fig. 5 Determination coefficients between burn severity and backscatter coefficient with respect to local incidence angle for the image acquired on 2008.12.19.

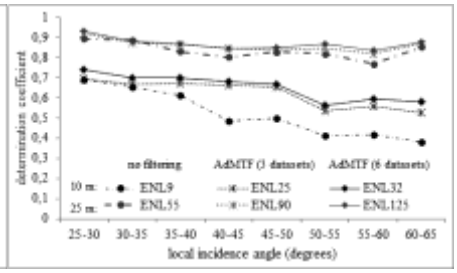

Fig. 6 The influence of speckle reduction on the association strength between burn severity and backscatter coefficient for 2008.11.16 dataset (9 pixels per plot).

AdMTF to the 25 m spatial resolution data. The results suggest that when strong multi-looking factors (17×10) were applied, AdMTF improved little the retrieval of burn severity. At higher spatial resolution (10 m) the use of AdMTF greatly improved burn severity retrieval, higher R^2s (up to 0.2) being observed for the filtered images. Nevertheless, doubling the number of images used for temporal filtering (from 3 to 6) did not improve significantly burn severity retrieval.

CONCLUSIONS

In this paper several aspects concerning the use of multi-temporal dual-polarized (HH and HV) TerraSAR-X data for burn severity evaluation have been investigated. For unburned areas the backscatter showed temporal variability comparable to the declared radiometric accuracy (0.6 dB). With increasing burn severity the temporal variability of the backscatter increased reaching up to 2 dB for highly burned areas on slopes oriented towards the sensor (HH-polarization). The high temporal stability provided consistent results in terms of burn severity evaluation. Evaluation of burn severity is possible up to nine months after fire. Light rain prior to image acquisition influenced backscatter marginally. The backscatter and the determination coefficients were practically unchanged with respect to images acquired under dry conditions. The backscatter level increased while the determination coefficients decreased for images acquired after heavy rainfall or when vegetation presented surface moisture. The look geometry strongly influenced the backscatter, especially at HH polarization, in form of an offset. Nonetheless the association strength between backscatter and burn severity did not change. For burn severity evaluation, multi-temporal filtered images provided better results than unfiltered images. The association strength between backscatter coefficient and burn severity increased with the increase of ENL for data processed at high spatial resolution. Nevertheless, determination coefficients for backscatter obtained from temporally filtered images using six datasets were not significantly different compared to the case of using three datasets. When high multi-looking factors were used MTF did not improve significantly the determination coefficients.

ACKNOWLEDGMENT

This work has been financed by the Spanish Ministry of Science and Education and the European Social Fund. TerraSAR-X data were provided by Deutsches Zentrum für Luft- und Raumfahrt (DLR) in the framework of LAN0464 project.

REFERENCES

Andreae, M.O., and Merlet, P. (2001). Emission of trace gases and aerosols from biomass burning. *Global Biogeochemical Cycles, 15*, 955-966.

Chuvieco, E., Riaño, D., Danson, F.M., and Martín, P. (2006). Use of a radiative transfer model to simulate the postfire spectral response to burn severity. *Journal of Geophysical Research, 111*, 1-15.

Gimeno, M., San-Miguel, J., Barbosa, P., and Schmuck, G. (2002). Using ERS-SAR images for burnt area mapping in Mediterranean landscapes. In D.X. Viegas (Ed.), *Forest Fire Research &Wildland Fire Safety: Proceedings of IV International Conference on Forest Fire Research* (pp. 18-23). Coimbra, Portugal: Millpress Science Publishers.

Key, C.H., and Benson, N.C. (2006). Landscape assessment (LA). In D.C. Lutes, R.E. Keane, J.F. Caratti, C.H. Key, N.C. Benson, S. Sutherland and L.J. Gangi (Eds.), *FIREMON: Fire effects*

monitoring and inventory system (pp. 1-55). Fort Collins, CO: U.S. Department of Agriculture, Forest Service, Rocky Mountain Research Station, Gen. Tech. Rep. RMRS-GTR-164-CD.

Oliver, C.J., and Quegan, S. (1998). *Understanding synthetic aperture radar images*: Artech House.

Simmonds, P.G., Manning, A.J., Derwent, R.G., Ciais, P., Ramonet, M., Kazan, V., and Ryall, D. (2005). A burning question. Can recent growth rate anomalies in the greenhouse gases be attributed to large-scale biomass burning events?. *Atmospheric Environment, 39*, 2513-2517.

Tanase, M., Pérez-Cabello, F., Riva, J.de la, and Santoro, M. (2010). TerraSAR-X data for burn severity evaluation in Mediterranean forests on sloped terrain. *IEEE Transactions on Geoscience and Remote Sensing, 48*, 917-929.

Ulander, L.M.H. (1996). Radiometric slope correction of synthetic-aperture radar images. *IEEE Transactions on Geoscience and Remote Sensing, 34*, 1115-1122.

Wegmüller, U., Werner, C., and Strozzi, T. (1998). SAR interferometric and differential interferometric processing. In, *Geoscience and Remote Sensing Symposium, 1998. IGARSS '98. Proceedings. 1998 IEEE International* (pp. 1106-1108). Seattle, USA.

4.2.3. Sensitivity of X-, C- and L-band SAR backscatter to burn severity in Mediterranean pine forests

Tanase, M.A., de la Riva, J., Santoro M., Le Toan, T. and, Pérez-Cabello, F. (2010) Sensitivity of X-, C- and L-band SAR backscatter to fire severity in a Mediterranean pine forest. ***IEEE Transactions on Geoscience and Remote Sensing*****, doi:10.1109/ TGRS.2010.2049653, in press.**

Resumen

Se utilizan imágenes SAR de las bandas X, C y L para determinar la relación entre el coeficiente de retro-dispersión y la severidad del incendio en tres áreas quemadas del nordeste de España. Se analiza también la dependencia de la retro-dispersión SAR del ángulo de incidencia local y de las condiciones medioambientales. Para las polarizaciones HH y VV la retro-dispersión aumenta con la severidad en las bandas X y C, mientras que en la banda L se reduce con el incremento de la severidad. Para la polarización cruzada (HV) la retro-dispersión disminuye con la severidad en todas las frecuencias SAR analizadas. El coeficiente de determinación se utiliza para cuantificar la relación entre la retro-dispersión radar y la severidad en función del ángulo de incidencia local. La sensibilidad de la retro-dispersión co-polarizada para la estimación de la severidad disminuye con el aumento del ángulo de incidencia local para todas las frecuencias SAR, excepto para la banda L. Para las bandas X y C co-polarizadas se obtienen coeficientes de determinación mayores en las pendientes orientadas hacia el sensor, mientras que para la polarización cruzada los coeficientes de determinación mayores se asocian a las laderas con orientación opuesta al sensor.

Los coeficientes de determinación son altos en banda L para todos los ángulos de incidencia local en la polarización cruzada. La retro-dispersión en banda C y L de polarización cruzada manifiesta un potencial mayor para la estimación de la severidad del incendio en un entorno mediterráneo cuando el ángulo de incidencia local es tenido en cuenta. El pequeño rango dinámico observado en la banda X podría dificultar su uso en bosques afectados por incendios.

Sensitivity of X-, C- and L-band SAR backscatter to burn severity in Mediterranean pine forests

M. A. Tanase[(1)], J. de la Riva[(1)], M. Santoro[(2)], T. Le Toan[(3)], and F. Pérez-Cabello[(1)]

[(1)]Department of Geography,
University of Zaragoza,
Pedro Cerbuna 12, 50009 Zaragoza, Spain
Email: mihai@tma.ro, delariva@unizar.es, fcabello@unizar.es

[(2)]Gamma Remote Sensing AG,
Worbstr. 225, CH-3073 Gümligen, Switzerland
Email: santoro@gamma-rs.ch

[(3)]Center for the Study of the Biosphere from Space
18 av. Edouard Belin, bpi 2801, 31401 Toulouse, France
Email: Thuy.Letoan@cesbio.cnes.fr

Abstract

Synthetic aperture radar (SAR) data at X-, C- and L-band have been investigated to determine the relationship between backscatter and forest burn severity over three sites in Spain. The dependency of the SAR backscatter upon local incidence angle and environmental conditions has been analyzed. At HH and VV polarizations the backscatter increased with burn severity for X- and C-band whereas for L-band it decreased. Cross-polarized (HV) backscatter decreased with burn severity for all frequencies. The sensitivity of the co-polarized backscatter to burn severity decreased for increasing local incidence angle for all frequencies except at L-band. Determination coefficients were used to quantify the relationship between radar backscatter and burn severity for given intervals of local incidence angle. For X- and C-band co-polarized data higher determination coefficients were observed for slopes oriented towards the sensors whereas for cross-polarized data the determination coefficients were higher for slopes oriented away from the sensor. At L-band the association strength of cross-polarized data to burn severity was high for all local incidence angles. C- and L-band cross-polarized backscatter showed better potential for burn severity estimation in the Mediterranean environment when the local incidence angle is accounted for. The small dynamic range observed for X-band data could hinder its use in forests affected by fires.

Keywords*: SAR backscatter, burn severity, forest fire, mediterranean forest*

INTRODUCTION

The high number of forest fires occurring every year constitutes one of the major degradation factors of the Mediterranean ecosystems. On average, half million hectares are annually burnt in the European part of the Mediterranean basin making fires an important environmental problem. Fire occurrence alteration during the last decades closely reflects socio-economic changes in the traditional land use and lifestyle which

implied the abandonment of large areas of farmland leading to recovery of vegetation (Roxo et al. 1996) and an increased pressure from tourism activities (Pausas and Ramon 1999).

Forest fires are an important source of atmospheric aerosols and green-house gases, causal relationship between biomass burning and interannual variability of related emissions being observed (Simmonds et al. 2005). Severity indicates the way fire impacts the ecosystem and has significant effects on gas emission from burned areas (Andreae and Merlet 2001), with fire duration and intensity being the primary factors controlling the amount of released gases. The effects of fire on ecosystem are nowadays expressed by burn severity indexes defined as the degree of the environmental changes caused by fire. The composite burn index (CBI) provides a continuous scale between 0.0 (unburned) and 3.0 (highest burn severity) which summarizes the average burn condition of a forest plot. Usually, the field assessment of burn severity is carried out on a 15 m radius using a hierarchical sampling design. Each vegetation stratum is scored separately and the results are averaged for the entire plot (Key and Benson 2006).

The difficulty associated with the collection of extensive information on burn severity implies that remote sensing imagery is considered to assess the effect of fire in forests. One of the most widely employed spectral index for burn severity assessment is the normalized burn ratio (NBR) (Key and Benson 2006) used in a bi-temporal approach with pre- and post-fire datasets (dNBR). The NBR index combines reflectance of near and shortwave infrared {1} whereas dNBR uses the difference between pre- and post-fire datasets {2} to isolate burned areas and to provide a quantitative measure of change with respect to the pre-fire status, unburned areas retaining values close to zero (i.e. -100 to 100). The aforementioned equations are given as follows:

$$NBR = (R4 - R7) / (R4 + R7) \quad \{1\}$$

$$dNBR = NBRpre - fire - NBRpost - fire \{2\}$$

where: R is per pixel reflectance for Landsat TM bands.

With increasing severity dNBR values increase reaching the upper limit (i.e. 1000 to 1300) for extremely burned areas. Generally, empirical modeling is used to correlate dNBR to CBI field estimates of burn severity. The method is routinely used for burn severity mapping and provides accurate results in most of the environments, from boreal to mediterranean forests (Cocke et al. 2005; Miller et al. 2009; Santis and Chuvieco 2009; Wagtendonk et al. 2004). Nevertheless, reflectance based indices often fail to produce accurate results (Allen and Sorbel 2008; Hoy et al. 2008; Murphy et al. 2008). These indices use mostly indirect properties of the burned areas such as: near infrared reflectance decrease due to loss of healthy green vegetation; short-wave infrared reflectance increase due to less moisture content of vegetation and soils, increased substrate exposure and the presence of charred fuels. These properties are stable for unburned or highly burned areas but become inconsistent for intermediate severity levels where multiple effects combine. Some studies found it problematic to discriminate intermediate severity burns (Chuvieco et al. 2006). Reflectance based indices are also sensitive to plant phenology and solar elevation, so that monitoring severity trends over time or across regions can be subject to errors (Verbyla et al. 2008).

For studying fire effects in forested areas complementary information might be provided by SAR data since the backscattered signal contains information related to the

vegetation structure and biomass (Ferrazzoli et al. 1997). For wavelengths of the order of few centimeters (X- and C- bands) scattering from the upper part of the tree crown is the predominant component of forest backscatter. The contribution of the understory and the forest floor is influenced primarily by the canopy architecture. For mediterranean species the first 30 cm of the crown contain most of the foliage biomass. In addition, relative water content of the leaves is higher than of woody parts in the upper part of the crown (Sternberg and Shoshany 2001). The high density of leaves and their relative high water content may therefore prevent the penetration of the high frequency waves to the lower layers of woody parts and soil (Svoray and Shoshany 2003) which may have high backscattering potential as suggested by (Svoray et al. 2001). Lower frequency L-band waves (23 cm) penetrate to a higher extent the canopy, interacting more with the large branches, tree stems or the forest floor (Le Toan et al. 1992). Removal of leaves and branches by fire induces a decrease of backscatter from the canopy. Fire also increases soil exposure which could be used to estimate burn severity when using co-polarized channels. However, the destruction of the vegetation canopy makes the radar measurements sensitive to the state of the underlying ground (Saich et al. 2001) which results in backscatter dependency not only on the forest parameters but also on the soil moisture and roughness.

The impact of fire on the backscattering coefficient was found to cause ambiguous effects. Strong backscatter decrease was found for burned tropical forests at C-band VV polarization under dry weather conditions due to the decreased volume scattering and increased heat flux which led to a dryer ground (Ruecker and Siegert 2000; Siegert et al. 1999). After rainfall the backscatter increased, discrimination from the unburned surrounding forests being difficult (Siegert and Ruecker 2000). For temperate forests lower backscatter was found in fire affected areas (Rignot et al. 1999) at C- and L-band (HV polarization) than for the adjacent unburned forest whereas for burned Australian woodlands and open forests L-band backscatter increased for co-polarized and decreased for cross-polarized waves (Menges et al. 2004). In boreal forests higher backscatter values than for the adjacent unburned areas were observed at C-band VV polarization when soil moisture was high due to poor soil drainage (Bourgeau-Chavez et al. 1997; Bourgeau-Chavez et al. 2002; Huang and Siegert 2006; Kasischke et al. 1994) whereas lower backscatter was observed for sites with better drainage conditions (Kasischke et al. 1994). Finally, for mediterranean forests (Gimeno et al. 2004) found that post-fire C-band co-polarized backscattering coefficient increased independently of the accumulated precipitation index. However, the scenes characterized by wet conditions at acquisition presented higher backscatter levels than those acquired under dry conditions. Changes in the backscatter level appear to be strongly related to changes in soil moisture (Grover et al. 1999) data acquired after rainfall being less suitable for classification (Ranson and Sun 2000; Saatchi et al. 1997) or forest biophysical parameters retrieval (Harrell et al. 1995). However, some fire related studied reported increased differentiation after rainfall for mediterranean burn scars (Gimeno and San-Miguel-Ayanz 2004). All reported studies focused primarily on fire detection and mapping using SAR data. The potential of radar for estimating burn severity in forest has been reported in (Bourgeau-Chavez et al. 1994; Kasischke et al. 1994; Rignot et al. 1999). However, no extensive study on this topic is available in the literature according to our knowledge.

A major issue when using SAR images for thematic mapping and retrieval of biophysical parameters is represented by the local topography. Its influence on the backscattering coefficient is more pronounced for co-polarized beams and longer wavelengths, small tilt of terrain changing the scattering mechanism (van Zyl 1993). At

low incidence angles the proportion of surface scattering to the total backscatter is larger compared to volume scattering (Luckman 1998). Even for mild topography the backscattering coefficient is still altered and the radar signal needs to be compensated (Holecz et al. 1995). Topography also influences the backscattering coefficient from burned areas, sensor facing slopes appearing brighter than slopes oriented away from the sensor. Small local incidence angles were required for discriminating burned areas in a hilly Mediterranean region using co-polarized C-band data (Gimeno and San-Miguel-Ayanz 2004).

This work builds upon a first investigation on the signatures of fire affected areas using X-band backscatter data (Tanase et al. 2010). The promising results on burn severity estimation using a dual-polarized TerraSAR-X backscatter dataset suggested looking at lower frequencies, which can be assumed to be more sensitive to fire parameters because of the higher sensitivity of the backscattered signal to forest structural properties. In the following sections, the relationship between SAR backscatter acquired at C- and L-band is considered. For completeness, X-band data is also considered. Scope of this paper is to provide a comprehensive overview on burn severity evaluation and estimation from SAR backscatter for typical mediterranean forests. The specific objectives of the study were as follows:

1. evaluate the backscatter response in relation to burn severity for X-, C- and L-band data;
2. assess the role of the local topography and environmental conditions at acquisition on the backscatter coefficient;
3. infer the prediction power of the backscatter for burn severity estimation.

STUDY AREA

Three burn scars located in the central Ebro valley near, Zaragoza, Spain were the focus of this study. The area is characterized by Mediterranean climate and moderate topography elevation ranging from 500 to 750 m above sea level on slopes below 30°. The dominant land cover is forest interspersed with agricultural fields. Forests extend on approximately 22,000 hectares and are mainly formed by *Pinus halepensis* Mill. *Quercus coccifera* represented the main understory species. The structure of the forest was homogeneous more than 85% of the trees being in the codominant stratum. About 50% of the trees are 35 to 55 years old, 75% of them being less than 65 years old. The average number of trees per hectare is 440 with a maximum of 2900 trees/ha and a minimum of 20 trees/ha in open areas. Forest average height is around 6.5 m and the average biomass around 45 tons/ha. Old stands reach heights of 12-13 m and 90 tons/ha.

At the first site (Zuera95) approximately 3,100 ha of forests burned between 23rd and 25th of June 1995 after a spark from a farming tractor ignited the vegetation next to the pine forest. In the adjacent second site (Zuera08) the fire ignited after a traffic accident. Around 2,200 ha of forests burned between 6th and 16th of August 2008. A third fire (Jaulin09) located approximately 60 km south, ignited due to a lightning storm on 21st of July 2009 and burned approximately 1,800 hectares. Fig. 1 gives an overview of the area affected by the fires. Burn severity expressed by means of dNBR was overlaid on the pre-fire Landsat TM image using the intervals proposed in (Key and Benson 2006). Most of the forest was affected by high burn severity. Moderate and low severity areas are located mostly close to the perimeter of the forest were firefighters were able to control the fire spread.

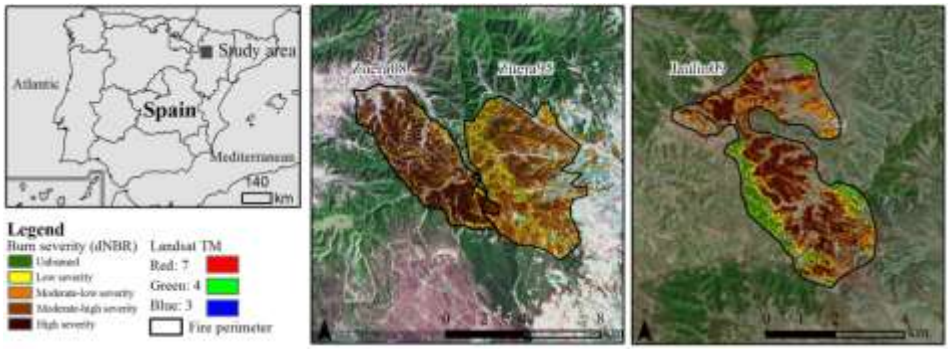

Fig. 1 The study area and the forest fire sites. The burn severity expressed by dNBR index was overlaid on a false color composite of pre-fire Landsat TM images (2008.07.21 and 2009.06.22).

DATA SETS

Satellite observations

The SAR images available to this study were acquired by the European Remote Sensing (ERS) SAR, the Environmental Satellite (Envisat) Advanced SAR (ASAR), the Advanced Land Observing Satellite (ALOS) Phased Array type L-band SAR (PALSAR) and the TerraSAR-X (TSX) SAR. In Table 1 the main characteristics of the radar sensors and processing parameters are provided. The datasets were delivered as single look complex (SLC) or precision (PRI) images. For each site a pair of Landsat TM images was used to estimate burn severity levels by means of dNBR index.

For the oldest fire scar (Zuera95) only ERS SAR 1/2 images were available (Table 2). To study the consequence of rainfall on the backscatter coefficient ERS SAR images (23° look angle) were ordered for dates with and without precipitation. The matching Landsat TM scenes were acquired on March, 28 (pre-fire) and August, 3 (post-fire) 1995. Information on the geometric correction, calibration, atmospheric correction and topographic normalization of the Landsat scenes is given in (Vicente-Serrano et al. 2008).

For the Zuera08 site images from all satellites were available allowing the assessment of the backscatter coefficient response to burn severity at different SAR frequencies and polarizations (Table 2). Dual-polarization TerraSAR-X dataset was

Table 1 SAR data characteristics and processing parameters.

Satellite/Parameter	PALSAR	PALSAR	ERS 1 / 2	ASAR	ASAR	ASAR	TSX
Band [wavelength cm]	L- [23.6]	L- [23.6]	C- [5.7]	C- [5.7]	C- [5.7]	C- [5.7]	X- [3.1]
Pass	ascending	ascending	descending	descending	ascending	descending	descending
Acquisition mode	PLR	FBD	-	IM	IM	AP	SM
Incidence angle	26°	39°	23°	23º	23º	23º	26º/40°
Polarization	HH,VV,HV,VH	HH,HV	VV	HH	VV	HH,HV	HH,HV
Range pixel spacing (m)	9.4	9.4	12.5	7.8	12.5	12.5	0.9
Azimuth pixel spacing (m)	3.8	3.2	12.5	4.0	12.5	12.5	2.2
Multi-look factor (range/azimuth)	1/7	2/10	2 / 2	1 / 5	2 / 2	2 /2	17/10
Data format	SLC	SLC	PRI	SLC	PRI	PRI	SLC
Pixel spacing (map geometry)	25 m	25 m	25 m	25 m	25 m	25 m	25 m
Equivalent number of looks	11	22	12	4	12	6	50/55
Geolocation error	~2 m	~ 2 m	~ 2.5 m	~ 2.5 m	~ 2.5 m	~ 2.5 m	~ 0.75 m
Projection / Ellipsoid	Universal Transverse Mercator, Zone 30 / International 1924						
Datum	European 1950						

Table 2 SAR acquisitions and climate data (AcPp in mm and Tmax. and Tmin. in °C).

Sensor and polarization	Mode	Date	AcPp	Tmax	Tmin	Sensor and polarization	Mode	Date	AcPp	Tmax	Tmin
ERS-1 VV[a]	IM	1992.08.31[1]	0	24	13	ASAR VV[b]	IM	2008.09.12	1.6	18	11
ERS-1 VV[a]	IM	1995.07.05	0	26	11	ASAR HH[b]	IM	2009.01.08	0.5	0	-6
ERS-2 VV[a]	IM	1995.08.10	6.5*	29	16	ASAR HH[b]	IM	2009.02.12	0.5*	10	4
ERS-2 VV[a]	IM	1995.09.14	0	23	9	ASAR HH,HV[b]	AP	2009.03.19	0	20	-1
ERS-2 VV[a]	IM	2008.06.12[1]	-	-	-	ASAR HH, HV[c]	AP	2009.09.29	5*	22	11
ERS-2 VV[a]	IM	2008.08.21	0	30	15	TSX HH,HV[b]	SM	2008.11.16	0	14	-2
ERS-1 VV[a]	IM	1995.12.14	0	4	-4	TSX HH,HV[b]	SM	2008.12.19	0	11	4
ERS-2 VVv	IM	1995.12.15	2.7*	0	-5	TSX HH,HV[b]	SM	2008.12.24[2]	0	-3	-6
ERS-2 VV[a]	IM	1996.01.19	1*	10	-2	TSX HH,HV[b]	SM	2009.01.21	2.3	7	-3
ERS-1 VV[a]	IM	1996.03.28	0	15	5	TSX HH,HV[b]	SM	2009.02.12	0.5*	10	4
ERS-2 VV[a]	IM	1996.03.29	0	17	6	TSX HH,HV[b]	SM	2009.02.23	0	12	5
ERS-1 VV[a]	IM	1995.11.28	0	12	-4	TSX HH,HV[b]	SM	2009.03.06	11.8*	9	1
ERS-1 VV[a]	IM	1996.01.02	4.5	11	4	TSX HH, HV[c]	SM	2009.09.20	5	20	8
ERS-2 VV[a]	IM	1996.01.03	1.5	11	0	PALSAR[b]	PLR	2009.04.28	3.5*	18	10
ASAR VV[b]	IM	2008.07.04[1]	0	31	8	PALSAR[c]	FBD	2009.10.05[3]	0	28	10

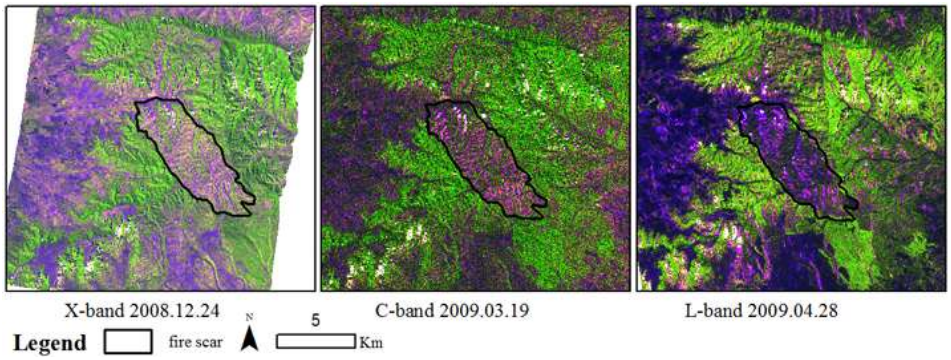

Fig. 2 Zuera08 fire scar as revealed by TerraSAR-X, Envisat ASAR and ALOS PALSAR (red: HH backscatter, green: HV backscatter, blue: HH/HV backscatter ratio).

acquired in dual-polarization strip map (SM) mode. Envisat ASAR images were acquired in the single-polarization imaging mode (IM) and in the dual-polarization alternating polarization (AP) mode. The ALOS PALSAR image was acquired in polarimetric (PLR) mode. TerraSAR-X data were available for two nominal incidence angles (i.e. 25° and 40°) whereas ERS SAR, Envisat ASAR and ALOS PALSAR data were available only for 22° to 26° nominal incidence angles (Table 2). The Landsat TM images for the Zuera08 site were acquired on July 21, 2008 (pre-fire) and August 22, 2008 (post-fire). Subsets of the Landsat scenes were calibrated, atmospherically corrected and orthorectified using a linear polynomial model and incorporating information of the local topography. Detailed information regarding the processing of the Landsat TM scenes is given in (Tanase et al. 2010). Fig. 2 shows the burned area using a composite of backscatter (HH and HV) and their ratio at each SAR frequency. The fire scar can be easily distinguished from the surrounding forests. The green areas correspond to high cross-polarized (HV) backscatter, which is characteristic for dense vegetation. The blue/purple areas correspond to high co-polarized (HH) and little cross-polarized backscatter typically found in areas with no or low vegetation. The fire scar was characterized at all frequencies by increased co-polarized and reduced cross-polarized backscatter when compared to adjacent unburned forest. Inside the fire perimeter zones affected by lower burn severity can be distinguished especially towards the borders.

One image at each frequency was available for the Jaulin09 site. The images were acquired at different nominal incidence angles. The TerraSAR-X image was acquired at 40°. The Envisat ASAR image was acquired at 23° whereas ALOS PALSAR fine beam dual polarization (FBD) image was acquired at 39°. The Landsat TM images were acquired on 2009.06.22 (pre-fire) and 2009.09.26 (post-fire) and were processed using the same method as for the Zuera08 site.

SAR data were absolutely calibrated using the calibration factors provided by the processing facilities and multi-looked to obtain the desired 25 m pixel size. To express the speckle reduction achieved after multi-looking, the number of statistically independent looks was estimated by means of the equivalent number of looks (ENL) (Oliver and Quegan 1998) using forested areas not affected by fires (Table 1). All SAR images were geocoded to Universal Transverse Mercator (UTM) projection using a digital elevation model (DEM) with 20 m pixel spacing which was resampled to 25 m for the analysis. Geocoding was based on a lookup table describing the transformation between the radar and the map geometry (Wegmüller et al. 1999; Wegmüller et al. 2002) which was generated based on the DEM and the orbital information of the SAR sensors. A refinement step was applied to correct for the possible inaccuracies of the orbital state vectors. The offsets between SAR image and a reference SAR image simulated from the DEM were estimated using a cross-correlation algorithm. A simple linear model was derived to improve the original lookup table. To correct for the radiometric distortions introduced by the rough topography normalization for the varying incidence angle from near to far range and the effective pixel area was applied (Ulander 1996). As a result images in gamma nought (γ°) format that only includes variations of the scattering properties of a target due to the local orientation were obtained.

In situ measurements of burn severity and ancillary datasets

CBI plots were established in high-severity, moderate-severity and low-severity areas inside Zuera08 (123 plots) and Jaulin09 (45 plots) fire perimeters. Burn severity was evaluated, as described in (Key and Benson 2004), using the magnitude of environmental change at each site with respect to the presumed pre-fire state. Detailed information on CBI plots assessment together with photos illustrating the main burn severity levels at Zuera08 site are given in (Tanase et al. 2010). To aid the interpretation, meteorological data collected from nearby meteorological stations were provided by the Spanish national meteorological agency (AEMET). The daily maximum and minimum temperature and precipitation are presented in Table 2. For the images acquired after mid November 2008 precipitation data were also obtained from an automatic rain gauge (ARG) installed roughly at the center of the Zuera08 fire perimeter. Since the burned sites were located at different altitudes compared to the meteorological stations the temperatures were adjusted with the environmental lapse rate (i.e. -2° C / 300 m). Accumulated precipitation (AcPp) was computed taking into account the last four days before acquisition.

Spectral estimates of burn severity

The dataset of reference measurements on burn severity consisted of a set of sample plots measured in the field (CBI plots) as well as pseudo-plots randomly generated using as basis the dNBR images. Although an extensive field campaign to estimate burn severity was undertaken at Zuera08 and Jaulin09 sites, it turned out that the sample population was not sufficiently dense to allow the characterization of the SAR backscatter signatures. The consistency between field and remotely sensed

estimates of severity was high for Zuera08 and for Jaulin09 sites (R^2 = 0.81 and R^2 = 0.83, $p<0.05$) supporting the decision of using dNBR as a measure of burn severity. Considering the availability of a dNBR image for each fire and the strong correlation between CBI and dNBR, pseudo-plots of burn severity were generated by averaging pixels of similar dNBR and identical local incidence angle. Similar dNBR values were obtained by reclassifying the continuous dNBR interval into twenty-four dNBR classes each being 50 units wide. Since Zuera08 and Zuera95 test sites were contiguous, and forest structure and tree species were the same, we considered appropriate to generalize the use of dNBR despite the lack of burn severity field estimates for the 1995 fire. In the study area dNBR ranged between -150 and 1050. Values up to 100 represent unburned forest whereas larger values represent increased burn severity. To avoid bias related to size only pseudo-plots containing a large number of pixels were considered. The fixed number of pixels to be averaged implied a trade-off between the within plot variability (smaller variance for higher number of pixels per plot) and the number of pseudo-plots available for each severity level (less plots were available when higher number of pixels/plot were averaged). In the first investigation on burn severity assessment using a TerraSAR-X image nine pixel per pseudo-plot (~ 0.5 ha) appeared to be optimal for the selected spatial resolution (25 m) of the geocoded images (Tanase et al. 2009). For consistency reasons this criterion has been applied in this study as well. From the generated pseudo-plots nine hundred were randomly selected for the statistical analysis.

METHODS

To understand the relationship between forest burn severity and backscatter coefficient CBI plots and dNBR base pseudo-plots were compared for Zuera08 fire. The investigation was mainly focused on Zuera08 site for which co- and cross-polarized data acquired with similar incidence angle were available at all frequencies. The Jaulin09 site was analyzed in order to confirm the trends observed at the Zuera08 site whereas the Zuera95 site was considered to evaluate the effect of different environmental conditions on the relationship between the backscatter coefficient at C-band and dNBR thanks to the large dataset of historical ERS-1/2 images available over the site (Table 2).

Descriptive statistics were applied to analyze and compare backscatter as a function of burn severity. The potential of backscatter coefficient for burn severity estimation was assessed at both plot and pseudo-plot level using inferential statistics. To minimize the effect of topography on the backscatter coefficient the analyses were carried out by 5º groups of local incidence angle. This interval provided optimal sampling rate for the study of the local incidence angle effects in case of TerraSAR-X data (Tanase et al. 2010) so that it was used in this study as well. A higher sampling rate would have increased the data noise whereas at a lower sampling rate the topography effects would have been less evident. The homogeneity of the forest and the large extent of high burn severity allowed the evaluation of the influence of local incidence angle and weather condition on the backscatter.

RESULTS AND DISCUSSION

Backscatter properties of burned areas

For each SAR system backscatter as a function of burn severity is presented in Fig. 3 to Fig. 6 for slopes oriented toward the sensor (11-15°), flat or near flat areas (21-25°) and slopes oriented away from the sensor (36-40°). The datasets were acquired at similar

look angle, around 25°. ERS SAR 1/2 VV polarized data are plotted for the Zuera95 site whereas for the Zuera08 site HH and HV polarized TerraSAR-X, Envisat ASAR and ALOS PALSAR data are presented. To evaluate the relationship between field- and remotely-sensed estimates of burn severity the CBI plots were also included when available. The datasets shown in Figs. 3 to 6 were characterized by the

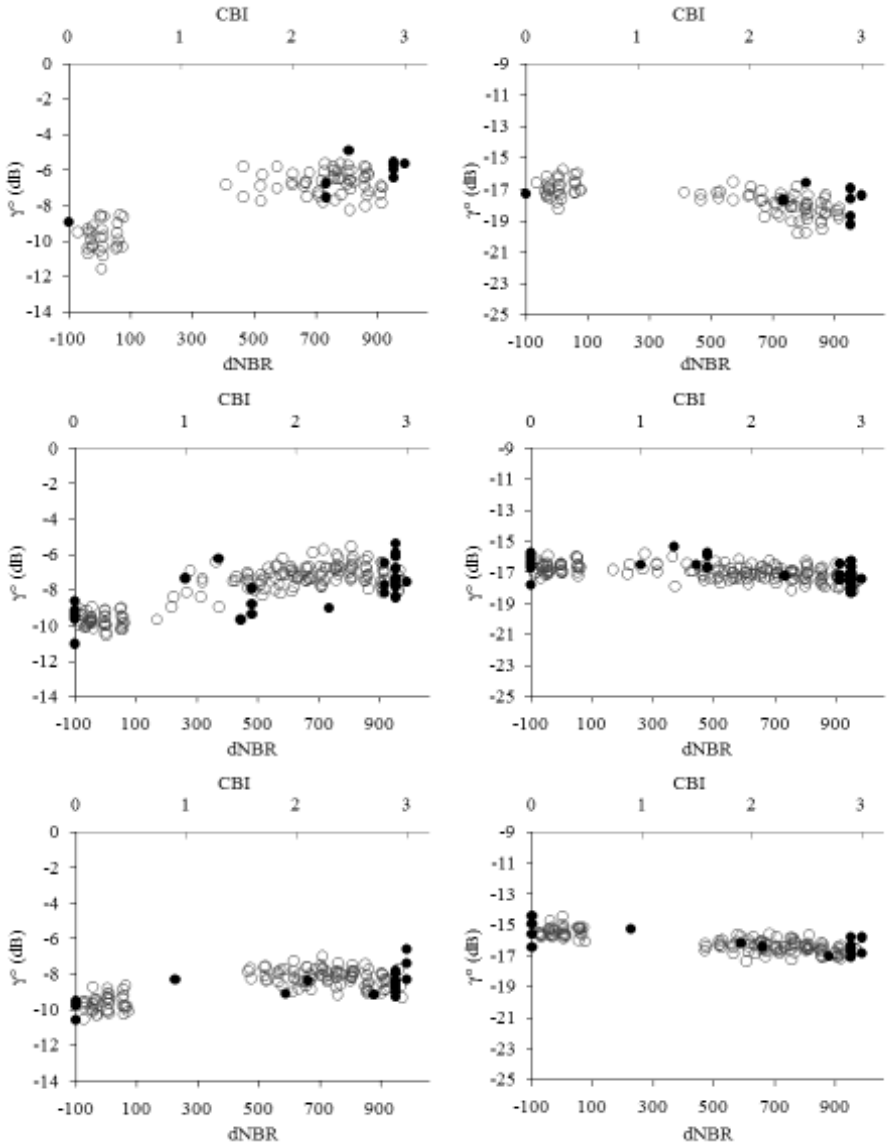

Fig. 3 Backscatter (γ^0) with respect to burn severity for X-band HH (left) and HV (right) for the Zuera08 site (TerraSAR-X, 2008.12.24) for slopes oriented towards the sensor (top), flat areas (center) and slopes oriented away from the sensor (bottom). Circles refer to dNBR measurements. Filled circles refer to CBI measurements.

largest difference of backscatter between unburned and burned forest. Co-polarized ERS SAR and Envisat ASAR images were acquired under wet conditions. Co- and cross-polarized TerraSAR-X and cross-polarized Envisat ASAR images were acquired under dry environmental conditions. The only image available at L-band for the Zuera08 site was acquired under wet conditions. A detailed analysis of weather influence on backscatter coefficient is reported further on in this section.

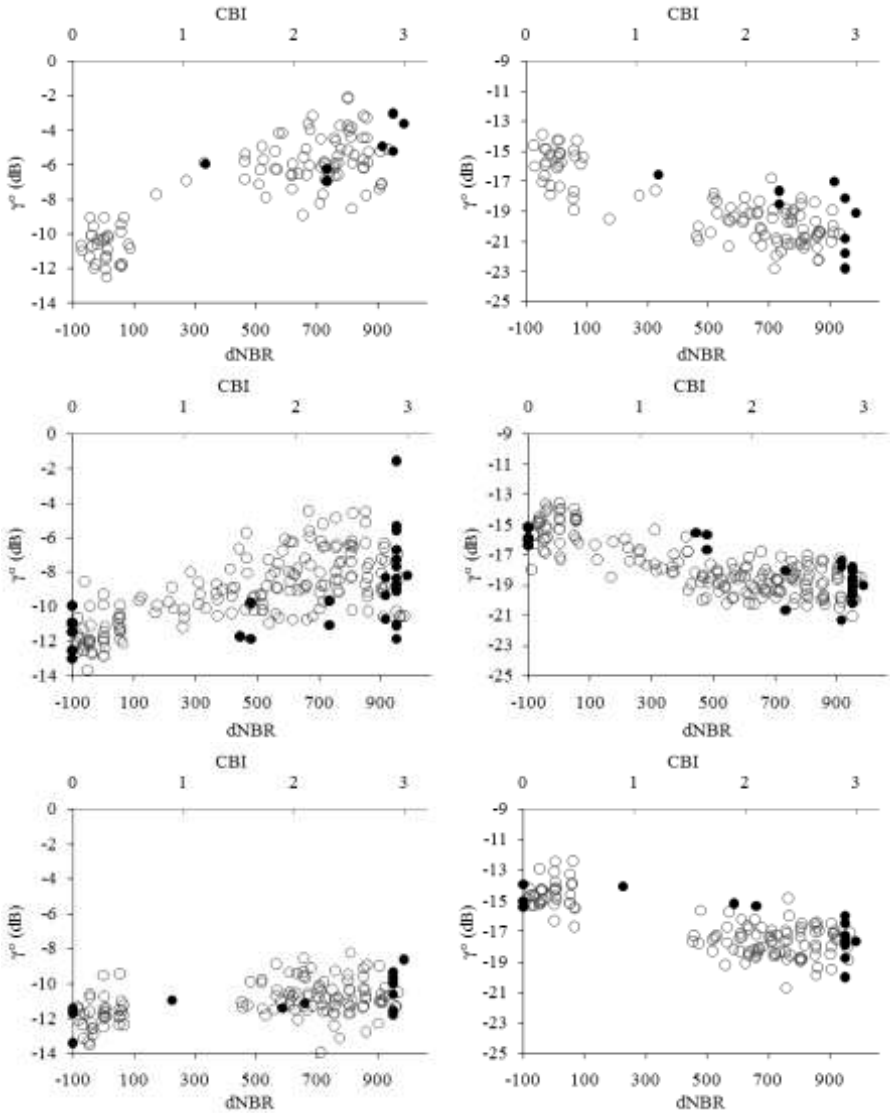

Fig. 4 Scatter plots of C-band HH (left) and HV (right) backscatter with respect to burn severity (dNBR) for the Zuear08 site (Envisat ASAR 2009.01.08 - HH and 2009.03.19 - HV images). Top slopes oriented towards sensor, center flat areas, bottom slopes oriented away from the sensor. Circles refer to dNBR measurements. Filled circles refer to CBI measurements.

Figs. 3 and 4 showed that at X- and C-band the HH co-polarized backscatter coefficient increased with burn severity at the Zuera08 site. The same trend was observed for C-band VV polarization (ERS SAR) at the Zuera95 site (Fig. 5). The tendency was found mainly for slopes facing the sensor. For slopes pointing away from the sensor the backscatter coefficient was less sensitive to changes in burn severity. Increased backscatter for the burned areas could be explained as a consequence of the weaker attenuation in the canopy due to the consumption of the needles by the fire, the subsequent exposure of the small twigs and branches with higher backscattering potential (Svoray et al. 2001) and the increased backscatter from the ground. Co-polarized X- and C-band signal saturated at medium to high severity levels. The saturation level depended on the local incidence angle. It was higher for steeper slopes oriented toward the sensor due to the larger proportion of backscatter from the forest floor. Contrarily to short wavelengths L-band HH polarized backscatter decreased with the increase of burn severity especially for slopes pointing away from the sensor (Fig. 6). At L-band the radar wave is less affected by absorption and attenuation especially in low biomass forests. Thus, the scattering component from the ground does not change significantly from unburned to burned areas leaving the vegetation component as main factor determining the backscatter trend. Hence, the total backscatter is mostly a function of the crown backscatter component which decreased with increasing burn severity. The weak sensitivity of the L-band HH backscatter to burn severity for slopes facing the sensor was explained as a consequence of increased moisture due to rainfall at the time of image acquisition. The increase of backscatter due to higher soil moisture masked the effect of the burn severity for low incidence angles where the ground component plays a major role in the total backscatter.

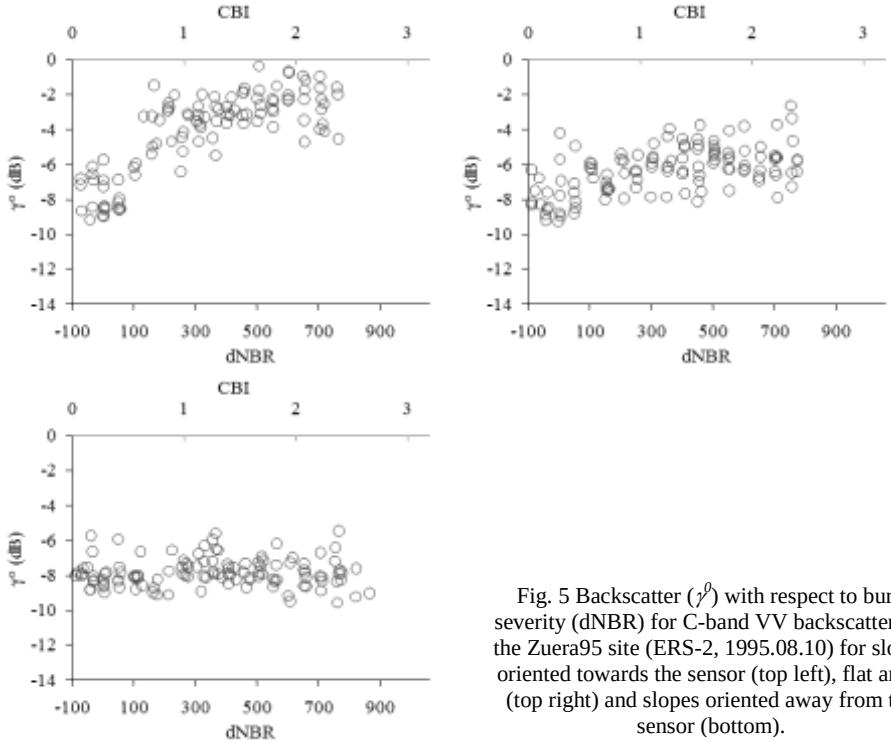

Fig. 5 Backscatter (γ^0) with respect to burn severity (dNBR) for C-band VV backscatter for the Zuera95 site (ERS-2, 1995.08.10) for slopes oriented towards the sensor (top left), flat areas (top right) and slopes oriented away from the sensor (bottom).

The cross-polarized backscatter coefficient, which is sensitive primarily to volume scattering, decreased with the increase of burn severity at all frequencies (Figs. 3, 4 and 6). This is explained by the smaller number of scatterers within the canopy for higher burn severity. The relatively low levels of biomass (around 45 tons/ha) resulted in a consistent trend at all local incidence angles and no evident saturation of the signal was recorded even for X-band data.

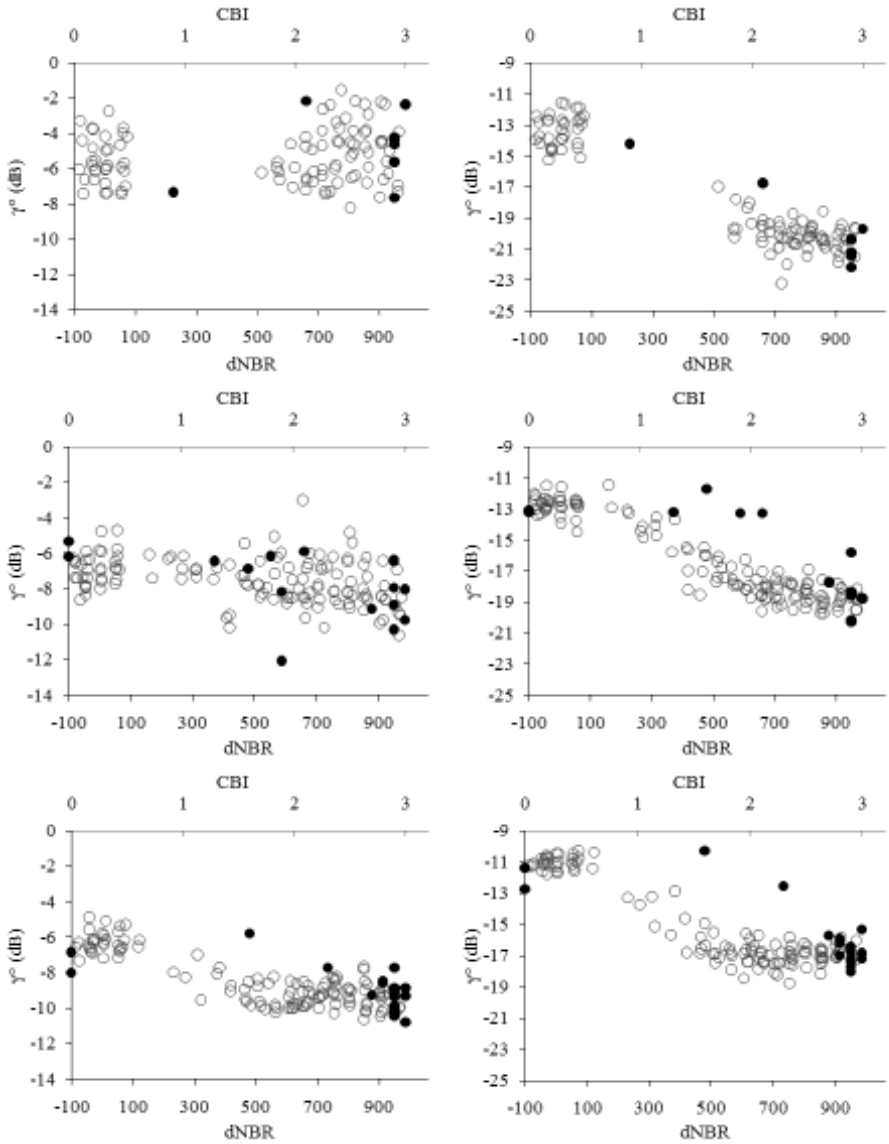

Fig. 6 Backscatter (γ^0) with respect to burn severity for L-band HH (left) and HV (right) for the Zuera08 site (ALOS PALSAR, 2009.04.28) for slopes oriented towards the sensor (top), flat areas (center) and slopes oriented away from the sensor (bottom). Circles refer to dNBR measurements. Filled circles refer to CBI measurements.

The backscatter of the CBI plots was similar to the backscatter measured at pseudo-plot level for co-polarized waves (Figs. 3, 4 and 6). CBI field protocol takes into account the consumption of the attenuation layer (i.e. canopy and understory layer) thus providing indirect estimates of the increased soil exposure which explains the relatively high association to burn severity for slopes oriented to the sensor where the scattering component from the forest floor is significant. For cross-polarized waves the backscatter correspondence between CBI plots and dNBR pseudo-plots was similar only for unburned and highly burned areas. At intermediate severity levels the backscatter coefficient of the CBI plots was close to the levels registered for the unburned forest. The CBI protocol does not take into account structural modification of the crown beyond the loss of foliage. C- and X-band retained partly their sensitivity for low and intermediate CBI levels being more sensitive to small sized crown elements. On the other hand, at L-band the sensitivity to low and intermediate CBI levels decreased since no information of larger scatterers consumption was considered during the field assessment.

The trends identified at the Zuera08 site were confirmed at the Jaulin09 site. Fig. 7 presents the backscatter coefficient as a function of burn severity for flat areas at HH and HV polarization. As for the Zuera08 site, high frequency co-polarized backscatter (X- and C-band) increased whereas cross-polarized backscatter decreased with burn severity. The same decreasing trend was observed for co-polarized L-band backscatter. The similar trends suggested that radar response as a function of burn severity does not

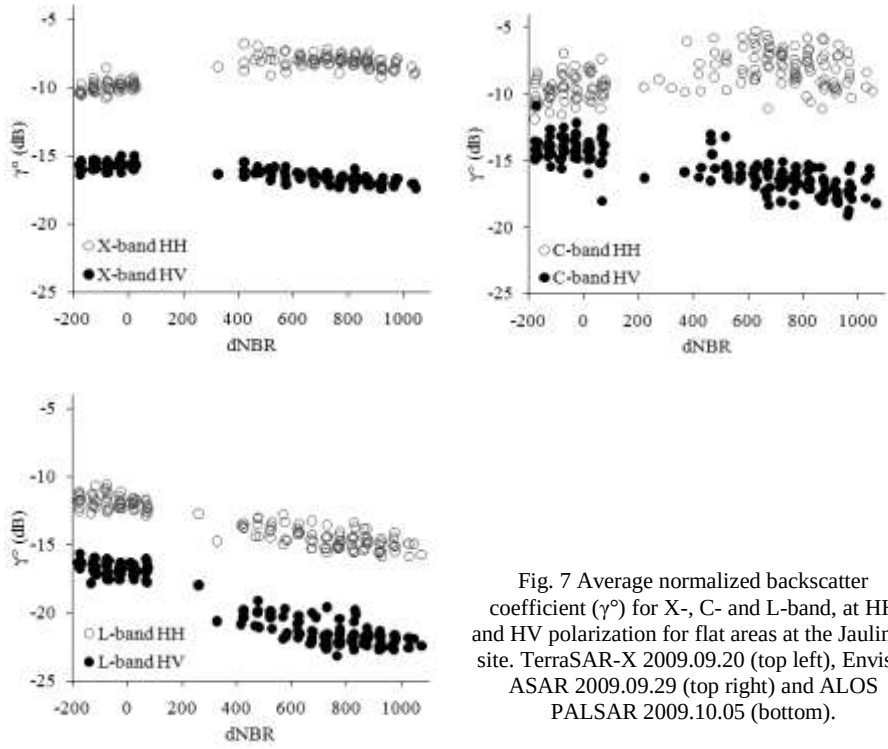

Fig. 7 Average normalized backscatter coefficient (γ°) for X-, C- and L-band, at HH and HV polarization for flat areas at the Jaulin09 site. TerraSAR-X 2009.09.20 (top left), Envisat ASAR 2009.09.29 (top right) and ALOS PALSAR 2009.10.05 (bottom).

depend on the local burn conditions. In addition, the larger nominal incidence angle in the case of L-band data (see Table 2) did not have a significant effect on the backscatter trends. Although, high incidence angle could cause changes in backscatter levels the sensitivity to burn severity does not seem to be affected confirming the initial results obtained with a dual-polarized X-band dataset (Tanase et al. 2009).

Further insight on the backscatter sensitivity to burn severity is presented in Fig. 8 which shows backscatter variation (dynamic range) from unburned to burned forest. The dynamic range was computed by taking the difference between average backscatter of adjacent unburned forest and of the burned forest. The definition of burned forest depended on the trend of the backscatter with respect to dNBR. For co-polarized data we have taken into account the saturation of the signal which depended on frequency, acquisition conditions (dry vs. wet) and the local incidence angle. Co-polarized X- and C-band saturated between 500 and 800 dNBR. Cross-polarized data did not present evident saturation and therefore the dynamic range was computed with respect to the highest severity levels recorded (950-1050 dNBR). Data acquired under wet (AcPp>0) and dry conditions (AcPp=0) are shown where available. The dynamic range for X- and C-band co-polarized backscatter decreased with the increasing local incidence angle from approximately 4 respectively 6 dB to about 1 dB which resulted in decreased sensitivity to burn severity for slopes oriented away from the sensor. The dynamic range of cross-polarized backscatter was relatively stable for all local incidence angles and decreased with the increase of SAR frequency from approximately 6 dB at L-band to around 1 dB at X-band.

The large number of ERS SAR scenes available for the Zuera95 site allowed investigating in more detail the influence of precipitation on the C-band backscatter coefficient at VV polarization, in summer and winter seasons. Higher moisture enhanced the co-polarized backscatter from the forest floor, thus increasing the dynamic range from unburned to highly burned areas at C- and X-band (Fig. 8). During summer, soil

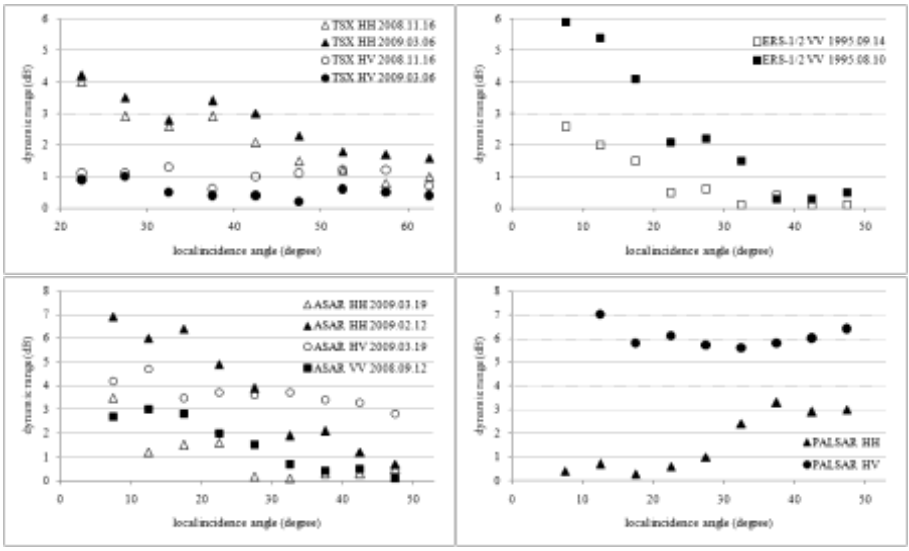

Fig. 8 Dynamic range of backscatter with respect to local incidence angle. The filled markers refer to data acquired under wet conditions.

and vegetation moisture is low due to the sporadic rainfall and the high evapo-transpiration potential in the Mediterranean basin. After rainfall, soil and vegetation moisture increased which implied an increase of the backscatter coefficient. However, the increase of backscatter from unburned forest was lower (around 1 dB) than the increase for burned area (up to 6 dB depending on the local incidence angle). This explains the larger dynamic range after rainfall for acquisitions recorded during summer season. In winter, the moisture of soil and vegetation is relatively high due to the frequent rains and low evapo-transpiration. After rainfall the change of soil and vegetation water content is lower than in summer explaining the smaller variation of dynamic range from dry to wet conditions during winter season (ERS SAR 1/2 data, Fig. 8). The larger dynamic range in case of co-polarized data was observed at low local incidence angles where the contribution to the total backscatter of the ground component is largest.

To understand whether the dependence of the dynamic range on local incidence angle is related to variations of the backscatter in unburned or burned forest, in Fig. 9 mean values of the SAR backscatter are reported with respect to the local incidence angle for unburned (i.e. dNBR<100) and highly burned (i.e. dNBR ≥ 600) pseudo-plots. For increasing local incidence angle decreasing backscatter trends were registered for co-polarized waves confirming the sensitivity to ground scattering especially at steep viewing geometries. The increased backscatter observed at the largest incidence angles for X- and C-band could be a consequence of larger vegetation contribution to the total forest backscatter (Tanase et al. 2010). The decrease of the contribution from the forest floor is smaller compared to the increase of the vegetation scattering component, thus explaining the increase of the total backscatter when compared to steeper incidence angles. In unburned areas the influence of the local incidence angle was lower since the backscatter coefficient is less dependent on the ground component due to the two-way

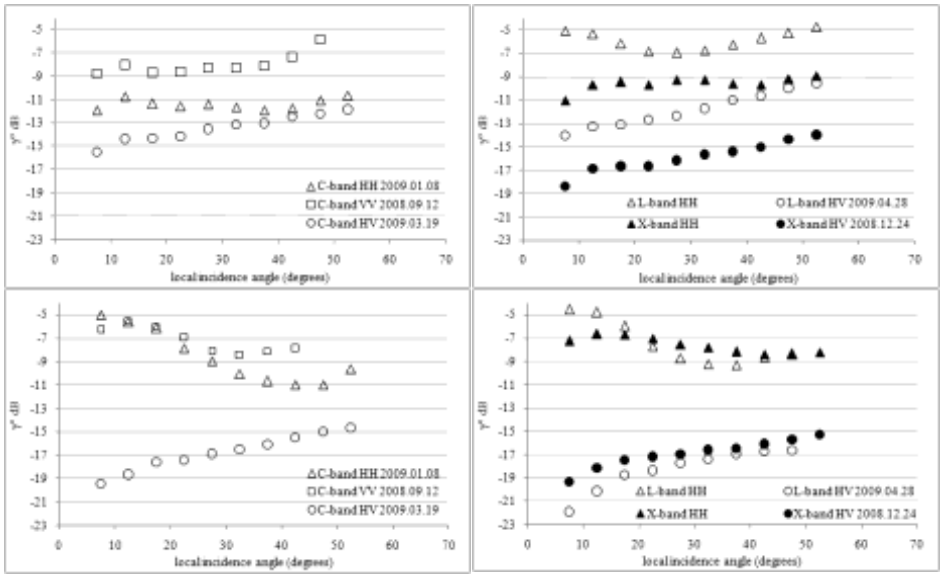

Fig. 9 Average normalized backscatter coefficient (γ°) with respect to local incidence angle for unburned (top) and highly burned pseudo-plots (bottom).

vegetation attenuation. A slight decrease of the co-polarized backscatter was observed for the flat areas with respect to the slopes facing the sensor. Cross-polarized backscatter coefficient increased with increasing local incidence angle for all SAR frequencies (unburned and burned forests) due to the longer path traveled by the radar waves through the vegetation layer.

Backscatter for burn severity evaluation

To infer the utility of the backscatter for burn severity estimation, linear regression determination coefficients (R^2) expressing the proportion of burn severity variance predicted by SAR backscatter and the standard error are presented in Table 3 and Table 4 for each sensor and polarization. A linear relation might not always represent the best fit of the data. However, this form was chosen due to the advantage of using multiple independent variables for burn severity prediction. Thus the association strenght between backscatter and burn severity could be directly compared when using one or two polarizations. For multiple regression the beta standardized regression coefficients (Beta°) have been included in Table 3 and Table 4 for C- and L-band whereas for

Table 3 Determination coefficients explaining the agreement between burn severity expressed as dNBR and C-band backscatter.

Sensor	C-Band ERS-1/2				C-band ASAR									
Polarization	VV		VV		HH		HH		HV		HH&HV			
Scene date	1995.07.05		1995.08.10		2009.03.19		2009.01.08		2009.03.19		2009.01.08 HH & 2009.03.19 HV			
	R^2	Std. err.	R^2	Std. err.	R^2	Std. err.	R^2	Std. err.	R^2	Std. err.	R^2	Std. err.	Beta° HH	Beta° HV
all pseudo-plots														
	0.020	261.7	0.127	247.0	0.013	344.5	0.172	327.9	0.493	256.6	0.542	252.1	0.149	-0.640
pseudo-plots grouped by local incidence angle														
6-10	0.442	201.6	0.677	153.2	0.466	299.4	0.768	197.1	0.779	192.5	0.894	135.2	0.491	-0.528
10-15	0.246	214.8	0.556	164.8	0.117	334.0	0.555	234.6	0.660	207.2	0.782	167.1	0.434	-0.554
16-20	0.128	223.0	0.505	168.0	0.195	316.9	0.449	257.6	0.592	225.7	0.760	173.7	0.442	-0.606
21-25	0.005	259.6	0.248	225.7	0.053	3339	0.354	269.4	0.621	211.2	0.684	193.5	0.280	-0.664
26-30	0.004	266.5	0.162	244.5	0.008	338.0	0.198	303.2	0.481	244.6	0.542	230.5	0.258	-0.623
31-35	0.013	261.3	0.064	254.5	0.008	342.2	0.154	321.4	0.653	202.3	0.682	194.4	0.179	-0.758
36-40	0.143	250.7	0.001	270.7	0.009	368.8	0.174	330.9	0.694	204.9	0.722	196.3	0.178	-0.771
41-45	0.001	292.0	0.010	290.5	0.120	357.9	0.109	361.9	0.704	207.5	0.729	199.6	0.161	-0.807

Table 4 Determination coefficients explaining the agreement between burn severity expressed as dNBR and X- and L-band backscatter.

Sensor	X-band TerraSAR-X						L-band PALSAR							
Polariz.	HH		HV		HH & HV		HH		HV		HH & HV			
Scene	2008.12.24						2009.04.28							
	R^2	Std. err.	R^2	Std. err.	R^2	Std. err.	R^2	Std. err.	R^2	Std. err.	R^2	Std. err.	Beta° HH	Beta° HV
all pseudo-plots														
	0.425	273.3	0.162	330.0	0.478	260.6	0.054	345.9	0.692	197.3	0.693	200.2	-0.046	-0.821
pseudo-plots grouped by local incidence angle														
6-10	0.734	201.7	0.173	355.5	0.890	131.5	0.029	401.2	0.845	160.2	0.869	148.8	0.153	-9.916
10-15	0.714	196.3	0.510	257.0	0.915	107.5	0.028	379.8	0.833	157.3	0.862	143.7	0.170	-0.913
16-20	0.586	225.1	0.331	286.1	0.836	142.3	0.001	363.4	0.858	136.9	0.862	135.8	0.061	-0.929
21-25	0.681	198.4	0.231	308.3	0.843	139.6	0.093	331.9	0.861	130.2	0.861	130.7	0.005	-0.929
26-30	0.374	269.6	0.387	266.6	0.742	173.6	0.274	293.7	0.841	137.6	0.841	138.0	0.024	-0.931
31-35	0.370	274.2	0.525	238.0	0.783	161.7	0.623	214.9	0.829	144.8	0.829	145.3	-0.020	-0.893
36-40	0.555	242.0	0.654	213.4	0.812	158.3	0.703	185.8	0.822	143.7	0.822	144.3	-0.004	-0.904
41-45	0.544	245.7	0.665	210.4	0.831	150.4	0.779	165.7	0.876	124.1	0.883	121.3	-0.197	-0.758
46-50	0.562	262.1	0.805	175.0	0.897	128.1	0.764	158.2	0.853	124.9	0.867	120.7	-0.257	-0.696
51-55	0.598	238.9	0.805	166.3	0.895	125.3	-	-	-	-	-	-	-	-

X-band they have been previously reported in (Tanase et al. 2010). Beta coefficients can be used to compare the relative strength of the various polarizations included in the model as well as the sign of the relationship between the SAR backscatter and burn severity when multiple channels are jointly used in the regression analysis. The statistics were computed for all 900 pseudo-plots and by local incidence angle intervals of 5º. For co-polarized ERS SAR and Envisat ASAR data the values are reported for images acquired under dry and wet conditions. To maximize the results wet co- and dry cross-polarized data were used for multiple regression analysis for C-band Envisat ASAR.

Empirical fitting showed modest relations between dNBR and the backscatter coefficient when the local incidence angle was not accounted for (Tables 3 and 4). After grouping by 5^0 intervals the association strength increased for all SAR frequencies and polarizations. The determination coefficients decreased with increasing incidence angle while the error increased for X- and C-band co-polarized images. Higher determination coefficients were obtained for ERS SAR 1/2 (1995.08.10) and Envisat ASAR (2009.01.08) images acquired after rainfall (Table 3). However, the increase of the association strength to burn severity was not always related to rainfall. Therefore, it is difficult to predict whether images acquired under wet condition would always represent the better choice especially after heavy precipitation. L-band co-polarized data presented low association strength to burn severity for sensor oriented slopes whereas for the back-slopes the R^2s increased (Table 4). For cross-polarized data the strength of association increased with the increase of the local incidence angle at X-band whereas at C- and L-band was relatively high over the entire range of local incidence angles. The simultaneous use of co- and cross-polarized channels provided the highest determination coefficients and the smallest errors for X- and C-band (Table 3). For L-band the use of co-polarized data within a multiple regression model did not improve the determination coefficients with respect to the cross-polarized case. The high determination coefficients registered at X-band despite the smaller dynamic range are related mainly to the burn type. The crown burn severity was highly correlated with the total plot severity. Therefore, it was feasible to estimate burn severity at plot level although the X-band is sensitive to changes in the upper part of the canopy. In addition, TerraSAR-X data were acquired at much higher spatial resolution compared to Envisat ASAR and ALOS PALSAR which resulted in higher ENL (see table 1) which in turn increased the association strength to burn severity. This increase was previously demonstrated for the dual–polarized X-band dataset acquired over the Zuera08 site (Tanase et al. 2009).

A similar analysis was carried out for the CBI plots. Nonetheless, the small number of field plots available at each local incidence angle interval, the large proportion of plots with high CBI values (see Figs. 3 to 6) and the lack of detailed measurements on forest structure parameters assessed by CBI protocol implied that the statistical analysis was not sufficiently significant.

CONCLUSIONS

The properties of SAR backscatter in mediterranean burned forests were investigated for X-, C- and L-bands co- and cross-polarized data. The influence of the local topography and weather conditions on backscatter response was studied.

X- and C-band co-polarized backscatter increased with burn severity for slopes facing the sensor whereas for slopes pointing away from the sensor the backscatter showed no sensitivity to burn severity. L-band co-polarized backscatter showed a different behavior decreasing with increasing burn severity. Cross-polarized backscatter

from burned forests was lower than for unburned forests at all SAR frequencies and the sensitivity to burn severity was rather constant over the entire range of local incidence angles. Higher moisture enhanced the co-polarized signal at X- and C-band, thus increasing the dynamic range of the backscatter between unburned and highly burned areas. Changes from very dry to wet conditions resulted in increased sensitivity of co-polarized waves to burn severity especially in summer season. However, rainfall during acquisition could diminish the sensitivity of cross-polarized data to burn severity. The local incidence angle strongly affected the backscatter coefficient from burned areas at all SAR frequencies and polarizations and its influence has to be taken into account when estimating burn severity.

At X- and C-band strong relation to burn severity was found for co-polarized waves only on slopes oriented towards the sensor whereas cross-polarized data correlated better with burn severity on the back-slopes. The highest sensitivity to burn severity was obtained for C- and L-band for which burn severity estimation was consistent using only the cross-polarized channel. The sensitivity of radar data to burn severity decreased with the increase of SAR frequency. At X-band, the lower dynamic range from unburned to burned forests was compensated by the higher spatial resolution and the combined use of co- and cross-polarized channels. However, the small dynamic range of X-band could cause difficulties for burn severity estimation.

This study indicates that SAR systems have potential for burn evaluation in mediterranean environments. Empirical modeling could be used to relate SAR data to burn severity. Nevertheless, field assessed indices should contain information on the forest structure which is the main factor influencing the backscatter. SAR data could provide more consistent estimates over the entire range of burn severities than reflectance based indices especially for cross-polarized waves and low frequencies. Although forest fires in temperate climate produce similar effects (e.g. loss of foliage, branches and the understory layer) additional data are needed to confirm these findings over mixed forests of larger biomass variability. For different environments (e.g. boreal or tropical forests) the backscatter trends from burned areas could vary since forest structure and environmental conditions are significantly different.

ACKNOWLEDGMENT

Dr. Sergio M. Vicente-Serrano is acknowledged for providing the orthorectified, atmospherically corrected Landsat TM scenes for Zuera95 site and Ana Ma Cabanillas Saldaña for providing information on the forest structure. This work has been financed by the Spanish Ministry of Science and Education and the European Social Fund: FPI grant BES-2006-11684 and projects CGL2005-04863 and CGL2008-01083. TerraSAR-X data were provided by Deutsches Zentrum für Luft- und Raumfahrt in the framework of LAN0464 project. Envisat ASAR and ALOS PALSAR data were provided by the European Space Agency in the framework of C1P.5446 project and Japan Aerospace Exploration Agency in the framework of Kyoto and Carbon Initiative.

REFERENCES

Allen, J.L., and Sorbel, B. (2008). Assessing the differenced Normalized Burn Ratio's ability to map burn severity in the boreal forest and tundra ecosystems of Alaska's national parks. *International Journal of Wildland Fire, 17*, 463-475.

Andreae, M.O., and Merlet, P. (2001). Emission of trace gases and aerosols from biomass burning. *Global Biogeochemical Cycles, 15*, 955-966.

Bourgeau-Chavez, L.L., Harrell, P.A., Kasischke, E.S., and French, N.H.F. (1997). The detection and mapping of Alaskan wildfires using a spaceborne imaging radar system. *International Journal of Remote Sensing, 18*, 355-373.

Bourgeau-Chavez, L.L., Kasischke, E.S., Brunzell, S., and Mudd, J.P. (2002). Mapping fire scars in global boreal forests using imaging radar data. *International Journal of Remote Sensing, 23*, 4211-4234.

Bourgeau-Chavez, L.L., Kasischke, E.S., French, N.H.F., Szeto, L.H., and Kherkher, C.M. (1994). Using ERS-1 SAR Imagery to Monitor Variations in Burn Severity in an Alaskan Fire-Disturbed Boreal Forest Ecosystem. In, *Geoscience and Remote Sensing Symposium, 1994. IGARSS '94. Proceedings. 1994 IEEE International* (pp. 243-245). Pasadena, California.

Cocke, A.E., Fule, P.Z., and Crouse, J.E. (2005). Influence of fire severity on plant regeneration by means of remote sensing imagery. *International Journal of Wildland Fire, 14*, 189-198.

Chuvieco, E., Riaño, D., Danson, F.M., and Martín, P. (2006). Use of a radiative transfer model to simulate the postfire spectral response to burn severity. *Journal of Geophysical Research, 111*, 1-15.

Ferrazzoli, P., Paloscia, S., Pampaloni, P., Schiavon, G., Sigismondi, S., and Solimini, D. (1997). The Potential of Multifrequency Polarimetric SAR in Assessing Agricultural and Arboreous Biomass. *IEEE Transactions on Geoscience and Remote Sensing, 35*, 5-17.

Gimeno, M., and San-Miguel-Ayanz, J. (2004). Evaluation of RADARSAT-1 data for identification of burnt areas in Southern Europe. *Remote Sensing of Environment, 92*, 370-375.

Gimeno, M., San-Miguel-Ayanz, J., and Schmuck, G. (2004). Identification of burnt areas in Mediterranean forest environments from ERS-2 SAR time series. *International Journal of Remote Sensing, 25*, 4873-4888.

Grover, K., Quegan, S., and Freitas, C.daC. (1999). Quantitative Estimation of Tropical Forest Cover by SAR. *IEEE Transactions on Geoscience and Remote Sensing, 37*, 479-489.

Harrell, P.A., Bourgeau-Chavez, L.L., Kasischke, E.S., French, N.H.F., and Christensen, N.L. (1995). Sensitivity of ERS-1 and JERS-1 Radar Data to Biomass and Stand Structure in Alaskan Boreal Forest. *Remote Sensing of Environment, 54*, 247-260.

Holecz, F., Wegmüller, U., Rignot, E., and Wang, Y. (1995). Observed radar backscatter from forested areas with terrain variations. In, *Geoscience and Remote Sensing Symposium, 1995. IGARSS '95. Proceedings. 1995 IEEE International* (pp. 613-615). Firenze, Italy.

Hoy, E.E., French, N.H.F., Turetsky, M.R., Trigg, S.N., and Kasischke, E.S. (2008). Evaluating the potential of Landsat TM/ETM+ imagery for assessing fire severity in Alaskan black spruce forests. *International Journal of Wildland Fire, 17*, 500-514.

Huang, S., and Siegert, F. (2006). Backscatter Change on Fire Scars in Siberian Boreal Forests in ENVISAT ASAR Wide-Swath Images. *IEEE Transactions on Geoscience and Remote Sensing Letters, 3*, 154-158.

Kasischke, E.S., Bourgeau-Chavez, L.L., and French, N.H.F. (1994). Observations of Variations in ERS-1 SAR Image Intensity Associated with Forest Fires in Alaska. *IEEE Transactions on Geoscience and Remote Sensing, 32*, 206-210.

Key, C.H., and Benson, N.C. (2004). *Ground Measure of Severity, The Composite Burn Index*. Ogden, UT: U.S. Department of Agriculture, Forest Service, Rocky Mountain Research Station.

Key, C.H., and Benson, N.C. (2006). Landscape assessment (LA). In D.C. Lutes, R.E. Keane, J.F. Caratti, C.H. Key, N.C. Benson, S. Sutherland and L.J. Gangi (Eds.), *FIREMON: Fire effects*

monitoring and inventory system (pp. 1-55). Fort Collins, CO: U.S. Department of Agriculture, Forest Service, Rocky Mountain Research Station, Gen. Tech. Rep. RMRS-GTR-164-CD.

Luckman, A.J. (1998). The Effects of Topography on Mechanism of Radar Backscatter from Coniferous Forest and Upland Pasture. *IEEE Transactions on Geoscience and Remote Sensing, 36*, 1830-1834.

Menges, C.H., Bartolo, R.E., Bell, D., and Hill, G.J.E. (2004). The effect of savanna fires on SAR backscatter in northern Australia. *International Journal of Remote Sensing, 25*, 4857-4871.

Miller, J.D., Knapp, E.E., Key, C.H., Skinner, C.N., Isbell, C.J., Creasy, R.M., and Sherlocke, J.W. (2009). Calibration and validation of the relative differenced Normalized Burn Ratio (RdNBR) to three measures of fire severity in the Sierra Nevada and Klamath Mountains, California, USA. *Remote Sensing of Environment, 113*, 645-656.

Murphy, K.A., Reynolds, J.H., and Koltun, J.M. (2008). Evaluating the ability of the differenced Normalized Burn Ratio (dNBR) to predict ecologically significant burn severity in Alaskan boreal forests. *International Journal of Wildland Fire, 17*, 490-499.

Oliver, C.J., and Quegan, S. (1998). *Understanding synthetic aperture radar images*: Artech House.

Pausas, J., and Ramon, V. (1999). The role of fire in European Mediterranean ecosystems. In E. Chuvieco (Ed.), *Remote Sensing of Large Wildfires* (pp. 3-16): Springer.

Ranson, K.J., and Sun, G. (2000). Effects of Environmental Conditions on Boreal Forest Classification and Biomass Estimates with SAR. *IEEE Transactions on Geoscience and Remote Sensing, 38*, 1242-1252.

Rignot, E., Despain, D.G., and Holecz, F. (1999). The 1988 Yellowstone fires observed by imaging radars. In, *Proceedings of the Joint Fire Sciences Conference and Workshop*, 1-24.

Roxo, M.J., Cortesao, P., and Soeiro, B. (1996). Inner Lower Alentajo field site: Cereal cropping, soil degradation and desertification In C.J. Brandt and J. Thornes (Eds.), *Mediterranean desertification and land use* (pp. 111-135): J. Wiley & Sons.

Ruecker, G., and Siegert, F. (2000). Burn scar mapping and fire damage assessment using ERS-2 Sar images in East Kalimantan, Indonesia. *International Archives of Photogrammetry and Remote Sensing, 33*, 1286-1293.

Saatchi, S.S., Soares, J.V., and Alves, D.S. (1997). Mapping Amazon Deforestation and Land Use in Amazon Rainforest by Using SIR-C Imagery. *Remote Sensing of Environment, 59*, 191-202.

Saich, P., Rees, W.G., and Borgeaud, M. (2001). Detecting Pollution Damage to Forests in the Kola Peninsula Using the ERS SAR. *Remote Sensing of Environment, 75*.

Santis, A.de, and Chuvieco, E. (2009). GeoCBI: A modified version of the Composite Burn Index to estimate burn severity for remote sensing applications. In, *Remote Sensing of Environment* (pp. 554-562).

Siegert, F., Rucker, G., and Hoffman, A. (1999). Evaluation of the 1998 Forest Fires in East-Kalimantan (Indonesia) Using NOAA-AVHRR hotspot Data and Multitemporal ERS-2 SAR images. In, *Geoscience and Remote Sensing Symposium, 1999. IGARSS '99. Proceedings. 1999 IEEE International* (pp. 185-187). Hamburg, Germany.

Siegert, F., and Ruecker, G. (2000). Use of multitemporal ERS-2 SAR images for identification of burned scars in south-east Asian tropical rainforest. *International Journal of Remote Sensing, 21*, 831-837.

Simmonds, P.G., Manning, A.J., Derwent, R.G., Ciais, P., Ramonet, M., Kazan, V., and Ryall, D. (2005). A burning question. Can recent growth rate anomalies in the greenhouse gases be attributed to large-scale biomass burning events? *Atmospheric Environment, 39*, 2513-2517.

Sternberg, M., and Shoshany, M. (2001). Aboveground biomass allocation and water content relationships in Mediterranean trees and shrubs in two climatological regions in Israel. *Plant Ecology, 157*, 171-179.

Svoray, T., and Shoshany, M. (2003). Herbaceous Biomass Retrieval in Habitats of Complex Composition: A Model Merging SAR Images With Unmixed Landsat TM Data. *IEEE Transactions on Geoscience and Remote Sensing, 41*, 1592-1601.

Svoray, T., Shoshany, M., Curran, P.J., Foody, G.M., and Perevolotsky, A. (2001). Relationship between green leaf biomass volumetric density and ERS-2 SAR backscatter of four vegetation formations in the semi-arid zone of Israel. *International Journal of Remote Sensing, 22*, 1601-1607.

Tanase, M., Pérez-Cabello, F., Riva, J.de la, and Santoro, M. (2010). TerraSAR-X data for burn severity evaluation in Mediterranean forests on sloped terrain. *IEEE Transactions on Geoscience and Remote Sensing, 48*, 917-929.

Tanase, M., Santoro, M., Riva, J.de la, and Pérez-Cabello, F. (2009). Backscatter properties of multitemporal TerraSAR-X data and the effects of influencing factors on burn severity evaluation, in a Mediterranean pine forest. In, *Geoscience and Remote Sensing Symposium, 2009. IGARSS '09. 2009 IEEE International* (pp. 593-596). Cape Town, South Africa.

Le Toan, T., Beaudoin, A., and D.Guyon (1992). Relating forest biomass to SAR data. *IEEE Transactions on Geoscience and Remote Sensing, 30*.

Ulander, L.M.H. (1996). Radiometric slope correction of synthetic-aperture radar images. *IEEE Transactions on Geoscience and Remote Sensing, 34*, 1115-1122.

Verbyla, D.L., Kasischke, E.S., and Hoy, E.E. (2008). Seasonal and topographic effects on estimating fire severity from Landsat TM/ETM+ data*International Journal of Wildland Fire, 17*, 527-534.

Vicente-Serrano, S.M., Pérez-Cabello, F., and Lasanta, T. (2008). Assessment of radiometric correction techniques in analyzing vegetation variability and change using time series of Landsat images. *Remote Sensing of Environment, 112*, 3916-3934.

Wagtendonk, J.W.van, Root, R.R., and Key, C.H. (2004). Comparison of AVIRIS and Landsat ETM+ detection capabilities for burn severity. *Remote Sensing of Environment, 92*, 397-408.

Wegmüller, U., Strozzi, T., and Bitelli, G. (1999). Validation of ERS differential SAR interferometry for land subsidence mapping: the Bologna case study. In, *Geoscience and Remote Sensing Symposium, 1999. IGARSS '99. Proceedings. 1999 IEEE International* (pp. 1131 -1133). Hamburg, Germany.

Wegmüller, U., Werner, C., Strozzi, T., and Wiesmann, A. (2002). Automated and precise image registration procedures. In L. Bruzzone and P. Smits (Eds.), *Analysis of multi-temporal remote sensing images* (pp. 37-49). Singapore: World Scientific 2002.

van Zyl, J.J. (1993). The Effect of Topography on Radar Scattering from Vegetated Areas. *IEEE Transactions on Geoscience and Remote Sensing, 31*, 153-160.

4.2.4. L-band SAR backscatter prospects for burn severity estimation in boreal forests

Tanase, M.A., Santoro, M., de la Riva, J., Kasischke, E. and, Korets, M. A. (2010) L-band SAR backscatter prospects for burn severity estimation in boreal forests. ***ESA Living Planet Symposium, SP-668 (CD-ROM) ESA Publications Division, European Space Agency, Noordwijk, The Netherlands.***

Resumen

Se investiga la relación entre el coeficiente de retro-dispersión y la severidad del incendio en bosques boreales mediante imágenes radar de apertura sintética (SAR) de banda L. Se utilizan para ello imágenes de doble polarización de Advanced Land Observation Satellite (ALOS) Phased Array-type L-band Synthetic Aperture Radar (PALSAR) para el estudio del coeficiente de retro dispersión en dos áreas distintas. Mediante análisis estadístico se evalúa el coeficiente promedio de retro-dispersión en función del nivel de severidad después de estratificar los datos en función del ángulo de incidencia local. Los coeficientes de determinación se utilizan para cuantificar la relación entre la retro-dispersión y la severidad del incendio.

El análisis de un determinado rango de ángulo de incidencia local muestra que la retro-dispersión HH y HV disminuye con la severidad cuando se trata de imágenes adquiridas en condiciones ambientales secas. En cambio, para imágenes obtenidas en condiciones de humedad elevada la retro-dispersión HH aumenta con la severidad. El coeficiente de retro-dispersión mayor en zonas de alta severidad se explica por la mayor contribución del suelo en la retro-dispersión ocasionada por el mayor contenido de humedad. La variación de la retro-dispersión entre los bosques quemados y no quemados se sitúa en torno a 2-3 dB para la polarización HH y a 3-6 dB para la polarización HV. La investigación desarrollada pone de manifiesto que las tendencias observadas del coeficiente de retro-dispersión en banda L en función de la severidad en zonas boreales no son significativamente diferentes de las tendencias observadas para zonas mediterráneas.

L-band SAR backscatter prospects for burn severity estimation in boreal forests

M. A. Tanase[(1)], M. Santoro[(2)], J. de la Riva[(1)], E. Kasischke[(3)], and M. A. Korets[(4)]

[(1)]Department of Geography,
University of Zaragoza,
Pedro Cerbuna 12, 50009 Zaragoza, Spain
Email: mihai@tma.ro, delariva@unizar.es

[(2)]Gamma Remote Sensing AG,
Worbstr. 225, CH-3073 Gümligen, Switzerland
Email: santoro@gamma-rs.ch

[(3)]Department of Geography
University of Maryland
2181 LeFrak Hall, College Park MD 20742, USA
Email: ekasisch@umd.edu

[(4)]V.N. Sukachev Institute of Forest,
660036 Krasnoyarsk, Russia
Email: mik@ksc.krasn.ru

Abstract

L-band Synthetic Aperture Radar (SAR) data has been investigated to establish the relationship between backscatter and burn severity in boreal forests. Advanced Land Observation Satellite (ALOS) Phased Array-type L-band Synthetic Aperture Radar (PALSAR) dual polarized images were available for the study of the backscattering coefficient at two locations. Statistical analysis was used to assess the average backscatter coefficient as a function of burn severity level after stratifying the data by local incidence angle. Determination coefficients were used to quantify the relationship between radar data and burn severity estimates.

The analysis for a given range of local incidence angle showed that HH and HV polarized backscatter decreases with burn severity for both polarizations when images are acquired under dry environmental conditions. For data acquired under wet conditions HH polarized backscatter increased with burn severity. The higher backscatter of the severely burned areas was explained by the enhanced contribution of the ground component due to higher soil moisture content. Backscatter variation between burned and unburned forest was around 2-3 dB at HH polarization and around 3-6 dB at HV polarization. This study indicates that L-band SAR backscatter trend as a function of burn severity is not significantly different when compared to previously studied mediterranean forests.

***Keywords**: backscatter, burn severity, forest fire, boreal forest*

INTRODUCTION

Boreal forests cover approximately 15 % of Earth's land surface and contain over 35 % of all carbon stored in the terrestrial biome playing a significant role as carbon pool (Kasischke et al. 1995). These forests are vulnerable to fire especially while considering their slow recovery rate and the potential of carbon release into atmosphere. The fire regime across North American boreal region changed during the last decades, the annual burned area and large fires frequency recording a twofold increase since 1950 which may alter post-fire ecosystems processes (Kasischke and Turetsky 2006). Variations in burned area and fire severity control fire emissions from boreal forest which in turn affect the atmospheric concentration of atmospheric CO at global scale (Kasischke et al. 2005). Burned area estimation is the simplest and most common remote measure of fire effects and has been conducted using a wide variety of satellite sensors at local to regional scales (Lentile et al. 2006). Mapping studies used mostly information of the difference in spectral response before and after fire which allowed accurate detection of the burned areas (Garcia-Haro et al. 2001; Roy et al. 2005). Active sensors such as synthetic aperture radar (SAR) were also found useful for discriminating fire affected areas (Bourgeau-Chavez et al. 2002; Gimeno and San-Miguel-Ayanz 2004). SAR data could be more useful in boreal or tropical forests where algorithms based on optical data are more likely to be limited by persistent cloud cover (Roy et al. 2005).

Estimation of fire effects has received considerable interest in the recent literature since it determines post-fire ecosystems processes (French et al. 2008) and has a significant influence on gas emission from burned areas (Andreae and Merlet 2001). Fire ecological effect is expressed by burn severity which estimates the degree of environmental changes caused by fire. The difficulty associated with field data collection made remote sensing the method of choice for burn severity assessment across large areas. One of the most widely employed spectral index is the normalized burn ratio (NBR) (Key and Benson 2006) used in a bi-temporal approach with pre- and post-fire datasets (dNBR). However, reflectance based indices are sensitive to plant phenology and solar elevation, so that monitoring severity trends over time or across regions can be subject to errors especially at high latitudes (Verbyla et al. 2008).

Recently it has been shown that burn severity is directly related to information provided by SAR sensors in mediterranean pine forests (Tanase et al. 2010; Tanase et al. in press). The removal of leaves and branches by fire and the increased soil exposure influenced the backscattering from fire affected areas. L-band cross-polarized backscatter showed the highest sensitivity to burn severity. The current study complements these investigations focusing on boreal forests affected by fires. The main objective was to provide a preliminary assessment of Advanced Land Observation Satellite (ALOS) Phased Array-type L-band Synthetic Aperture Radar (PALSAR) L-band SAR backscatter sensitivity to burn severity in boreal forests. Signatures of fire affected areas and the prediction power of SAR intensity data for burn severity estimation were studied.

STUDY AREA AND DATASETS

Two sites located in the boreal zone were considered. The first site was located in interior Alaska, approximately 200 km west of Fairbanks. The area stretches on a gently sloping alluvial outwash plane north of the Alaska Range, with elevations ranging between 100 and 400 m. In this region, the average annual temperature is -2.1 °C, with the warmest month being July (15.6 °C) and the coldest January (-19.7 °C). Average

annual precipitation is 29 cm, with three-quarters of this amount occurring during the growing season (May to September). Three fires were selected for the study (Table 1) using information provided by the Monitoring Trends in Burn Severity (MTSB) project. Two of the fires burned during the 2007 summer season (Mooseheart and Jordan Creek) whereas the third (Boney Creek) burned in summer 2005. The second site was located in central Siberia, approximately 200 km NW of Ust-Ilimsk, nearby the Angara river. The area is characterized by annual average temperature of -2 °C, the warmest month being July (18 °C) and the coldest January (-23°C). The average annual precipitation is 43 cm. The relief was represented mainly by plateaus and small hills, with elevation ranging between 200 and 400 meters. Two fires (Angara1 and Angara2) which burned during summer 2006 were selected for the analysis (Table 1).

The SAR dataset (Table 2) was acquired by ALOS PALSAR in Fine Beam dual polarization mode (FBD) with a 34 degrees look angle. SAR images were absolutely calibrated, multi-looked to obtain the desired 30 m spatial resolution and geocoded to Universal Transverse Mercator (UTM) projection using a digital elevation model (Wegmüller 1999). Although most of the area was located on a flat or nearly flat terrain, topographic normalization of the backscatter was applied in order to obtain similar metrics (γ°) as for the previous studies (Tanase et al. 2010; Tanase et al. in press).

Fig. 1 shows the fire locations using a composite of L-band backscatter (HH and HV) and their ratio overlaid on the MODIS Vegetation Continuous Fields (VFC) product. In the PALSAR color composite, the fire scars can be distinguished from the surrounding forests. The green areas correspond to high cross-polarized (HV) backscatter and low backscatter ratio, which is characteristic for dense vegetation. The blue/purple areas correspond to low cross-polarized backscatter and high backscatter ratio, which is typical for areas with no or low vegetation. The fire scars appear in purple in consequence of the lower HV backscatter when compared to adjacent unburned forest. For each fire a pair of Landsat TM images (pre- and post-fire) was used to estimate burn severity levels by means of dNBR index (Table 1). Terrain corrected Level 1T Landsat scenes were acquired from U.S. Geological Survey (USGS) in UTM projection (Table1). From each image the additive haze component was removed using the dark-object subtraction technique.

Table 1 Analyzed fire scars and the affected area together with the acquisition date of the Landsat images.

		Landsat	
Fire	Area (ha)	Pre-fire	Post-fire
Mooseheart[A]	8150	2005.07.20	2008.08.21
Jordan Creek[A]	3700	2001.09.02	2008.08.21
Boney Creek[A]	24700	2002.09.21	2006.09.08
Angara 1[S]	5700	2004.06.28	2007.09.01
Angara 2[S]	4500	2004.06.28	2007.09.01

A Alaskan site //S Siberian site

Table 2 ALOS PALSAR acquisitions and climate data (AcPp in mm and Tmax. and Tmin. in °C).

Date	AcPp	Tmax	Tmin
2007.06.10[S]	20.6	22.5	4.1
2007.07.09[S]	27.4	32.4	14.9
2007.07.26[S]	12.2	30.2	14.0
2007.08.24[S]	63.0	19.8	7.9
2008.08.03[A]	53.5*	12.7	3.3

A Alaskan site //S Siberian site
* precipitations registered partly during the day of SAR acquisition

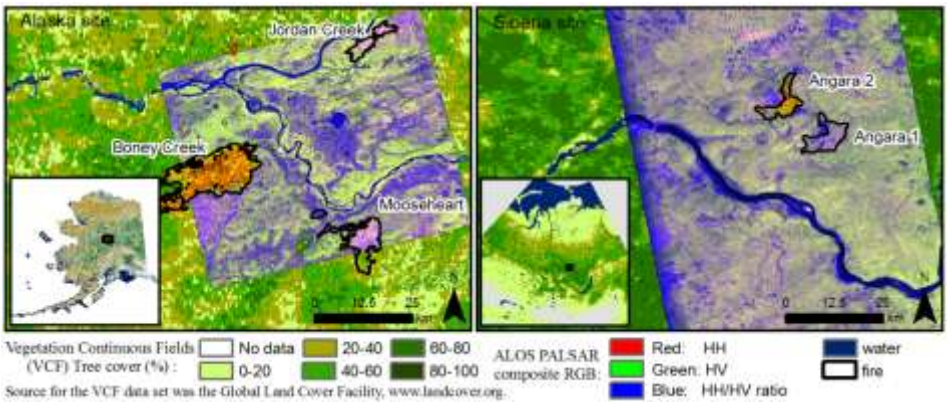

Fig. 1 Study sites and the fire perimeters. PALSAR images are overlaid on tree cover percentage map.

To aid the interpretation, meteorological data collected from the nearest available meteorological station were used. For the Siberian site meteorological data were available from the Bogucany station located at approximately 150 km west of the fires whereas for the Alaskan site meteorological data were available from The Tanana station located 25 km N of the Boney Creek fire. The daily maximum and minimum temperature is presented in Table 2 for the dates of acquisition of the SAR images. Accumulated precipitation (AcPp) was computed taking into account the last two weeks before acquisition.

METHODS

The study was focused on relatively small size fires in order to assure certain forest homogeneity. Thus, any variability of the backscatter coefficient could be assumed to be related primarily to different burn conditions rather than to differences in forest structure and species composition. To understand the relationship between forest burn severity and backscatter coefficient dNBR based pseudo-plots were used. The reason for using pseudo-plots was the lack of field assessed estimated of burn severity. Pseudo-plots were generated by averaging pixels of similar burn severity (expressed by the dNBR index) for the same local incidence angle. The quality of these pseudo-plots with respect to field assessed conventional plots has been discussed in (Tanase et al. 2010) for mediterranean pine forests. For Alaskan boreal forests, weaker relationships were reported between dNBR and a field assessed indicator of burn severity, the composite burn index (CBI) at some locations (Hoy et al. 2008; Murphy et al. 2008). Therefore, the relationship between SAR backscatter and burn severity could be hindered by inaccuracies of dNBR based estimates of burn severity.

Detailed information on pseudo-plots generation process is given in (Tanase et al. 2010). To avoid bias related to size, only pseudo-plots containing a constant number of pixels were considered. For consistency with the previous studies nine pixels per pseudo-plot were used. Descriptive statistics were applied to analyze and compare backscatter as a function of burn severity. The potential of backscatter coefficient for burn severity estimation was assessed using inferential statistics. To minimize the effect of topography on the backscatter coefficient the analyses were carried out by 5º groups of local incidence angle as for the previous studies (Tanase et al. 2010; Tanase et al. in press).

RESULTS AND DISCUSSION

Signature analysis

Co- and cross-polarized backscatter coefficient as a function of burn severity are presented in Fig. 2 and 3 for slopes oriented towards the sensor (31-35°), flat or near flat areas (36-40°) and slopes oriented away from the sensor (41-45°). For the Siberian site two images acquired under different environmental conditions (dry and wet) are shown whereas for the Alaskan site the available image was acquired under wet conditions.

For the image acquired under dry conditions (2007.07.26) HH and HV backscatter decreased with the increase of burn severity in accordance with the results reported for mediterranean pine forests (Tanase et al. in press). The backscatter variation from unburned to burned forest (dynamic range) was around 2-3 dB at HH polarization and between 3 and 6 dB at HV polarization, depending on the local incidence angle. The largest dynamic range was recorded for the higher local incidence angles. This could be explained by the higher severity recorded for the slopes oriented away from the sensor when compared to flat areas or slopes oriented towards the sensor. For the image acquired under wettest conditions (2007.08.24), the backscatter at HH polarization increased slightly with increasing burn severity for slopes oriented towards the sensor or flat areas. For slopes oriented away from the sensor the sensitivity of L-band co-polarized backscatter to burn severity was low (Fig. 2). The increased co-polarized backscatter for severely burned areas was explained by the enhanced contribution from the ground due to higher moisture content. The HV polarization trend did not change when compared to the image acquired under dryer conditions. Nonetheless, the increased moisture negatively affected the dynamic range with respect to the dry conditions case. It decreased to around 1.5 dB for HH polarization and 2 dB for HV polarization. The remaining two images acquired under wet environmental conditions (2007.06.10 and 2007.07.09) showed low sensitivity to burn severity especially at HH polarization. The dynamic range of co-polarized backscatter was below 1 dB for both fires. The reason for the different behavior of the HH backscatter should be attributed to local dielectric properties of the scatterers. Knowledge of the forest conditions and soil conditions at the time of image acquisition would have helped substantially in understanding these signatures.

Similar backscatter trends and dynamic ranges as those reported for the Siberian site under wet conditions were observed for the Alaskan site (Fig. 3) for which the image was acquired after a period of intense precipitations (see Table 2). HH polarized backscatter increased whereas HV polarized backscatter decreased with increasing burn severity.

Statistical analysis

To infer the utility of PALSAR FBD SAR backscatter for burn severity estimation, linear regression determination coefficients (R^2) expressing the proportion of burn severity variance predicted by SAR backscatter and the standard error are presented in Table 3 and 4. Beta standardized regression coefficients (Beta°) which express the relative strength of metrics have been included for multiple regression analysis. The statistics were computed for all the generated pseudo-plots and by local incidence angle intervals of 5º. Values are reported for images acquired under dry and wet conditions at the Siberian site (Angara 2 fire) and for wet conditions at the Alaskan site (Boney Creek fire).

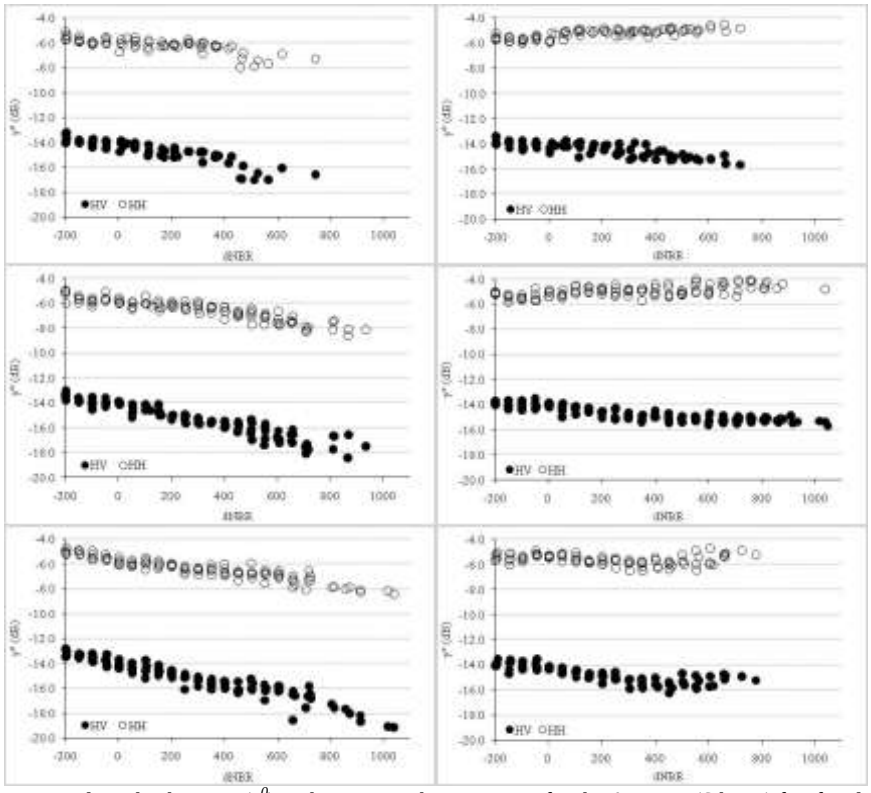

Fig. 2 HH and HV backscatter (γ^0) with respect to burn severity for the Angara2 (Siberia) fire for slopes oriented towards the sensor (top), flat areas (center) and slopes oriented away from the sensor (bottom). Dry (left, 2007.07.26) and wet (right, 2007.08.24) environmental conditions.

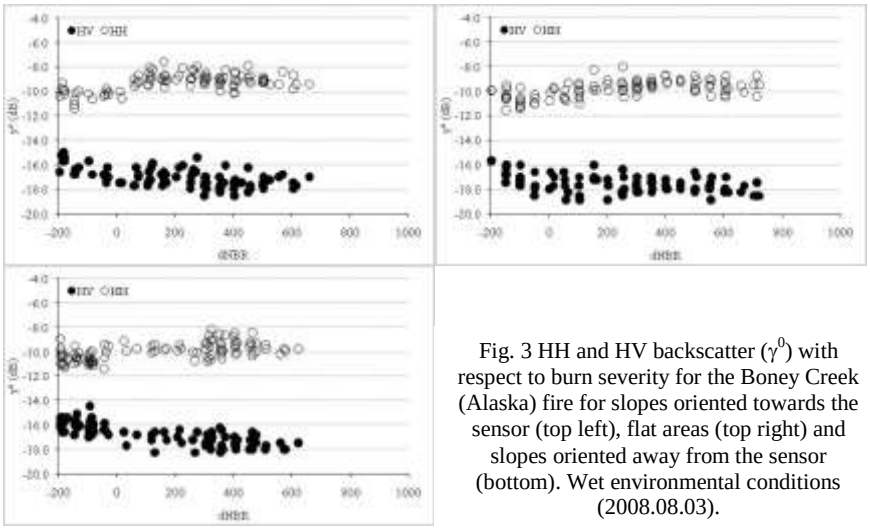

Fig. 3 HH and HV backscatter (γ^0) with respect to burn severity for the Boney Creek (Alaska) fire for slopes oriented towards the sensor (top left), flat areas (top right) and slopes oriented away from the sensor (bottom). Wet environmental conditions (2008.08.03).

Table 3 Determination coefficients explaining the agreement between burn severity expressed as dNBR and L-band backscatter (Siberia site, Angara 2 fire).

Scene	2007.07.26 (dry)								2007.08.24 (wet)							
	HH		HV		HH & HV				HH		HV		HH and HV			
	R^2	Std. err.	R^2	Std. err.	R^2	Std. err.	Beta° HH	Beta° HV	R^2	Std. err.	R^2	Std. err.	R^2	Std. err.	Beta° HH	Beta° HV
all pseudo-plots																
	0.793	135.4	0.875	105.1	0.875	105.3	-0.024	-0.913	0.266	251.2	0.583	189.1	0.824	122.7	0.492	-0.748
pseudo-plots grouped by local incidence angle																
31-35°	0.574	152.5	0.815	100.6	0.837	95.2	0.351	-1.222	0.590	164.6	0.666	148.5	0.841	103.1	0.482	-0.577
36-40°	0.817	138.2	0.850	124.8	0.862	120.3	-0.319	-0.623	0.473	250.5	0.709	186.4	0.859	130.4	0.422	-0.675
41-45°	0.862	119.3	0.908	97.4	0.909	97.4	-0.118	-0.839	0.046	261.4	0.634	161.8	0.806	118.4	0.551	-1.160
46-50°	0.872	82.0	0.949	51.6	0.950	52.0	-0.140	-0.961	0.628	108.1	0.821	75.0	0.853	68.8	0.530	-1.405

Table 4 Determination coefficients explaining the agreement between burn severity expressed as dNBR and L-band backscatter (Alaska site, Boney Creek fire).

Scene	2008.08.03 (wet)							
	HH		HV		HH and HV			
	R^2	Std. err.	R^2	Std. err.	R^2	Std. err.	Beta° HH	Beta° HV
all pseudo-plots								
	0.232	220.4	0.384	197.4	0.581	162.4	0.448	-0.595
pseudo-plots grouped by local incidence angle								
31-35°	0.190	203.0	0.315	186.6	0.539	153.9	0.475	-0.593
36-40°	0.260	227.5	0.227	232.6	0.557	177.0	0.579	-0.549
41-45°	0.294	214.7	0.595	162.8	0.714	137.4	0.359	-0.673

Empirical fitting showed strong relationships between backscatter coefficient and dNBR for data acquired under dry conditions at the Siberian sites (Table 3). Slightly higher determination coefficients and smaller errors were observed for HV polarization. The simultaneous use of co- and cross-polarized channels resulted in increases of the determination coefficients, HV polarization explaining most burn severity variations (higher Beta° coefficients). The influence of the local incidence angle on the determination coefficient was negligible due to the relatively flat topography.

For the image acquired under wet conditions (2007.08.24) the association strength to burn severity decreased for both polarizations. The combined use of the co- and cross-polarized channel partially compensated this loss of sensitivity, the determination coefficients increasing up to 0.85. However, for the remaining two images acquired under wet conditions at the Siberian site (2007.06.10 and 2007.07.09) the association strength to burn severity was much lower ($R^2 < 0.4$) for both fires (Angara 1 and 2) at HH polarization. Low association strength to burn severity was observed at the Alaskan site (Table 4). For HV polarization slightly higher determination coefficients were recorded when compared to HH polarization (Boney Creek fire). The combined use of HH and HV polarization increased the association strength to burn severity levels. Similar results were obtained also for the remaining two fires. The high precipitation levels throughout 2008 summer season and the rainfall recorded during the acquisition of the SAR image negatively influenced the sensitivity of the backscatter coefficient to burn severity. The lower determination coefficients found for the Alaskan fires could also be the result of inaccurate estimation of the burn severity by dNBR index.

The results here presented are similar to those obtained with PALSAR data in mediterranean forests (Tanase et al. in press), with higher association strength to burn severity and lower estimation errors for data acquired under dry conditions. Slightly lower dynamic range from unburned to severely burned forests was observed for boreal forests at both HH and HV polarization. As for the mediterranean forests the

simultaneous use of HH and HV polarizations did not improve burn severity estimation when using images acquired in relatively dry environmental conditions. For images acquired after precipitation the estimation error increased significantly.

CONCLUSIONS

The properties of ALOS PALSAR L-band dual polarized backscatter were investigated for burned boreal forests. The influence of the weather conditions on backscatter response was also studied.

Co- and cross-polarized backscatter decreased with the increase of burn severity due to decreasing volume scattering component under dry and unfrozen environmental conditions. For images acquired under wet environmental conditions an opposite trend was observed for HH polarization in consequence of higher soil moisture. The highest sensitivity to burn severity was observed for HV polarized backscatter acquired under dry conditions. Precipitations negatively influenced the association strength to burn severity at both HH and HV polarizations. The simultaneous use of both polarizations within a linear regression model seemed to compensate this decrease in sensitivity to a certain extent. This study indicates that L-band SAR backscatter is useful for burn severity estimation in boreal forest. However, the work points out the strong dependence of the results on weather conditions.

Several aspects of this study could limit drawing conclusions for the entire boreal zone: *i)* no field estimates of burn severity were available which hindered the assessment of dNBR reliability when estimating severity; *ii)* only images from summer season were studied. SAR images acquired during winter season could present completely different trends since the environmental conditions are significantly different; *iii)* the study took into consideration a small number of burns located within relatively small areas. Therefore it is essential to extend the analysis over larger areas with higher variability of forest biomass and species composition; and *iv)* the influence of environmental conditions should be more thoroughly studied. Soil and vegetation moisture content could prove a decisive factor when estimating burn severity in such environments. Further studies should also consider interferometric coherence which was more useful than SAR backscatter for burn severity estimation in mediterranean environments.

ACKNOWLEDGMENT

This work has been financed by the Spanish Ministry of Science and Education and the European Social Fund: FPI grant BES-2006-11684 and projects CGL2005-04863 and CGL2008-01083. The PALSAR data over Siberia was obtained within the framework of the JAXA Kyoto & Carbon Initiative.

REFERENCES

Andreae, M.O., and Merlet, P. (2001). Emission of trace gases and aerosols from biomass burning. *Global Biogeochemical Cycles, 15*, 955-966.

Bourgeau-Chavez, L.L., Kasischke, E.S., Brunzell, S., and Mudd, J.P. (2002). Mapping fire scars in global boreal forests using imaging radar data. *International Journal of Remote Sensing, 23*, 4211-4234.

French, N.H.F., Kasischke, E.S., Hall, R.J., Murphy, K.A., Verbyla, D.L., Hoy, E.E., and Allen, J.L. (2008). Using Landsat data to assess fire and burn severity in the North American boreal

forest region: an overview and summary of results *International Journal of Wildland Fire, 17*, 443-462.

Garcia-Haro, F.J., Gilabert, M.A., and Melia, J. (2001). Monitoring fire-affected areas using Thematic Mapper data. *International Journal of Remote Sensing, 22*, 533-549.

Gimeno, M., and San-Miguel-Ayanz, J. (2004). Evaluation of RADARSAT-1 data for identification of burnt areas in Southern Europe. *Remote Sensing of Environment, 92*, 370-375.

Hoy, E.E., French, N.H.F., Turetsky, M.R., Trigg, S.N., and Kasischke, E.S. (2008). Evaluating the potential of Landsat TM/ETM+ imagery for assessing fire severity in Alaskan black spruce forests. *International Journal of Wildland Fire, 17*, 500-514.

Kasischke, E.S., Hyer, E.J., Novelli, P.C., Bruhwiler, L.P., French, N.H.F., Sukhinin, A.I., Hewson, J.H., and Stocks, B.J. (2005). Influences of boreal fire emissions on Northern Hemisphere atmospheric carbon and carbon monoxide. *Global Biogeochemical Cycles, 19, GB1012*, 1-16.

Kasischke, E.S., Christensen, N.L., and Stocks, B.J. (1995). Fire, Global Warming, and the Carbon Balance of Boreal Forests. *Ecological Applications, 5*, 437-451.

Kasischke, E.S., and Turetsky, M.R. (2006). Recent changes in the fire regime across the North American boreal region—Spatial and temporal patterns of burning across Canada and Alaska. *Geophysical Research Letters, 33, L09703.*

Key, C.H., and Benson, N.C. (2006). Landscape assessment (LA). In D.C. Lutes, R.E. Keane, J.F. Caratti, C.H. Key, N.C. Benson, S. Sutherland and L.J. Gangi (Eds.), *FIREMON: Fire effects monitoring and inventory system* (pp. 1-55). Fort Collins, CO: U.S. Department of Agriculture, Forest Service, Rocky Mountain Research Station, Gen. Tech. Rep. RMRS-GTR-164-CD.

Lentile, L.B., Holden, Z.A., SmithA, A.M.S., Falkowski, M.J., Hudak, A.T., Morgan, P., Lewis, S.A., Gessler, P.E., and Bwnson, N.C. (2006). Remote sensing techniques to assess active fire characteristics and post-fire effects. *International Journal of Wildland Fire, 15*, 319-345.

Murphy, K.A., Reynolds, J.H., and Koltun, J.M. (2008). Evaluating the ability of the differenced Normalized Burn Ratio (dNBR) to predict ecologically significant burn severity in Alaskan boreal forests. *International Journal of Wildland Fire, 17*, 490-499.

Roy, D.P., Jin, Y., Lewis, P.E., and Justice, C.O. (2005). Prototyping a global algorithm for systematic fire-affected area mapping using MODIS time series data. *Remote Sensing of Environment, 97*, 137-162.

Tanase, M., Pérez-Cabello, F., Riva, J.de la, and Santoro, M. (2010). TerraSAR-X data for burn severity evaluation in Mediterranean forests on sloped terrain. *IEEE Transactions on Geoscience and Remote Sensing, 48*, 917-929.

Tanase, M., Riva, J.de la, Santoro, M., Le Toan, T., and Perez-Cabello, F. (in press). Sensitivity of X-, C- and L-band SAR backscatter to fire severity in mediterranean pine forests. *IEEE Transactions on Geoscience and Remote Sensing*.

Verbyla, D.L., Kasischke, E.S., and Hoy, E.E. (2008). Seasonal and topographic effects on estimating fire severity from Landsat TM/ETM+ data*International Journal of Wildland Fire, 17*, 527-534.

Wegmüller, U. (1999). Automated terrain corrected SAR geocoding. In, *Geoscience and Remote Sensing Symposium, 1999. IGARSS '99. Proceedings. 1999 IEEE International* (pp. 1712-1714). Hamburg, Germany.

4.3. Sensibilidad de la coherencia interferométrica a la severidad del incendio. Factores que influyen en la estimación

4.3.1. Properties of X-, C- and L-band repeat-pass interferometric SAR coherence in Mediterranean pine forests affected by fires

Tanase, M.A., Santoro, M., Wegmüller, U., de la Riva, J. and, Pérez-Cabello, F. (2010) Properties of X-, C- and L-band repeat-pass interferometric SAR coherence in Mediterranean pine forests affected by fires. ***Remote Sensing of Environment, Vol. 114, Issue 10, pp. 2182-2194, 2010*****.**

Resumen

Se utilizan imágenes Radar de Apertura Sintética (SAR) para determinar la relación entre la severidad del fuego y la coherencia interferométrica en tres áreas afectadas por incendios forestales en un ambiente mediterráneo.

La presente investigación se apoya en el tratamiento de imágenes SAR procedentes de los sensores TerraSAR-X, ERS-1/2, Envisat ASAR y ALOS PALSAR. La coherencia interferométrica se relaciona con estimaciones de severidad derivadas de trabajo de campo (Composite Burn Index) y del tratamiento de imágenes ópticas mediante el índice Normalized Burn Ratio (NBR). Además, se evalúan también los efectos de la topografía y el clima en las estimaciones de la coherencia. El análisis por rangos de ángulo de incidencia local pone de manifiesto cómo la coherencia co-polarizada aumenta al hacerlo la severidad en las bandas X y C, mientras que la coherencia de polarización cruzada es prácticamente insensible a la severidad del incendio. Así mismo, se evidencia la mayor sensibilidad a la severidad de la banda L para las dos polarizaciones. Se observan mayores coeficientes de determinación entre la coherencia y la severidad en las imágenes adquiridas en condiciones estables y secas. Cuando se tiene en consideración la influencia del ángulo de incidencia local los coeficientes de determinación aumentan de 0,6 a 0,9 para las bandas X y C; en cambio, en la banda L el ángulo de incidencia local tiene una menor influencia en la estimación de la severidad del incendio.

Properties of X-, C- and L-band repeat-pass interferometric SAR coherence in Mediterranean pine forests affected by fires

M.A. Tanase[(1)], M. Santoro[(2)], U. Wegmüller[(2)], J. de la Riva[(1)], and F. Pérez -Cabello[(1)]

[(1)]Department of Geography,
University of Zaragoza,
Pedro Cerbuna 12, 50009 Zaragoza, Spain
Email: mihai@tma.ro, delariva@unizar.es, fcabello@unizar.es

[(2)]Gamma Remote Sensing AG,
Worbstr. 225, CH-3073 Gümligen, Switzerland
Email: santoro@gamma-rs.ch,wegmuller@gamma-rs.ch

Abstract

Synthetic Aperture Radar (SAR) data has been investigated to determine the relationship between burn severity and interferometric coherence at three sites affected by forest fires in a hilly Mediterranean environment. Repeat-pass SAR images were available from the TerraSAR-X, ERS-1/2, Envisat ASAR and ALOS PALSAR sensors. Coherence was related to measurements of burn severity (Composite Burn Index) and remote sensing estimates expressed by the differenced normalized burn ratio (dNBR) index. In addition, the effects of topography and weather on coherence estimates were assessed. The analysis for a given range of local incidence angle showed that the co-polarized coherence increases with the increase of burn severity at X- and C-band whereas cross-polarized coherence was practically insensitive to burn severity. Higher sensitivity to burn severity was found at L-band for both co- and cross-polarized channels. The association strength between coherence and burn severity was strongest for images acquired under stable, dry environmental conditions. When the local incidence angle is accounted for the determination coefficients increased from 0.6 to 0.9 for X- and C-band. At L-band the local incidence angle had less influence on the association strength to burn severity.

Keywords*: forest fire, interferometric coherence, burn severity, X-, C-, L-band SAR*

INTRODUCTION

Changes in traditional land use patterns have modified the incidence of fires in the Mediterranean area. Rural abandonment led to unusual accumulation of forest fuels, which notably augmented fire risk. The increased use of forests as recreational resource incurred higher incidence of man-induced fires (Chuvieco 1999), the average number of fires per year rising by 60% from 1980 to 2007 (Schmuck et al. 2008). Increased fire activity over the last decades also reflects regional responses to changes in climate, fire intensity and duration being, at least partially, influenced by higher temperatures (warmer springs) and reduced moisture availability (dryer summer seasons). A fourfold increase in the fire frequency was observed for the last two decades when compared to

the previous period in the western United States. The length of the active fire season increased with more than two months and the average burn duration of large fires increased from one week to more than a month (Westerling et al. 2006). Deforestation-related fires contribute substantially to the global green-house gas emissions and the associated global warming they cause, which in turn causes increase of extreme-weather related fires leading to further spikes of carbon emissions (Werf et al. 2004). Fire severity is an important indicator of the way fire impacts ecosystems. Since the carbon content of fuels varies in a limited range the combustion conditions have a decisive role in burned area emissions (Andreae and Merlet 2001).

Burn severity is generally estimated using a field assessed indicator called composite burn index (CBI) and is defined as the degree of the environmental change caused by fire (Key and Benson 2004). The index describes post-fire conditions at a site by scoring different factors (e.g. litter consumption, percentage of altered foliage etc.) for individual vegetation layers (i.e. substrate, shrubs, trees). The results are aggregated to obtain a numerical value between 0 (unburned) and 3 (highly burned) representing the average burn severity at a specific site. The poor spatial representation and the considerable effort to gather field estimates of burn severity over large areas make the use of remotely sensed data not only advisable but crucial. The estimation of burn severity from satellite data is currently accomplished using vegetation indices derived from optical sensors, data being routinely processed using the normalized burn ratio (NBR) (Key and Benson 2006) in a bi-temporal approach (dNBR) with pre- and post-fire images (1).

$$dNBR = \frac{(R4-R7)}{(R4+R7)}pre - \frac{(R4-R7)}{(R4+R7)}post \quad \{1\}$$

where: R is per pixel reflectance for Landsat TM bands.

NBR combines information from near- and mid-infrared wavelengths whereas dNBR expresses the magnitude of the environmental change caused by fire, unburned areas retaining values close to zero (i.e. little or no change). Generally, dNBR coupled with CBI provided accurate detection of burn severity (R^2>0.75) (Allen and Sorbel 2008; Cocke et al. 2005; Epting et al. 2005; Wagtendonk et al. 2004). However, some authors (Hoy et al. 2008; Landmann 2003; Murphy et al. 2008) reported weaker relationships between dNBR and CBI in savannas, tropical or boreal forests. This was attributed to dNBR`s inability to discern between high severity sites, to variations in topography and solar elevation angle (Verbyla et al. 2008) or the specific fuel conditions (Kasischke et al. 2008).

The use of synthetic aperture radar (SAR) data could overcome the often encountered problem of optical-based spectral indices, i.e. the discrimination of the intermediate burn severities (Chuvieco et al. 2006). Since the backscattered signal contains information on forest structure, removal of leaves and branches by fire directly influences the signal from forests. Previous work confirmed the utility of SAR data for burnt area mapping (Bourgeau-Chavez et al. 2002; Gimeno et al. 2002), the estimation of burn severity (Bourgeau-Chavez et al. 1994) or of parameters related to variations in burn severity (Kasischke et al. 1994). Statistically significant relations have been found between radar backscatter and burn severity expressed by means of dNBR (Tanase et al. 2010). The backscattering coefficient expresses the total intensity received by the radar after scattering, thus not giving information about the structural arrangement of the individual scatterers within the forest volume. SAR interferometry provides instead a

direct measure of the distribution of the scatterers in a forest structure through the phase information. Furthermore, the degree of interferometric coherence or simpler the coherence measures the correlation between the backscattered signal from a given target seen under two slightly different look angles, thus being related to temporal and geometric decorrelation effects (Askne et al. 1997; Zebker and Villasenor 1992). Coherence takes values between 0 (total decorrelation) and 1 (no decorrelation).

Coherence and interferometric phase are affected by a number of factors related to SAR frequency, image acquisition geometry, spatial separation in space between antennas and temporal interval between the two image acquisitions (Bamler and Hartl 1998). In a repeat-pass scenario, i.e. when the two images forming an interferometric pair are acquired with a certain separation in time, coherence is primarily influenced by the latter factor, which causes temporal decorrelation. Temporal decorrelation is determined by changes in the arrangement of the scatterers within the resolution cell, thus meaning that the sensitivity to temporal decorrelation is frequency-dependent. In forested areas wind is considered the main source of temporal decorrelation (Askne et al. 2003; Castel et al. 2000; Gaveau et al. 2000). Rapid decorrelation takes place even for low wind speeds (Askne et al. 2003) in particular for high-frequency SAR systems (X- and C- band) for which a large proportion of scattering originates within the first few meters of the canopy where temporally unstable scatterers are located (twigs, needles, small branches). Other sources of temporal decorrelation are related to variations of the environmental conditions such as precipitation and freeze/ thaw events (Askne and Santoro 2009; Koskinen et al. 2001; Santoro et al. 2002) or the soil moisture distribution within a resolution cell (Luo et al. 2001).

The slight separation in space between the antennas, referred to as interferometric baseline, implies that the spectra of the two images being interfered are slightly shifted with respect to each other. If not accounted for, the spectral shift causes spatial decorrelation (Gatelli et al. 1994). While this can be compensated for if information about the orientation of the resolution cell is available in case of surface scattering, a residual part remains in case of layered media (Hagberg et al. 1995). The residual decorrelation goes under the name of volume decorrelation. Residual spatial decorrelation, in case of uncompensated topography within the resolution cell, and volume decorrelation, in case of layered media, increase with increasing perpendicular component of the interferometric baseline (Askne et al. 1997; Hagberg et al. 1995). Volume decorrelation is also directly related to the thickness of the volume. As a result of the effect of temporal and volume decorrelation, the interferometric coherence in case of repeat-pass acquisitions is significantly lower over dense mature forest than in case of small vegetation and bare soils (Wegmüller and Werner 1995). The dynamic range of coherence between young forest and dense mature forest is related to the stability of the weather conditions throughout the interval between the acquisition of the two images forming the interferometric pair.

The potential of repeat-pass coherence in forest-related applications has been shown in a number of thematic applications including forest mapping (Castel et al. 2000; Wegmüller and Werner 1997), change detection (Smith and Askne 2001) and retrieval of bio- and geophysical properties (Askne et al. 2003; Eriksson et al. 2003; Santoro et al. 2002). In forests affected by fires coherence increased significantly with respect to unburned forests for European Remote Sensing Satellite (ERS) VV polarized and Japanese Earth Remote Sensing 1 (JERS-1) HH polarized data (Liew et al. 1999; Takeuchi and Yamada 2002). Most investigations were carried out using ERS-1/2 tandem coherence because of the short repeat-pass interval and the nearly global

availability of archived data. Few investigations were carried out at L-band with HH-polarized JERS-1 data. The long repeat-pass and the temporally variable interferometric baseline did not favor forest applications. X-band interferometric data from space has been previously acquired during the SIR-C mission but only in single-pass mode. Polarization effects on the interferometric signatures have not been investigated yet, according to our knowledge.

For X- and C-band the repeat-pass coherence of burned forests is primarily affected by temporal decorrelation due to the movement of the forest elements within the canopy. The removal of the needles and small twigs reduces the strongest decorrelation source of forest since the remaining branches are less susceptible to movement by wind. This reduces the decorrelation of the low- and moderately- burned forest contributing to the increased coherence of the burned areas. The level observed for bare soils is in theory reached for areas with complete combustion of the vegetation since scattering would originate from the large branches and stem, which are less affected by temporal and volume decorrelation. The frequent occurrence of forest fires at several locations in Spain and the recent availability of SAR data acquired at different frequencies, polarization states and suitable for interferometry suggested investigating to what extent the interferometric coherence can be used for burn severity assessment. The moderate topography of typical mediterranean pine forests and the different environmental conditions at the time of image acquisition allowed studying the relative contribution of geometric and temporal decorrelation to the total forest coherence.

The objectives of the study were to:

1. investigate the signatures of interferometric repeat-pass coherence response in relation to burn severity at X-, C- and L- band;
2. infer the prediction power of interferometric coherence for burn severity estimation for each frequency;
3. assess the role of the local incidence angle and weather conditions on coherence and on the prediction power of coherence for burn severity evaluation.

This study complements a parallel investigation on burn severity assessment using SAR intensity data from the same sensors considered here (Tanase et al. in press). Since the factors determining the SAR backscatter and the interferometric coherence are different and the interferometric dataset could be formed only at a later stage, it was decided to report the results on the signatures of the two radar observables separately. Nonetheless, for a complete overview of the usefulness of SAR data in burn severity estimation, reference to the results obtained with the backscatter is given. In addition, the joint use of backscatter and coherence is also addressed.

STUDY AREA

The study area was located in central Ebro Valley, Spain (Fig.1) which is the northernmost semi-arid region in Europe. The climate is Mediterranean with continental characteristics and annual precipitations above the average of the Ebro valley. Most of the study area stretches on moderate topography elevation ranging from 500 m to 750 m above sea level. The dominant land cover includes forests interspersed with winter cereal crops. The vegetation is xerophilous, drought resistant and highly flammable providing abundant fuels after long periods without rain.

The forest extends on approximately twenty-two thousands hectares of homogeneous, even aged pine forests of *Pinus halepensis L.* as a result of rural

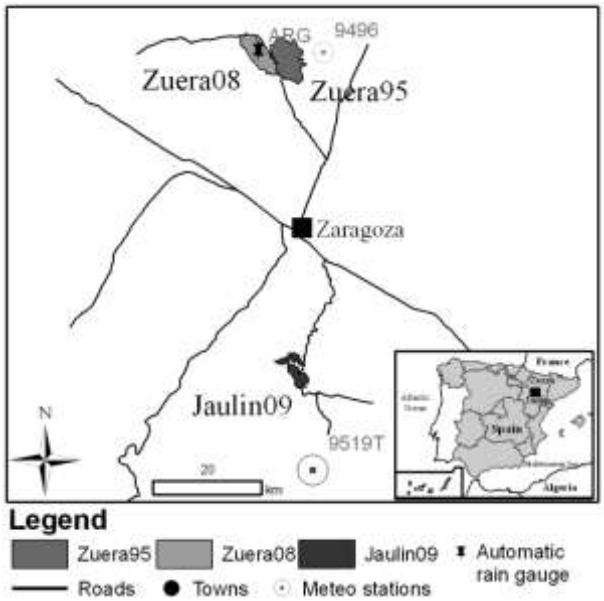

Fig. 1 The study area and the forest fire sites.

economic activities cease and past reforestation projects. The lithology is characterized by limestone and marl sediments arranged on horizontal layers that contribute to its aridity, since soils are unable to retain water as a consequence of the high hydraulic conductivity. Three sites (Fig. 1) were affected by fire during the last two decades. Around 3100 ha burned between 23 and 25 of June 1995 due to a spark from a farming tractor (test site: Zuera95). The second fire (test site: Zuera08) ignited on August 6, 2008 after a traffic accident and affected around 2200 ha by the second day whereas the third fire (test site: Jaulin09) was ignited by a thunderstorm and burned approximately 1700 ha between 21 and 23 of July, 2009.

SATELLITE DATA AND ANCILLARY DATASETS

The SAR dataset consisted of images acquired by the ERS sensors (ERS-1/2) during the tandem mission over the Zuera95 test site, the Environment Satellite Advanced Synthetic Aperture Radar (Envisat ASAR) and the TerraSAR-X sensor (TSX) over the Zuera08 test site, and the Advanced Land Observing Satellite (ALOS) Phased Array type L-band SAR (PALSAR) over the Jaulin09 test site. Table 1 illustrates the main characteristics of the SAR image datasets and related processing information. The temporal baseline (Bt), i.e. the separation in time between two images forming an interferometric image pair, ranged between one day (ERS-1/2 tandem mission) and several repeat-pass cycles. Generation of coherence from two different scenes implies a number of processing steps which could be grouped into pre-processing, coherence estimation and post-processing. The pre-processing step consisted in improvement of the orbital state vectors when possible (ERS-1/2 and Envisat ASAR) and co-registration (less than one pixel RMSE) of the scenes from the same sensor and track. To limit the noise component of the interferometric products spatial multi-looking was applied (Table 1). In the interferogram computation common band filtering was applied to only

consider the overlapping part of the reflectivity spectra in range and azimuth. Then, the differential interferograms were generated (on pair by pair basis), subtracting the simulated topographic phase based on an available digital elevation model (DEM) with a spatial resolution of 20 m. The coherence was estimated using the differential interferogram as phase correction term with an estimation approach based on an adaptive window size between 3×3 and 9×9 pixels (Wegmüller et al. 1998). Post processing included geocoding of the coherence products to Universal Transverse Mercator (UTM) 30 coordinate system. Because of the higher spatial resolution the TerraSAR-X scenes were geocoded to 10 m pixel spacing. The ERS-1/2, Envisat ASAR and ALOS PALSAR scenes were geocoded to 25 m.

Three pairs of Landsat 5 Thematic Mapper (TM) images recorded before and immediately after each fire event were also acquired. Details on the image datasets for each test site are described in the following related Sections.

Zuera95 site

For this site eight images acquired during the ERS-1/2 tandem mission were considered. Three one-day image pairs and ten image pairs with 35-, 70- and 105 days repeat-pass were formed. The test site was covered by images acquired along two ascending orbital tracks (58 and 330). Table 2 provides information on the acquisition dates and the perpendicular component of the baseline for the analyzed combinations. The baselines were estimated from the orbital data. The Landsat scenes (path 199, row 031) were acquired on March 28 (pre-fire) and August 3 (post-fire), 1995. Detailed information regarding calibration, atmospheric and geometric corrections of the scenes is given in (Vicente-Serrano et al. 2008). Fig. 2 shows the post-fire Landsat TM image and the coherence image product (red: coherence; green: backscatter, blue: backscatter ratio) for the image pair acquired on 1996.03.28/29. In the Landsat image the fire scar can be distinguished from the surrounding unburned forest which appears in different shades of green. Burn severity expressed by means of dNBR was superimposed over the fire scar using the intervals proposed in (Key and Benson 2006). The agricultural fields were masked out when computing the burn severity. The coherence image product shows up primarily in red and orange because of overall high coherence and constant backscatter. Yellow tones appear in areas of higher backscatter corresponding to burned areas. The backscatter difference is overall very small except for a few agricultural fields. Forests appear in green nuances due to the increased backscatter.

Table 1 SAR data characteristics and processing parameters.

Satellite/Parameter	ERS-1/2	Envisat ASAR	TerraSAR-X	ALOS PALSAR
Band [wavelength cm]	C- [5.7]	C- [5.7]	X- [3.1]	L- [23.6]
Pass	ascending	descending	descending	ascending
Acquisition mode	-	Image	StripMap	Fine Beam Dual
Repeat-pass cycle (days)	1 and 35	35	11	46
Incidence angle	23°	23º	40º	34°
Polarization	VV	HH	HH, HV	HH,HV
Range pixel spacing	7.9 m	7.8 m	0.9 m	9.4 m
Azimuth pixel spacing	4.0 m	4.0 m	2.4 m	3.1 m
Multi-look factor(range/azimuth)	1/5	1/5	8/5	2/10
Spacing of geocoded images	25 m	25 m	10 m	25 m
Geolocation error	~2.5 m	~2.5 m	~0.75 m	~2.5 m
Projection / Ellipsoid/ Datum	UTM 30 / International 1924/ European 1950			

Table 2 Perpendicular baseline and meteorological conditions at image acquisition for the ERS1/2 image pairs over the Zuera95 test site: maximum temperature (Tmax), minimum temperature (Tmin) and the accumulated precipitations (AcPp).

Track	Acquisition date 1	Acquisition date 2	Perpendicular baseline (m)	Temporal baseline (days)	Average wind speed (m/s)	Tmax (°C) date1	Tmin (°C) date1	AcPp (mm) date1	Tmax (°C) date2	Tmin (°C) date2	AcPp (mm) date2
	1995.12.14	1995.12.15	262.9	1	2.9 / 0.0	4	-6	1	0	-5.5	27.5
	1995.12.14	1996.01.19	599.2	35	2.9 / 2.5	4	-6	1	10	-2	1.3
	1995.12.14	1996.03.28	688.7	105	2.9 / 5.3	4	-6	1	15	5	0
58	1995.12.14	1996.03.29	746.5	106	2.9 / 2.1	4	-6	1	17.5	6	0
	1995.12.15	1996.01.19	336.4	34	0.0 / 2.5	0	-5.5	27.5	10	-2	1.3
	1995.12.15	1996.03.28	425.9	104	0.0 / 5.3	0	-5.5	27.5	15	5	0
	1995.12.15	1996.03.29	483.7	105	0.0 / 2.1	0	-5.5	27.5	17.5	6	0
	1996.01.19	1996.03.28	89.5	70	2.5 / 5.3	10	-2	1.3	15	5	0
	1996.01.19	1996.03.29	147.4	71	2.5 / 2.1	10	-2	1.3	17.5	6	0
	1996.03.28	1996.03.29	57.8	1	5.3 / 2.1	15	5	0	17.5	6	0
	1995.11.28	1996.01.02	137.8	35	1.8 / 2.4	12	-4	0	12	4	17.5
330	1995.11.28	1996.01.03	-112.6	36	1.8 / 1.7	12	-4	0	11	0	4.5
	1996.01.02	1996.01.03	250.5	1	2.4 / 1.7	12	4	17.5	11	0	4.5

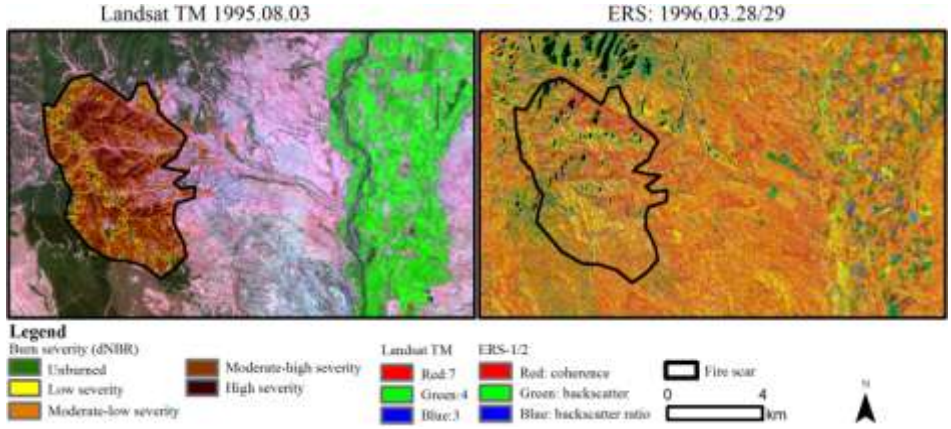

Fig. 2 Burn severity as revealed by Landsat TM (left) and ERS-1/2 (1996.03.28/29, Bn 58 m, Bt 1 day) coherence product (right). Zuera95 test site.

Zuera08

For the Zuera08 site six TerraSAR-X dual-polarized images (HH- and HV-polarization) were available from which 15 interferograms with reasonable coherence could be obtained. From two Envisat ASAR single-polarized (HH-polarization) images one interferogram could be obtained. Acquisition dates and interferometric baselines (Bn) estimated from the orbital data are presented in Table 3. The Landsat dataset was formed by two scenes (pre-fire 2008.07.21 and post-fire 2008.08.22) from the same path and row as for the 1995 fire. Subsets of the two Landsat scenes were calibrated, atmospherically corrected and orthorectified using a linear polynomial model and incorporating information of the local topography. Detailed information regarding the processing method of the Landsat TM scenes for the Zuera08 test site is given in (Tanase et al. 2010).

Table 3 Perpendicular baseline and meteorological conditions at the time of image acquisition for Envisat ASAR and TerraSAR-X image pairs acquired over Zuera08 test site and for the ALOS PALSAR image pair acquired over the Jaulin09 test site: maximum temperature (Tmax), minimum temperature (Tmin) and the accumulated precipitations (AcPp).

Sensor	Acquisition date 1	Acquisition date 2	Perpendicular baseline (m)	Temporal baseline (days)	Average wind speed (m/s)	Tmax (°C) date1	Tmin (°C) date1	AcPp (mm) date1	Tmax (°C) date2	Tmin (°C) date2	AcPp (mm) date2
ASAR	2009.01.08	2009.02.12	33.7	35	2.3 / 6.7	0	-6	0.5	10	4	0.5
	2008.11.16	2008.12.19	-230.8	33	4.4 / 7.4	14	-2	0	11	4	0
	2008.11.16	2009.01.21	-108.9	66	4.4 / 3.8	14	-2	0	7	-3	2.3
	2008.11.16	2009.02.12	-242.5	88	4.4 / 7.8	14	-2	0	10	4	0.5
	2008.11.16	2009.02.23	3.5	99	4.4 / 9.0	14	-2	0	12	5	0
	2008.11.16	2009.03.06	165.8	110	4.4 / 8.4	14	-2	0	9	1	21.3
	2008.12.19	2009.01.21	121.9	33	7.4 / 3.8	11	4	0	7	-3	2.3
TSX	2008.12.19	2009.02.12	-11.7	55	7.4 / 7.8	11	4	0	10	4	0.5
	2008.12.19	2009.02.23	234.3	66	7.4 / 9.0	11	4	0	12	5	0
	2008.12.19	2009.03.06	65.0	77	7.4 / 8.4	11	4	0	9	1	21.3
	2009.01.21	2009.02.12	-133.6	22	3.8 / 7.8	7	-3	2.3	10	4	0.5
	2009.01.21	2009.02.23	112.4	33	3.8 / 9.0	7	-3	2.3	12	5	0
	2009.01.21	2009.03.06	-56.9	44	3.8/ 8.4	7	-3	2.3	9	1	21.3
	2009.02.12	2009.02.23	246.0	11	7.8 / 9.0	10	4	0.5	12	5	0
	2009.02.12	2009.03.06	76.7	22	7.8 / 8.4	10	4	0.5	9	1	21.3
	2009.02.23	2009.03.06	169.3	11	9.0 / 8.4	12	5	0	9	1	21.3
ALOS	2009.08.20	2009.10.05	503.6	46	-	34	15	0	26	11	0

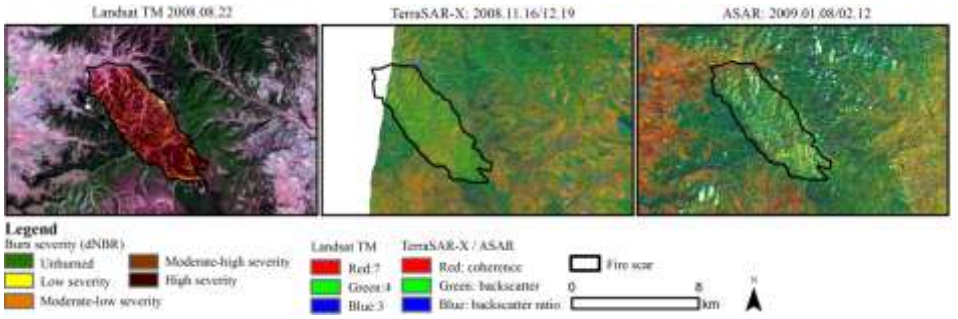

Fig. 3 Burn severity as revealed by Landsat TM (left), TerraSAR-X HH-polarization (2008.11.16/12.19 Bn 231 m, Bt 33 days) coherence product (center) and Envisat ASAR HH-polarization (2009.01.08/02.12, Bn 34 m, Bt 35 days) coherence product (right). Zuera08 test site.

Fig. 3 shows the area of the Zuera08 test site as imaged by Landsat TM, Envisat ASAR and TerraSAR-X sensors. The moderate coherence (0.3-0.5) inside the fire perimeter and moderate backscatter helps differentiating the burned area (predominantly yellow-greenish colors) from the adjacent bare soil characterized by higher (0.6-0.7) coherence and lower backscatter (predominantly red/orange colors). In the TerraSAR-X coherence product the fire scar appears greener compared to Envisat ASAR coherence product as a consequence of the increased backscatter from small twigs and branches. The unburned forest appears in green-bluish tones at both X- and C- band as a consequence of low coherence and high backscatter. dNBR values were superimposed on the Landsat image over the area affected by the fire as in Fig. 2.

Jaulin09

Two ALOS PALSAR dual polarized images recorded immediately after fire (2009.08.10 and 2009.10.05) were used for the analysis (Table 3). Subsets of Landsat TM scenes acquired on 2009.06.22 (pre-fire) and 2009.09.26 (post-fire) were processed using the same method as for the Zuera08 site. Although the Landsat images pairs used to compute the dNBR were corrected using slightly different approaches, the design of NBR removes at least partially within–scene topographic effects and between-scenes solar illumination effects (Key and Benson 2006). Moreover, the Landsat TM datasets were not used for multi-temporal studies, each one being analyzed with respect to the corresponding SAR datasets. Fig. 4 illustrates the fire scar and the surrounding area as imaged by Landsat TM and ALOS PALSAR satellites. The burn severity is expressed by dNBR intervals as for the other two sites. For ALOS PALSAR two coherence image products are shown corresponding to the HH and HV datasets, respectively. Unburned areas appear in yellow color as a consequence of high coherence, high backscatter and small backscatter change whereas the burned area appears in blue as a consequence of a low coherence and backscatter, and strong backscatter change between the images after the fire event.

Ancillary datasets

To aid the interpretation, meteorological data collected from stations located close to the fire scars (see also Fig. 1) were provided by the Spanish national meteorological agency (AEMET). The daily maximum and minimum temperatures and the accumulated precipitations (AcPp) during 4 days previous to acquisitions are presented in Tables 2 and 3. Since the fire scars were located at different altitudes with respect to the meteorological stations the average temperatures were adjusted with the environmental lapse rate (i.e. -2° C / 300 m). For the Zuera08 site the accumulated precipitations were obtained from an automatic rain gauge (ARG) installed roughly at the center of the fire perimeter. Measurements of wind speed were not available within the perimeter of the fire-affected sites. The station closest to the test sites where wind speed was recorded was located at the airport of Zaragoza (35 km south and respectively 25 km north of the sites). Wind speed was measured hourly. The average wind speed was computed using 3 hours intervals centered at the time of image acquisition.

Field estimates of burn severity were collected at the Zuera08 and Jaulin09 sites within two months after the fires. Respectively 123 and 45 CBI plots were assessed in

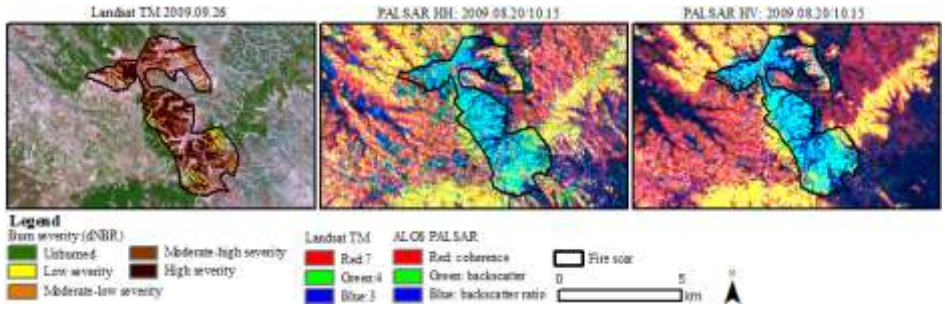

Fig. 4 Burn severity as revealed by Landsat TM (left) and ALOS PALSAR (2009.08.20/10.05, Bn 504 m, Bt 46 days) coherence product: HH-polarization (center) and HV-polarization (right). Jaulin09 test site.

high, moderate and low severity burnt areas. The description of the field work together with photos illustrating different fire severity levels encountered within Zuera08 fire perimeter were presented in (Tanase et al. 2010). Field evaluation of burn severity for Jaulin09 scar was conducted in a similar fashion and the similar forest structure and fire regime resulted in comparable burn conditions. In low severity areas, litter and understory were partially affected while the trees remained largely unaffected. The moderate severity areas presented increasing consumption of litter, understory and the tree canopy whereas in high severity areas the consumption of the understory layer and tree canopy was complete. For the highest severities small and medium sized branches were also consumed.

METHODS

Evaluation of the coherence over burned areas was carried out using descriptive statistics whereas determination coefficients (R^2) and the root mean square error (RMSE) were used to evaluate the potential of interferometric coherence for burn severity estimation. In addition, the roles of the local incidence angle and weather conditions on coherence were evaluated. To reduce the effect of topography the analysis was carried out by 5º intervals of local incidence angle. This interval represented a trade-off between identifying consistent behavior of coherence and backscatter for given range of local slope and the number of samples within each class (see also Tanase et al. 2010). A higher sampling rate increased the data noise whereas for lower sampling rates the topography-induced effects on the coherence and the backscatter were less evident.

Due to the limited number of reference CBI plots where burn severity was assessed in situ it was preferred to prioritize the study on the basis of a set of surrogate plots, hereafter referred to as pseudo-plots. Pseudo-plots are based on optical estimates of burn severity. The consistency between CBI plots and remotely sensed (dNBR) estimates of burn severity was previously assessed at the Zuera08 site (Tanase et al. 2010). For the most recent fire at the Jaulin09 site, similar results were found. The high determination coefficients (R^2 = 0.81 and R^2 = 0.83, $p<0.05$) between field and remotely sensed estimates supported the use of dNBR as a radiometric index related to the severity levels recorded in the field. Since Zuera95 site presented similar forest structure and tree species compared to the other two test sites we considered appropriate to generalize the use of dNBR for studying 1995 fire, despite the lack of burn severity field estimates.

The pseudo-plots were generated by averaging pixels of similar dNBR for the same local incidence angle rounded to unity. The minimum number of pixels to be averaged within a pseudo-plot implied a trade-off between coherence variance and the number of pseudo-plots available for each severity level. On one hand it is likely that for larger pseudo-plots the variance of the coherence decreases; on the other hand the number of samples at low-medium burn severity decreased significantly when a high number of pixels/pseudo-plot was considered. Pseudo-plots of different sizes were generated and their frequency distribution by local incidence angle intervals was studied. For the imagery with lower spatial resolution (ERS-1/2 and Envisat ASAR) pseudo-plots including 9 pixels, i.e. corresponding to approximately 0.55 ha, provided the best trade-off between the number of plots for each local incidence angle interval and the standard deviation of coherence at pseudo-plot level. For the higher spatial resolution TerraSAR-X data pseudo-plots including 25 pixels, corresponding to 0.25 ha, were selected. From the generated pseudo-plots 900 were randomly selected for the statistical analysis.

RESULTS

Coherence properties of burned areas

To investigate the dependency of the coherence upon local topography plots of coherence as a function of burn severity have been generated for slopes oriented towards the sensor, flat areas and slopes oriented away from the sensor. To minimize the effect of weather conditions on the analysis images acquired under dry and unfrozen environmental conditions were preferred were available. For the Zuera95 site ERS-1/2 coherence is plotted as a function of dNBR in Fig. 5. For the Zuera08 site 35-days Envisat ASAR HH-polarized coherence is plotted in Fig. 6 whereas TerraSAR-X HH-polarized coherence is plotted in Fig 7. A 33-days TerraSAR-X pair is shown since both 11-days pairs available were affected by rainfall. X-band cross-polarized coherence is not presented since its sensitivity to burn severity was practically negligible and close to the bias level of 0.1. HH and HV polarization L-band coherence is presented as a function of dNBR for the Jaulin09 site in Fig. 8 and 9, respectively. To provide a measure of reference for the highest measured coherence, the average value for bare soil was computed and included in the form of a horizontal line in each of the plots from Fig. 5 to 9. To provide an idea of the coherence bias the average coherence over water was computed. The mean value was around 0.07-0.09 for C-band data and approximately 0.04 for L-band data. For X-band data the average coherence over water could not be computed since no water body of sufficient size was found within the area covered by the images. To evaluate the association between field- and remotely-sensed estimates of burn severity the CBI plots were overlaid on the dNBR pseudo-plots where available.

In (Castel et al. 2001) it was reported that in the case of grassland the ERS-1/2 tandem coherence for slopes facing the radar were characterized by strong spatial decorrelation compared to other aspect angles for an at least 10 degrees slope angle. Fig. 10 shows the coherence of unburned forests versus the local aspect angle for a given range of local incidence angles. An aspect angle of 270° corresponds to a normal terrain surface pointing in the direction of the radar sensor.

The effect of changing weather between image acquisitions on coherence is presented in Fig. 11. To avoid distortions due to topography, only pseudo-plots located on flat terrain were considered. Two image pairs affected by rainfall are shown for X- and C-band for which multiple datasets were available. The coherence from a third pair acquired under dry conditions is displayed for reference. At X-band the images affected by rainfall were acquired on 2009.02.12 (0.5 mm) and 2009.03.06 (21.3 mm). At C-band rainfall was registered during the acquisition of 1995.12.15 (27.5 mm) and prior to the acquisition of the 1996.01.02 (17.5 mm) images.

Burn severity evaluation

To infer the utility of the intererometric coherence for burn severity estimation, a second order polynomial model was used. This model form provided better fit compared to a linear model given the non linear trend of the data at high burn severities. The determination coefficients (R^2) expressing the proportion of burn severity variance predicted by the coherence are presented in Table 4. The empirical fitting was evaluated

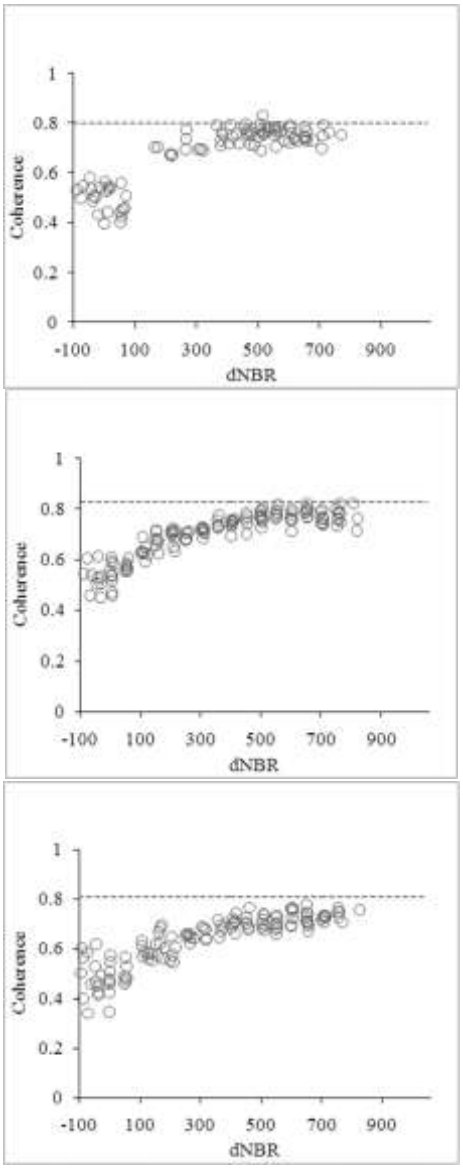

Fig. 5 Plots of ERS-1/2 C-band coherence (VV-polarization) as a function of burn severity (dNBR) for the Zuera95 test site (top slopes oriented towards sensor, center flat areas, bottom slopes oriented away from the sensor). Dashed horizontal lines represent the average coherence for bare soil nearby the test site.

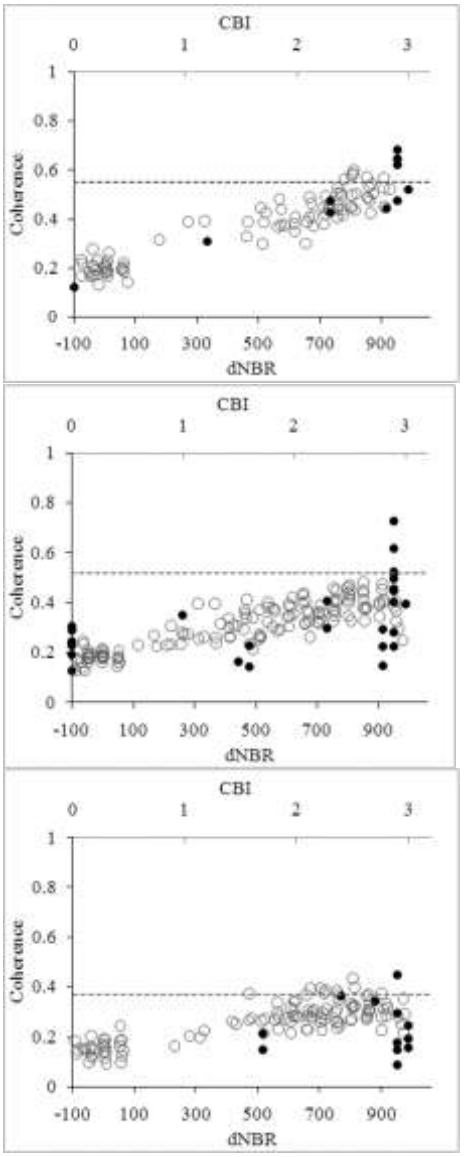

Fig. 6 Plots of Envisat ASAR C-band coherence (HH-polarization) as a function of burn severity (dNBR) for the Zuera08 test site (top slopes oriented towards sensor, center flat areas, bottom slopes oriented away from the sensor). The filled circles represent measurements of CBI. Dashed horizontal lines represent the average coherence for bare soil nearby the test site.

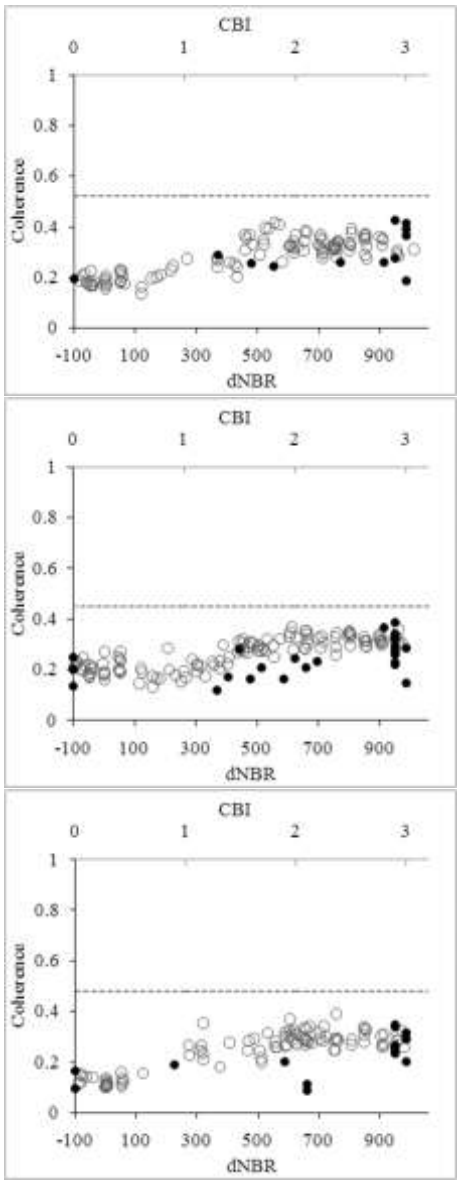

Fig. 7 Plots of TerraSAR-X X-band coherence (HH-polarization) as a function of burn severity for the Zuera08 test site (top slopes oriented towards sensor, center flat areas, bottom slopes oriented away from the sensor). The filled circles represent measurements of CBI. Dashed horizontal lines represent the average coherence for bare soil nearby the test site.

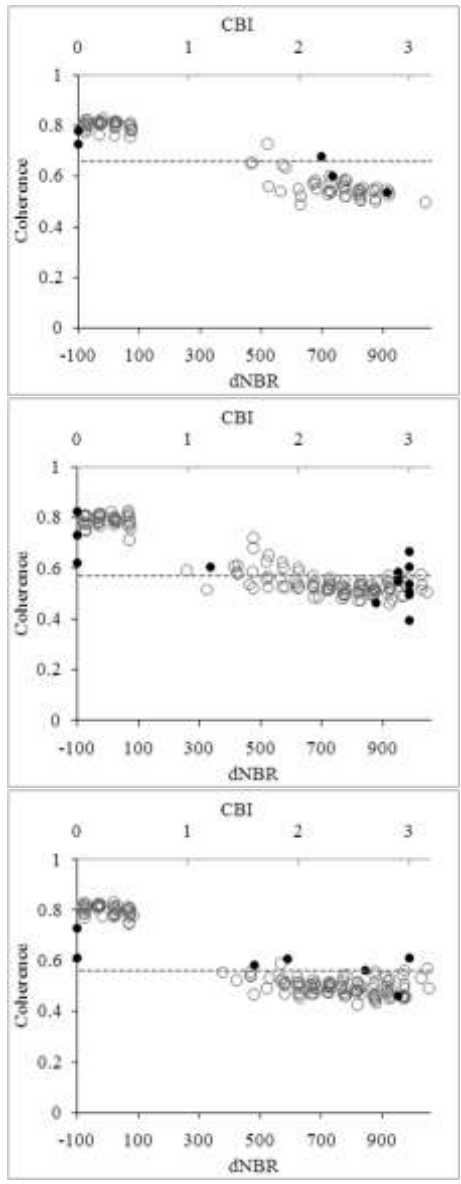

Fig. 8 Plots of ALOS PALSAR L-band coherence (HH-polarization) as a function of burn severity for the Jaulin09 test site (top slopes oriented towards sensor, center flat areas, bottom slopes oriented away from the sensor). The filled circles represent measurements of CBI. Dashed horizontal lines represent the average coherence for bare soil nearby the test site.

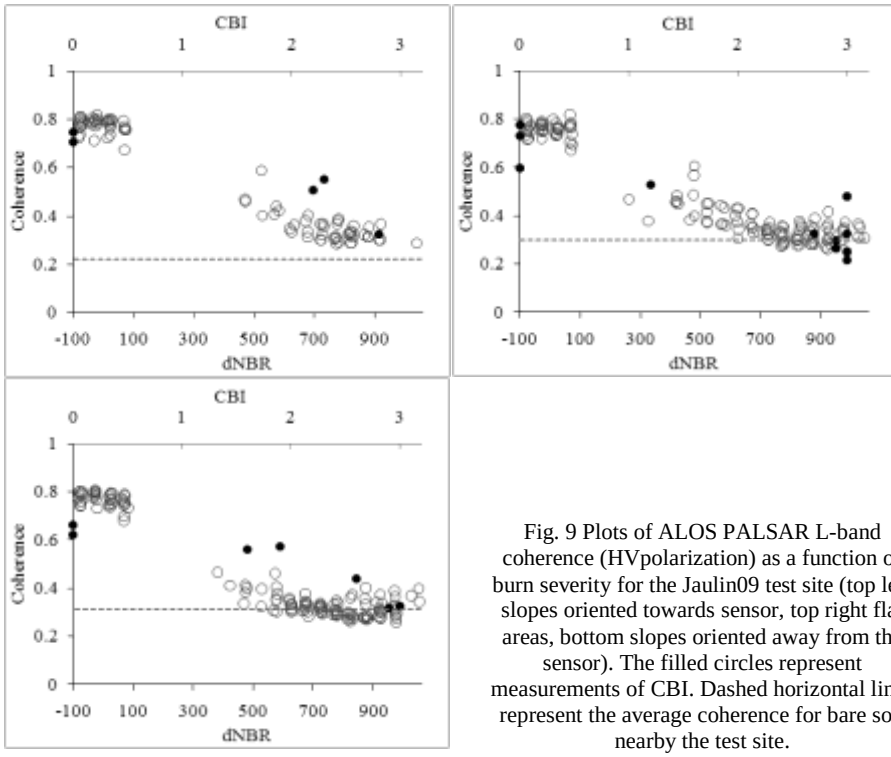

Fig. 9 Plots of ALOS PALSAR L-band coherence (HVpolarization) as a function of burn severity for the Jaulin09 test site (top left slopes oriented towards sensor, top right flat areas, bottom slopes oriented away from the sensor). The filled circles represent measurements of CBI. Dashed horizontal lines represent the average coherence for bare soil nearby the test site.

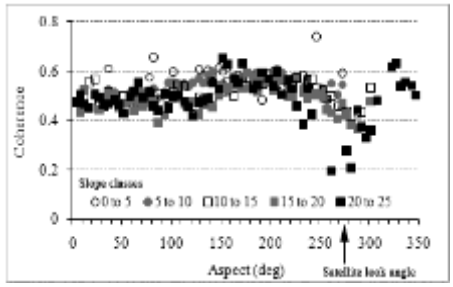

Fig. 10 Average coherence of unburned forest as a function of aspect for different ranges of local slope angle.

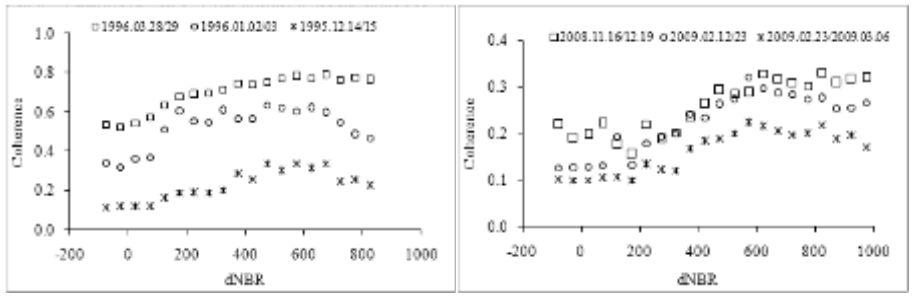

Fig. 11 Coherence with respect to burn severity (dNBR) for image pairs acquired under different types of environmental conditions. Squares are used for image pairs acquired under stable conditions. Circles and crosses are used for image pairs acquired under unstable conditions. Left: ERS-1/2 tandem coherence; right: TerraSAR-X.

using the RMSE between observed and predicted dNBR after randomly splitting the 900 selected pseudo-plots into training (75%) and validation (25%) sets. Ten iterations were used in order to obtain the average fit of each model and avoid exceptional high determination coefficients and low errors due to random effects (Table 4). Although the dependence of the interferometric coherence on topography appears to be less pronounced than for the SAR backscatter intensity (Castel et al. 2000; Santoro et al. 2007; Wegmüller and Werner 1995) the RMSE and R^2 were computed at two levels: using all available pseudo-plots and by local incidence angle intervals of 5º. For the analysis, image pairs which showed limited influence of changing weather conditions were selected when available:

- 1996.03.28/29 (ERS-1/2 tandem mission),
- 1996.01.19/03.28 (ERS-1/2),
- 2009.01.08/12.12 (Envisat ASAR),
- 2008.11.16/.12.19 (TerraSAR-X) and
- 2009.08.20/10.05 (ALOS PALSAR).

The prediction power of a joint use of coherence and backscatter coefficient for burn severity assessment was analyzed at each frequency using generalized linear models (GLZ). GLZ allowed predicting burn severity using multiple, nonlinearly related independent variables (Agresti 2007). Burn severity values were predicted from a linear combination of coherence and backscatter connected to the dependent variable via a link function (Table 5 and 6). The statistical significance was tested using the likelihood ratio. The distribution of the burn severity was assumed to be normal. For the TerrsaSAR-X, ERS-1/2 and Envisat ASAR datasets a power link function was used whereas for the ALOS PALSAR dataset a log function provided the highest variability explained by the models. The statistic fit of each model was evaluated using the deviance (D^2) interpreted as the proportion of variability explained by the model. The Akaike`s information criterion (AIC) was used to test which of the models best predicts burn severity (Akaike 1974). For each dataset the competing models may be ranked

Table 4 Determination coefficients explaining the agreement between burn severity (dNBR plots) and the interferometric coherence.

sensor	TerraSAR-X		ERS-1/2 tandem		Envisat ASAR		ERS		ALOS PALSAR			
dataset	2008.11.16/12.19		1996.03.28/29		2009.01.08/02.12		1996.01.19/03.28		2009.08.20/10.05			
Polarization	HH		VV		HH		VV		HH		HV	
	R^2	RMSE	R^2	RMSE	R^2	RMSE	R^2	RMSE	R^2	RMSE	R^2	RMSE
all pseudo-plots												
	0.640	159.5	0.650	117.0	0.489	199.9	0.466	152.3	0.912	95.6	0.939	82.2
pseudo-plots grouped by local incidence angle												
6-10	-	-	0.754	103.9	0.947	156.5	0.717	114.0	-	-	-	-
11-15	-	-	0.686	121.2	0.881	102.5	0.618	147.5	-	-	-	-
16-20	0.937	99.7	0.700	104.9	0.843	113.4	0.581	130.5	-	-	-	-
21-25	0.941	88.6	0.797	87.0	0.752	127.6	0.450	162.6	0.961	70.2	0.958	73.9
26-30	0.880	112.4	0.774	83.3	0.772	113.3	0.585	132.8	0.952	62.8	0.961	67.6
31-36	0.779	146.0	0.805	92.6	0.738	150.3	0.568	137.7	0.934	81.1	0.951	79.3
36-40	0.708	123.3	0.738	96.6	0.765	132.7	0.585	117.6	0.889	103.5	0.921	91.4
41-45	0.670	158.1	0.737	100.2	0.716	185.2	0.493	150.0	0.896	113.1	0.917	99.7
46-50	0.764	155.7	0.805	106.8	0.548	222.2	0.597	168.7	0.922	93.7	0.936	82.0
51-55	0.787	139.7	-	-	-	-	-		0.959	60.1	0.971	61.6
56-60	0.871	119.9	-	-	-	-	-	-	0.954	58.3	0.967	42.8
61-65	0.899	91.4	-	-	-	-	-	-	-	-	-	-

all models were extremely significant ($p<0.001$)

Table 5 Models fit statistics for the single and the joint use of the independent variables SAR backscatter and interferometric coherence when predicting burn severity (dNBR) in the case of X- and C-band data. The subscripts next to the polarization indicate the SAR metric (b=backscatter, c=coherence).

	TerraSAR-X 2008.11.16/12.19						Envisat ASAR 2009.01.08/02.12				ERS-1/2 1996.03.28/29			
model	HH_c		HH_c& HH_b		HH_c& HV_b		HH_c		HH_c& HH_b		VV_c		VV_c& VV_b	
	D^2	AIC	D^2	AIC	D^2	AIC	D^2	AIC	D^2	AIC	D^2	AIC	D^2	AIC
6-10							0.925	446	0.938	442	0.747	1133	0.788	1119
11-15							0.800	1173	0.801	1175	0.655	1483	0.659	1483
16-20	0.907	296	0.932	290	0.955	280	0.758	1568	0.758	1570	0.699	1626	0.707	1625
21-25	0.910	711	0.911	712	0.918	708	0.672	1913	0.672	1915	0.793	1654	0.804	1649
26-30	0.813	979	0.816	980	0.847	966	0.633	1790	0.639	1790	0.783	1531	0.804	1520
31-36	0.608	1451	0.629	1448	0.723	1416	0.571	1562	0.572	1563	0.797	1504	0.816	1494
36-40	0.638	1674	0.653	1671	0.683	1660	0.636	1453	0.638	1454	0.732	1334	0.739	1333
41-45	0.664	1648	0.686	1642	0.703	1635	0.530	1320	0.530	1322	0.741	629	0.766	626
46-50	0.679	1371	0.689	1370	0.736	1353	0.460	718	0.460	720	0.787	230	0.788	232
51-55	0.664	1243	0.666	1245	0.708	1232								
56-60	0.795	1218	0.803	1216	0.806	1215								
61-65	0.795	834	0.836	821	0.800	834								

all models were extremely significant ($p<0.001$)

Table 6 Models fit statistics for the single and the joint use of the independent variables SAR backscatter and interferometric coherence when predicting burn severity (dNBR) in the case of L-band data. The subscripts next to the polarization indicate the SAR metric (b=backscatter, c=coherence).

	ALOS PALSAR 2009.08.20/10.05											
model		HH_c	HH_c& HH_b		HH_c& HV_b			HV_c	HV_c& HH_b		HV_c& HV_b	
	D^2	AIC	D^2	AIC	D^2	AIC	D^2	AIC	D^2	AIC	D^2	AIC
21-25	0.886	389	0.893	388	0.932	375	0.907	382	0.908	384	0.936	373
26-30	0.875	901	0.879	901	0.906	883	0.918	871	0.919	872	0.922	869
31-36	0.836	1286	0.840	1285	0.916	1222	0.891	1246	0.891	1248	0.910	1229
36-40	0.803	2011	0.829	1991	0.888	1927	0.853	1966	0.862	1959	0.892	1922
41-45	0.813	2057	0.847	2028	0.887	1981	0.859	2014	0.871	2001	0.890	1977
46-50	0.865	1896	0.895	1861	0.905	1847	0.891	1864	0.897	1858	0.905	1847
51-55	0.896	1267	0.900	1265	0.923	1239	0.935	1220	0.936	1220	0.939	1215
56-60	0.843	458	0.924	433	0.921	435	0.888	446	0.932	429	0.921	435

all models were extremely significant ($p<0.001$)

by AIC values. The model with the lowest AIC is the one which better predicts burn severity. The D^2 and the AIC are presented by groups of local incidence angle.

DISCUSSION

Signature analysis

Fig. 5 show that the ERS-1/2 tandem coherence increased with respect to burn severity regardless of the specific range of local incidence angle. The dynamic range from unburned to highly burned forest was constant (around 0.3) for all orientations. For the highest burn severity coherence reached the values computed for the adjacent bare areas (approximately 0.8). The same trend was found for all ERS-1/2 tandem datasets acquired under stable weather conditions and Bn < 300 m. Coherence increased from approximately 0.5 in unburned forest to approximately 0.8 in the highly burned areas, reaching the levels registered for bare soils. The increase was almost linear from unburned to highly burned forest and saturation appeared at high dNBR values. The data

spread was low due to the small interval between the two acquisitions and the lack of precipitation which implied a high temporal stability of ground component to the total forest coherence. For ERS-1/2 pairs acquired with perpendicular baselines longer than 350 m, the sensitivity to burn severity was weak because of the significant geometric decorrelation.

As for the ERS-1/2 tandem data, the Envisat ASAR co-polarized coherence increased with the increase of burn severity (Fig. 6) from approximately 0.15 (unburned forest) up to 0.45 (burned forest). Nonetheless, the sensitivity decreased for increasing local incidence angle. The trend was rather linear and saturation occurred only for high local incidence angles at burn severity levels beyond 750 dNBR. The coherence of forest affected by highest burn severity was similar to the average coherence measured for bare soils (approximately 0.5). However, the overall values were lower compared to ERS-1/2 tandem data. The lower coherence was caused by the significantly larger temporal baseline, which allowed substantially stronger temporal decorrelation to take place. Freezing temperatures were registered at the acquisition of the first image whereas light precipitation and unfrozen conditions were registered at the time of the latter image acquisition.

X-band co-polarized coherence increased only slightly (around 0.15) for increasing burn severity (Fig.7). No sensitivity to burn severity was observed at high burn severity (dNBR> 600) for all local incidence angles. In contrast to C-band, the coherence levels for the highest burn severity were lower (0.3-0.4) compared to bare surfaces (0.4-0.5). The lower coherence recorded is likely a consequence of the shorter wavelength. At X-band the contribution of targets prone to rapid temporal decorrelation (e.g. leaves, twigs and small branches) to the total coherence is larger than at C-band.

At L-band HH and HV polarized coherence decreased by 0.5 and 0.4 respectively (Fig. 8 and Fig. 9) with increasing burn severity. L-band microwaves are less affected by absorption and attenuation especially in the low biomass Mediterranean forest. The scattering occurs primarily at the level of the large branches and the tree trunks which are rarely consumed by fire and are less susceptible to wind induced movements providing more stable wave scattering scenario. Thus, the decrease of coherence for increasing burn severity can be explained in terms of changes of the plant physiology after the fire. For increasing severity, the water content of the vegetation and soil decreases more rapidly in time. The stronger decorrelation in the forest most affected by fire is therefore a consequence of an increased transmissivity which changes the distribution of the scatterers within the resolution cell.

Coherence observed for the CBI plots (Zuera08 and Jaulin09 fires) was similar to that of dNBR pseudo-plots for unburned and highly burned forests. However, larger spread was registered for CBI plots at high burn severity (i.e. CBI >2.5) especially at C-band (Fig. 6). The variability of the soil properties between acquisitions resulted in different coherence levels for the same burn severity. At X-band the proportion of the scattering from the forest floor is smaller, thus reducing the influence of dissimilar soil conditions between image acquisitions. The smaller spread of the coherence for the pseudo-plots is explained by the process of their generation. Only forest pixels presenting high values of the normalized differenced vegetation index (NDVI) in the pre-fire optical image were selected for the generation of the pseudo-plots. Thus, sparse or young forests which present higher variability of forest cover and tree density were avoided. In addition, the monotype conditions and the even-aged structure of the forest assured a high homogeneity of the forests in the pseudo-plot dataset. In contrast, the CBI

plots were also assessed in sparse and young forests which presented greater diversity of the forest structure.

Coherence corresponding to a normal terrain surface oriented toward the sensor registered high decorrelation for slopes above 10-15° due to uncompensated non-overlapping fraction of the range bandwidth (Fig. 10), thus confirming results presented in (Castel et al. 2001). For slopes pointing away from the sensor (i.e. 90° aspect) lower coherence was observed for unburned forests due to the decreasing relative contribution of the ground component to the total backscattering with increasing local incidence angle.

Weather conditions at the time of acquisition had considerable impact on coherence. Lower coherence and smaller dynamic range were observed at X- and C-band (Fig. 11) for image pairs containing images acquired under different meteorological conditions compared to image pairs acquired under dry conditions. Rainfall during the acquisition of the second image pair (1995.12.14/15) and weather instability prior to acquisition of the 1996.01.02/03 image pair caused higher decorrelation in the case of ERS-1/2 tandem data. Over unburned areas coherence decreased from 0.5 (dry conditions) to less than 0.2 (Fig. 11). The strongest decorrelation occurred when rainfall was registered at the time of acquisition of one of the two images forming the interferometric image pair (1995.12.15). At X-band (Fig. 11 bottom) the two TerraSAR-X 11-days image pairs affected by rainfall (2009.02.12/23 and 2009.02.23/03.06, see Table 3) showed lower coherence compared to the 33-days image pair acquired under dry conditions (2008.11.16/12.19). Also for X-band the lowest coherence (0.1) was observed when one of the images was affected by heavy rainfall at acquisition (2009.03.06).

Another effect of changing weather conditions was the decreasing coherence trend (Fig. 11) registered at the highest burn severity levels (dNBR > 600). The trend was clearer at C-band than at X-band because of the larger proportion of the ground component to the total forest coherence. The decrease was explained as a consequence of evapo-transpiration. To test this hypothesis we separated the data into groups of aspect angles and subsequently formed the pseudo-plots. The assumption was that for similar orientation the spatio-temporal variability of soil moisture is lower which would result in similar decorrelation at high burn severities. The pseudo-plots obtained after stratifying by aspect did not present the decreasing coherence trend at high burn severity levels (Fig. 12). However, for the pseudo-plots located on slopes oriented towards north-west (NW) the decorrelation was stronger than for pseudo-plots located on slopes oriented towards south-east (SE). The higher solar illumination of the south slopes increased evapo-transpiration and thus diminished faster the differences in soil moisture condition between acquisitions

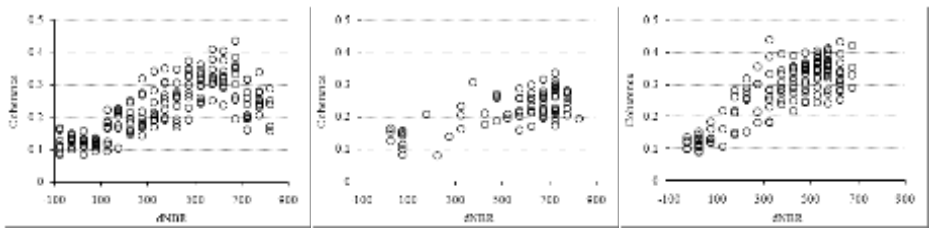

Fig.12 Effect of slope orientation on ERS-1/2 coherence (1995.12.14/15).The plot on the top left shows the pseudo-plots formed regardless of orientation angle. The remaining plots for pseudo-plots formed after dividing the data by orientation: center (NW aspects) and left (SE aspects).

Burn severity evaluation

Regression analysis showed moderate agreement between dNBR values and X- and C-band interferometric coherence (Table 4) when the local incidence angle was not accounted for. The analysis of burn severity as a function of coherence after grouping by 5^0 local incidence angle intervals showed increased values of the determination coefficients for both X- and C-band. Determination coefficients were high for data acquired under dry conditions ($R^2 > 0.65$). For image pairs acquired after rainfall (e.g. ERS-1/2 1995.12.14/15, TSX 2009.02.23/2009.03.06) or with long temporal baselines (e.g. ERS-1/2 1995.12.14/1996.03.28, TSX 2008.11.16/2009.02.23) the association strength to burn severity decreased. The largest difference in R^2 (computed using all pseudo-plots) with respect to dry conditions was recorded for the image pairs acquired with long temporal baseline (around 0.4) whereas the decrease due to rainfall was smaller (around 0.2). For all models the independent variables were extremely significant, reliably predicting burn severity ($p<0.001$). The error of estimation mostly varied between 10% and 15% of the dNBR range for the images acquired under dry conditions.

At L-band the local incidence angle influence on the association strength between coherence and burn severity was low. The association strength to burn severity was high ($R^2 > 0.9$, $p<0.01$) even when using all pseudo plots without separating by incidence angle. The determination coefficients were higher when compared to X- and C-band whereas the estimation errors mostly varied between 5% and 10% of the dNBR range. However, at Jaulin test site the area affected by low burn severity was small which resulted in very few pseudo-plot. Thus, models were based mostly on unburned and moderate to highly burned pseudo-plots which could explain in part the higher association strength to burn severity.

Backscatter and/or coherence for burn severity estimation

Interferometric coherence trends with burn severity were similar to those found for the backscatter coefficient at all SAR frequencies (Tanase et al. in press). X- and C-band co-polarized backscatter increased whereas L-band co-polarized backscatter decreased with increasing burn severity. Cross-polarized backscatter from burned forests was lower than for unburned forests at all SAR frequencies. Soil moisture increase between image acquisitions in consequence of rainfall implied that the backscatter sensitivity to burn severity increased whereas it decreased for the interferometric coherence. The local incidence angle had a stronger effect on the backscatter coefficient than on coherence at all SAR frequencies. Significantly higher determination coefficients (0.45 to 0.65) were found for the interferometric coherence at X- and C-band when the data was not analyzed by local incidence angle. In contrast, the backscatter analysis of pooled pseudo-plots resulted in lower association strength to burn severity (0.05 to 0.45). Although interferometric coherence was still affected by local slope its influence seemed less important. Therefore, larger local incidence angle intervals (e.g. 10°) could be used thus reducing the number of models needed for burn severity assessment in hilly regions. Co-polarized coherence maintained its sensitivity to burn severity even for slopes oriented away from the sensor which was not the case when analyzing co-polarized backscatter coefficient. X- and C-band HV polarized backscatter coefficient was sensitive to burn severity as opposed to HV interferometric coherence which showed no sensitivity at both frequencies. At L-band both backscatter and interferometric coherence showed high sensitivity to burn severity for both HH and HV polarization. However, the association

strength to burn severity was slightly higher (0.05 to 0.1) for interferometric coherence data.

The joint use of the interferometric coherence and the backscatter coefficient did not significantly improve the estimation of burn severity (see Tables 5 and 6) when compared to the use of a single metric (e.g. coherence). For all analyzed datasets the increase of the deviance and the decrease of AIC were minimal (< 0.05 and <1% respectively) when combining the HH polarized coherence and the HH backscatter. The combination of HH polarized coherence and HV backscatter slightly improved the fit statistics. Deviance increased with up to 0.1 whereas AIC decreased with up to 5 %. However, model simplicity should always be preferred and therefore, the marginal improvements obtained by adding the backscatter to the coherence for the estimation of burn severity advise against the joint use of the two metrics.

CONCLUSIONS

This paper analyzed the prospects of using repeat-pass X-, C- and L-band SAR interferometric coherence for burn severity evaluation in mediterranean forests. The effects of topography and environmental conditions on coherence estimates from burned areas were also studied. The interferometric data was related to burn severity measured in situ (Composition Burn Index, CBI) and estimated from a spectral index (dNBR). The use of an indirect measure of burn severity was necessary to obtain a uniform dataset in terms of burn severity distribution.

The HH polarized coherence increased at X- and C-band whereas at L-band HH and HV polarized coherence decreased with the increase of burn severity. The HV polarized coherence at X- and C-band was affected by the predominant contribution from the vegetation and the negligible contribution from the forest floor thus showing very low values regardless of burn severity. The dynamic range of co-polarized coherence between highly burnt and unburned forest was rather stable regardless of frequency being slightly higher for slopes oriented towards the sensor. L-band cross-polarized coherence showed high sensitivity to burn severity. The association strength to burn severity estimates increased while the estimation error decreased when data was analyzed by local incidence angle intervals for X- and C-band. At L-band a single unified model seemed to be most useful regardless of the incidence angle for both co- and cross-polarized data. The addition of the backscatter coefficient into the model did not significantly improve the results. Environmental conditions have to be considered for successful burn severity estimation. Scenes acquired under dry conditions provided the highest association strength to burn severity.

This study indicates that interferometric SAR coherence is useful for burn severity mapping in mediterranean environments. However, the work points out some limitations: *i)* slopes steeper than 15°, tilted orthogonally to the sensor view should be masked out; *ii)* the lower dynamic range between unburned and burned areas observed for slopes oriented away from the sensor is likely to decrease the accuracy of burn severity retrieval for these areas at X- and C-band and *iii)* the correlation between burn severity and coherence strongly depends on the weather conditions at the time of image acquisition.

The trends of the interferometric coherence with respect to burn severity were similar to those observed for the backscatter coefficient. However, environmental conditions and topography had a diverse influence on the two metrics. For X-band data co-polarized interferometric coherence provides better association strength to burn

severity than both HH and HV backscatter coefficient. If C- or L-band dual polarized data are available the estimation of burn severity could be carried out using either the cross-polarized backscatter coefficient or the interferometric coherence. However, the use of the interferometric coherence would provide slightly better results over the cross-polarized backscatter. Nonetheless, one should take into account the increased difficulty to obtain data acquired in similar meteorological conditions.

ACKNOWLEDGMENT

Dr. Sergio M. Vicente-Serrano is acknowledged for providing the orthorectified, atmospherically corrected Landsat TM scenes for the Zuera95 test site. Dr. Thuy Le Toan is acknowledged for providing the ALOS PALSAR datasets. This work has been financed by the Spanish Ministry of Science and Education and the European Social Fund: FPI grant BES-2006-11684 and projects CGL2005-04863 and CGL2008-01083. TerraSAR-X data were provided by Deutsches Zentum für Luft-und Raumfahrt (DLR) in the framework of LAN0464 project. ERS and Envisat data were provide in the frame of C1P.5446 ESA Cat-1 project. ALOS PALSAR data were provided by Japan Aerospace Exploration Agency (JAXA) in the frame of the Kyoto & Carbon Initiative.

REFERENCES

Agresti, A. (2007). *An Introduction to Categorical Data Analysis*. New Jersey: John Wiley.

Akaike, H. (1974). A new look at the statistical model identification. *IEEE Transactions on Automatic Control, 19*, 716-723.

Allen, J.L., and Sorbel, B. (2008). Assessing the differenced Normalized Burn Ratio's ability to map burn severity in the boreal forest and tundra ecosystems of Alaska's national parks. *International Journal of Wildland Fire, 17*, 463-475.

Andreae, M.O., and Merlet, P. (2001). Emission of trace gases and aerosols from biomass burning. *Global Biogeochemical Cycles, 15*, 955-966.

Askne, J.I.H., Dammert, P.B.G., Ulander, L.M.H., and Smith, G. (1997). C-Band Repeat-Pass Interferometric SAR Observations of the Forest. *IEEE Transactions on Geoscience and Remote Sensing, 35*, 25-35.

Askne, J.I.H., and Santoro, M. (2009). Automatic Model-Based Estimation of Boreal Forest Stem Volume From Repeat Pass C-band InSAR Coherence. *IEEE Transactions on Geoscience and Remote Sensing, 47*, 513-516.

Askne, J.I.H., Santoro, M., Smith, G., and Fransson, J.E.S. (2003). Multitemporal Repeat-Pass SAR Interferometry of Boreal Forests. *IEEE Transactions on Geoscience and Remote Sensing, 41*, 1540-1550.

Bamler, R., and Hartl, P. (1998). Synthetic aperture radar interferometry. *Inverse Problems, 14*, 1-54.

Bourgeau-Chavez, L.L., Kasischke, E.S., Brunzell, S., and Mudd, J.P. (2002). Mapping fire scars in global boreal forests using imaging radar data. *International Journal of Remote Sensing, 23*, 4211-4234.

Bourgeau-Chavez, L.L., Kasischke, E.S., French, N.H.F., Szeto, L.H., and Kherkher, C.M. (1994). Using ERS-1 SAR Imagery to Monitor Variations in Burn Severity in an Alaskan Fire-Disturbed Boreal Forest Ecosystem. In, *Geoscience and Remote Sensing Symposium, 1994. IGARSS '94. Proceedings. 1994 IEEE International* (pp. 243-245). Pasadena, California.

Castel, T., Beaudoin, A., Stach, N., Stussi, N., Le Toan, T., and Durand, P. (2001). Sensitivity of space-borne SAR data to forest parameters over sloping terrain. Theory and experiment. *International Journal of Remote Sensing, 22*, 2351-2376.

Castel, T., Martinez, J.-M., Beaudoin, A.,Wegmüller, U., and Strozzi, T. (2000). ERS INSAR Data for Remote Sensing Hilly Forested Areas. *Remote Sensing of Environment, 73*, 73-86.

Cocke, A.E., Fule, P.Z., and Crouse, J.E. (2005). Influence of fire severity on plant regeneration by means of remote sensing imagery. *International Journal of Wildland Fire, 14*, 189-198.

Chuvieco, E. (1999). Remote sensing of large wildfires. In E. Chuvieco (Ed.) (p. 212): Springer.

Chuvieco, E., Riaño, D., Danson, F.M., and Martín, P. (2006). Use of a radiative transfer model to simulate the postfire spectral response to burn severity. *Journal of Geophysical Research, 111*, 1-15.

Epting, J., Verbyla, D., and Sorbel, B. (2005). Evaluation of remotely sensed indices for assessing burn severity in interior Alaska using Landsat TM and ETM+. *Remote Sensing of Environment, 96*, 328-339.

Eriksson, L.E.B., Santoro, M., Andreas Wiesmann, and Schmullius, C.C. (2003). Multitemporal JERS Repeat-Pass Coherence for Growing-Stock Volume Estimation of Siberian Forest. *IEEE Transactions on Geoscience and Remote Sensing, 41*, 1561-1570.

Gatelli, F., Guarnieri, A.M., Parizzi, F., Pasquali, P., C.Prati, and Rocca, F. (1994). The wavenumber shift in SAR interferometry. *IEEE Transactions on Geoscience and Remote Sensing, 32*, 855-865.

Gaveau, D.L.A., Balzter, H., and Plummer, S. (2000). Boreal Forest INSAR Classification properties. In, *Proceedings of the CEOS SAR Workshop, Toulose, 26-29 October 1999, ESA Sp-450, March 2000* (pp. 509-512).

Gimeno, M., San-Miguel, J., Barbosa, P., and Schmuck, G. (2002). Using ERS-SAR images for burnt area mapping in Mediterranean landscapes. In D.X. Viegas (Ed.), *Forest Fire Research & Wildland Fire Safety: Proceedings of IV International Conference on Forest Fire Research* (pp. 18-23). Coimbra, Portugal: Millpress Science Publishers.

Hagberg, J.O., Ulander, L.M.H., and Askne, J.I.H. (1995). Repeat-Pass SAR Interferometry Over Forested Terrain. *IEEE Transactions on Geoscience and Remote Sensing, 33*, 331-340.

Hoy, E.E., French, N.H.F., Turetsky, M.R., Trigg, S.N., and Kasischke, E.S. (2008). Evaluating the potential of Landsat TM/ETM+ imagery for assessing fire severity in Alaskan black spruce forests. *International Journal of Wildland Fire, 17*, 500-514.

Kasischke, E.S., Bourgeau-Chavez, L.L., and French, N.H.F. (1994). Observations of Variations in ERS-1 SAR Image Intensity Associated with Forest Fires in Alaska. *IEEE Transactions on Geoscience and Remote Sensing, 32*, 206-210.

Kasischke, E.S., Turetsky, M.R., Ottmar, R.D., French, N.H.F., Hoy, E.E., and Kane, E.S. (2008). Evaluation of the composite burn index for assessing fire severity in Alaskan black spruce forests. *International Journal of Wildland Fire, 17*, 515-526.

Key, C.H., and Benson, N.C. (2004). *Ground Measure of Severity, The Composite Burn Index*. Ogden, UT: U.S. Department of Agriculture, Forest Service, Rocky Mountain Research Station.

Key, C.H., and Benson, N.C. (2006). Landscape assessment (LA). In D.C. Lutes, R.E. Keane, J.F. Caratti, C.H. Key, N.C. Benson, S. Sutherland and L.J. Gangi (Eds.), *FIREMON: Fire effects monitoring and inventory system* (pp. 1-55). Fort Collins, CO: U.S. Department of Agriculture, Forest Service, Rocky Mountain Research Station, Gen. Tech. Rep. RMRS-GTR-164-CD.

Koskinen, J.T., Pulliainen, J.T., Hyyppä, J.M., Marcus E. Engdahl, and Hallikainen, M.T. (2001). The Seasonal Behavior of Interferometric Coherence in Boreal Forest. *IEEE Transactions on Geoscience and Remote Sensing, 39*, 820-829.

Landmann, T. (2003). Characterizing sub-pixel Landsat ETM+ fire severity on experimental fires in the Kruger National Park, South Africa. *South African Journal of Science, 99*, 357-359.

Liew, S.C., Kwoh, L.K., Padmanabhan, K., Lim, O.K., and Lim, H. (1999). Delineating Land/Forest Fire Burnt Scars with ERS Interferometric Synthetic Aperture Radar. *Geophysical Research Letters, 26*, 2409-2412.

Luo, X., Askne, J.I.H., Smith, G., and Dammert, P. (2001). Coherence characteristics of radar signals from rough soil. *Progress in Electromagnetic Research, 31*, 69-88.

Murphy, K.A., Reynolds, J.H., and Koltun, J.M. (2008). Evaluating the ability of the differenced Normalized Burn Ratio (dNBR) to predict ecologically significant burn severity in Alaskan boreal forests. *International Journal of Wildland Fire, 17*, 490-499.

Santoro, M., Askne, J.I.H, Smith, G., and Fransson, J.E.S. (2002). Stem volume retrieval in boreal forests from ERS-1/2 interferometry. *Remote Sensing of Environment, 81*, 19-35.

Santoro, M., Askne, J.I.H., Wegmüller, U., and Werner, C.L. (2007). Observations, Modeling, and Applications of ERS-ENVISAT Coherence Over Land Surfaces. *IEEE Transactions on Geoscience and Remote Sensing, 45*, 2600-2611.

Schmuck, G., San-Miguel-Ayanz, J., Camia, A., Kucera, J., Libertá, G., Boca, R., Durrant, T., and Amatulli, G. (2008). Forest Fires in Europe 2007. In, *JRC Scientific and Technical Reports*. Ispra, Italy: Joint Research Center.

Smith, G., and Askne, J.I.H. (2001). Clear-cut detection using ERS interferometry. *International Journal of Remote Sensing, 22*, 3651-3664.

Takeuchi, S., and Yamada, S. (2002). Monitoring of Forest Fire Damage by Using JERS-1 InSAR. In, *Geoscience and Remote Sensing Symposium, 2002. IGARSS '02. Proceedings. 2002 IEEE International* (pp. 3290-3292). Toronto, Canada.

Tanase, M., Pérez-Cabello, F., Riva, J.de la, and Santoro, M. (2010). TerraSAR-X data for burn severity evaluation in Mediterranean forests on sloped terrain. *IEEE Transactions on Geoscience and Remote Sensing, 48*, 917-929.

Tanase, M., Riva, J.de la, Santoro, M., Le Toan, T., and Pérez-Cabello, F. (in press). Sensitivity of X-, C- and L-band SAR backscatter to fire severity in mediterranean pine forests. *IEEE Transactions on Geoscience and Remote Sensing*.

Verbyla, D.L., Kasischke, E.S., and Hoy, E.E. (2008). Seasonal and topographic effects on estimating fire severity from Landsat TM/ETM+ data*International Journal of Wildland Fire, 17*, 527-534.

Vicente-Serrano, S.M., Pérez-Cabello, F., and Lasanta, T. (2008). Assessment of radiometric correction techniques in analyzing vegetation variability and change using time series of Landsat images. *Remote Sensing of Environment, 112*, 3916-3934.

Wagtendonk, J.W.van, Root, R.R., and Key, C.H. (2004). Comparison of AVIRIS and Landsat ETM+ detection capabilities for burn severity. *Remote Sensing of Environment, 92*, 397-408.

Wegmüller, U., and Werner, C. (1997). Retrieval of Vegetation Parameters with SAR Interferometry. *IEEE Transactions on Geoscience and Remote Sensing, 35*, 18-24.

Wegmüller, U., Werner, C., and Strozzi, T. (1998). SAR interferometric and differential interferometric processing. In, *Geoscience and Remote Sensing Symposium, 1998. IGARSS '98. Proceedings. 1998 IEEE International* (pp. 1106-1108). Seattle, USA.

Wegmüller, U., and Werner, C.L. (1995). SAR Interferometric Signatures of Forest. *IEEE Transactions on Geoscience and Remote Sensing, 33*, 1153-1161.

Werf, G.R.v.d., Randerson, J.T., Collatz, G.J., Giglio, L., Kasibhatla, P.S., Jr., A.F.A., Olsen, S.C., and Kasischke, E.S. (2004). Continental-Scale Partitioning of Fire Emissions During the 1997 to 2001 El Niño/La Ninña period. *Science, 303*, 73-76.

Westerling, A.L., Hidalgo, H.G., Cayan, D.R., and Swetnam, T.W. (2006). Forest Wildfire Activity Warming and Earlier Spring Increase Western U.S. *Science, 313*, 940-943.

Zebker, H.A., and Villasenor, J. (1992). Decorrelation in interferometric radar echoes. *IEEE Transactions on Geoscience and Remote Sensing, 30*, 950-959.

4.4. El uso del SAR para la evaluación de la recuperación de la vegetación tras el fuego

4.4.1. Sensitivity of SAR data to post-fire forest regrowth in mediterranean and boreal forests

Tanase, M.A., Santoro, M., de la Riva, J., Kasischke, E. and, Pérez-Cabello, F. Sensitivity of SAR data to post-fire forest regrowth in mediterranean and boreal forests. *Remote Sensing of Environment,* undergoing review.

Resumen

Mediante datos satelitales procedentes de radar de apertura sintética (SAR) se analiza la retro-dispersión y la coherencia interferométrica de bosques regenerados tras incendios en dos regiones, una en España y otra en Alaska.

La retro-dispersión en la banda X muestra una baja sensibilidad a la recuperación vegetal, con un incremento promedio del coeficiente de retro-dispersión de 1-2 dB de diferencia entre las áreas más recientemente afectadas por el fuego y el bosque sin quemar. La sensibilidad a la recuperación vegetal aumenta en la banda C, siendo el rango dinámico entre el coeficiente de retro-dispersión de las áreas quemadas y sin quemar de alrededor de 4 dB. Por último, la L presenta la mayor sensibilidad a la recuperación de la estructura forestal, con un rango dinámico de aproximadamente 8 dB entre las áreas quemadas recientemente y las áreas no afectadas por incendio. La sensibilidad de la retro-dispersión SAR a la recuperación del bosque varia, para cualquier frecuencia, con el ángulo de incidencia local y la polarización. La coherencia interferométrica muestra una baja sensibilidad a la recuperación de la estructura forestal en todas las frecuencias SAR.

A partir de datos SAR de banda L se han diferenciado, en los bosques mediterráneos, cinco fases correspondientes a diferentes estructuras forestales y cuatro en el caso de los bosques boreales. Frente a ello, el índice de vegetación de diferencia normalizada (NDVI) tan sólo ha sido capaz de diferenciar con fiabilidad las etapas de desarrollo incipientes del bosque, dada su mayor sensibilidad a la información relacionada con el grado de cubrimiento vegetal. Los resultados obtenidos han sido consistentes en los dos medios estudiados: mediterráneo y boreal.

Sensitivity of SAR data to post-fire forest regrowth in mediterranean and boreal forests

M. A. Tanase[(1)], J. de la Riva[(1)], M. Santoro[(2)], E. Kasischke[(3)], and F. Pérez-Cabello[(1)]

[(1)]Department of Geography,
University of Zaragoza,
Pedro Cerbuna 12, 50009 Zaragoza, Spain
Email: mihai@tma.ro, delariva@unizar.es, fcabello@unizar.es

[(2)]Gamma Remote Sensing AG,
Worbstr. 225, CH-3073 Gümligen, Switzerland
Email: santoro@gamma-rs.ch

[(3)]Department of Geography
University of Maryland
2181 LeFrak Hall, College Park MD 20742, USA
Email: ekasisch@umd.edu

Abstract

Space borne synthetic aperture radar (SAR) data from two test regions in Spain and Alaska have been used to analyze SAR backscatter and interferometric coherence in regrowing forests previously affected by fire. TerraSAR-X X-band backscatter showed low sensitivity to forest regrowth, the average backscatter increasing by 1-2 dB between the most recent fire scars and the unburned forest. Envisat Advanced Synthetic Aperture (ASAR) C-band backscatter showed higher sensitivity, the backscatter difference between burned and unburned forest being around 4 dB. The Advanced Land Observing Satellite (ALOS) Phased Array-type L-band Synthetic Aperture Radar (PALSAR) L-band backscatter presented the highest sensitivity to forest regrowth, the backscatter difference being approximately 8 dB. For a given frequency the sensitivity of the SAR backscatter to forest regrowth varied with local incidence angle and polarization. The interferometric coherence showed low sensitivity to forest regrowth at all SAR frequencies. For mediterranean forests five phases of forest regrowth were discerned whereas for boreal forest, up to four different regrowth phases could be discerned with L-band SAR data which is sensitive to vegetation structure. In comparison, the Normalized Difference Vegetation Index (NDVI) provided reliable differentiation only for the most recent development stages, as it registers information related to the vegetation cover. The results obtained were consistent in both environments.

***Keywords**: SAR backscatter, interferometric coherence, forest regrowth*

INTRODUCTION

Information on forest condition is of great interest for many agencies dealing with environmental issues (e.g. carbon budget, forest management, etc.) since forest needs

long time to reach the biomass level, structure and carbon sink capacity prior to the fire event. Satellite imagery covers large regions and the temporal recurrence of the data collection facilitates the temporal analysis of wide areas. Fire impacts and subsequent processes may be identified and monitored by means of remote sensing using optical (Marchetti et al. 1995; Patterson and Yool 1998; Viedma et al. 1997), radar (Bourgeau-Chavez et al. 1997; Bourgeau-Chavez et al. 2002; Ruecker and Siegert 2000; Siegert and Ruecker 2000) or lidar (Goetz et al. 2010) sensors. Remote sensing data are particularly suitable for monitoring post-fire vegetation development at regional scales for two reasons: (i) its sensitivity to alterations in the radiometric response to wildfire-induced changes and post disturbance vegetation development and (ii) the spatial resolution and temporal recurrence of satellite imagery which allows the characterization of the response patterns.

Disappearance of charcoal-ash remains, increase of vegetation and the subsequent decrease of bare soil cover are targets for remote sensing satellites operating in the visible and infrared region of the electromagnetic spectrum. In consequence of such dynamics, increase of infrared reflectance and decrease of red and blue reflectance caused by chlorophyll increase are detected by optical sensors. A number of studies evidenced this as useful for post-fire vegetation monitoring (Díaz-Delgado and Pons 2001; Henry and Hope 1998; Pérez-Cabello 2002; Wagtendonk et al. 2004). The Normalized Different Vegetation Index (NDVI) (Rouse et al. 1973) has been the most frequently used tool for monitoring, analyzing, and mapping temporal and spatial post-fire variations (Díaz-Delgado et al. 2003; Díaz-Delgado et al. 2002; Viedma et al. 1997). However, NDVI responds more to changes in leaf area than to changes in overall biomass (Henry and Hope 1998) and its relation to leaf area index (LAI) varies both intra and inter-annually reaching saturation levels at high LAI values (Wang et al. 2005). Therefore, tracking post fire vegetation development using NDVI is limited to the first years after fire. The analysis of post-fire vegetation condition of an oak forest in NE Spain showed that pre-fire NDVI values were reached after only 7 years (Díaz-Delgado and Pons 2001). Similar trends were found by (Clemente et al. 2009; Vila and Barbosa 2010) in other mediterranean regions whereas in boreal forests pre-fire NDVI values were reached after 13 years (Cuevas-Gonzalez et al. 2009).

Forests need decades to reach the mature stage and the short period within which optical based vegetation indices reach pre-fire levels implies limited value for regrowth monitoring. SAR data have the potential to significantly extend the monitoring period since the backscattered signal is directly influenced by the forest structure. Backscatter sensitivity to forest structural parameters increases with the increase of wavelength. Typically, the backscatter coefficient increases with forest biomass reaching saturation as a function of forest type and structure. Increased sensitivity to forest regrowth was reported for L-band HH polarization compared to C-band VV polarization for a ten year old fire scar in China (Sun et al. 2002). The longer L-band wavelength allowed the differentiation among young (i.e. post-fire regrowth) and mature forest stands. In a mediterranean environment temporal changes in forest biomass were assessed using multi-temporal C-band VV polarized images in order to characterize post-fire processes (Minchella et al. 2009). Nonetheless, these studies only used co-polarized backscatter imagery. Cross-polarized data is more sensitive to forest structure and could provide better differentiation between recovery stages of disturbed forests. Furthermore, interferometric coherence could provide additional information for burned area monitoring. Repeat-pass interferometric coherence is usually low over mature forests and increases significantly for areas covered by small vegetation or bare soil (Wegmüller

and Werner 1995). In forests affected by fire C- and L-band co-polarized coherence was found to increase with respect to unburned areas (Liew et al. 1999; Takeuchi and Yamada 2002).

Previous studies on post-fire forest monitoring were largely carried out using optical based indices which are prone to mix different stages of forest regrowth after a certain age. The few studies on regrowth monitoring carried out using SAR data did not take advantage of the more sensitive cross-polarized backscatter nor evaluated the sensitivity to backscatter and coherence at different wavelengths to forest regrowth in burned areas. The current study addresses these topics and compares the results with those obtained from optical based indices. More specifically, this study evaluates X-, C- and L-band backscatter and interferometric coherence from fire affected areas and infers their utility for post-fire regrowth monitoring of mediterranean forest. In addition, boreal forests affected by fire are also studied using L-band data. The sensitivity of SAR measurements to regrowth is then analyzed and compared to results obtained with NDVI.

STUDY REGIONS

Two regions located in mediterranean and boreal environments were considered. The first region (Zuera) was located in central Ebro valley, northeastern Spain and has a mediterranean climate with continental features and marked seasonal variation of precipitations. The area is characterized by a hilly relief, elevations ranging from 400 m to 750 m above sea level. The topography is moderate, around 65% of the surface presenting slopes smaller than 15°. Pine forests cover approximately 22,000 hectares being interspersed with shrub vegetation and cereal crops. The vegetation is xerophilous, drought resistant and highly flammable providing abundant fuels. The forest has a homogeneous structure. Around 50% of the trees are between 35 to 55 years old while 25% are more than 65 years old. The average height is approximately 6.5 m and the average biomass around 45 tons/ha. Old stands reach heights of 12-13 m and 90 tons/ha (Notivol et al. 2005). During the last century the region has been repeatedly affected by fires, some areas having been burned up to three times. Sixteen fires larger than 10 ha were identified in the area using ancillary information. The year of burn and the surface affected are presented in Table 1. Five fire scars larger than 250 ha were the main focus of the study. In addition, two smaller fire perimeters (2001 and 2006) were included in the analysis to cover the last decade. Fire scar selection was carried out taking into account size, availability of the SAR data at all frequencies, pre-fire vegetation type (scrubland and open forest were eliminated) and the fire rate of recurrence (at least 30 years since the last fire). The selected fires were visited at the time of SAR image acquisition to check current forest status. Since vegetation conditions inside each fire scar were rather homogeneous, two to three points per scar were used for the assessment of vegetation cover fraction and the average tree height and diameter. For trees taller than 2 m, the diameter (D) was measured at breast height whereas for the small trees the diameter was measured at half of their height. For the two smaller fire scars the entire area was visible from the assessed points. For larger burns vegetation conditions assessed at the sampling points were validated by exploring the remaining fire perimeter. Vegetation layers present in Zuera area consisted of herbs and low shrubs less than 1 m tall for the most recent fires, shrubs and small trees up to 5 m tall trees for 20 to 40 years old fires and intermediate trees up to 15 m tall for the oldest fire. Most of the area was covered by *Pinus halepensis* Mill. but *Quercus ilex* L. and *Pinus nigra* JF Arnold can be

found disseminated. The main shrub species were *Quercus coccifera* L., *Juniperus oxycedrus Sibth. & Sm*, *Thymnus vulgaris* L. and sparsely *Buxus sempervirens* L. A short description of the average vegetation status at each burn is presented in Table 2 whereas Fig. 1 illustrates vegetation development phases found at some of the assessed points.

The boreal region used for this study was located in interior Alaska near Delta Junction. Twenty fires were identified using information provided by the Alaska Interagency Coordination Center. The fires were mostly located on a gently sloping alluvial outwash plane north of the Alaska Range, with elevations ranging between 300 and 600 m, and slopes being less than 3°. In this region, the average annual temperature is –2.1 °C, with the warmest month being July (15.6 °C) and the coldest January (-19.7 °C). Average annual precipitation is 290 mm, with three-quarters of this amount occurring during the growing season (May to September). A detailed description of the region can be found in (Kasischke and Johnstone 2005). The year of burn and the surface affected by fire are presented in Table 1. Nine fire scars were selected for the analysis. Other fire scars were discarded due to various reasons: i) size (2001), ii) significantly different vegetation type (scrublands and/or woody wetlands) (1951, 1954, 1981 and 1984), iii) availability of a larger fire scar from the same year (1994 and 1969b) and iv) obvious human intervention (1979b, 1979c, 1980 and 1995). The upland

Table 1 Fire scars and the affected area. Forest age is referred to the year of acquisition of the SAR dataset (see Table 3).

Zuera site						Delta Junction site					
Year	Burned area (ha)	Forest age (years)	Year	Burned area (ha)	Forest age (years)	Year	Burned area (ha)	Forest age (years)	Year	Burned area (ha)	Forest age (years)
1922	1030	87	1994	96	15	1947*	2097	60	1981	8269	26
1952*	2000	57	1995*	3100	14	1951	9387	56	1984	1233	23
1970*	272	39	2001*	26	8	1954	7312	53	1987*	18336	20
1979	680	30	2005	30	4	1969*	28101	38	1993*	192	14
1983	25	26	2006*	31	3	1969b	892	38	1994	318	13
1984	29	25	2008*	2200	<1	1971*	2150	36	1994*	8904	13
1985	10	24				1979*	13588	28	1995	951	12
1986*	303	23				1979b	2518	28	1998*	22045	9
1990	23	19				1979c	1342	28	1999*	7581	8
1994	37	15				1980	3338	27	2001	44.7	6

* analyzed fires

Table 2 Average vegetation conditions for the analyzed fire scars.

Fire	Strata	Cover (%)	Height (m)	D (cm)	Fire	Strata	Cover (%)	Height (m)	D (cm)
	Herbs	20-70	0.3-1			Herbs	10	0.2-0.3	
Not burned	Shrubs	5-60	0.5-2		1995	Shrubs	30-35	0.5-1	
	Trees	40-75	8-12	8-35		Trees	55-65	0.7-2	2-3
	Herbs	10	0.2-0.3			Herbs	80	0.2-1	
1952	Shrubs	20-25	0.7-1.5		2001	Shrubs	10	0.5-1	
	Trees	60-75	8-9	10-25		Trees	5-10	0.5-1	< 3
	Herbs	10-20	0.1-0.3			Herbs	70	50-80	
1970	Shrubs	50-60	0.5-2		2006	Shrubs	5	0.5-0.8	
	Trees	90	3-6	9-16		Trees	N/A	0.1-0.2	< 1
	Herbs	10	0.4			Herbs	5-20	0.1-0.3	
1986	Shrubs	5-10	0.5-1		2008	Shrubs	5-20	0.1-0.3	
	Trees	70-80	1.5-4	3-5		Trees	N/A	8-12	8-35

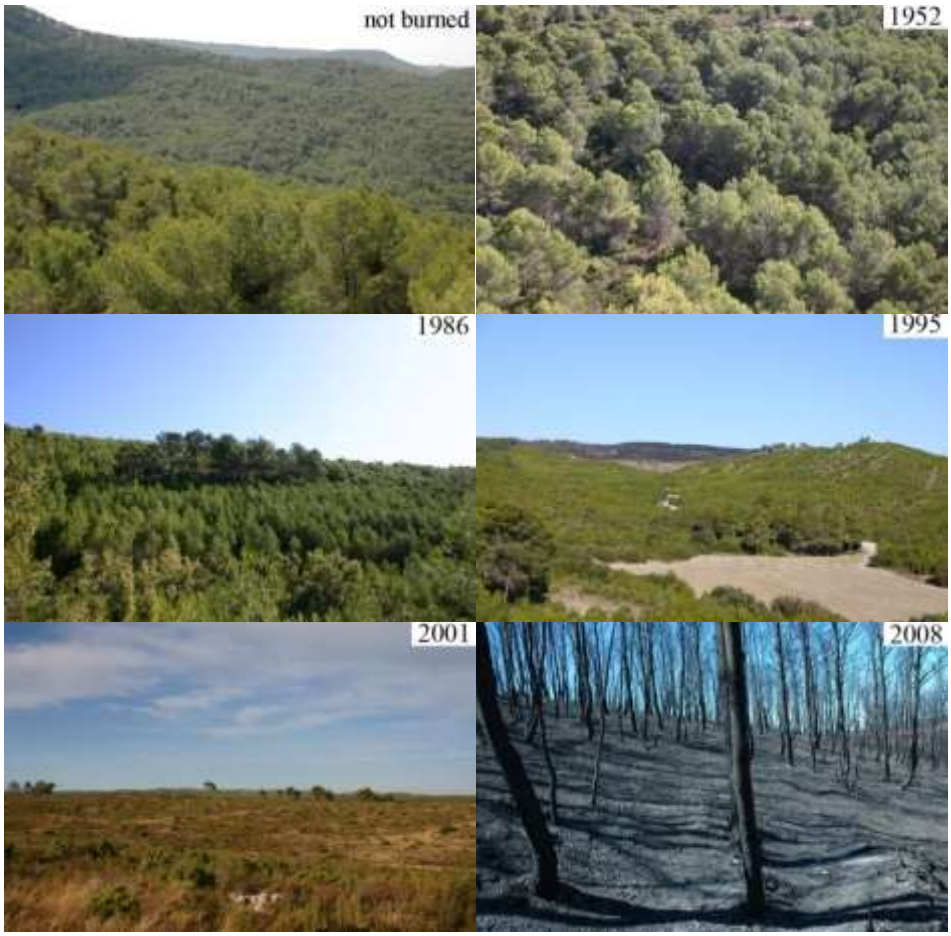

Fig. 1 Examples of vegetation recovery at the Zuera site. The pictures were taken during summer 2009.

forests at the Alaskan site are undergoing secondary succession following fires, where poorly drained soils are occupied by black spruce *Picea mariana* Mill. forests on cooler, wetter sites and *Picea glauca* (Moench) forests on warmer drier sites (Viereck et al. 1983). Post fire succession in *Picea mariana* forests involves self-replacement (e.g., shrubs to immature spruce/shrub mixture followed by mature forests), while relay floristics occur after fire on sites occupied by *Picea glauca* forests (shrubs followed by *Populus* sp. or *Betula* sp. forests followed by mixed deciduous/spruce forests followed by mature *Picea glauca* forests). No field data were available for Delta Junction region. Post-fire vegetation is shown in Fig. 2 for three of the analyzed fires.

EARTH OBSERVATION DATA

For the Zuera site, the SAR dataset consisted of images acquired by the TerraSAR-X (TSX), Environmental Satellite (Envisat) Advanced SAR (ASAR) and Advanced Land Observing Satellite (ALOS) Phased Array type L-band SAR (PALSAR) sensors.

Fig. 2 Examples of vegetation recovery at the Delta Junction site. The pictures were taken during summer 2008.

For the Delta Junction site, only ALOS PALSAR data were available. Table 3 presents the acquisition dates together with the main characteristics of the datasets. TerraSAR-X dual-polarized (HH and HV) images were acquired in strip map mode (SM). One Envisat ASAR dual-polarized (HH and HV) image was acquired in Alternating Polarization mode (AP) whereas the two images used for interferometric processing were acquired in Image Mode (IM) at HH polarization. ALOS PALSAR data were acquired in full polarimetric (PLR) and dual polarization (HH and HV) Fine Beam Dual (FBD) modes. For the Zuera site, backscatter measurements (HH and HV polarization) were available for similar incidence angle for all sensors whereas the incidence angle of the image pairs used for interferometric coherence analysis varied.

The SAR data for the Zuera site were absolutely calibrated, multi-looked to obtain the desired 25 m spatial resolution and geocoded to Universal Transverse Mercator (UTM) projection using a 20 m spatial resolution digital elevation model (DEM). Topographic normalization of the backscatter to account for the effect of varying incidence angle from near to far range and the effective pixel area was applied (Ulander 1996). The resulting images were in gamma nought (γ°) format, and only included variations of the scattering properties of a target due to local orientation. Coherence generation consisted in co-registration of the images, spatial multi-looking, common band filtering and differential interferogram computation, coherence estimation and geocoding to UTM projection. Detailed description of the processing is given in (Tanase et al. in press-a) and (Tanase et al. in press-b).

The PALSAR dataset for the Delta Junction site was processed in a similar way. The images were geocoded to 30 m using a 60 m spatial resolution DEM and UTM projection. Although most of the area was on a flat or nearly flat topography, normalization of the backscatter was applied in order to obtain similar metrics (γ°) as for the Zuera site.

Fig. 3 shows the coherence image product (red: coherence; green: backscatter, blue: backscatter ratio) for the ALOS PALSAR FBD image pairs acquired over Zuera and Delta Junction sites. Fire perimeters together with the burn year were superimposed over the satellite images at both sites. The coherence image product shows up primarily in red and orange because of overall high coherence and low backscatter. Forests appear in green tones (high backscatter and low coherence) at the Delta Junction site whereas at the Zuera site they appear in yellow tones (high backscatter and high coherence). The large difference in forest coherence values for the two sites was explained by the more stable weather conditions at the Zuera site and the greater stiffness of the scatterers at L-band in mediterranean pines. Red colors correspond to sparsely vegetated areas which did not change (high coherence and low backscatter) whereas blue colors represent areas of considerable backscatter change between image acquisitions.

Two Landsat images (one for each region) acquired on 2008.08.22 (Zuera) and 2009.08.12 (Delta Junction) were used to estimate the NDVI in the fire affected areas and compare it to the measurements of backscatter and coherence.

Table 3 SAR acquisition date, incidence angle and perpendicular and temporal baselines.

Area	Sensor	Polarization	Incidence angle	Acquisition date 1	Acquisition date 2	Perpendicular baseline (m)	Temporal baseline (days)
				Backscatter analysis			
	TSX	HH,HV	25°	2008.12.24			
	ASAR	HH,HV	23°	2009.03.19			
Zuera	PALSAR	HH,VV,HV,VV	25°	2009.04.28			
	PALSAR	HH,HV	34°	2009.08.20			
	Interferometric coherence analysis						
	TSX	HH,HV	40°	2008.11.16	2008.12.19	231	33
	ASAR	HH	23°	2009.01.08	2009.02.12	34	35
	PALSAR	HH,HV	34°	2009.08.20	2009.10.05	508	46
				Backscatter & Interferometric coherence analysis			
Delta Junction	PALSAR	HH,HV	34°	2007.08.15	2007.09.30	483	46

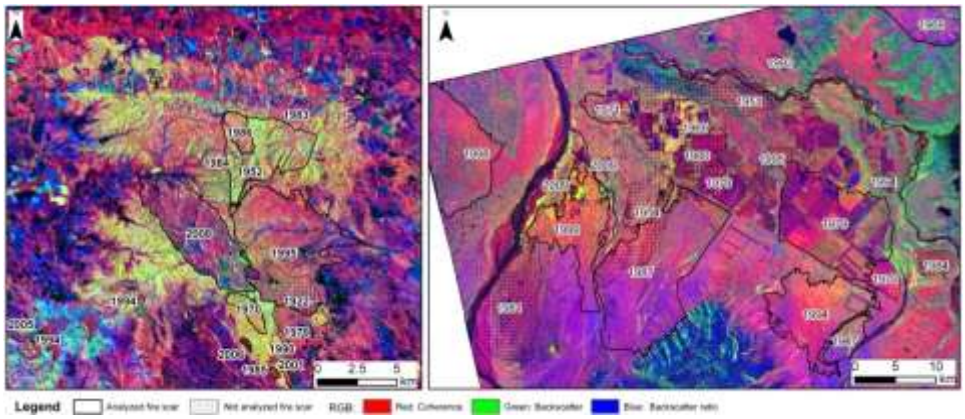

Fig. 3 Fire scars as revealed by ALOS PALSAR data at Zuera (left) and Delta Junction (right) sites. False color composite of (red) HH coherence, (green) HH backscatter and (blue) HH backscatter ratio.

METHODS

The research focused on the assessment of SAR sensitivity to forest regrowth by means of burns of different age using single date imagery. The small study areas offered relatively homogeneous forest conditions and guaranteed that the SAR backscatter and the coherence were not affected by possible spatial heterogeneities of the environmental conditions. The availability of images acquired at different polarizations allowed a broader assessment of backscatter and coherence sensitivity to forest regrowth.

To reduce pixel wise noise of backscatter and coherence measurements the analysis was conducted on samples produced by averaging over several pixel values. For the Zuera site, the study was carried out using a set of random plots generated by averaging inside each burn random pixels of similar local incidence angle and aspect with respect to the radar viewing geometry, so called pseudo-plots. The reason for using pseudo-plots and their quality with respect to field assessed conventional plots has been discussed in (Tanase et al. 2010). To avoid bias related to size, only pseudo-plots containing a constant number of pixels were considered. Nine pixel per pseudo-plot (0.55 ha) appeared to be optimal for the selected spatial resolution (25 m) of the geocoded images (Tanase et al. 2009). Due to differences in fire scar size the number of pseudo-plots was not the same for each fire scar. For the unburned areas and the large burns the number of pseudo-plots varied between 150 and 500 depending on the fire size and the orientation with respect to the radar looking geometry. For each fire the pseudo-plots were separated among several ranges of local incidence angle, with 25 to 100 pseudo-plots being available for the analysis in each group. For the small size fires (i.e. 2001 and 2006) the total number of available pseudo-plots was small, i.e. between 10 and 25. Since these fires were located on rather flat terrain most of the pseudo-plots belonged only to one or two local incidence angle intervals.

The larger fire scars and the rather flat topography at the Delta Junction site allowed the generation of large contiguous plots (1 ha) using a systematic grid spaced at 600 m. A threshold on NDVI was used to assure within plot homogeneity. Plots with large NDVI differences were discarded due to the increased probability of containing different land cover types. Furthermore, plots located inside repeatedly burned areas were also eliminated. From the approximately 1500 generated plots 970 fulfilled these conditions. The number of plots per fire scar was between 15 and 250 depending on the fire scar size.

Descriptive statistics were used to analyze backscatter and coherence sensitivity to forest regrowth stage. To minimize the effect of topography the analysis was carried out by 5º groups of local incidence angle for the Zuera site. This interval provided optimal sampling rate for the study of the local incidence angle effects on the backscatter of burned areas in sloped terrain in the case of TerraSAR-X data (Tanase et al. 2010). Analysis of variance (ANOVA) was used to assess the possibility to discern between forest recovery stages using mean values of SAR backscatter and coherence, for fire scars larger than 200 ha. Pair wise comparison using Games-Howell test (Games and Howel 1976) provided information on the significantly different mean values. This test was used because it does not assume equal variances, the sample size were unequal and the homogeneity of variance assumption was violated in the ANOVA analysis. The smaller burns (i.e. less than 200 ha) were not included in the analysis due to the small number of samples.

RESULTS AND DISCUSSION

Signature analysis

The signal backscattered from forests is the result of complex interactions between microwave electromagnetic energy and the ground and vegetation scattering components. It depends on the amount of vegetation on site as well as soil dielectric and geometric (roughness) properties on one hand and on the radar frequency, polarization and look direction on the other hand. For the three frequencies considered in this study the dominant scattering mechanism from mature forest is volume scattering whereas for young forest is divided between surface and volume scattering depending on the incidence angle and wavelength. X-band waves mostly interact with leaves/needles, twigs and small branches, C-band waves with leaves and small and secondary branches whereas L-band waves interact mostly with primary braches and tree trunks. In fire affected areas the properties of X- C- and L-band backscatter at different polarizations and look angle has been thoroughly discussed in (Tanase et al. in press-a; Tanase et al. 2009). In (Tanase et al. in press-b) the properties of the repeat-pass interferometric coherence at the same frequencies has been discussed. These findings are here considered to explain the trends of backscatter with respect to forest regrowth conditions.

SAR backscatter

Plots of mean backscatter (HH and HV polarization) are presented as a function of the local incidence angle for each SAR frequency in Figs. 4 and 5 for the Zuera site. Flat areas correspond to local incidence angles around 25°. Slopes oriented towards the sensor correspond to local incidence angles smaller than 25° whereas slopes oriented away from the sensor correspond to local incidence angles larger than 25°. The average backscatter of the small size fires is represented by the filled symbols whereas the average backscatter of unburned areas (NB) is represented by the grey circles.

X- and C-band HH polarized backscatter increased for the most recent burns with respect to the older forest (Fig. 4) whereas at HV polarization the backscatter decreased (Fig. 5). The increase of backscatter at HH polarization was explained by the larger ground component contribution to the total scattering due to the removal of the attenuation layer (needles). At HV polarization the reduced volume scattering of the young forest reduced the total scattering in recently burned areas. X-band dynamic range from unburned to recently burned forest (2008) was low (1-2 dB in flat areas) for both polarizations and decreased to 1 dB for the largest incidence angles. For small local incidence angles it reached up to 4 dB for HH polarization. Stronger sensitivity to changes in forest structure was observed at C-band. The dynamic range between unburned forest and the most recent burn (2008) was around 3 dB in flat areas for both polarizations (Fig. 4 and 5). For small incidence angles the difference increased up to 7 dB whereas for large incidence angles it decreased to 1 dB for HH polarization. C-band HV polarized backscatter dynamic range was relatively constant over the entire range of incidence angles. The decreasing ground component contribution to the total backscatter explained the decrease of dynamic range for HH polarization with increasing incidence angle at both X- and C-bands. Generally, X- and C-band backscatter difference between unburned forest and different stages of forest regrowth was low except for the most

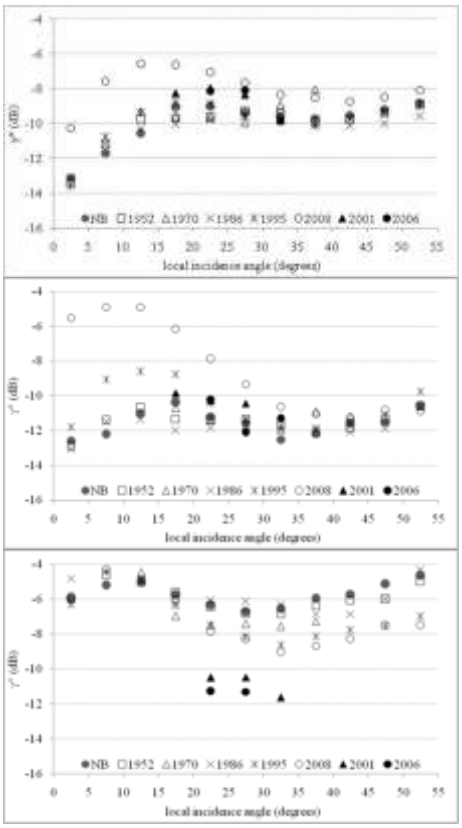

Fig. 4 Co-polarized (HH) normalized backscatter coefficient (γ°) trend as a function of the local incidence angle. X-band 2008.12.24 (top), C-band 2009.01.28 (center) and L-band 2009.04.28 (bottom). Zuera site.

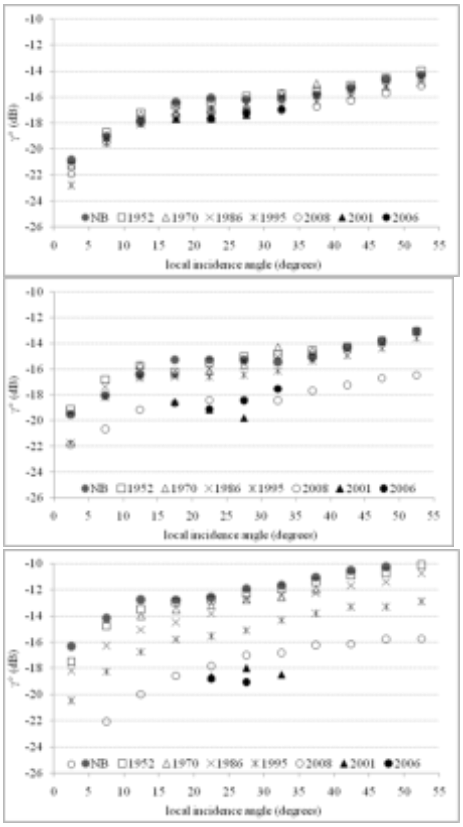

Fig. 5 Cross-polarized (HV) normalized backscatter coefficient (γ°) trend as a function of the local incidence angle. X-band 2008.12.24 (top), C-band 2009.03.19 (center) and L-band 2009.04.28 (bottom). Zuera site.

recent burns (one to seven years after fire) were the regrowth was negligible. Burned trees still present inside the 2008 fire perimeter increased C-band cross-polarized backscatter for 2008 burn compared to 2001 and 2006 burns from which the dead trees had been removed before the acquisition of the Envisat ASAR image.

The largest difference of the backscatter coefficient between forest regrowth stages was observed at L-band. Fig. 4 and 5 illustrate L-band average backscatter of the PLR data (2009.04.28) since it was acquired at similar incidence angle as for X- and C-band. The image was acquired during precipitation, which influenced the backscattering coefficient especially at HH polarization. For slopes oriented towards the sensor the backscatter differences between forest regrowth stages were not evident (Fig. 4). On slopes oriented away from the sensor the proportion of backscattering from the forest floor plays a smaller role which allowed for an increased dynamic range (approximately 4 dB) from unburned to recently burned forests. At HV polarization rainfall affected less the radar signal which implied a larger dynamic range (around 7 dB) with respect to the

HH case. As for C-band, the backscatter coefficient was sensitive to the burned trees still standing on site (2008 burn). With respect to higher frequency waves (X- and C-band) L-band HH polarization backscatter decreased for decreasing forest age due to the smaller reflecting elements (when compared to L-band wavelength) inside the canopy.

Fig. 6 illustrates the HH and HV backscatter as a function of the forest age (years from burn) for both Delta Junction and Zuera regions for PASALR FBD data acquired at 35° look angle under dry conditions. Because of the flat topography at Delta Junction, the analysis is focused only on flat terrain. Horizontal lines represent the average backscatter of unburned (NB) areas. Higher values were obtained for the Alaskan site at HH polarization most probably due to the higher soil moisture specific for the boreal environment. At HV polarization the backscatter mean values were similar due to the lower influence of the ground backscattering component. The most obvious difference between the two regions is the lower backscatter values observed at Zuera during the first years after the fire, which was explained by the different type of post-fire management. Spanish administration usually removes the burned standing trees after fire whereas in boreal forest trees are left at on site. Thus, the backscatter from boreal burns contains a significant component of the remaining vegetation whereas in mediterranean burns this component is usually missing. This explanation was supported by the backscatter levels observed for Zuera 2008 burn scar (where trees were not removed) which were closer to the values observed at Delta Junction. The smaller dynamic range between mature and young forests (3 dB for HH and 5 dB for HV polarization) could be explained by the higher variability of forest structure and soil moisture typical of the boreal environment which also explained the increased standard error of the mean when compared to mediterranean forests (see Tables 4 and 5 in the following section). At the Zuera site, increased dynamic range (6 dB for HH and 10 dB for HV polarization) was observed for the FBD data acquired under dry conditions when compared to PLR data acquired during rain. The larger dynamic range is also the consequence of the shallower look direction of the FBD mode with respect to the PLR mode.

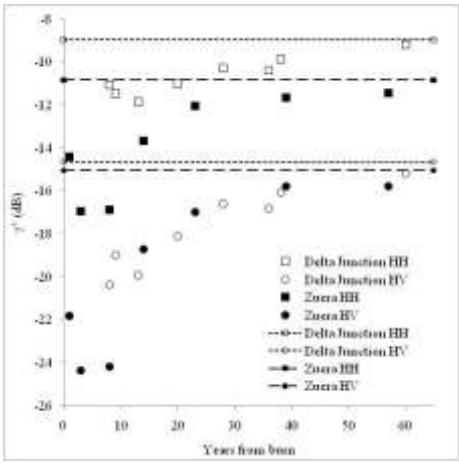

Fig. 6 Average L-band normalized backscatter coefficient (γ°) as a function of burn age for fire scars located on flat terrain. Delta Junction (2007.08.15) and Zuera (2009.08.20) site. Horizontal lines represent backscatter levels of unburned forests for HH and HV polarizations.

Interferometric coherence

Figs. 7 and 8 illustrate co- and cross-polarized coherence trends for the Zuera site. Regardless of the range of local incidence angles, lower coherence was observed with increasing forest age at X- (HH and HV) and C-band (HH). The highest values were recorded for the most recent burns which presented little or no vegetation cover. The interactions of the high frequency waves with the forest canopy explained the low values obtained in areas of significant forest regrowth. It is interesting to notice that the presence of burned standing trees on the 2008 fire site was sufficient to decorrelate the signal almost completely at X-band. L-band presented completely opposed coherence trends with respect to X- and C-band. High coherence was observed for older burns while for the most recent fires the coherence was significantly lower. This unusual trend could be related to the scattering elements observed in the forest of Zuera at L-band. At the time of acquisition of the PALSAR data, the environmental conditions had been dry for a long period. This caused the upper part of the canopy to be rather transparent to the impinging microwave. Furthermore, mediterranean pines are stiff trees so that typical decorrelating agents in forests (wind, moisture changes) are not playing a significant role and the coherence is preserved. Yet unclear is the low coherence of recent fires which were characterized primarily by shrubs. Drying of the soil in between the two image acquisitions (46 days) can be considered a plausible explanation; nonetheless, we did not have direct evidence of this. The decreasing trend of coherence with local incidence angle was observed at all frequencies especially for recent burns and was related to the smaller ground component for the slopes oriented away from the sensor. At Delta Junction site the L-band coherence decreased with the age of the fire (Fig. 9) as expected. Higher coherence values were observed for recently burned areas whereas for older forests coherence decreased due to the increased vegetation cover. Both polarizations presented similar trends with lower values being recorded at HV

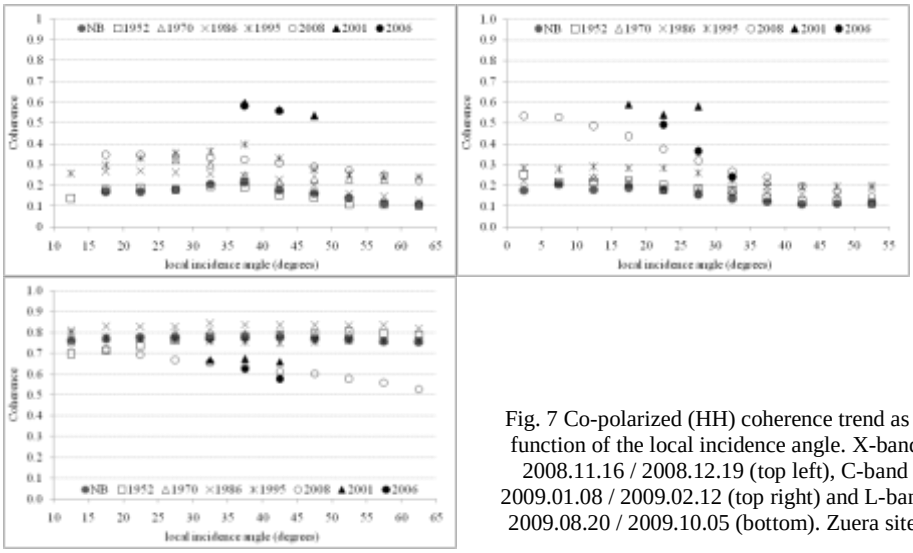

Fig. 7 Co-polarized (HH) coherence trend as a function of the local incidence angle. X-band 2008.11.16 / 2008.12.19 (top left), C-band 2009.01.08 / 2009.02.12 (top right) and L-band 2009.08.20 / 2009.10.05 (bottom). Zuera site.

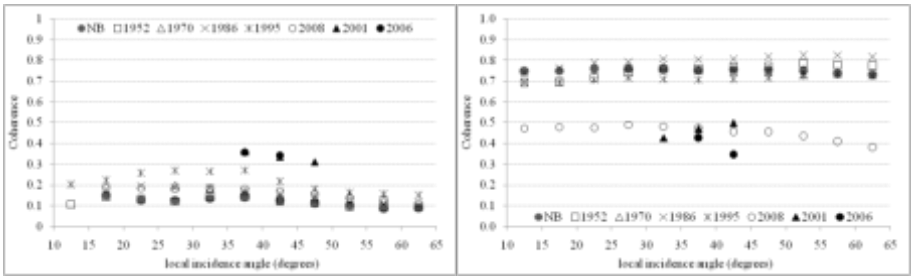

Fig. 8 Cross-polarized (HV) coherence trend as a function of the local incidence angle. X-band 2008.11.1 / 2008.12.19 (left) and L-band 2009.08.20 / 2009.10.05 (right). Zuera site.

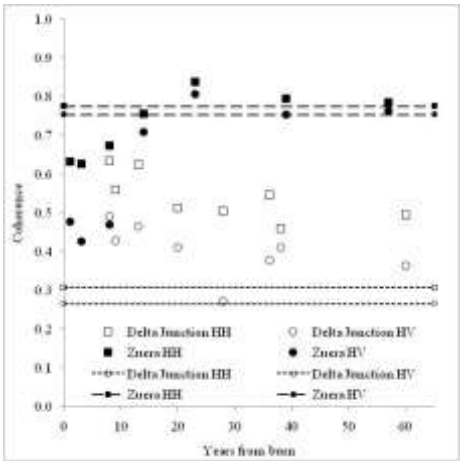

Fig. 9 Average L-band coherence as a function of burn age for fire scars located on flat terrain. Delta Junction and Zuera sites. Horizontal lines represent coherence levels of unburned forests for HH and HV polarizations.

polarization due to the predominant contribution to the coherence from the forest canopy. The coherence was however overall low due to the long repeat-pass interval of ALOS, during which movements of the scattering elements and temporal changes cause temporal decorrelation.

Statistical analysis

The analysis of variance helped understanding the potential of SAR data to monitor forest regrowth status. For the Zuera site, Table 4 illustrates backscatter and coherence response for three intervals of local incidence angle corresponding to the main type of relief orientation with respect to the radar viewing geometry: i) slopes tilted towards the sensor, ii) flat or nearly flat areas and iii) slopes tilted away from the sensor. The mean values and the standard error are presented for the large fire scars at each SAR frequency. Due to the rather flat topography, the statistics for the area affected by fire in 1970 are presented only for the flat terrain class. For the Delta Junction site, the analysis was carried out considering only the flat terrain conditions. The results from Delta Junction site are presented in Table 5.

For simplicity we grouped the burn scars into the same regrowth phase when the difference in mean backscatter or interferometric coherence between consecutive burns was less than 1 dB and 0.1 units respectively. We considered a mean backscatter

difference of less than 1 dB between two consecutive groups impractical for operational regrowth differentiation. The threshold was based on the highest standard error (see Tables 4 and 5) for a confidence interval of 99%. Residual speckle was negligible since the statistical analysis was carried out over several thousands of the original pixels (multi-look processing, pseudo-plots averaging and analysis at fire scar level). Therefore, it was reasonable to assume that the variability inside of a given burn corresponded mostly to differences in forest regrowth. Similar reasoning was applied for the coherence analysis. The results from the pair-wise comparison are coded by letters. Average backscatter/coherence for fire scars sharing the same letter is not significantly different, $p<0.05$.

Zuera site

The analysis of variance for the backscatter coefficient revealed statistically significant differences between stages of forest regrowth at all frequencies, polarizations and slope orientation (Table 4). Nevertheless, some of these differences were considered of impractical use. For X-band HH polarization data only 2008 burn for which the mean backscatter was up to 3 dB higher with respect to the other burns was identified with sufficient confidence in all slope conditions. It is important to notice that the 2008 burn represented the case of a recently burned forest with tree stems standing on site rather than the case of a forest regrowth phase. The removal of burned tree stems after fire changes completely the scattering mechanism of the regrowth areas which afterwards are dominated by low shrubs and herbs. The small dynamic range from unburned to recently burned sites observed at X-band HV polarization would ultimately prevent its use despite the statistically significant differences found between some of the regrowth phases. C-band data showed increased discrimination potential for both polarizations. Younger forest (1995 burn) was consistently discerned from older forests at HH polarization on slopes looking towards the sensor and flat areas whereas for slopes looking away from the sensor only the 2008 burn was identified. The mean backscatter difference with respect to the older forests varied between 1 and 4 dB depending on slope orientation. At HV polarization only the last burn (2008) was reliably differentiated for all slopes; the average backscatter difference with respect to older burns was between 1 and 2 dB. Although statistically significant differences were found between some of the burns the rather similar backscatter values would prevent their reliable identification. The highest number of forest regrowth stages was differentiated at L-band. Five groups were consistently separated at HH and HV polarization and for all slope orientations. Each individual burn was separated with the exception of the oldest fire scars from 1952 and 1970. The average backscatter difference between consecutive groups was larger than the 1 dB limit. Only for slopes tilted towards at HH polarization the differentiation potential of L-band was lower. A clear ascending trend of the average backscatter was observed with increasing forest age at both polarizations.

Statistically significant differences were found between forest regrowth phases when analyzing the interferometric coherence at all frequencies, polarizations and slope conditions. However, the small dynamic range (< 0.2) did not allow reliable identification among different phases of forest regrowth at C- and L-band due to the small variation among individual burns (0.03-0.05). The only exception was the 2008 fire scar where the forest floor provided a stable scattering scenario not greatly influenced by the remaining burned trees. At X-band the burned trees present within2008 burn were sufficient to completely decorelate the signal. The proximity to

Table 4 Average properties of the fire scars for different slope orientations. Data represent mean values and their standard error. Letters indicate differences between groups ($p<0.05$).

Zuera site.

	Slope orientation	Not burned	1952	1970	1986	1995	2008
				Backscatter			
	Toward sensor	-11.7 (0.28)a	-11.2 (0.25)a	N/A	-11.2 (0.18)a	-10.8 (0.24)a	-7.6 (0.19)b
X-band	Flat area	-9.4 (0.08)a	-9.3 (0.11)a	-9.9 (0.08)b	-9.5 (0.14)ab	-9.6 (0.14)ab	-7.7 (0.08)c
HH	Away from sensor	-9.2 (0.05)a	-9.4 (0.05)a	N/A	-10.0 (0.06)b	-9.4 (0.10)a	-8.5 (0.07)c
	Toward sensor	-19.1 (0.36)a	-18.7 (0.25)a	N/A	-19.2 (0.18)a	-19.6 (0.22)a	-19.5 (0.21)a
X-band	Flat area	-16.2 (0.06)a	-15.9 (0.11)b	-16.8 (0.05)bc	-16.6 (0.11)b	-17.1 (0.10)cd	-17.1 (0.06)d
HV	Away from sensor	-14.6 (0.04)a	-14.5 (0.05)a	N/A	-15.2 (0.05)b	-15.2 (0.06)b	-15.7 (0.05)c
	Toward sensor	-12.2 (0.37)a	-11.4 (0.22)a	N/A	-11.5 (0.22)a	-9.1 (0.21)b	-4.9 (0.14)c
C-band	Flat area	-11.3 (0.16)a	-11.4 (0.24)a	-11.7 (0.13)a	-11.9 (0.27)a	-10.5 (0.17)b	-7.9 (0.27)c
HH	Away from sensor	-12.2 (0.14)a	-12.1 (0.13)a	N/A	-12.0 (0.14)a	-11.9 (0.13)a	-11.1 (0.15)b
	Toward sensor	-18.0 (0.27)a	-16.8 (0.20)b	N/A	-17.4 (0.22)ab	-18.2 (0.22)a	-20.7 (0.20)c
C-band	Flat area	-15.3 (0.14)a	-15.5 (0.24)ab	-16.2 (0.11)bc	-16.0 (0.14)b	-16.6 (0.15)c	-18.4 (0.16)d
HV	Away from sensor	-15.1 (0.14)ab	-14.6 (0.15)a	N/A	-14.8 (0.15)ab	-15.3 (0.12)b	-17.7 (0.12)c
	Toward sensor	-11.9 (0.12)a	-12.5 (0.25)ab	N/A	-12.7 (0.10)b	-13.4 (0.14)c	-13.1 (0.17)bc
L-band	Flat area	-10.8 (0.05)a	-11.4 (0.08)b	-11.7 (0.05)b	-12.1 (0.09)c	-13.7 (0.07)d	-14.4 (0.11)e
HH*	Away from sensor	-9.1 (0.07)a	-9.9 (0.07)b	N/A	-11.2 (0.07)c	-12.5 (0.08)d	-14.1 (0.12)e
	Toward sensor	-16.9 (0.09)a	-18.3 (0.15)b	N/A	-19.8 (0.13)c	-21.7 (0.12)d	-25.0 (0.14)e
L-band	Flat area	-15.0 (0.05)a	-15.8 (0.07)b	-15.8 (0.04)b	-17.0 (0.09)c	-18.7 (0.10)d	-21.8 (0.16)e
HV*	Away from sensor	-13.3 (0.05)a	-14.0 (0.08)b	N/A	-15.0 (0.12)c	-16.9 (0.10)d	-20.9 (0.20)e
				Coherence			
X-band	Toward sensor	0.17 (0.00)a	0.19 (0.00)b	N/A	0.27 (0.01)c	0.33 (0.00)d	0.34 (0.00)d
HH	Flat area	0.18 (0.00)a	0.15 (0.00)b	0.22 (0.00)c	0.23 (0.01)c	0.33 (0.01)d	0.31 (0.00)d
	Away from sensor	0.11 (0.00)a	0.10 (0.00)a	N/A	0.13 (0.00)b	0.24 (0.00)c	0.22 (0.00)d
X-band	Toward sensor	0.13 (0.00)a	0.13(0.00)a	N/A	0.20 (0.00)b	0.25 (0.00)c	0.18 (0.00)b
HV	Flat area	0.12 (0.00)a	0.12 (0.00)a	0.14 (0.00)b	0.16 (0.00)c	0.21 (0.00)d	0.17 (0.00)c
	Away from sensor	0.09 (0.00)a	0.09 (0.00)a	N/A	0.09 (0.00)a	0.15 (0.00)b	0.11 (0.00)c
C-band	Toward sensor	0.21 (0.01)a	0.22 (0.01)a	N/A	0.21 (0.00)a	0.28 (0.01)b	0.53 (0.01)c
HH	Flat area	0.18 (0.00)a	0.20 (0.00)b	0.18 (0.00)a	0.19 (0.01)ab	0.28 (0.01)c	0.38 (0.01)d
	Away from sensor	0.12 (0.00)a	0.14 (0.00)a	N/A	0.16 (0.00)b	0.19 (0.00)c	0.24 (0.01)d
L-band	Toward sensor	0.77 (0.00)a	0.71 (0.01)b	N/A	0.83 (0.00)c	0.77 (0.00)a	0.72 (0.00)b
HH	Flat area	0.77 (0.00)a	0.78 (0.00)ab	0.79 (0.00)b	0.84 (0.00)c	0.76 (0.00)d	0.63 (0.00)e
	Away from sensor	0.76 (0.00)a	0.80 (0.00)b	N/A	0.83 (0.00)c	0.76 (0.00)a	0.56 (0.01)d
L-band	Toward sensor	0.75 (0.00)a	0.69 (0.01)b	N/A	0.76 (0.00)a	0.69 (0.00)b	0.48 (0.00)c
HV	Flat area	0.75 (0.00)a	0.76 (0.00)a	0.75 (0.00)a	0.81 (0.00)b	0.71 (0.00)c	0.48 (0.00)d
	Away from sensor	0.73 (0.00)a	0.78 (0.00)b	N/A	0.83 (0.00)c	0.73 (0.00)a	0.41 (0.01)d

the bias level (i.e. 0.1) of the X-band cross-polarized coherence regardless of the date of the fire implied that no discrimination between forest regrowth stages was possible.

Delta Junction site

At the Alaskan site the analysis of variance produced less obvious results due to smaller time interval between fires, slower regrowth rates and larger variability of the boreal forest in terms of structure, species and moisture conditions (Table 5). Thus, most of the burns pertained to at least two groups in the pair-wise comparison illustrating the transitional nature of the forest regrowth. According to the 1 dB threshold three main regrowth phases were differentiated at HH polarization using backscatter information: i) unburned forest and 1947 burn, ii) 1969, 1971 and 1979 burns and iii) 1987, 1994, 1998 and 1999 burns; whereas for HV polarization a fourth regrowth phase (1987 burn) was separated. The identified phases corresponded largely to the decade of burn suggesting temporally consistent traits. As for Zuera, the interferometric coherence showed low discrimination potential for forest regrowth at both polarizations. Statistically significant differences were found between burns but their use for operational application is limited by the small variability among individual burns. Only the unburned forests were reliably identified at HH polarization since their mean coherence was significantly lower.

Table 5. Average properties of the fire scars. Data represent mean values and their standard error. Letters indicate differences between groups (p<0.05). Delta Junction site.

	NB	1947	1969	1971	1979	1987	1994	1998	1999
L-band	Backscatter								
HH	-9.0(0.28)a	-9.2(0.12)a	-9.9(0.27)b	-10.4(0.29)b	-10.3(0.16)b	-11.0(0.08)c	-11.9(0.19)c	-11.5(0.10)c	-11.1(0.12)c
HV	-14.7(0.37)a	-15.2(0.18)a	-16.1(0.37)b	-16.8(0.31)b	-16.6(0.14)b	-18.1(0.11)c	-19.9(0.17)d	-19.0(0.09)d	-20.4(0.17)d
L-band					Coherence				
HH	0.31(0.02)a	0.49(0.02)b	0.46 (0.03)b	0.55(0.01)b	0.50(0.01)b	0.51(0.00)b	0.62(0.01)b	0.56(0.01)b	0.63(0.01)b
HV	0.26(0.02)a	0.36(0.02)a	0.41(0.02)a	0.38(0.02)a	0.27(0.01)a	0.41(0.00)a	0.46(0.01)a	0.43(0.01)a	0.49(0.01)a

Forest regrowth dynamic - SAR and optical data

To assess the capability of a remote sensing parameter to monitor forest regrowth, the relative difference of the remote sensing parameter (e.g. backscatter) of a fire-affected area with respect to the unburned conditions is here introduced. We will refer to this quantity as percentage of change.

$$\%_{change} = \frac{\overline{x}_{NB} - \overline{x}_{fire}}{\overline{x}_{NB}} * 100 \quad \{1\}$$

In (1) $\overline{x}_{NB}$ represents the value of the remote sensing parameter for unburned conditions whereas $\overline{x}_{\mathrm{fire}}$ represents the corresponding value for a specific fire scar. Since it was shown in this Section that the SAR parameter most sensitive to regrowth is L-band HV backscatter, the analysis will be restricted to this parameter. In addition, we consider the percentage of change for the most widely parameter used for assessing vegetation recovery, i.e. NDVI.

The percentage of change with respect to the unburned forest is presented as a function of time from the fire event for L-band cross-polarized backscatter and NDVI in Fig. 10. For clarity reasons the two parameters are represented on opposite sides of the zero change line. The change in backscatter was computed using the average of the plots located in flat areas whereas for optical data all plots were used when averaging for a given fire scar. Mature unburned forests were represented on the zero change line. For Zuera site, the average age of the forest (65 years) was used to estimate the fire-return interval whereas for interior Alaska the fire regime of Picea mariana dominated forests was previously estimated as low as 80 (Hu et al. 2006) to 120 (Kasischke et al. 2002) years. There is a certain lag between forest age at the Zuera and the Delta Junction site due to the different date of the last burns.

Fig. 10 shows that the percentage of change for L-band HV backscatter and NDVI decreased with forest age during the first years. After a certain age the trend flattened, indicating that the signal had reached values similar to those of mature forest. At the Zuera site, the loss of sensitivity of the NDVI metric occurred approximately 10-15 years after the disturbance; the percentage of change for 20 years old forests was negligible when compared to mature forests. On the contrary, the percentage of change of the L-band cross-polarized backscatter reached mature forest values approximately 40 to 50 years after disturbance. For the slower growing boreal forests, NDVI reached pre-fire values approximately 35 years after burn whereas the L-band cross-polarized backscatter needed approximately 65 years. Fig. 10 also shows that the radar data were sensitive to the trees remaining on site after fire. If burned trees are not removed, the backscatter from recent fire scars may be confused with forest regrowth especially during the first years (e.g. 2008 burn at Zuera site).

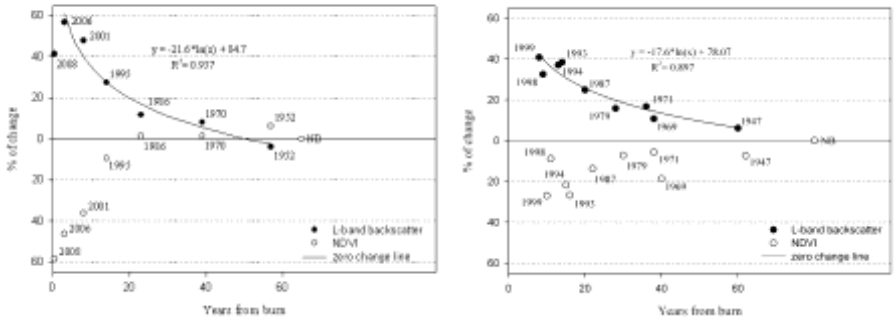

Fig. 10 Forest recovery as seen by L-band SAR and optical based NDVI – percentage of change with respect to the unburned area for Zuera (left) and Delta Junction (right) sites.

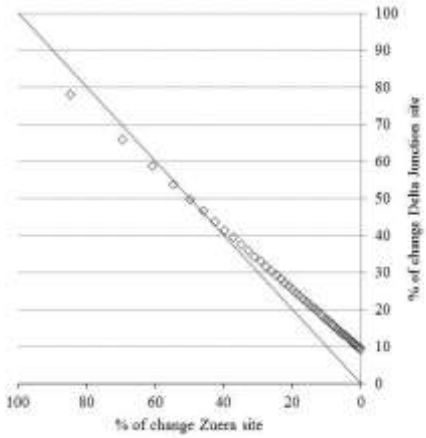

Fig. 11 Co-plotted model-based percentage of change with respect to the unburned area for Zuera and Delta Junction sites.

To evaluate the association strength between forest age and the percentage of change with respect to unburned forest a logarithmic model was fitted to the data (Fig. 10). The 2008 burn at the Zuera site was excluded since it represented an atypical regrowth phase which usually disappears past the second year after disturbance. Both sites showed similar trends suggesting consistent behavior of the L-band HV backscatter over different environments when estimating forest regrowth with L-band SAR data. Fig. 11 illustrates a comparison of the values predicted by the two logarithmic functions. As reference we considered the 1:1 line, indicating perfect correspondence between trends. Fig. 11 shows that the regrowth trends are similar at the beginning of the regrowth (i.e. for the highest percentage of change). The slower growth rate of the boreal forest is revealed by the additional time needed to reach pre-fire forest structure when compared to mediterranean forests. When the mediterranean forest has reached the level of maturity after 65 years (0 % change), at Delta Junction the forest still needs to recover about 10% of the pre-fire structure for which it would need approximately 30 additional years when compared to Zuera pine forests.

CONCLUSIONS

The properties of multi-frequency SAR backscatter and interferometric coherence from mediterranean and boreal forests affected by fire were investigated with the aim of assessing the potential of active microwave remote sensing for forest regrowth monitoring. A comparison with NDVI index was carried out to establish the advantages and limitations of SAR data with respect to optical sensors. For mediterranean forests L-band backscatter allowed the best differentiation of regrowth phases (five phases for six dates) whereas at X- and C-band the backscatter was less sensitive to modification in forest structure due to the rapid saturation of the signal. For boreal forest, up to four different regrowth phases could be discerned with L-band backscatter data, depending on the polarization used. At both test sites, co- and cross-polarized coherence presented weak sensitivity to the different forest regrowth phases, separation being possible only for the most recent burns (15 years).

Analysis of the NDVI in terms of percentage of change with respect to unburned forests in the case of mediterranean pine forest showed saturation at about 10-20 years after disturbance provided that forest cover recovery is not hindered by other factors (e.g. recurrent fires). For boreal forest the optical based indices reached pre-fire levels within 30 years after fire. L-band SAR backscatter provided much larger monitoring intervals of forest regrowth: around 45 years for mediterranean and 65 years for boreal forests. Therefore, L-band SAR cross-polarized data appears more suitable to differentiate among forest regrowth stages after fire compared to optical based data. The usefulness of SAR data for regrowth monitoring is further supported by the independence from solar illumination and visibility. At high latitudes, the availability of usable optical images is scarce due to frequent clouds. Only six images with modest cloud cover were available for Delta Junction site during the vegetation season between 1999 and 2009 from which just one was cloud free over all burns.

Finally, it needs to be mentioned that this study took advantage of the minimum human intervention influencing the regeneration process and the vigorous forest recovery at Zuera site due to the specific microclimate of the area and the resilience of *Pinus halepensis* L. forest. The combination of these factors allowed almost ideal conditions for natural regeneration that could not be met in other regions. In addition, repeatedly burned areas could present different regeneration patterns especially when fires occur at short time intervals, before forests reach maturity. Therefore, the temporal recovery trend registered for the Zuera site could take longer in forests exposed to harsh environment or when fire cycle is short.

ACKNOWLEDGMENTS

This work has been financed by the Spanish Ministry of Science and Education and the European Social Fund: FPI grant BES-2006-11684 and projects CGL2005-04863 and CGL2008-01083. TerraSAR-X data were provided by Deutsches Zentrum für Luft- und Raumfahrt (DLR LAN0464 project). ASAR and PALSAR data were provided by European Space Agency (ESA C1P.5446 project).

REFERENCES

Bourgeau-Chavez, L.L., Harrell, P.A., Kasischke, E.S., and French, N.H.F. (1997). The detection and mapping of Alaskan wildfires using a spaceborne imaging radar system. *International Journal of Remote Sensing, 18*, 355-373.

Bourgeau-Chavez, L.L., Kasischke, E.S., Brunzell, S., and Mudd, J.P. (2002). Mapping fire scars in global boreal forests using imaging radar data. *International Journal of Remote Sensing, 23*, 4211-4234.

Clemente, R.H., Cerrillo, R.M.N., and Gitas, I.Z. (2009). Monitoring post-fire regeneration in Mediterranean ecosystems by employing multitemporal satellite imagery. *International Journal of Wildland Fire, 18*, 648-658.

Cuevas-Gonzalez, M., Gerard, F., Balzter, H., and Riaño, D. (2009). Analysing forest recovery after wildfire disturbance in boreal Siberia using remotely sensed vegetation indices. *Global Change Biology, 15*, 561-577.

Díaz-Delgado, R., Lloret, F., and Pons, X. (2003). Influence of fire severity on plant regeneration by means of remote sensing imagery. *International Journal of Remote Sensing, 24*, 1751-1763.

Díaz-Delgado, R., Lloret, F., Pons, X., and Terradas, J. (2002). Satellite evidence of decreasing resilience in Mediterranean plant communities after recurrent wildfires. *Ecology, 83*, 2293-2303

Díaz-Delgado, R., and Pons, X. (2001). Spatial patterns of forest fires in Catalonia (NE Spain) along the period 1975-1995 Analysis of vegetation recovery after fire. *Forest Ecology and Management, 147*, 67-74.

Games, P.A., and Howel, J.F. (1976). Pairwise Multiple Comparison Procedures with Unequal N's and/or Variances: A Monte Carlo Study. *Journal of Education and Behavioral Statistics, 1*, 113-125.

Goetz, S.J., Sun, M., Baccini, A., and Beck, P.S.A. (2010). Synergistic use of spaceborne lidar and optical imagery for assessing forest disturbance: An Alaska case study. *Journal of Geophysical Research, 115*, 1-14.

Henry, M.C., and Hope, A.S. (1998). Monitoring post-burn recovery of chaparral vegetation in southern California using multi-temporal satellite data. *International Journal of Remote Sensing, 19*, 3097-3107.

Hu, F.S., Brubaker, L.B., Gavin, D.G., Higuera, P.E., Lynch, J.A., Rupp, T.S., and Tinner, W. (2006). How Climate and Vegetation Influence the fire Regime of the Alaskan Boreal Biome: The Holocene Perspective. *Mitigation and Adaptation Strategies for Global Change, 11*, 829-846.

Kasischke, E.S., and Johnstone, J.F. (2005). Variation in post-fire organic layer thickness in a black spruce forest complex in Interior Alaska and its effects on soil temperature and moisture. *Canadian Journal of Remote Sensing, 35*, 2164-2177.

Kasischke, E.S., Williams, D., and Barry, D. (2002). Analysis of the patterns of large fires in the boreal forest region of Alaska. *International Journal of Wildland Fire, 11*, 131-144.

Liew, S.C., Kwoh, L.K., Padmanabhan, K., Lim, O.K., and Lim, H. (1999). Delineating Land/Forest Fire Burnt Scars with ERS Interferometric Synthetic Aperture Radar. *Geophysical Research Letters, 26*, 2409-2412.

Marchetti, M., Ricotta, C., and Volpe, F. (1995). A qualitative approach to the mapping of postfire regrowth in Mediterranean vegetation with Landsat- TM. *International Journal of Remote Sensing, 16*, 2487-2494.

Minchella, A., Del Frate, F., Capogna, F., Anselmi, S., and Manes, F. (2009). Use of multitemporal SAR data for monitoring vegetation recovery of Mediterranean burned areas. *Remote Sensing of Environment, 113*, 588-597.

Notivol, E., Cabañillas, A., González, R., and Revuelta, C. (2005). Caracterización de masas naturales de pino carrasco (Pinus halepensis Mill.) en la depresión del Ebro. In, *IV Congreso Forestal Español* (p. 299). Zaragoza: Sociedad Española de Ciencias Forestales.

Patterson, M.W., and Yool, S.R. (1998). Mapping Fire-Induced Vegetation Mortality Using Landsat Thematic Mapper Data: A Comparison of Linear Transformation Techniques. *Remote Sensing of Environment, 65*, 132-142.

Pérez-Cabello, F. (2002). *Paisajes forestales and fuego en el Prepirineo occidental oscense. Un modelo regional de reconstrucción ambiental. Zaragoza*. Zaragoza.

Rouse, J.W., Haas, R.H., Schell, J.A., and D.W., D. (1973). Monitoring vegetation systems in the Great Plains with ERTS In, *Third ERTS Symposium* (pp. 309-317).

Ruecker, G., and Siegert, F. (2000). Burn scar mapping and fire damage assessment using ERS-2 Sar images in East Kalimantan, Indonesia. *International Archives of Photogrammetry and Remote Sensing, 33*, 1286-1293.

Siegert, F., and Ruecker, G. (2000). Use of multitemporal ERS-2 SAR images for identification of burned scars in south-east Asian tropical rainforest. *International Journal of Remote Sensing, 21*, 831-837.

Sun, G.Q., Rocchio, L., Masek, J., Williams, D., and Ranson, K.J. (2002). Characterization of forest recovery from fire using Landsat and SAR data. In, *Geoscience and Remote Sensing Symposium, 2002. IGARSS '02. Proceedings. 2002 IEEE International* (pp. 1076-1078). Toronto, Canada.

Takeuchi, S., and Yamada, S. (2002). Monitoring of Forest Fire Damage by Using JERS-1 InSAR. In, *Geoscience and Remote Sensing Symposium, 2002. IGARSS '02. Proceedings. 2002 IEEE International* (pp. 3290-3292). Toronto, Canada.

Tanase, M., Pérez-Cabello, F., Riva, J.de la, and Santoro, M. (2010). TerraSAR-X data for burn severity evaluation in Mediterranean forests on sloped terrain. *IEEE Transactions on Geoscience and Remote Sensing, 48*, 917-929.

Tanase, M., Riva, J.de la, Santoro, M., Le Toan, T., and Perez-Cabello, F. (in press-a). Sensitivity of X-, C- and L-band SAR backscatter to fire severity in mediterranean pine forests. *IEEE Transactions on Geoscience and Remote Sensing*.

Tanase, M., Santoro, M., Riva, J.de la, and Pérez-Cabello, F. (2009). Backscatter properties of multitemporal TerraSAR-X data and the effects of influencing factors on burn severity evaluation, in a Mediterranean pine forest. In, *Geoscience and Remote Sensing Symposium, 2009. IGARSS '09. 2009 IEEE International* (pp. 593-596). Cape Town, South Africa.

Tanase, M., Santoro, M., Wegmüller, U., Riva, J.de la, and Pérez-Cabello, F. (in press-b). Properties of X-, C- and L-band repeat-pass interferometric SAR coherence in Mediterranean pine forests affected by fires. *Remote Sensing of Environment*.

Ulander, L.M.H. (1996). Radiometric slope correction of synthetic-aperture radar images. *IEEE Transactions on Geoscience and Remote Sensing, 34*, 1115-1122.

Viedma, Melia, J., Segarra, D., and Garcia-Haro, J. (1997). Modeling Rates of Ecosystem Recovery after Fires by Using Landsat TM Data. *Remote Sensing of Environment, 61*, 383-398.

Viereck, L.A., Dyrness, C.T., Van Cleve, K., and Foote, M.J. (1983). Vegetation, soils, and forest productivity in selected forest types in interior Alaska. *Canadian Journal of Remote Sensing, 13*, 703-720.

Vila, J.P.S., and Barbosa, P. (2010). Post-fire vegetation regrowth detection in the Deiva Marina region (Liguria-Italy) using Landsat TM and ETM+ data. *Ecological Modelling, 221*, 75-84.

Wagtendonk, J.W.van, Root, R.R., and Key, C.H. (2004). Comparison of AVIRIS and Landsat ETM+ detection capabilities for burn severity. *Remote Sensing of Environment, 92*, 397-408.

Wang, Q., Adiku, S., Tenhunen, J., and Granier, A. (2005). On the relationship of NDVI with leaf area index in a deciduous forest site. *Remote Sensing of Environment, 94*, 244-255.

Wegmüller, U., and Werner, C.L. (1995). SAR Interferometric Signatures of Forest. *IEEE Transactions on Geoscience and Remote Sensing, 33*, 1153-1161.

4.4.2. Soil moisture limitations on monitoring boreal forest regrowth using spaceborne L-band SAR data

Kasischke, E., Tanase, M.A., Bourgeau-Chavez, L. and, Borr, M. "Soil moisture limitations on monitoring boreal forest regrowth using spaceborne L-band SAR data" ***Remote Sensing of Environment,*** **accepted.**

Resumen

En este trabajo se investiga el uso de imágenes radar de apertura sintética en banda L para la estimación de biomasa en zonas con bajo nivel de regeneración del bosque. Los datos para estimar la biomasa se obtuvieron a partir de 59 parcelas ubicadas en áreas alteradas por el fuego en bosques de abeto negro en Alaska. Se han utilizado imágenes de doble polarización (HH y HV) del satélite ALOS PALSAR para dos fechas en el verano/otoño de 2007 y para una fecha en el verano de 2009.

Correlaciones positivas entre la biomasa (rango de 0,02 a 22,2 t ha^{-1}*) y el coeficiente de retro-dispersión en la banda L se han encontrado para todas las imágenes analizadas (ambas polarizaciones). La mayor correlación (*R^2*=0,63, p <0,0001) se ha conseguido para la imagen adquirida en condiciones de mayor humedad (polarización HV). Las variaciones en la humedad del suelo en el momento de la toma de las imágenes SAR se traducen en cambios en la correlación entre la biomasa y el coeficiente de retro-dispersión de banda L, evidenciando que la influencia de la humedad del suelo depende de la cantidad de biomasa presente.*

Los resultados indican que el uso de imágenes SAR de banda L para el seguimiento de la recuperación forestal requiere el desarrollo de métodos que tomen en consideración la influencia de la humedad del suelo en la retro-dispersión, que puede ser especialmente importante en niveles bajos de biomasa.

Soil moisture limitations on monitoring boreal forest regrowth using spaceborne L-band SAR data

E. Kasischke[(1)], **M. A. Tanase**[(2)], Laura L. Bourgeau-Chavez[(3)], and Matthew S. Borr[(1)]

[(1)]Department of Geography
University of Maryland
2181 LeFrak Hall, College Park MD 20742, USA
Email: ekasisch@umd.edu, matthewborr@gmail.com

[(2)]Department of Geography,
University of Zaragoza,
Pedro Cerbuna 12, 50009 Zaragoza, Spain
Email: mihai@tma.ro,

[(3)]Michigan Tech Research Institute
Michigan Technological University
3600 Green Court, Ann Arbor, MI 48105 USA
Email: laurmatta.chavez@mtu.edu,

Abstract

A study was carried out to investigate the utility of L-band SAR data for estimating aboveground biomass in sites with low levels of vegetation regrowth. Data to estimate biomass were collected from 59 sites located in fire-disturbed black spruce forests in interior Alaska. PALSAR L-band data (HH and HV polarizations) collected on two dates in the summer/fall of 2007 and one date in the summer of 2009 were used. Significant linear correlations were found between the log of aboveground biomass (range of 0.02 to 22.2 t ha^{-1}) and σ° (L-HH) and σ° (L-HV) for the data collected on each of the three dates, with the highest correlation found using the L-HV data collected when soil moisture was highest. Soil moisture, however, did change the correlations between L-band σ°, and the analyses suggest that the influence of soil moisture is biomass dependent. The results indicate that to use L-band SAR data for monitoring forest regrowth will require development of approaches to account for the influence that variations in soil moisture have on L-band microwave backscatter, which can be particularly strong when low levels of aboveground biomass occur.

***Keywords**: SAR backscatter, interferometric coherence, forest regrowth*

INTRODUCTION

Riom and Le Toan (1981), Sader (1987) and Wu (1987) first demonstrated a relationship between pine forest biomass and synthetic aperture radar (SAR) image intensity, providing the impetus for subsequent research using SAR data from airborne and spaceborne platforms. While analyses of data from airborne platforms showed that P-band (64 cm wavelength) SAR data provided the best correlations to aboveground biomass (Dobson et al. 1992; LeToan et al. 1992; Rignot et al. 1994; Kasischke et al.

1995; Santos et al. 2003), recent research has focused on L-band (24 cm wavelength) data because of its availability from spaceborne systems (the Japanese Earth Resources or JERS SAR and Shuttle Imaging Radar-C or SIR-C SAR).

Research evaluating the potential for spaceborne L-band SAR data to estimate aboveground biomass have taken place in a number of different forest types, including boreal forests (Harrell et al. 1995; Pulliainen et al. 1999; Kurvonen et al. 1999; Tsolmon et al. 2002; Rauste 2005), temperate forests (Dobson et al. 1995; Harrell et al. 1997), savanna woodlands (Lucas et al. 2000; Santos et al. 2002; Austin et al. 2003; Mitchard et al. 2009), and tropical forests (Luckman et al. 1997, 1998; Kuplich et al. 2000; Takeuchi et al. 2000; Salas et al. 2002). The consensus emerging from extensive studies was that at L-band: (1) HV-polarized microwave backscatter was the most sensitive to variations in aboveground biomass; and (2) across all forest types, the sensitivity to biomass reached saturation at biomass levels of 80 to 120 t ha^{-1} (dry weight).

Very few studies have been carried out to examine relationships between L-band SAR/biomass relationships under low biomass situations (0 to 20 t ha^{-1}) (Tsolmon et al 2002). Under low biomass conditions, microwave backscatter from the earth's surface will also be sensitive to variations in soil moisture as well as differences in biomass (Wang et al. 1994). For example, using data from the ERS C-band (6 cm wavelength) SAR, both French et al. (1996) and Bourgeau-Chavez et al. (2007) found strong correlations between SAR backscatter and soil moisture in young (6 to 12 years) boreal forests regenerating following fires. While detailed studies of the relationship between L-band SAR backscatter and soil moisture in non-agricultural landscapes have yet to occur, surface scatterometer measurements by Ulaby et al. (1978) showed that backscatter at L-band frequencies was strongly correlated to soil moisture. In addition, Pulliainen et al. (1999) showed that the L-band backscatter obtained by the JERS SAR over mature boreal forests differed by 1 dB between wet and dry conditions. Research using SIR-C L-band data showed that the relationship between biomass and backscatter in pine forests was sensitive to variations in soil moisture (Harrell et al. 1997). Finally, Salas et al. (2002) noted considerable temporal variation in JERS SAR backscatter in regenerating tropical forest sites that they attributed to variations in soil and vegetation moisture.

Here, we investigated the relationship between L-band SAR backscatter and aboveground biomass in sites located in fire-disturbed black spruce forests in interior Alaska using ALOS PALSAR data. The sites used in this study were located in areas that had burned between 9 and 21 years prior to the data collections and had lower biomass levels (0.02 to 22.2 t ha^{-1}) than typically found in temperate and tropical forests. Variations in precipitation in the days preceding the PALSAR data collections resulted in differences in soil moisture on the three dates that SAR data were available. This data set was used to determine if: (1) L-band SAR backscatter is sensitive to lower biomass variations typically found in regenerating boreal forests; and (2) variations in soil moisture resulted in a systematic shift in the relationship between biomass and L-band SAR backscatter.

STUDY SITE AND METHODS

The 59 sites used for this research were located within the perimeters of three fire events near Delta Junction, Alaska, including: (a) the 20,000 ha Granite Creek Fire that burned in the spring of 1987 (center of fire: 63° 53.1' N Lat., 145° 30.5' W Long.); (b) the 8,900 ha Hajdukovich Creek Fire that burned in the summer of 1994 (center of fire:

63° 48.9' N Lat., 145° 7.6' W Long.); and (c) the 7,900 ha Donnelly Flats Fire that burned in the early summer of 1999 (center of fire: 63° 55.4' N Lat., 145° 43.8' W Long.). These three fire events occurred on relatively flat terrain (< 2 degree slope) on a broad alluvial outwash plain located between the Alaskan Range to the north and the Tanana River to the south. The elevation of the sites ranged between 370 and 500 m above sea level. More detailed descriptions of these study sites can be found in O'Neill et al. (2003) and Kasischke and Johnstone (2005).

The study sites were located in areas that had been occupied by mature black spruce (*Picea mariana*) prior to burning, where the depth of the pre-fire surface organic layer ranged between 10 and 25 cm (Kasischke and Johnstone 2005). In Alaskan black spruce forests, depth of burning strongly regulates patterns of post-fire succession (Johnstone and Kasischke 2005; Johnstone et al. 2010). In sites where a deep organic layer remains after the fire, succession is driven by vegetative reproduction of shrubs and recruitment of black spruce seedlings. In sites experiencing deep burning of the surface organic layer, the exposure of dense humic and mineral soils provides the opportunity for aspen (*Populous tremuloides*) seedling recruitment and growth, initiating a pattern of relay floristics that is more common to post-fire succession in white spruce (*P. glauca*) forests in interior Alaska (Viereck et al. 1983) (Fig. 1).

Each of the fire events used in this study contained areas with shallow and deep burning of the surface organic layers that were the result of variations in organic layer moisture driven by mineral soil texture and seasonal thawing of permafrost (Kasischke and Johnstone 2005; Harden et al. 2006). These areas provided the opportunity to simultaneously investigate how fire severity influences post fire succession and biomass

Fig. 1 Ground photographs showing differences in post-fire regeneration occurring in study sites used for this study. (top left) 1994 burn site dominated by willow shrubs and black spruce seedlings; (top right) 1987 burn site dominated by black spruce saplings and willow shrubs; (bottom left) 1994 burn site dominated by aspen seedlings and willow shrubs; (bottom right) 1994 burn site dominated by aspen saplings. All photographs taken by E. Kasischke in the summer of 2008.

regeneration (Shenoy et al. in preparation), and the sensitivity of L-band backscatter to variations in biomass.

Aboveground biomass was sampled during the summers of 2008 and 2009 for black spruce and aspen seedlings as well as for willow (*Salix sp*.), the dominant understory shrub component in the regenerating forests in the study region. A field reconnaissance was first undertaken to identify areas with different patterns and levels of post-fire regeneration. For specific sites, we first identified an area that had a uniform vegetation cover over a 100 by 100 m (1 ha) area, and then placed the plot at the center. Vegetation and organic layer sampling was accomplished by locating a 30 m long baseline oriented in a random direction at the plot center. One 30 m long sample transect was located perpendicular to the baseline at plot center and an additional sample transect was located at a random distance between 5 and 15 m from the plot center in each direction. All black spruce and aspen seedlings within a distance of ± 1 m of the 3 sample transects were counted to determine seedling density. The diameter distribution of black spruce and aspen seedlings were determined by measuring all seedlings within a 1 by 10 m belt transect located at a random distance along each sample transect. The diameters of all willow stems were also measured in these 1 by 10 m sample areas. Finally, depth of the surface organic layer was measured every 5 m along the sample transects.

Biomass of the black spruce, aspen and willow seedlings were determined using allometric equations from Johnstone and Kasischke (2005), with the exception of aspen, where additional trees were harvested and combined with the data from Johnstone and Kasischke (2005) and Mack et al. (2008) to create a single biomass equation (Shenoy et al. in review).

The SAR data used in this study were collected by the Advanced Land Observing Satellite (ALOS) Phased Array type L-band SAR (PALSAR) sensor. The PALSAR data were received and processed by the Alaska Satellite Facility (ASF). The PALSAR data were collected in the dual polarization (FBD) mode (HH and HV polarizations), where the local incidence angle at swath center was near 39º. PALSAR data collected over the study sites on three separate occasions (15 August 2007, 30 September 2007, and 20 August 2009) were used in this study. The ASF PALSAR data were provided as single look complex images (Level 1.1 product) with a pixel spacing of 9.4 m in slant range and 3.1 m in azimuth. The images were multi-looked (2 range and 10 azimuth) in order to obtain a ground pixel spacing around 30 m in both directions. Prior to geocoding, the PALSAR image intensity values were calibrated using radiometric correction coefficients provided by ASF.

The three PALSAR images were geocoded to within ± 30 m using a 60 m spatial resolution digital elevation model and a UTM projection. Geocoding of the SAR data was based on a lookup table describing the transformation between the radar and the map geometry (Wegmüller et al. 2002) which was generated using a digital elevation model (DEM) and the orbital information of the PALSAR images. To correct for possible inaccuracies in the input data a refinement of the lookup table was applied in the form of offsets estimation between the SAR images and a reference image (e.g. a DEM based simulated SAR image) transformed to the radar geometry. Finally, the SAR images were transformed to the map geometry using the refined lookup table. The locations of each study site within the PALSAR scenes were determined using GPS data that had been collected during the field observations. Average radar image intensity (I)

Table 1 Summary of precipitation (mm) on the 3 dates used in this study. Data are from Delta Junction, Alaska, which is between 10 and 32 km from the sites used in this study.

	15-Aug-07 High soil moisture	30-Sep-07 Very high soil moisture	20-Aug-09 Moderate soil moisture
Previous 60 days	115	128	82
Previous 30 days	59	68	38
Previous 15 days	53	58	38
Previous 24 hours	9	0	6

from the PALSAR data were based on all pixels within a 55 m radius (approximately 10 pixels) of the center of the site. The image intensity values were converted to radar backscatter coefficient (σ°) using the following relationship

$$\sigma^\circ = 10\log(I/A) \quad \{1\}$$

where A is the area (m^2) of the pixels used to generate the average image intensity

While soil moisture data were not available for this study, variations in the relative ground moisture conditions were inferred from precipitation records collected at Delta Junction, Alaska. Previous studies (Bourgeau-Chavez et al. 2007) determined that variations in the time and amount of precipitation were the primary drivers of near-surface soil moisture in the burned sites being used in this study. The highest levels of precipitation occurred prior to the 30 September 2007 and the lowest occurred prior to the 20 August 2009 (Table 1). The soil moisture levels during the 30 September 2007 collection were likely higher than those on 15 August 2007 for several additional reasons. First, the rates of surface evaporation would have been lower in late September because the average maximum daytime temperature decreased from August (21.5 ºC) to September (12.3 ºC). Second, senescence of deciduous foliage occurs in late August in Alaska, thus the removal of soil water via plant transpiration drops significantly in September. Based upon the above assessment, the likely range in soil moisture for the three dates was as follows: 20 August 2009: moderate (best guess of volumetric moisture: 20-40%); 15 August 2007: high (best guess of volumetric moisture: 30-50%); and 30 September 2007: very high (best guess of volumetric moisture: 40-60%).

To analyze the relationship between radar backscatter and biomass, we performed a linear regression using the log of aboveground biomass as the dependent variable and σ° as the independent variable. To analyze the influence of variations in soil moisture, a backscatter ratio (σ°_r) using the scattering coefficients from two dates was generated using the following relationship

$$\sigma^\circ_r = \sigma^\circ(date1) - \sigma^\circ(date2) \quad \{2\}$$

In this analysis we subtracted the site values from the two dates with the lower backscatter (20 August 2009 and 15 August 2007) from the site values from the date with the highest backscatter (30 September 2009) to produce σ°_r. We evaluated this relationship by using σ°_r as the dependent variable and log of the aboveground biomass as the independent variable.

RESULTS

The aboveground biomass levels for the sites used in this study ranged between 0.02 and 22.4 t ha^{-1}. These values are conservative because some sites did include other

low-lying woody shrubs, including blueberry (*Vaccinium* sp.), Labrador tea (*Ledum groenlandicum*), and shrub birch (*Betula glandulosa*). As expected, aboveground biomass was highly correlated with depth of the residual organic layer in the sites located in the 1987 and 1994 burns, with the biomass levels increasing non-linearly in the sites with the shallowest organic layers (Fig. 2). The reason the biomass levels in the 1999 burn were among the lowest found across all sites and did not vary as a function of organic layer depth is most likely because of the low soil moisture experienced in this burn resulted in low recruitment of tree seedlings (Kasischke et al. 2007).

Overall, the dynamic range in σ° for the 59 sites averaged 5.9 dB at HH polarization and 8.3 dB at HV polarization. The correlation between the log of the aboveground biomass and σ° (L-HH) was very low for all three dates: R^2 = 0.20, 0.32, and 0.15 ($p < 0.0005$) for the 15 August 2007, 30 September 2007, and 20 August 2009 data, respectively.

The linear correlations between σ° (L-HV) and the log of the aboveground biomass were much higher (Table 2). The highest R^2 was found on the day when the soil moisture was greatest, 30 September 2007 (Fig. 3). The regression equations developed using the 15 August and 30 September 2007 PALSAR data had identical slope and intercepts, but the regression equation developed using the data from 20 August 2009 (the driest date) had a slightly higher intercept and slope. The RSM errors for the three PALSAR data sets ranged between 2.8 and 3.3 t ha^{-1} (Table 2).

There was a linear relationship between the log of biomass and the backscatter ratio (σ°_r), where the ratio decreased as the biomass increased in both comparisons (Fig. 4). The biomass influence was greatest where the differences in soil moisture were the highest (30 September 2007 versus 20 August 2009) (Fig. 4). The analysis showed that both the slope of the regression line and the intercept for regression lines presented in Fig. 4 were significantly different (Table 3). While the L-HH backscatter ratio was correlated to biomass as well, the correlations were not as strong (R^2 = 0.27, $p < 0.0001$ for 30 September 2007 versus 20 August 2009 ratio and R^2 = 0.16, $p < 0.001$ for 30 September 2007 versus 15 August 2007 ratio).

Table 2 Summary of linear regression of log of aboveground biomass as a function of PALSAR σ° (HV).

Date	F-value	R^2	RMSE (t ha^{-1})	Intercept	std error	t-statistic	95% CI	Slope	std error	t-statistic	95% CI
15-Aug-07	55.1	0.49*	2.8	2.11*	0.55	11.1	± 1.10	0.221*	0.030	7.4	± 0.059
30-Sep-07	97.4	0.63*	3.2	4.11*	0.41	14.8	± 0.83	0.214*	0.022	9.9	± 0.043
20-Aug-09	54.0	0.49*	3.3	5.56*	0.75	10.1	± 1.50	0.311*	0.042	7.3	± 0.085

*significant at $p < 0.0001$

Table 3. Summary of linear regression of the backscatter ratio (σ°_r) as a function of the log of aboveground biomass

Dates	F-value	r^2	Intercept	std error	t-statistic	95% CI	Slope	std error	t-statistic	95% CI
(20 Aug 09)/ (30 Sept 07)	84.9	0.60*	1.37*	0.10	13.6	0.20	-1.39*	0.15	9.2	0.30
(15 Aug 07)/ (30 Sept 07)	20.8	0.27*	0.65*	0.11	6.1	0.21	-0.72*	0.16	4.6	0.32

*significant at $p < 0.0001$

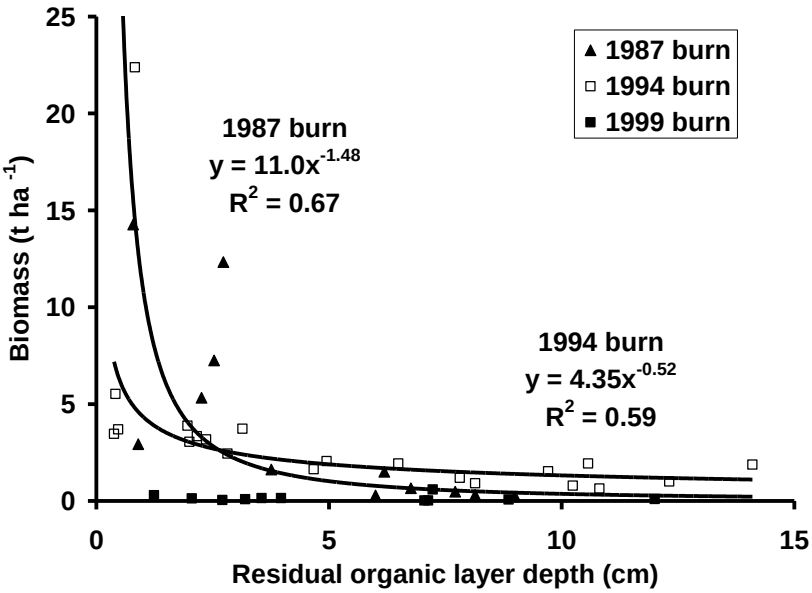

Fig. 2 Relationship between post-fire organic layer depth and aboveground biomass from sites in the 1987, 1994, and 1999 burns. Lines are presented for the 1987 and 1994 data, but not for the 1999, where no significant correlation existed. R^2 values are significant at $p < 0.001$.

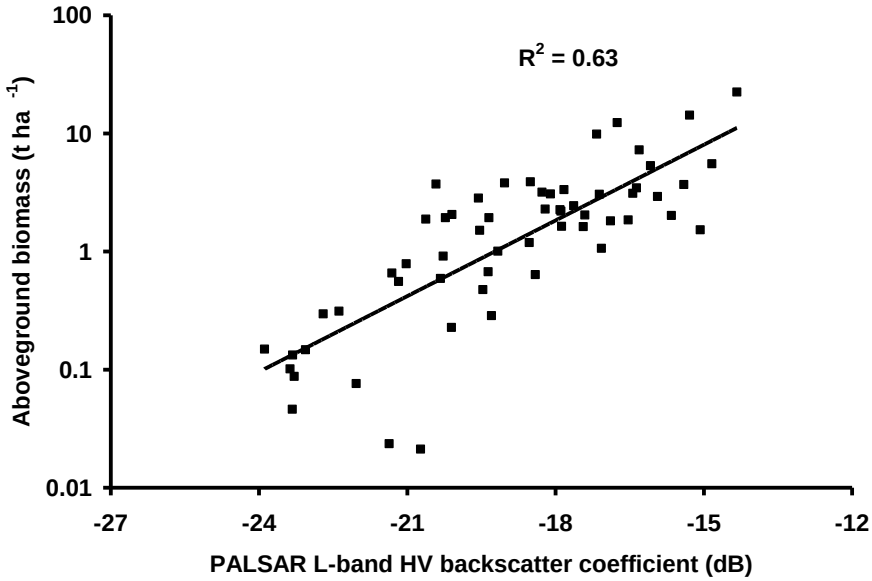

Fig. 3 Aboveground biomass plotted as a function PALSAR σ° (L-HV) from the date with the highest soil moisture conditions (30 September 2007). R^2 value is significant at $p<0.0001$.

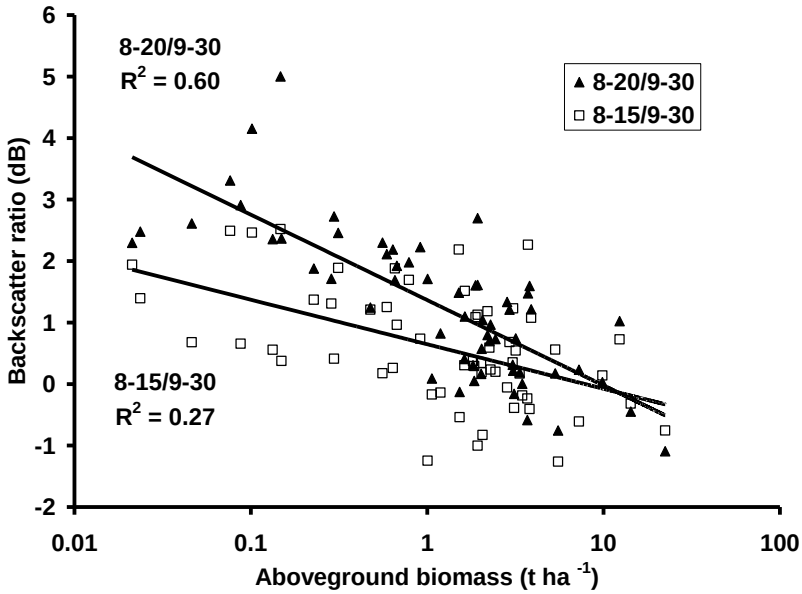

Fig. 4 The L-HV backscatter ratio (σ°_{r}) between wet and dry dates as a function of aboveground biomass. R^2 values are significant at $p < 0.0001$. (8-20/9-30 denotes that the backscatter ratio between 20 August 2009 and 30 September 2007. 8-15/9-30 denotes the backscatter ratio between 15 August 2007 and 30 September 2007).

DISCUSSION

While many previous studies have been conducted on the correlation of L-band SAR backscatter to biomass, only one study has investigated this relationship in low biomass situations (Tsolmon et al. 2002). The results from this study show that the degree of microwave backscattering at L-band from land surfaces is sensitive to variations in biomass in areas where the rate of post-disturbance regrowth is low, such as in many boreal forests, with the highest correlations being obtained using HV polarized data. The results of this study were robust from the standpoint of species composition, where in some sites biomass was dominated by willow shrubs and black spruce saplings, and in others by aspen seedlings and saplings. Thus, these results demonstrate there is the potential for using multi-temporal SAR data for estimating changes in aboveground biomass, a potential that was shown by Takeuchi et al. (2000) in regenerating plantations in a tropical region.

The results of this study demonstrate, however, that the sensitivity of L-band backscatter to variations in soil moisture affects the correlation between backscatter and biomass in areas with low levels of forest regrowth. In modeling study, Wang et al. (2000) found while L-HH backscatter was sensitive to variations in biomass in low biomass situations (biomass = 0 to 3 t ha^{-1}), that backscatter from the soil surface provided the dominant return. The modeling results of Wang et al. (2000) indicated that at volumetric soil moistures between 5 and 45%, the direct backscatter from the soil surface was so great that variations in backscatter from biomass would not be detected. Our results showed this not to be the case – there was a ~ 4 dB increase in L-HH backscatter as biomass increased from 0 to 3 t ha^{-1}.

The highest correlation between L-HV backscatter on biomass occurred when the soil moisture conditions were the highest. This is the opposite of the finding of Harrell et al. (1997), who found that the highest correlations between biomass and L-band SAR backscatter in mature pine forests occurred when the soils were drier.

CONCLUSIONS

Variations in L-band SAR backscatter from the sites containing regenerating forests used in this study came from two sources: (a) variations in biomass; and (b) variations in soil moisture. While the changes in L-HV SAR backscatter as a function of biomass (8 dB) were greater than those observed due to the differences in soil moisture (up to 5 dB), there was a systematic shift in backscatter as a function of biomass when data from very high and moderate soil moisture conditions were compared. The sensitivity of L-band backscatter to variations in soil moisture in low biomass settings is supported by modeling results (Wang et al. 2000) and observations made in tropical forest regions (Salas et al. 2002).

The sites used for this research were located in a region which experiences periods of low precipitation during the growing season. The conditions present during the times when the PALSAR data were collected did not represent the driest conditions that can occur during the growing season. Thus, the differences in L-band backscatter between dry and wet conditions in regrowing boreal forests are likely to be higher than observed in this study.

It should be noted that the black spruce ecosystems of interior Alaska used in this study experience extremely low levels of growth, with aboveground biomass reaching 40 to 60 t ha^{-1} in mature black spruce forests that are 100 to 200 years old (Harrell et al. 2005). The maximum biomass levels of 10 to 20 t ha^{-1} that occurred in the sites used in this study were at locations that had been disturbed 14 to 21 years prior to disturbance. Regrowth is much more rapid in temperature and tropical forests. For example, stand biomass in 15 year old pine forests used by Harrell et al. (1997) ranged between 60 and 140 t ha^{-1}. In these situations, large variations in L-band backscatter caused by variations in soil moisture will only occur during the first several years of regrowth following disturbance or planting.

While L-band backscatter is clearly sensitive to variations in low biomass situations, there is also evidence that variations in soil moisture influence the SAR backscatter biomass relationship in higher biomass situations (Harrell et al. 1997; Puliainen et al. 1999). In a modeling study where forest biomass ranged between 60 and 350 t ha^{-1}, the results of Wang et al. (1998) showed that variations in litter and soil moisture were much greater for L-HH and L-VV polarizations than for L-HV polarization at shallow incidence angles (20-40º), but that at steeper incidence angles, the effects were minimal for L-HV polarization.

These results show that using spaceborne SAR systems to monitor forest regrowth will not only require collection of biomass data to establish the relationship between biomass and backscatter, but may also require developing methods to account for variations in soil moisture. While the case for the impacts of soil moisture is compelling at low biomass (< 20 t ha^{-1}), the evidence for a systematic change in backscatter due to soil moisture at higher biomass is less clear.

Mitchard et al. (2009) suggested that the influence of soil moisture on approaches to estimate savanna woodland biomass using PALSAR L-HV data could be accounted for through the analysis of data collected over multiple dates. The equations developed

by Mitchard et al. (2009), however, had the highest errors in the region with the lowest biomass (for the NCCP Mozambique site the average aboveground biomass was 40.7 t ha^{-1} while the RMSE errors were between 19.2 and 25.2 t ha^{-1}), and unaccounted for variations in soil moisture will only increase these uncertainties.

To reduce the errors associated with using L-band SAR data to estimate biomass in regrowing forests, additional research is required. This includes studies where soil moisture is systematically measured in sites with varying levels of aboveground biomass over multiple dates when spaceborne or airborne SAR data are collected.

These studies are needed across a range of sites experiencing both fast and slow regrowth. Ideally, similar data would be collected across a range of forest and woodland types in order to understand the influence of tree architecture on soil moisture-biomass-backscatter relationships. These data would provide the basis for the validation of theoretical models, which can then be used to examine the influence of soil moisture on backscatter/biomass relationships across a broad range of conditions. Without such research, it will not be possible to use time-series L-band SAR data to assess changes in forest biomass because of uncertainties introduced by variations in soil moisture.

ACKNOWLEDGEMENTS

The research was supported by the National Aeronautics and Space Administration through grant number NNG04GR24G to the University of Maryland and by the Spanish Ministry of Science and Education and the European Social Fund: FPI grant BES-2006-11684. The authors would like to thank Aditi Shenoy and Kirsten Barrett for their assistance in the collection of the biomass data used in this study.

REFERENCES

Austin, J. M., B. G. Mackey, and Van Niel, K. P. 2003. Estimating forest biomass using satellite radar: an exploratory study in a temperate Australian Eucalyptus forest. *Forest Ecology and Management 176* , 575-583.

Bourgeau-Chavez, L. L., E. S. Kasischke, K. Riordan, S. M. Brunzell, M. Nolan, E. J. Hyer, J. J. Slawski, M. Medvecz, T. Walters, and Ames., S. 2007. Remote monitoring of spatial and temporal surface soil moisture in fire disturbed boreal forest ecosystems with ERS SAR imagery. *Internatinal Journal of Remote Sensing 28*, 2133-2162.

Dobson, M. C., F. T. Ulaby, T. Le Toan, A. Beaudoin, E. S. Kasischke, and Christensen., N. L. 1992. Dependence of radar backscatter on conifer forest biomass. *IEEE Transactions on Geoscience and Remote Sensing 30*, 412-415.

Dobson, M. C., F. T. Ulaby, L. E. Pierce, T. L. Sharik, K. M. Bergen, J. Kellndorfer, J. R. Kendra, E. Li, Y. C. Lin, A. Nashashibi, K. L. Sarabandi, and Siqueira., P. 1995. Estimation of forest biomass characteristics in northern Michigan with SIR-C/XSAR data. *IEEE Transactions on Geoscience and Remote Sensing 3*3, 877-894.

French, N. H. F., E. S. Kasischke, L. L. Bourgeau-Chavez, P. Harrell, and N. L. Christensen, Jr. 1996. Monitoring variations in soil moisture on fire disturbed sites in Alaska using ERS-1 SAR imagery. *International Journal of Remote Sensing* 17, 3037-3053.

Harden, J. W., K. L. Manies, M. R. Turetsky, and Neff., J. C. 2006. Effects of wildfire and permafrost on soil organic matter and soil climate in interior Alaska. *Global Change Biology 12*, 2391-2403.

Harrell, P. A., L. L. Bourgeau-Chavez, E. S. Kasischke, N. H. F. French, and Christensen Jr., N. L. 1995. Sensitivity of ERS-1 and JERS-1 radar data to biomass and stand structure in Alaskan boreal forest. *Remote Sensing of Environment 54*, 247-260.

Harrell, P. A., E. S. Kasischke, L. L. Bourgeau-Chavez, E. Haney, and Christensen., N. L. 1997. Evaluation of approaches to estimating of aboveground biomass in southern pine forests using SIR-C imagery. *Remote Sensing of Environment 59*, 223-233.

Johnstone, J. F., and Kasischke., E. S. 2005. Stand-level effects of burn severity on post-fire regeneration in a recently-burned black spruce forest. *Canadian Journal of Forest Research 35*, 2151-2163.

Johnstone, J. F., T. N. Hollingsworth, F. S. I. Chapin, and Mack., M. C. 2010. Changes in fire regime break the legacy lock on successional trajectories in Alaskan boreal forest. *Global Change Biology 16*, 1281-1295.

Kasischke, E. S., N. L. Christensen, and Bourgeau-Chavez., L. L. 1995. Correlating radar backscatter with components of biomass in loblolly-pine forests. *IEEE Transactions on Geoscience and Remote Sensing 33*, 643-659.

Kasischke, E. S., and Johnstone., J. F. 2005. Variation in post-fire organic layer thickness in a black spruce forest complex in Interior Alaska and its effects on soil temperature and moisture. *Canadian Journal of Forest Research 35*, 2164-2177.

Kasischke, E. S., L. L. Bourgeau-Chavez, and Johnstone., J. F. 2007. Assessing spatial and temporal variations in surface soil moisture in fire-disturbed black spruce forests using spaceborne synthetic aperture radar imagery - implications for post-fire tree recruitment. *Remote Sensing of Environment 108*, 42-58.

Kuplich, T. M., V. Salvatori, and Curran., P. J. 2000. JERS-1/SAR backscatter and its relationship with biomass of regenerating forests. *International Journal of Remote Sensing 21*, 2513-2518.

Kurvonen, L., J. Pulliainen, and Hallikainen., M. 1999. Retrieval of biomass in boreal forests from multitemporal ERS-1 and JERS-1 SAR images. *IEEE Transactions on Geoscience and Remote Sensing 37*, 198-205.

Le Toan, T., A. Beaudoin, J. Riom, and Guyon., D. 1992. Relating forest biomass to SAR data. *IEEE Transactions on Geoscience and Remote Sensing 30*, 403-411.

Lin, D. S., E. F. Wood, K. Beven, and Saatchi., S. S. 1994. Soil-moisture estimation over grass-covered areas using AIRSAR. *International Journal of Remote Sensing 15*, 2323-2343.

Lucas, R. M., A. K. Milne, N. Cronin, C. Witte, and Denham., R. 2000. The potential of synthetic aperture radar (SAR) for quantifying the biomass of Australia's woodlands. *Rangeland Journal 22*, 124-140.

Luckman, A., J. Baker, T. M. Kuplich, C. D. F. Yanasse, and Frery., A. C. 1997. A study of the relationship between radar backscatter and regenerating tropical forest biomass for spaceborne SAR instruments. *Remote Sensing of Environment 60*, 1-13.

Luckman, A., J. Baker, M. Honzak, and Lucas., R. 1998. Tropical forest biomass density estimation using JERS-1 SAR: seasonal variation, confidence limits, and application to image mosaics. *Remote Sensing of Environment 63*, 126-139.

O'Neill, K. P., E. S. Kasischke, and D. D. Richter. 2003. Seasonal and decadal patterns of soil carbon uptake and emission along an age-sequence of burned black spruce stands in interior Alaska. *Journal of Geophysical Research* 108, FFR 11-11 to 11-15.

Mitchard, E. T. A., S. S. Saatchi, I. H. Woodhouse, G. Nangendo, N. S. Ribeiro, M. Williams, C. M. Ryan, S. L. Lewis, T. R. Feldpausch, and Meir.,P. 2009. Using satellite radar backscatter to

predict above-ground woody biomass: A consistent relationship across four different African landscapes. *Geophysical Research Letters 36*, Article Number: L23401.

Pulliainen, J. T., L. Kurvonen, and Hallikainen., M. T. 1999. Multitemporal behavior of L- and C-band SAR observations of boreal forests. *IEEE Transactions on Geoscience and Remote Sensing 37*, 927-937.

Rauste, Y. 2005. Multi-temporal JERS SAR data in boreal forest biomass mapping. *Remote Sensing of Environment 97*, 263-275.

Rignot, E., J. B. Way, C. Williams, and Viereck., L. 1994. Radar Estimates of Aboveground Biomass in Boreal Forests of Interior Alaska. *IEEE Transactions on Geoscience and Remote Sensing 32*, 1117-1124.

Riom, J., and Le Toan., T. 1981. Relations entre des type de forests de pine maritimes et la retrodiffusion radar on bande L. in Proceedings of *Spectral Signatures of Objects in Remote Sensing. International Society Photogrammetry*, Avigon, France, 455-465.

Sader, S. A. 1987. Forest biomass, canopy structure, and species composition relationships with multipolarization L-band synthetic aperture radar data. *Photogrammetric Engineering and Remote Sensing 23*, 193-202.

Salas, W. A., M. J. Ducey, E. Rignot, and Skole., D. 2002. Assessment of JERS-1 SAR for monitoring secondary vegetation in Amazonia: I. spatial and temporal variability in backscatter across a chrono-sequence of secondary vegetation stands in Rondonia. *International Journal of Remote Sensing 23*, 1357-1379.

Santos, J. R., M. S. P. Lacruz, A. L.S., and Keil., M. 2002. Savanna and tropical rainforest biomass estimation and spatialization using JERS-1 data. *International Journal of Remote Sensing 23*, 1217-1229.

Santos, J. R., C. C. Freitas, A. L.S., L. V. Dutra, J. C. Mura, F. F. Gama, L. S. Soler, and Sant'Anna., S.J.S. 2003. Airborne P-band SAR applied to the aboveground biomass studies in the Brazilian tropical rainforest. *Remote Sensing of Environment 87*,482-493.

Shenoy, A., J.F. Johnstone, and Kasischke., E. In preparation. Variations in organic layer depth shape post-fire vegetation communities in black spruce forests of interior Alaska.

Takeuchi, S., Y. Suga, Y. Oguro, and Konishi., T. 2000. Monitoring of new plantation development in tropical rain forests using JERS-1 SAR data. *Advances in Space Research 26*, 1151-1154.

Tsolmon, R., R. Tateishi, and Tetuko., J. S. S. 2002. A method to estimate forest biomass and its application to monitor Mongolian Taiga using JERS-1 SAR data. *International Journal of Remote Sensing 23*, 4971-4978.

Ulaby, F. T., P. P. Batlivala, and Dobson., M. C. 1978. Microwave backscatter dependence on surface-roughness, soil-moisture, and soil texture: Part I - Bare soil. *IEEE Transactions on Geoscience and Remote Sensing 16*, 286-295.

Viereck, L. A., C. T. Dyrness, K. Van Cleve, and Foote., M. J. 1983. Vegetation, soils, and forest productivity in selected forest types in interior Alaska. *Canadian Journal of Forest Research 13*, 703-720.

Wang, Y., E. S. Kasischke, F. W. Davis, J. M. Melack, and Christensen., N. L. 1994. The effects of changes in loblolly pine biomass and soil moisture variations on ERS-1 SAR backscatter - a comparison of observations with theory. *Remote Sensing of Environment 49*, 25-31.

Wang, Y., Kasischke, E.S., Bourgeau-Chavez, L.L., O'Neill, K.P., and French, N.H.F. (2000). Assessing the influence of vegetation cover on soil-moisture signatures in fire-disturbed boreal

forests in interior Alaska: modeled results. *International Journal of Remote Sensing 21*, 689-708.

Wang, Y., Day, D.L., and Davis, F.W. (1998). Sensitivity of modeled C- and L-band radar backscatter to ground surface parameters in loblolly pine forest. *Remote Sensing of Environment 66*, 331-342

Wegmüller, U., Werner, C., Strozzi, T., and Wiesmann., A. 2002. Automated and precise image registration procedures, in Eds. Bruzzone, L., and Smits, P., *Analysis of Multi-Temporal Remote Sensing Images, Vol. 2*, Proceedings of the First International Workshop on MultiTemp 2001, University of Trento, Italy, 13-14 September 2001, 37-49.

Wu, S. T. 1987. Potential Application of Multipolarization SAR for Pine-Plantation Biomass Estimation. *IEEE Transactions on Geoscience and Remote Sensing 25*, 403-409.

Capítulo 5. DISCUSIÓN GENERAL - CONCLUSIONES Y LÍNEAS FUTURAS DE INVESTIGACIÓN

Los incendios forestales afectan cada año cientos de miles de hectáreas de bosque y matorral en la Cuenca Mediterránea, siendo uno de los principales factores de degradación del paisaje después de la intervención humana, a la que están íntimamente ligados. Sus principales efectos son la pérdida de biomasa y estructura forestal, la degradación del suelo y la emisión de gases con efecto invernadero. Para la gestión de las superficies afectadas se necesita no sólo información sobre el área total afectada y su localización exacta, sino también un análisis sistemático de los efectos del fuego. Éstos se estiman en términos de severidad a corto o a largo plazo: a corto plazo interesan las consecuencias ecológicas en los componentes del sistema, mientras que a largo plazo interesa el estado de la recuperación del ecosistema. La evaluación del daño ecológico en función de la severidad se evalúa frecuentemente, en su distribución espacial, mediante técnicas de teledetección, que también son utilizadas para el seguimiento temporal de los patrones de recuperación. Hasta la fecha la mayor parte de los estudios de la severidad y el seguimiento post–incendio apoyados en la teledetección han empleado sensores ópticos (pasivos) permaneciendo por conocer el potencial de los sensores radar (activos). Esta tesis doctoral explora las posibilidades del radar de apertura sintética para los estudios post-incendio destacando tanto sus puntos fuertes como las potenciales fuentes de error.

Sensores ópticos

Los modelos empíricos locales y regionales para la estimación de la severidad desarrollados mediante el uso de sensores ópticos y parcelas experimentales (primer apartado del Capítulo 4) apuntan que, para el conjunto de los pinares aragoneses, la información procedente del infrarrojo próximo y del medio de onda corta (bandas 4 y 7 de Landsat TM) es suficiente para cartografiar la distribución de los niveles de severidad altos y bajos. Comparando todos los índices analizados, se han detectado errores menores para aquellos que incluyen información espectral del infrarrojo medio de onda corta y utilizan el método bi-temporal con imágenes anteriores y posteriores al incendio. El modelo que mejor se ajusta a los datos a nivel regional ha sido el *saturated growth model*, siendo los errores de estimación entre un 10 y un 20% menores en comparación con los demás modelos analizados. En términos generales, los errores de estimación se sitúan en torno al 10% para las áreas fuertemente afectadas y las no quemadas, incrementándose para los niveles de severidad intermedios hasta un 25%. Este aumento limita el uso de los sensores ópticos para una representación precisa del patrón espacial de los efectos del fuego en incendios forestales con grandes áreas afectadas por severidades bajas e intermedias.

El uso del SAR para la estimación de la severidad

Las limitaciones de los sensores ópticos han inducido a investigar métodos alternativos, como el radar de apertura sintética, para el análisis de las áreas quemadas. Sin embargo, para desarrollar métodos operacionales robustos y aplicables en entornos heterogéneos respecto al tipo de vegetación y a las condiciones ambientales es necesario entender la relación existente entre la información procedente de los sensores radar y las características de las superficies quemadas. Por ello, la investigación se ha centrado, en primer lugar, en el análisis de las signaturas y sus variaciones en función de las

propiedades topográficas y climáticas del territorio. Posteriormente se ha investigado el potencial de los parámetros radar (el coeficiente de retro-dispersión y la coherencia interferométrica) de múltiples bandas y polarizaciones para la evaluación de áreas incendiadas, tanto para la estimación de la severidad como para el seguimiento de la recuperación vegetal post-incendio.

El coeficiente de retro-dispersión

El análisis realizado indica que el coeficiente de retro-dispersión de las microondas co-polarizadas (polarizaciones HH y VV) de alta frecuencia (bandas X y C) aumenta con el incremento de la severidad, especialmente en áreas quemadas para pendientes orientadas hacia el sensor; al mismo tiempo se ha observado la saturación de la señal en los niveles altos de severidad. Para las ondas co-polarizadas de baja frecuencia (banda L), las tendencias registradas siguen un patrón totalmente opuesto, disminuyendo el coeficiente de retro-dispersión con el incremento de la severidad como consecuencia de su menor sensibilidad a la atenuación por la vegetación. Una ventaja importante de la banda L con respecto a las bandas X y C lo constituye la ausencia de la saturación de la señal radar en los niveles altos de severidad. El coeficiente de retro-dispersión de polarización cruzada disminuye con el incremento de la severidad para todas las frecuencias. Además, la señal no se satura en ninguna banda, incluidas las frecuencias más altas (banda X). El rango dinámico entre las zonas no quemadas y las zonas fuertemente afectadas por el fuego disminuye con el ángulo de incidencia local (banda X y C). En cambio, para las ondas de polarización cruzada el rango dinámico del coeficiente de retro-dispersión es relativamente estable en todos los ángulos de incidencia local. La sensibilidad del coeficiente de retro-dispersión a la severidad del incendio aumenta al hacerlo la longitud de onda para todas las polarizaciones.

Se han observado mejoras en el rango dinámico del coeficiente de retro-dispersión (ondas co-polarizadas) en condiciones de mayor humedad ambiental (bandas X y C), especialmente durante los meses de verano, cuando el potencial de evapotranspiración en medios mediterráneos es alto. En consecuencia, las imágenes adquiridas después de lluvias presentan un mayor potencial para la estimación de la severidad en el caso de las ondas co-polarizadas de alta frecuencia. Sin embargo, el incremento de la humedad no siempre se traduce en una mejora en la discriminación de la severidad (ej. en el caso de eventos tormentosos); además, niveles altos de humedad ambiental han disminuido de modo significativo la sensibilidad de la polarización cruzada a la severidad. Por lo tanto, no es conveniente utilizar imágenes adquiridas en periodos de inestabilidad atmosférica caracterizados por fuertes lluvias.

Los cambios en el ángulo de incidencia local como consecuencia del relieve influyen de modo significativo en la señal radar. En el caso de las ondas co-polarizadas, el coeficiente de retro-dispersión disminuye con el aumento del ángulo de incidencia local, mientras que para las ondas de polarización cruzada la tendencia es opuesta. Esta influencia divergente debe ser tenida en cuenta en la estimación de cualquier característica forestal cuando se trabaja en zonas con relieve contrastado.

Los modelos empíricos empleados para evaluar la viabilidad del uso del coeficiente de retro-dispersión para la estimación de la severidad apuntan que las ondas de polarización cruzada y baja frecuencia presentan el mayor potencial. Las ondas co-polarizadas de alta frecuencia (X y C) se han mostrado útiles sólo para pendientes orientadas hacia el sensor. El uso conjunto de dos polarizaciones (HH y HV) aumenta la sensibilidad a la severidad, especialmente en la banda X, compensando el escaso rango dinámico de los datos. Resultados similares se han obtenido para diferentes geometrías

de observación del satélite (ángulos de incidencia variables), aunque los valores absolutos del coeficiente de retro-dispersión disminuyen con el incremento del ángulo de incidencia. Una mejora evidente de los coeficientes de determinación se produce en el caso de las imágenes procesadas con factores altos de multi-look por la menor influencia del moteado. El uso de filtros multi-temporales también se traduce en un incremento de la precisión de la estimación, especialmente para las imágenes procesadas con factores de multi-look bajos.

Las tendencias observadas han sido consistentes en los tres incendios estudiados en el ámbito mediterráneo, sugiriendo que la respuesta de la señal radar no depende de las condiciones locales del fuego. Además, se han observado tendencias similares para la banda L en bosques boreales para imágenes adquiridas en periodos relativamente secos.

La coherencia interferométrica

El coeficiente de retro-dispersión expresa la intensidad total recibida por el radar después de la dispersión; por tanto, no aporta información acerca de la disposición estructural de los dispersores individuales dentro del volumen de los bosques. En cambio, la interferometría SAR ofrece una medida directa de la distribución de los dispersores en el bosque mediante la fase y de la correlación entre la señal reflejada por un determinado objetivo visto bajo dos ángulos diferentes mediante la coherencia interferométrica.

Las tendencias observadas para la coherencia interferométrica han sido similares a las registradas para el coeficiente de retro-dispersión. Para las ondas co-polarizadas de alta frecuencia (banda X y C) la coherencia aumenta con el incremento de la severidad. El incremento es casi lineal y la saturación de la señal ocurre sólo en los más altos niveles de severidad para la banda C, mientras que para la banda X la señal se satura a niveles menores de severidad (~ 600 dNBR). Mayores niveles de coherencia (hasta 0,8) se han observado para las imágenes adquiridas durante la misión tándem del satélite ERS 1 y 2 en comparación con las registradas con mayor intervalo de tiempo, como es el caso de los satélites Envisat ASAR (hasta 0,55) o TerraSAR-X (hasta 0,4). Las tendencias han sido similares para las imágenes adquiridas en condiciones estables y con líneas base cortas. Un mayor rango dinámico se observa para las imágenes de banda C en comparación con la banda X. En general, las ondas de polarización cruzada han sido poco sensibles a la severidad del incendio. En la banda L coherencia disminuye con el incremento de la severidad para las dos polarizaciones (HH y HV), debido a los cambios fisiológicos en los árboles quemados; en general, el rango dinámico entre zonas fuertemente afectadas por el fuego y zonas no quemada es mayor que para las ondas de alta frecuencia (0,4-0,5).

Las condiciones meteorológicas durante la adquisición de las imágenes tienen un importante impacto, observándose niveles menores de coherencia y rango dinámico en los pares que contienen imágenes adquiridas después de lluvias intensas. Sin embargo, la topografía tiene una menor influencia sobre la coherencia en comparación con el coeficiente de retro-dispersión. No obstante, para zonas con orientación ortogonal hacia el sensor se ha observado una fuerte decorrelación en los pendientes mayores de 10°-15°.

Para las bandas X y C el análisis de regresión muestra una relación moderada entre la coherencia interferométrica y la severidad cuando el ángulo de incidencia no se tiene en cuenta. Los coeficientes de determinación aumentan para imágenes adquiridas en condiciones estables analizadas por rangos de ángulo de incidencia local. La relación con la severidad es más sensible a cambios en la línea base que a cambios en las

condiciones atmosféricas durante la adquisición. La coherencia de las ondas co-polarizadas ha sido útil para la evaluación de la severidad incluso en pendientes con orientación opuesta al sensor, a diferencia de lo que sucede con el coeficiente de retro-dispersión. Para la banda L, el análisis de regresión ha evidenciado una influencia mucho menor de la topografía, siendo altos los coeficientes de determinación incluso para el análisis conjunto de todos los datos.

El uso conjunto de la coherencia interferométrica y del coeficiente de retro-dispersión no mejora de modo significativo la estimación de la severidad. Por lo tanto, parece más apropiado utilizar sólo una de las dos características SAR con objeto de generar modelos lo más simples posibles.

El uso del SAR para el seguimiento de la recuperación vegetal

Se han investigado las propiedades del coeficiente de retro-dispersión y de la coherencia interferométrica de bosques afectados por el fuego con el fin de evaluar su potencial para el seguimiento de la recuperación vegetal. Así mismo, se ha llevado a cabo una comparación con el NDVI con objeto de establecer las ventajas y limitaciones de los datos SAR con respecto a los sensores ópticos.

El coeficiente de retro-dispersión

Para las ondas co-polarizadas de alta frecuencia (X y C) el coeficiente de retro-dispersión se incrementa en áreas de recrecimiento en comparación con el bosque no quemado, mientras que para la polarización cruzada el coeficiente de retro-dispersión es mayor en las zonas no quemadas. El rango dinámico entre las zonas no quemadas y las zonas con escasa regeneración vegetal es pequeño para la banda X (1-2 dB) y muestra dependencia del ángulo de incidencia local: se incrementa para ángulos pequeños y disminuye para ángulos elevados. En la banda C se ha observado un mayor rango dinámico para ambas polarizaciones (3 dB) en áreas planas; sin embargo, la influencia del ángulo de incidencia local se mantiene para las ondas co-polarizadas. En general, para las bandas X y C las diferencias entre el coeficiente de retro-dispersión procedente de áreas con distinto nivel de recuperación vegetal son pequeñas, excepto para las primeras etapas de crecimiento (los incendios más recientes).

Mayores diferencias en el coeficiente de retro-dispersión se han registrado en la banda L, alcanzando el rango dinámico unos 10 dB para la polarización HV y 6 dB para la polarización HH. La retro-dispersión aumenta con la edad del bosque para ambas polarizaciones (HH y HV). Tendencias similares se observan en bosques boreales (banda L) en una área afectada por incendios en Alaska, aunque los valores absolutos del coeficiente de retro-dispersión han sido más altos y el rango dinámico más bajo en comparación con los bosques mediterráneos.

El análisis estadístico ha revelado diferencias estadísticas significativas de la retro-dispersión para todas las frecuencias y polarizaciones. Sin embargo para las bandas X y C la mayoría de estas diferencias son de poca utilidad práctica, situándose por debajo de 1 dB. Por lo tanto, utilizando microondas de alta frecuencia se podrían diferenciar solamente áreas de recrecimiento más recientes, en las que la recuperación de la vegetación es incipiente. Sin embargo, la banda L permite discriminar hasta cinco fases de crecimiento en cada polarización (HH o HV). Para los bosques boreales la diferenciación de los fases de crecimiento ha sido algo menor, debido a la variación mucho mayor de la estructura forestal y a los condiciones locales de humedad; no obstante, se pueden diferenciar 3 ó 4 fases de crecimiento en función de la polarización empleada (HH o HV).

El análisis comparativo del coeficiente de retro-dispersión y del NDVI ha revelado la mayor utilidad del radar de apertura sintética para el seguimiento de la recuperación vegetal. El coeficiente de retro-dispersión no sólo ha proporcionado una mayor diferenciación entre las diferentes etapas de crecimiento, sino también un mayor intervalo útil para la monitorización del estado de la recuperación vegetal en áreas quemadas.

La coherencia interferométrica

La coherencia interferométrica disminuye con la edad del bosque para las bandas X y C, mientras que para la banda L la tendencia es completamente opuesta. La topografía afecta al nivel de coherencia en todas las bandas estudiadas. Para el bosque boreal la coherencia en la banda L disminuye con la edad del bosque. El análisis estadístico revela diferencias significativas entre los niveles de coherencia de las etapas de crecimiento; sin embargo, el reducido rango dinámico no permite una identificación certera de estas etapas para ninguno de los tipos de bosque estudiados. La única excepción es la más reciente área quemada en la Cuenca Mediterránea (Zuera08).

Conclusiones

1. Estimaciones fiables pueden obtenerse utilizando imágenes ópticas de sensores remotos para zonas de alta o baja severidad en los bosques aragoneses de pino. Sin embargo, para zonas de severidades intermedias el error de estimación aumenta y la inversión de los modelos es menos precisa.

2. Los sistemas radar de apertura sintética tienen un gran potencial para la estimación de la severidad tanto mediante el coeficiente de retro-dispersión como utilizando la coherencia interferométrica; el potencial del SAR disminuye con el incremento de la frecuencia para ambas características. Los mejores resultados se obtienen mediante la polarización cruzada en el caso del coeficiente de retro-dispersión y para las ondas co-polarizadas en el caso de la coherencia interferométrica.

3. El uso conjunto del coeficiente de retro-dispersión y la coherencia interferométrica no mejora de forma significativa la estimación de la severidad en ninguna de las frecuencias radar estudiadas.

4. La geometría de visualización del satélite (ángulo de incidencia) influye el coeficiente de retro-dispersión en forma de una constante (*offset*). Sin embargo la sensibilidad del sistema a la severidad no cambia de modo significativo.

5. La señal radar está fuertemente influida por la topografía. Por lo tanto, es imprescindible tener en consideración la orientación y la pendiente de las superficies para la estimación de la severidad. Aunque en el caso de la coherencia interferométrica la influencia de la topografía es menor, se obtienen mejores resultados cuando el análisis tiene en cuenta el ángulo de incidencia local.

6. La mayor fuente de error en la estimación de la severidad se relaciona con las condiciones de humedad del suelo y de la vegetación. En algunos casos específicos y para algunas polarizaciones las lluvias podrían aumentar la sensibilidad del SAR a la severidad; sin embargo, estos efectos no son constantes, siendo difícil separar la variabilidad de la señal debida a las diferencias en humedad de las ocasionadas por las variaciones en la severidad. Además, en el caso del coeficiente de retro-dispersión (polarización cruzada) o de la coherencia interferométrica (ambas polarizaciones) los cambios de humedad perjudican la estimación de la severidad.

7. La correlación entre el coeficiente de retro-dispersión y la severidad se incrementa con el aumento de la resolución espacial, es decir, con la posibilidad de reducir el moteado mediante la utilización de factores de *multi-look* superiores.

8. El seguimiento de la recuperación vegetal utilizando información procedente de sensores radar puede realizarse mediante el coeficiente de retro-dispersión de las bandas de baja frecuencia (L). Las de alta frecuencia (X y C) son poco sensibles a los cambios en la estructura forestal, teniendo un potencial mucho menor a la hora de diferenciar entre diferentes etapas de crecimiento.

9. La coherencia interferométrica ha sido poco sensible a las diferencias en la estructura forestal en todas las frecuencias, resultando poco útil para distinguir entre las diferentes etapas de la recuperación vegetal. La adquisición de las imágenes en el modo *repeat-pass* ha sido determinante dado a la decorrelación temporal de la señal debido a factores externos a la estructura forestal. (i.e. cambios en las condiciones ambientales).

10. Los estudios preliminares llevados a cabo en zonas boreales confirman los resultados obtenidos en la Cuenca Mediterránea, al menos en condiciones medioambientales específicas (imágenes adquiridas durante la temporada vegetativa y en condiciones relativamente secas).

Líneas futuras de investigación

Esta tesis doctoral ha iniciado una nueva línea de investigación en el campo de la evaluación post-incendio de las áreas quemadas que potencialmente permitiría conocer con una mayor exactitud la severidad y la recuperación de la estructura forestal a escalas locales o regionales. A pesar de la mejora cualitativa y/o cuantitativa que introducen los métodos desarrollados y que los resultados obtenidos son consistentes, debe profundizarse el análisis iniciado, especialmente considerando la necesidad de desarrollar nuevos métodos para la estimación de la severidad en el campo que sean más adecuados a la información estructural registrada por los sensores radar. El desarrollo de métodos de muestreo, más ajustados a los sensores radar, permitirá una mejor caracterización del potencial de esta nueva herramienta.

Asimismo se debe continuar indagando en la utilidad de las imágenes SAR en las zonas boreales o tropicales, donde el radar es la única fuente segura de datos debido a la frecuente cobertura nubosa. En esta tesis se han presentado resultados preliminares que apuntan tendencias similares, por lo menos en los bosques boreales y en determinadas condiciones. Sin embargo, la gran variedad estructural y ambiental de estos bosques requiere profundizar los estudios no sólo para su validación en otras áreas sino también para una mejor explicación de la influencia de los factores ambientales sobre la retro-difusión y la coherencia interferométrica en áreas quemadas.

Con respecto a la teledetección, la utilización de técnicas polarimétricas o de interferometría polarimétrica podría aportar una nueva dimensión a la investigación realizada. Las propiedades de muchos objetos son inherentemente polarimétricas; la severidad en áreas afectadas por incendios se podría identificar mejor como consecuencia de la dependencia de la polarización de las ondas reflejadas de las propiedades del objeto (contenido de humedad de la vegetación o del suelo). La estimación de la biomasa forestal o la identificación de las especies se han beneficiado del uso de datos polarimétricos que han incrementado el contenido temático de la información.

Por último, hay que resaltar el potencial ofrecido por el uso conjunto de diferentes bandas y polarizaciones para la estimación de las características biofísicas de las superficies, como ha sido demostrado mediante sensores radar aeroportados. Sin embargo, en esta tesis no ha sido posible indagar en esta dirección debido a la falta de sensores multi-banda a bordo de las plataformas espaciales. Aunque se ha intentado utilizar de modo conjunto la información procedente de los sensores espaciales mono-banda, los resultados obtenidos no han sido óptimos debido principalmente a la geometría de visualización diferente (ascendente/descendente y ángulo de incidencia variable) y a la variación de las propiedades de las superficies, entre adquisiciones, con las condiciones climáticas. Por lo tanto, hasta que no estén disponibles sensores satelitales multi-banda será difícil entender y utilizar este potencial, así como desarrollar algoritmos adecuados para la estimación automática de la severidad y la recuperación de la vegetación, aprovechando la sinergia inherente entre las diferentes bandas.

CONCLUSIONS

The properties of SAR backscatter and interferometric coherence in mediterranean and boreal burned forests were investigated for X-, C- and L-bands co- and cross-polarized data. In addition, the synergy of backscatter and coherence use for burn severity estimation was evaluated. Finally, the potential of active microwave remote sensing for forest regrowth monitoring in fire affected areas was also studied. The most important findings of the study are resumed below:

1. Reliable estimates of burn severity can be obtained using optical remote sensing images for areas of high or low severity in the pine forests of Aragon. However, for areas of intermediate severity the estimation error increases and model inversion is less accurate.

2. Synthetic aperture radar systems have potential for burn severity estimation using either backscatter coefficient or the interferometric coherence. The potential of SAR data decreased with increasing frequency for both SAR metrics. The best results were obtained using cross-polarized channel in the case of backscatter and co-polarized channel in the case of coherence.

3. The joint use of the backscatter and the coherence did not improve significantly the estimation of burn severity in any of the radar frequencies tested.

4. The satellite viewing geometry (look angle) influenced the backscatter coefficient in form of an offset. However, the system's sensitivity to burn severity did not change significantly.

5. The correlation between the backscatter coefficient and burn severity increased with increasing spatial resolution, i.e. stronger speckle reduction after applying high multi-look factors.

6. The radar signal was strongly influenced by the topography. It is therefore imperative to take into account the local slope of the surface. Although in the case of interferometric coherence topography influence was lower, better results were obtained when the local incidence angle was considered.

7. A major error source for the estimation of burn severity was the environmental condition at image acquisition. In some specific cases and for certain polarizations precipitation could increase the sensitivity of SAR data to burn severity. However, the increased sensitivity was not always related to rainfall. Therefore, it is difficult to predict whether images acquired under wet condition would always represent the better choice especially after heavy precipitations.

8. Vegetation recovery monitoring was feasible using the backscatter coefficient of low-frequency bands (L). The high frequency bands (X and C) were less sensitive to changes in forest structure having a much lower potential for differentiating between regrowth stages.

9. Interferometric coherence (all frequencies) was almost insensitive to differences in forest structure except for recently burned areas where only low vegetation (e.g. grass and shrubs) was present.

10. Preliminary results from boreal forest confirmed the data trends obtained in the Mediterranean basin at least for specific environmental conditions (images acquired during the growing season in relatively dry conditions).